Isogeometric analysis based on rational splines over hierarchical T-meshes and alpha finite element method for structural analysis

DISSERTATION

zur Erlangung des akademischen Grades
Doktor-Ingenieur (Dr.-Ing.)
an der Fakultät Bauingenieurwesen
der
Bauhaus Universität Weimar

vorgelegt von

M.Sc. Nhon NGUYEN-THANH
geboren am 26. Juli 1980 in Tien Giang, Viet Nam

Weimar, Mai 2013

Mentor:
    Prof. Dr.-Ing. Timon Rabczuk, Bauhaus Universität Weimar
Gutachter:
    Prof. Dr. Stéphane Bordas, Cardiff University, UK
    Prof. Dr. rer. nat. Klaus Güerlebeck, Bauhaus Universität Weimar

Disputation am 30. September 2013

To my whole family ...

Acknowledgements

The process carrying out this research and writing thesis has been wonder adventure and very exciting time. Nevertheless, it has not been without its share of pain and I could not have achieved this work without the help, support and encouragement of many around me.

First of all my deepest gratitude goes to my supervisor, Prof. Dr.-Ing Timon Rabczuk, for his guidance and encouragement thought my research work. His great enthusiasm as a teacher is inspiring, and his wise suggestions regarding my thesis work were always very useful.

Furthermore, I would like to thank to Prof. Dr. rer. nat. Klaus Güerlebeck for his comments during the review and the defense of my thesis. Special thank to Prof. Stephane Bordas for accepting the presidency of the examination board. In addition to that, an endless gratitude to him and his group for the cooperation during my three months attachment at Cardiff University, UK.

During my research, I spent eleven months at institute of Dr. Jacob Muthu in the University of Witwaterstand, South Africa. Many thanks to him for his kind friendly and the nice cooperation. I would also like to thanks to Prof. Hung Nguyen-Xuan, Prof. Yuri Bazilves and Dr. Joself Kiendl for their assistance insightful suggestions and collaboration in research.

I am grateful to thank to my colleagues at Institute of Structural Mechanics for their help and friendly support.

Finally, a precious thank you to my family especially to my parents for their emotional supports and encouragement during my studies.

Weimar, October 2013

Nhon NGUYEN-THANH

Abstract

This thesis presents two new methods in finite elements and isogeometric analysis for structural analysis. The first method proposes an alternative alpha finite element method using triangular elements. In this method, the piecewise constant strain field of linear triangular finite element method models is enhanced by additional strain terms with an adjustable parameter α, which results in an effectively softer stiffness formulation compared to a linear triangular element. In order to avoid the transverse shear locking of Reissner-Mindlin plates analysis the alpha finite element method is coupled with a discrete shear gap technique for triangular elements to significantly improve the accuracy of the standard triangular finite elements. The basic idea behind this element formulation is to approximate displacements and rotations as in the standard finite element method, but to construct the bending, geometrical and shear strains using node-based smoothing domains. Several numerical examples are presented and show that the alpha FEM gives a good agreement compared to several other methods in the literature.

Second method, isogeometric analysis based on rational splines over hierarchical T-meshes (RHT-splines) is proposed. The RHT-splines are a generalization of Non-Uniform Rational B-splines (NURBS) over hierarchical T-meshes, which is a piecewise bicubic polynomial over a hierarchical T-mesh. The RHT-splines basis functions not only inherit all the properties of NURBS such as non-negativity, local support and partition of unity but also more importantly as the capability of joining geometric objects without gaps, preserving higher order continuity everywhere and allow local refinement and adaptivity. In order to drive the adaptive refinement, an efficient recovery-based error estimator is employed. For this problem an imaginary surface is defined. The imaginary surface is basically constructed by RHT-splines basis functions which is used for approximation and interpolation functions as well as the construction of the recovered stress components. Numerical investigations prove that the proposed method is capable to obtain results with higher accuracy and convergence rate than NURBS results.

Contents

1 Introduction 1
1.1 Review of Finite Element Analysis . . . 1
1.2 Review of Isogeometric Analysis . . . 2
1.3 Outline . . . 5

2 Finite Element Analysis 7
2.1 Governing equations and weak form for solids . . . 7
2.2 Discrete governing equations and weak form for Reissner-Mindline plate . . . 9

3 An alternative alpha Finite Element Method for free and forced vibration analysis of solids using triangular element 13
3.1 Introduction . . . 13
3.2 Construction of an assumed strain field . . . 14
3.3 Weak form for modified strain field . . . 17
3.4 Forced and free vibration analysis . . . 18
3.5 Numerical results . . . 19
3.5.1 Static analysis . . . 19
3.5.1.1 Cantilever beam due to a parabolic traction at the free end . . . 19
3.5.1.2 Infinite plate with a circular hole . . . 20
3.5.2 Free and forced vibration analysis . . . 24
3.5.2.1 Free vibration analysis of a cantilever beam . . . 29
3.5.2.2 Free vibration analysis of tapered cantilever plate with central circular hole . . . 29
3.5.2.3 Free vibration analysis of a shear wall . . . 33
3.5.2.4 Free vibration analysis of a connecting rod . . . 33
3.5.2.5 Free vibration analysis of a machine part . . . 41
3.5.2.6 Forced vibration analysis of a cantilever beam . . . 41
3.6 Concluding remarks . . . 46

4 **An alternative alpha Finite Element Method for Mindlin-Reissner plates analysis with Discrete Shear Gap technique** 47

4.1 Introduction . . . 47
4.2 Weak form for modified strain field . . . 48
4.3 Numerical results . . . 52
4.3.1 Static analysis . . . 52
4.3.1.1 Patch test . . . 52
4.3.1.2 Square plates . . . 53
4.3.1.3 Skew plate subjected to a uniform load . . . 56
4.3.2 Free vibration of plates . . . 58
4.3.2.1 Square plates . . . 58
4.3.2.2 Circle plates . . . 61
4.3.2.3 Triangular plates . . . 61
4.3.2.4 Free vibration analysis of the machine part . . . 64
4.3.3 Buckling of plates . . . 64
4.3.3.1 Simply supported rectangular plates subjected to uniaxial compression . . . 68
4.3.3.2 Simply supported rectangular plates subjected to biaxial compression . . . 73
4.3.3.3 Simply supported rectangular plates subjected to in-plane pure shear . . . 73
4.4 Concluding remarks . . . 76

5 **Isogeometric Analysis** 77

5.1 Bézier basis function . . . 77
5.2 B-Splines basis function . . . 80

6 **Isogeometric analysis using rational splines over hierarchical T-meshes for two-dimensional elastic solids** 83

6.1 Introduction . . . 83
6.2 Rational splines over hierarchical T-meshes . . . 87
6.2.1 2D T-meshes . . . 87
6.2.2 Hierarchical T-meshes . . . 87
6.2.3 A dimension formula . . . 87
6.3 RHT-spline basis functions . . . 88
6.3.1 Definition of knot vectors . . . 88
6.3.2 Modification of the basis functions at level k . . . 89
6.3.3 Modification of the basis functions at level $k+1$ . . . 91
6.3.4 Properties of the basis functions . . . 92
6.4 Numerical results . . . 93

6.4.0.1 Cantilever beam subjected to a parabolic traction at the free end 93
6.4.0.2 Infinite plate with a circular hole 97
6.4.0.3 A hollow cylinder subjected to inner pressure: a plane stress problem 97
6.4.0.4 L-shaped panel subjected traction 104
6.5 Concluding remarks 104

7 An adaptive three-dimensional RHT-spline formulation in linear elasto-statics and elasto-dynamics 108
7.1 Introduction 108
7.2 Rational splines over 3D hierarchical T-meshes 109
7.2.1 3D T-meshes 109
7.2.2 Hierarchical T-meshes 109
7.2.3 A dimension formula 110
7.3 Stress recovery in isogeometric analysis 112
7.4 Numerical example 114
7.4.1 Static analysis 114
7.4.1.1 Three dimension Lame problem 114
7.4.1.2 Pinched Cylinder 117
7.4.1.3 Solid “horseshoe” subjected to equal and opposite in-plane flat edge displacements 117
7.4.2 Free vibration analysis 119
7.4.2.1 Free vibration analysis of a cantilevered rectangular plate 119
7.4.2.2 Free vibration analysis of square plate 125
7.5 Conclusion 129

8 Rotation free isogeometric thin shell analysis using RHT-splines 130
8.1 Introduction 130
8.2 Thin shell model 131
8.2.1 Kinematics of the shell 131
8.2.2 Equilibrium deformations of thin shells 133
8.2.3 Galerkin discretization 134
8.3 RHT-splines with multi-patches 135
8.3.1 Continuity conditions for RHT-splines surface 135
8.3.2 Connecting surface multi-patches 136
8.4 Numerical results 138
8.4.1 Single patch analysis 138
8.4.1.1 Scordelis - Lo roof 138
8.4.1.2 Pinched cylinder with diaphragm 143

8.4.1.3 Hemispherical shell 146
8.4.2 Multi-patches analysis 150
8.4.2.1 Pinched Cylinder 150
8.4.2.2 A wind turbine rotor 153
8.5 Concluding remarks 156

9 Conclusions **157**
9.1 Summary of achievements 157
9.2 Outlook 159

References **160**

Curriculum Vitae **175**

List of Figures

2.1 Geometry of a typical Mindlin-Reissner plate 10

3.1 Triangular elements and smoothing cells 15
3.2 A cantilever beam 20
3.3 Strain energy of the cantilever beam 21
3.4 Normalized strain energy of the cantilever beam 22
3.5 Vertical displacement of the cantilever beam 22
3.6 Convergence rate in the displacement error norm 23
3.7 Convergence rate in the energy error norm 23
3.8 Infinite plate with a circular hole and its quarter model 24
3.9 The infinite plate with a circular hole 25
3.10 Strain energy of the infinite plate with a hole 25
3.11 Normalized strain energy of the plate with a hole 26
3.12 Horizontal displacement of the plate with a hole 26
3.13 Vertical displacement of the plate with a hole 27
3.14 Distribution of stress along the left boundary 27
3.15 Distribution of stress along the bottom boundary 28
3.16 Solution bounds of energy 28
3.17 Convergence rate in the displacement norm 29
3.18 Convergence rate in the energy norm 30
3.19 A cantilever beam 30
3.20 First eight modes of a cantilever beam 32
3.21 Tapered cantilever plate 33
3.22 First eight modes of the tapered cantilever plate 34
3.23 A shear wall with four openings 35
3.24 Frequencies of the shear wall 36
3.25 Geometric model of an automobile connecting rod 37
3.26 First eight modes of a connecting rod 40
3.27 A machine part 41
3.28 First eight modes a machine part 43
3.29 Cantilever beam for forced vibration 44

3.30 Displacement u_y using Newmark method 44
3.31 Displacement with $(g(t) = sin(\omega t))$ 45
3.32 Transient displacement without damping 45
3.33 Transient displacement with damping 46

4.1 Area coordinates and three node triangle element 51
4.2 Patch test of the element 53
4.3 Simply supported and full clamped plate 54
4.4 The error in strain energy of supported plate 54
4.5 Normal deflection and moment 55
4.6 The error in strain energy of clamped plate plate 55
4.7 Normal deflection and moment of clamped plate plate 56
4.8 A simply supported skew Morley's model 56
4.9 Morley plates central deflection 57
4.10 Morley plates max principle moment 57
4.11 Supported and clamped plate 58
4.12 Convergence of normalized frequency 59
4.13 The shape models of clamped plate 60
4.14 The circle plates and initial mesh 61
4.15 The shape modes of the clamped circle plate 62
4.16 A triangular cantilever plates and mesh 64
4.17 The shape modes of triangular plates 65
4.18 A machine part and mesh 68
4.19 The shape modes of the machine part 69
4.20 The buckling load of the rectangular plates 70
4.21 Normalized buckling load square plate 70
4.22 Axial buckling modes of supported rectangular plates 71
4.23 Normalized shear buckling load 74
4.24 Shear buckling mode of supported rectangular plates 75

5.1 Bézier curve 78
5.2 Subdivision of Bézier curve using de Casteljau's algorithm 79
5.3 B-spline curves 81
5.4 Parametric and physical space 81
5.5 A bivariate cubic B-spline 82

6.1 Tensor product global refinement 85
6.2 An illustration of T-meshes 86
6.3 An illustration of boundary, crossing and T-junctional vertices 87
6.4 This figure illustrate cubic shape basis of B-spline 89
6.5 Four basis functions and their support 90

6.6 16 basis function values of a basis function $b_i^k(\xi, \eta)$ 90
6.7 Modification of a basis function 91
6.8 Modification of a basis function 92
6.9 A cantilever beam and the meshes 95
6.10 Normalized strain energy of the cantilever beam 95
6.11 Error in energy norm of the cantilever beam 96
6.12 Displacement and stress component of the cantilever beam 96
6.13 The elastic plate with circular hole and meshes. 98
6.14 Normalized displacement of the plate with a hole 99
6.15 Convergence rate in the energy norm 99
6.16 Displacement and stress components of the plate hole 100
6.17 A hollow cylinder subjected to inner pressure 101
6.18 Normalized strain energy of the hollow cylinder 102
6.19 Normalized strain energy of a hollow cylinder 102
6.20 Displacement and stress components of a hollow cylinder 103
6.21 L-shaped panel subjected traction and the meshes 105
6.22 Normalized strain energy of the L-shape panel 106
6.23 Error in the energy norm for the L-shape 106
6.24 Displacement and stress components for the L-shape 107

7.1 An illustration a typical 3D T-mesh with boundary vertices 109
7.2 A hierachical over 3D T-mesh. 110
7.3 An example regarding imaginary solid in three dimensional. 112
7.4 Hollow sphere model 115
7.5 Contour plot of displacement of hollow sphere 116
7.6 Distribution of the radial displacement and stresses 116
7.7 Convergence rate of hollow sphere 117
7.8 Contour plot displacement of the cylindrical shell 118
7.9 Convergence in displacement of pinched cylinder 118
7.10 Relative in the energy norm error 119
7.11 Pinched cylinder model 120
7.12 A horseshoe geometry 121
7.13 Contour plot of displacement 122
7.14 Relative in the energy norm error 122
7.15 A cantilevered rectangular plate model 123
7.16 The first six shape modes of a cantilevered rectangular plate 124
7.17 Square plate geometry and boundaries condition 125
7.18 The meshes of square plate 126
7.19 The first six shape modes 127
7.20 Convergence of normalized frequencies 128
7.21 Convergence rates in the eigenfrequencies of mode 1 128

8.1 The reference and deformed configurations of thin shell 132
8.2 Continuity condition for surface over T-mesh 136
8.3 Common boundary 137
8.4 The Scordelis-Lo roof and meshes 139
8.5 Convergence in displacement of the roof 140
8.6 Convergence of strain energy of the roof 140
8.7 Error in energy norm of the roof 141
8.8 Contour plots of the vertical displacement 141
8.9 Contour plot of the force and moment resultants 142
8.10 Convergence in displacement of pinched cylinder 143
8.11 Pinched cylinder and meshes 144
8.12 Convergence of strain energy of pinched cylinder 145
8.13 Error in energy norm of pinched cylinder 145
8.14 Contour plots of displacement 146
8.15 Hemispherical shell model and meshes 147
8.16 Convergence in displacements of a hemispherical shell 148
8.17 Convergence of strain energy 148
8.18 Error in energy norm of a hemispherical shell 149
8.19 Contour plots of displacement 149
8.20 Pinched cylinder is subdivided into 8-patches 150
8.21 Displacement, force and moment resultants 151
8.22 Convergence in displacement 152
8.23 Energy convergence of the pinched cylinder 152
8.24 The wind turbine rotor 153
8.25 The wind turbine blade is subdivided into 16-patches 154
8.26 Displacement and deformed of the blade 154
8.27 Displacement, force and moment resultants 155
8.28 Convergence in displacement 156

List of Tables

3.1 Natural frequencies of a cantilever beam 31
3.2 Numerical error of the beam natural frequencies 31
3.3 Frequencies of the tapered cantilever plate 37
3.4 Frequencies of a shear wall 38
3.5 Frequencies of a connecting rod 39
3.6 Frequencies of a machine part 42

4.1 Summary elements 52
4.2 Patch test of the element 52
4.3 A non-dimensional frequency parameter 59
4.4 The frequencies of a clamped circular plate with $t/2*R = 0.01$ 63
4.5 The frequencies of a clamped circular plate with $t/2*R = 0.1$ 63
4.6 The frequencies of a triangular platess with $t/b = 0.001$ 66
4.7 The frequencies of a triangular platess with $t/b = 0.2$ 67
4.8 Natural frequency of the machine part 68
4.9 The axial buckling load of support and clamped plates 71
4.10 Numerical error of support and clamped plates 72
4.11 The axial buckling load of plates with various boundary conditions . . 72
4.12 The axial buckling with various length-to-width ratios and various thickness-to-width ratios 73
4.13 The biaxial buckling load of plates with various boundary conditions . 73
4.14 The shear buckling load of supported plates 74
4.15 The shear buckling load of plates with various boundary condition . . 75

7.1 Natural frequency of a cantilevered rectangular plate 119
7.2 A non-dimensional frequency parameter of SSSS plate 125
7.3 A non-dimensional frequency parameter of CCCC plate 126

Nomenclature

Latin Symbols

$\mathbf{J}$	Jacobian matrix
$\bar{\mathbf{B}}_k$	Nodal strain displacement matrix of node k
$\mathbf{B}$	Gradient matrix
$\mathbf{b}_i^k$	RHT-splines basis functions at level k
$\mathbf{B}_m$	Bending strain matrices
$\mathbf{B}_n$	Membrane strain matrices
$\mathbf{C}$	Damping matrix
$\mathbf{D}$	Matrix of material
$\ddot{\mathbf{u}}$	Acceleration
$\dot{\mathbf{u}}$	Velocity
$\mathbf{e}$	Basis vectors of an orthonormal coordinate system
$\mathbf{F}$	Deformation gradient
$\mathbf{f}$	Global force vector
$\hat{\mathbf{K}}_{\alpha}^{\mathrm{A}\alpha\mathrm{FEM}}$	The global stiffness matrix with the scaled gradient strains
$\mathbf{I}$	Identity tensor
$\mathbf{K}$	Global stiffness matrix
$\mathbf{M}$	Mass matrix
$\mathbf{P}$	Control points

$\mathbf{R}$	Rational basis function
$\tilde{\mathbf{B}}_k^b$	Smoothed bending gradient matrices
$\tilde{\mathbf{B}}_k^g$	Smoothed geometrical gradient matrices
$\tilde{\mathbf{B}}_k^s$	Smoothed shear gradient matrices
$\mathbf{u}$	Displacement field
A^e	Area of the triangular element
A_k	Area of the smoothing domain Ω_k
$B_{i,p}$	Bernstein polynomials
E	Young's modulus
$E_{\alpha\beta}$	Covariant strain coefficients
$g_{\alpha\beta}$	Covariant metric tensor
g_α	Covariant base vectors
$N_{i,p}$	B-splines basis functions
V^+	Interior crossing vertices
V^b	Boundary vertices
w	Weights

Greek Symbols

α	Adjustable factor
$\bar{\varepsilon}$	A smoothed strain for node k
$\hat{\varepsilon}$	Strain field within a sub-triangular domain
$\kappa_{\alpha\beta}$	Curvature tensors
λ_{cr}	Critical buckling load
$\mathscr{L}$	Linear operator
$\mathscr{T}$	Dimensional space
ν	Poisson's ratio

ω	Natural frequency
ρ	Mass density
σ_{xx}	Normal stress in x direction
σ_{yy}	Normal stress in y direction
τ_{xy}	Shear stress
$\tilde{\varepsilon}_k^b$	Smoothed average curvature strains
φ	Deformed shell surface in terms of basis functions
φ_0	Reference geometry in terms of basis functions
σ	Exact stress
σ^*	Recovered stress
σ^h	Numerical stress
ε_k^g	Smoothed geometrical strains
ε_k^s	Smoothed shear strains
Ξ	Knot vector in ξ direction
ξ, η	Parametric coordinates

Abbreviations

AαFEM	Alternative alpha Finite Element Method
CAD	Computer Aided Design
CAE	Computer Aided Engineering
DOF	Degree(s) of freedom
FEA	Finite Element Analysis
FEM	Finite Element Method
IGA	Isogeometric Analysis
NURBS	Non-Uniform Rational B-splines
RHT-splines	Rational splines over hierarchical T-meshes
SPR	Superconvergent Patch Recovery

Chapter 1

Introduction

1.1 Review of Finite Element Analysis

The Finite Element Method (FEM) was developed in the 1950s to 1960s. Nowadays, the FEM has become one of the most powerful and popular tools for numerical simulations in various fields of natural science and engineering. For instance in most structural analysis applications, the FEM has become necessary to compute displacements and stresses at various points of interest. The finite element model is created by dividing the structure into a number of finite elements. Each element is connected by nodes. The selection of elements for modeling the structure depends on the behavior and geometry of the structure being analyzed. The modeling pattern, which is generally called the ”mesh” for the finite element method, is a very important part of the modeling process. The results obtained from the analysis depend upon the selection of the finite elements and the mesh size. Although the finite element model does not behave exactly like the actual structure, it is possible to obtain sufficiently accurate results for most practical applications. The deflections at each node of the finite element model are obtained by solving the equilibrium equations. The stresses and strains can then be obtained from the stress-strain and strain-displacement relations.

In the finite element method, higher-order elements (ZT00) are capable of providing excellent performance for complex problems including those involving materials with near incompressibility, whilst lower-order elements are preferable to employ in practice. However, these elements are often too stiff so that the elements become sensitive to locking. In practice, the lower-order linear triangular element is preferred by many engineers due to its simplicity, efficiency, lower demand on the smoothness of the solution, and ease of adaptive mesh refinements for solutions of desired accuracy. However, the fully-compatible FEM model using 3-node triangular element (T3) has certain inherent drawbacks: overestimation of the stiffness matrix (Liu08), especially for problems with locking behavior; poor performance when distorted meshes are used and poor accuracy in the stress results. One of the attempts to improve the constant strain triangular element is to add an in-plane rotational degree of freedom which was initially proposed by Allman (All84). Also the concept of enhanced strains Simo *et.al.* (SR90) has been applied by many authors to improve the performance of low order finite elements (PT00, BRB99, SJ99).

A superconvergent alpha finite element method (SαFEM) using triangular meshes was proposed by Liu *et al* (LNXNTX09). In the SαFEM (now AαFEM), an assumed strain field was formulated by adding the averaged nodal strains with an adjustable factor α to the compatible strains. The new Galerkin-like weak form, as simple as the Galerkin weak form, was then obtained for this constructed strain field. To solve the forced vibration system equations, implicit time integration schemes are used. It was also extended to Reissner-Mindlin plates analysis by using the Direct Shear Gap (DSG) technique to remove shear locking. This leads to a stiffness matrix that comprises an additive decomposition of two parts: (i) the DSG plate element stiffness matrix and (ii) the stiffness matrix contributed from the assumed strain field. Where was proven theoretically and numerically that the AαFEM is much more accurate than the original FEM-T3 and even more accurate than the FEM-Q4 when the same sets of degrees of freedom are used. The AαFEM can produce both lower and upper bounds to the exact solution in the energy norm for all elasticity problems by properly choosing an α. In addition, a preferable-α approach has also been devised for the alpha FEM to produce very accurate solutions for both displacement and energy norms and the superconvergent rate in the energy error norm.

1.2 Review of Isogeometric Analysis

In the past, engineers used splines to design aircraft wings and automobile chassis before computer graphics existed. A spline is a long flexible piece of wood or plastic with a rectangular cross section held in place at various positions by heavy lead weights with a protrusion called ducks, where the duck holds the spline in a fixed position against the drawing board (Bea91). The spline then conforms to a natural shape between the ducks. By moving the ducks around, the designer can change the shape of the spline. The drawbacks are obvious, recording duck positions and maintaining the drafting equipment necessary for many complex parts will take up much square footage in a storage facility, costs that would be absorbed by a consumer. In the 1960, Pierre Bézier developed computer aided geometric design (CAGD) tool called UNISURF. This new software allowed designers to draw smooth looking curves on a computer screen, and use less physical storage space for design materials. Bézier's contribution to computer graphics paved the road for CAD software like Maya, 3D

Max, etc,.. Consecutively, Paul de Faget de Casteljau who has proposed the Casteljau algorithm, one of the most common ways to evaluate Bézier curves.

The B-spline basis functions were introduced by Schoenberg (Sch46). In the field of computer science, B-splines have been referred to as piecewise polynomial curves (ANW67). Since their introduction, they have been used as a tool to create smooth curves and surfaces in computer graphics. These functions provide a smooth interpolated curve for a large number of control points, and also provide a higher continuity of derivatives. In the 1962, Carl De Boor's (Boo62) developed faster and numerically stable algorithms for the calculation of spline interpolation functions. B-Splines are now extensively used in the graphic design and CAD industry for creating smooth curves and surfaces.

In the 1970's, Non-uniform rational B-splines (NURBS) were developed and are the current industry standard for computational geometry. They are an ubiquitous tool in CAD and computer graphics and provide a general notation for representing a broad range of geometries. This includes straight lines, curves and complex curved surfaces and, most importantly, even allow the representation of solids. The concept of isogeometric analysis was developed by Hughes and co-workers in 2005 (HCB05) with the aim of integrating the conventional FEM and CAD. The idea behind this method is to base both the geometric description and the shape functions of the FEM on NURBS, a standard technology embedded in CAD systems, so the exact geometry is presented in both design and mechanics analysis procedures. The coarse mesh of the NURBS element constructed by the exact CAD geometry is subsequently refined without communication with the CAD system, but retaining exact geometry, which is the reason of so-called isogeometric analysis. Although NURBS is suggested as a direct step from CAD to FEA, the process is not as streamlined. NURBS models are often made of several patches and contain gaps which are invisible in modeling perspective, but inhibit on the analysis to be performed. Another weakness is that NURBS do not allow for local refinement. In order to refine a local area, a global refinement is required because the B-spline control grid traverses the entire domain. As a result of global refinement, many superfluous control points are created. NURBS also have certain drawbacks in the context of numerical analysis. Due to the tensor-product form of NURBS, their control points are required to lie in a structured grid (e.g. in a rectangle in 2D). This leads to an excessive overhead of control points with increasing refinement. Cottrell *et. al.* (CHR07) proposed a local refinement strategy, but constraint equations are required with increasing complexity and implementation effort. Moreover, refinement still propagates through a given patch. Another disadvantage of NURBS is that they usually achieve only C^0 continuity across patch boundaries. However, when two NURBS surfaces do not share a common boundary, they cannot even achieve C^0 continuity without disturbing at least one of the surfaces.

In the 2003, the T-splines were introduced by Sederberg *et. al.* (SZBA03) as a generalization of NURBS technology that is capable of substantially reducing the number of superfluous control points. T-splines offer a solution to this by their local refinement property by using T-junctions, which allows the ability to remove gaps at intersections of geometric model shapes. Therefore, very effective and efficient local refinement can be made by using T-splines and T-junctions, since control mesh lines do not have to traverse the entire control grids in order to maintain the B-spline structure. Consecutively, Sederberg *et. al.* (SCF+04) presented a robust algorithm for eliminating superfluous control points, refining blending functions, and updating the positions of control points. As a result, the number of control points is reduced and the computational efficiency is greatly improved by T-spline functions. Recently, an isogeometric analysis using T-splines was exploited by Bazilevs *et.al.* (BCC+10). Consecutively, an adaptive local h-refinement with T-splines was introduced by Döfel *et. al.* (DJS10). However, though T-splines allow for local adaptive refinement, the complexity of knot insertion under adaptive refinement is complex, particularly in 3D. Moreover, Buffa *et. al.* (BCS09) showed that linear independence of the basis functions is not guaranteed for generic T-meshes.

In the 2008, a new type of splines called polynomial splines over hierarchical T-meshes (PHT-splines) was introduced by Deng *et.al.* (DCL+08). The PHT-spline consisting of rectangles are special cases of T-splines, which are very useful for curve and surface design. The PHT-spline is a piecewise bicubic polynomial over a hierarchical T-mesh, which has the same important properties of NURBS such as linear independence of the basis functions, partition of unity and non-negativity. Not only do PHT-splines inherit of T-splines such as adaptivity and locality, but also extend T-splines in several aspects except that they are only C^1 continuous. The conversion between NURBS and PHT-splines is simple and very fast, while conversion between NURBS and T-splines is a bottleneck of T-splines in practical applications. Moreover, in contrast to NURBS, PHT-splines have the capability of joining geometric objects without gaps, preserving higher order continuity everywhere and allow for simple and effective h-refinement strategies. Thereafter, Nguyen-Thanh *et.al.* demonstrated the use of PHT-spline formulations in numerical analysis for problems in two-dimensional and thin shell analysis (NTNXBR11, NTKNX+11). Recently, the RHT-splines is extended of the PHT-splines to rational functions for 3D problems in elasto-statics and elasto-dynamics. In order to drive the adaptive refinement, an efficient recovery-based error estimator is employed. Numerical investigations prove that the proposed method is capable to obtain results with higher accuracy and convergence rate than NURBS results. A good agreement was achieved between the numerical and analytical results for both static and free vibration problems.

1.3 Outline

A briefly review the discrete governing equations and weak form of finite element method for two-dimensional and Reissner-Mindline plate element are presented in Chapter 2.

An alternative alpha finite element method is proposed in Chapter 3. In the alpha finite element method, the piecewise constant strain field of linear triangular FEM models is enhanced by additional strain terms with an adjustable parameter α which results in an effective softer stiffness formulation compared to a linear triangular element. Thereafter, some theoretical properties of the alpha FEM method for static and free vibration analysis are presented and discussed.

In Chapter 4, the alpha FEM method for plates analysis is presented. To avoid the transverse shear locking of Reissner-Mindlin plate analysis the alpha finite element method coupled with a discrete shear gap technique for triangular elements is introduced. The results obtained from static, free vibration and buckling analyses are shown that the alpha FEM achieves high reliability compared to other existing elements in the literature.

In Chapter 5, the computer aided design basic geometry for the development into the isogeometric analysis method is reviewed: First, a short overview of the general Bézier function and the drawbacks are given. Then, these problems can be overcome by using B-Spline basis function. The differences parametric mapping in finite element method and isogeometric analysis are presented in this chapter.

In Chapter 6, the concept of rational splines over hierarchical T-meshes (RHT-splines) is introduced. The RHT-splines is a piecewise bicubic polynomial over a hierarchical T-mesh. The RHT-splines basis functions not only inherit all the properties of NURBS such as non-negativity, local support and partition of unity but also more importantly as the capability of joining geometric objects without gaps, preserving higher order continuity everywhere and allow local refinement and adaptive. To describe and construct of the RHT-splines basis functions two-dimensional elastic solids are presented.

In Chapter 7, an adaptive three-dimensional RHT-splines formulation in linear elasto-statics and elasto-dynamics is introduced. The RHT-splines basis function in three-dimensional are described. In order to drive the adaptive refinement with stress recovery for RHT-splines is presented. The propose method is applied to several problems in elasto-statics and elasto-dynamics. The results obtained from the proposal method are shown and discussed in numerical example section.

Chapter 8, rotation free isogeometric thin shell analysis using RHT-splines for both single patch and multi-patches are presented. Due to the C^1-continuity of the RHT-splines, I only discretize the mid-surface of the shell and automatically fulfill the Kirchhoff-Love constraint. Therefore, only 3 DOFs per node are needed. The thin shell analysis based on Kirchhoff-Love theory avoids the use of rotational degrees of freedom. Numerical results show the excellent performance of the present method.

Finally, Chapter 9 presents concluding remarks and discusses further work.

Chapter 2

Finite Element Analysis

2.1 Governing equations and weak form for solids

In that follows, a two dimensional linear elastic solid is modeled as a planar domain Ω and a body force $\mathbf{g}$ within the domain. The displacement field satisfies the Dirichlet boundary conditions $\mathbf{u} = \bar{\mathbf{u}}$ on Γ_u and the stress field satisfies the Neumann boundary conditions $\mathbf{t}$ on boundary Γ_t. Arbitrary virtual displacements $\boldsymbol{\delta}\mathbf{d}$ result in compatible virtual strains $\delta\varepsilon$ and internal displacements $\boldsymbol{\delta}\mathbf{u}$.
The relation between the displacement field u, the strain field ε and the stress field σ are
The compatibility relations

$$\varepsilon_{i,j} = \frac{1}{2}\left(\partial_j u_i + \partial_i u_j\right) \qquad \text{in} \quad \Omega \qquad (\forall i, j \in 1,2,3) \tag{2.1}$$

$$u_i = \bar{u}_i \qquad \text{on} \quad \Gamma_u \tag{2.2}$$

The constitutive relations

$$\sigma_{ij} = C_{ijkl}\varepsilon_{kl} \qquad \text{in} \qquad \Omega \tag{2.3}$$

The equilibrium equations

$$\partial_j \sigma_{ij} + g_i = 0 \qquad \text{in} \qquad \Omega \tag{2.4}$$

$$\sigma_{ij} n_j = \bar{t}_i \qquad \text{on} \qquad \Gamma_t \tag{2.5}$$

where $\partial_j = \partial/\partial x_i$ are the partial derivatives of first order corresponding to $x_i \in \{x, y\}$ and ∂ denotes a differential operator for description of the strains obtained by the displacements. Let the two spaces of kinematically admissible displacements, denoted by $\mathscr{V}$ and $\mathscr{V}_0$, respectively

$$\mathscr{V} = \{\mathbf{u} \in (H^1(\Omega))^2\,, \quad \mathbf{u} = \bar{\mathbf{u}} \quad \text{on} \quad \Gamma_{\mathbf{u}}\}. \tag{2.6}$$

$$\mathscr{V}_0 = \{\mathbf{v} \in (H^1(\Omega))^2\,, \quad \mathbf{v} = \mathbf{0} \quad \text{on} \quad \Gamma_{\mathbf{u}}\} \tag{2.7}$$

Here, $H^1(\Omega)$ denotes the Hilbert space of order 1 defined as

$$H^1(\Omega) = \left\{ u | \|u\|_{H^1(\Omega)} \leq \infty \right\} \tag{2.8}$$

with

$$(u,v)_{H^1(\Omega)} = (u,v)_{L^2(\Omega)} + (\nabla u, \nabla v)_{L^2(\Omega)}\ ; \quad \|u\|_{H^1(\Omega)} = \left[(u,v)_{H^1(\Omega)}\right]^{1/2} \tag{2.9}$$

and ∇ is the gradient vector.
The spaces, $\mathscr{V}$ and $\mathscr{V}_0$, lead to a bounded energy in a stable solid

$$\int_\Omega C_{ijkl}\varepsilon_{ij}(\mathbf{u})\varepsilon_{kl}(\mathbf{v})\mathrm{d}\Omega < \infty\,. \tag{2.10}$$

From Eq. (2.10), both $\mathscr{V}$ and $\mathscr{V}_0$ may be equipped with the energy norm

$$\|\mathbf{u}\|_E = \left(\int_\Omega C_{ijkl}\varepsilon_{ij}(\mathbf{u})\varepsilon_{kl}(\mathbf{v})\mathrm{d}\Omega \right)^{1/2} \tag{2.11}$$

where $\mathbf{C}$ is a bounded positive definite matrix. The problem stated in the weak form is given by: find $\mathbf{u} \in \mathscr{V}$ such that

$$\forall \mathbf{v} \in \mathscr{V}_0,\ a(\mathbf{u},\mathbf{v}) = f(\mathbf{v}) \tag{2.12}$$

where

$$a(\mathbf{u},\mathbf{v}) = \int_\Omega \varepsilon^T(\mathbf{u})\mathbf{D}\varepsilon(\mathbf{v})\mathrm{d}\Omega\ \ ,\ \ f(\mathbf{v}) = \int_\Omega \mathbf{g}^T\mathbf{v}\mathrm{d}\Omega + \int_{\Gamma_\mathbf{t}} \bar{\mathbf{t}}^T\mathbf{v}\mathrm{d}\Gamma \tag{2.13}$$

Now let $\mathscr{V}^h$ be a finite-dimensional subspace of space $\mathscr{V}$. The statement of the discrete problem becomes finding a discrete solution $\mathbf{u}^h \in \mathscr{V}^h$ that satisfies

$$\forall \mathbf{v} \in \mathscr{V}_0^h,\ a(\mathbf{u}^h,\mathbf{v}) = f(\mathbf{v}) \tag{2.14}$$

where $\mathscr{V}_0^h = \{\mathbf{v} \in \mathscr{V}^h\ ,\ \ \mathbf{v} = \mathbf{0}\ \ \text{on}\ \ \Gamma_{\mathbf{u}}\}$. The principle of virtual work can be written as follows

$$\int_\Omega \delta\varepsilon^{\mathrm{T}}\mathbf{D}\varepsilon d\Omega - \int_\Omega \delta\mathbf{u}^{\mathrm{T}}\left[\mathbf{b} - \rho\ddot{\mathbf{u}} - c\dot{\mathbf{u}}\right] d\Omega - \int_{\Gamma_t} \delta\mathbf{u}^{\mathrm{T}}\mathbf{t}d\Gamma = 0 \tag{2.15}$$

where $\mathbf{g}$ is the body force vector; ρ is the mass density; c is damping factor; $\ddot{\mathbf{u}}$ is accelerator; $\dot{\mathbf{u}}$ is velocity. The virtual displacements and the compatible strains $\varepsilon = \nabla_s \mathbf{u}$ within any element can be written as follows

$$\delta \mathbf{u}^h = \sum_{I=1}^{np} \mathbf{N}_I \delta \mathbf{d}_I, \quad \delta \varepsilon^h = \sum_{I=1}^{np} \mathbf{B}_I \delta \mathbf{d}_I \ , \tag{2.16}$$

where np is the total number of nodes in the mesh, $\mathbf{d}_I = [u_I \ \ v_I]^T$ is the nodal displacement vector and $\mathbf{N}_I$ is the shape function. The assembly process gives,

$$\int_\Omega \delta \mathbf{d}^{\mathrm{T}} \mathbf{B}^{\mathrm{T}} \mathbf{D} \varepsilon d\Omega - \int_\Omega \delta \mathbf{d}^{\mathrm{T}} \mathbf{N}^{\mathrm{T}} \left[\mathbf{b} - \rho \ddot{\mathbf{u}} - c\dot{\mathbf{u}}\right] d\Omega - \int_{\Gamma_t} \delta \mathbf{d}^{\mathrm{T}} \mathbf{N}^{\mathrm{T}} \mathbf{t} d\Gamma = 0 \tag{2.17}$$

where $\mathbf{B}$ is the standard gradient matrix and $\mathbf{D}$ is a matrix of material constants. From the expressions related to any arbitrary virtual displacements δd, we have

$$\int_\Omega \mathbf{B}^{\mathrm{T}} \mathbf{D} \varepsilon d\Omega - \int_\Omega \mathbf{N}^{\mathrm{T}} \left[\mathbf{b} - \rho \ddot{\mathbf{u}} - c\dot{\mathbf{u}}\right] d\Omega - \int_{\Gamma_t} \mathbf{N}^{\mathrm{T}} \mathbf{t} d\Gamma = 0 \ . \tag{2.18}$$

The resulting discrete governing equations can be written as follows:

$$\mathbf{M}\ddot{\mathbf{u}} + \mathbf{C}\dot{\mathbf{u}} + \mathbf{K}\mathbf{u} = \mathbf{f} \tag{2.19}$$

in which

$$\mathbf{K} = \int_\Omega \mathbf{B}^T \mathbf{D} \mathbf{B} d\Omega \ ; \qquad \mathbf{f} = \int_\Omega \mathbf{N}^{\mathrm{T}} \mathbf{b} d\Omega + \int_{\Gamma_t} \mathbf{N}^{\mathrm{T}} \mathbf{t} d\Gamma \tag{2.20}$$

$$\mathbf{M} = \int_\Omega \mathbf{N}^{\mathrm{T}} \rho \mathbf{N} d\Omega \ ; \qquad \mathbf{C} = \int_\Omega \mathbf{N}^{\mathrm{T}} \mathbf{c} \mathbf{N} d\Omega \ . \tag{2.21}$$

2.2 Discrete governing equations and weak form for Reissner-Mindline plate

Let Ω be the domain in $\mathbb{R}^2$ occupied by the mid-plane of the plate and w and $\beta = (\beta_x, \beta_y)^T$ denote the transverse displacement and the rotations in the $x-z$ and $y-z$ planes, see Fig. 2.1, respectively. Assuming that the material is homogeneous and isotropic with Young's modulus E and Poisson's ratio ν, the governing differential equations of the Mindlin-Reissner plate are given by:

$$-\mathrm{div}\mathbf{D}^b \varepsilon^b(\beta) - \lambda t \varepsilon^s(\beta) = 0 \quad \text{in} \quad \Omega \tag{2.22}$$

$$-\lambda t \mathrm{div}(\varepsilon^s) = p \quad \text{in} \quad \Omega \tag{2.23}$$

$$w = \bar{w}, \beta = \bar{\beta} \quad \text{on} \quad \Gamma = \partial\Omega \tag{2.24}$$

where t is the plate thickness, $p = p(x,y)$ is the transverse loading per unit area, $\lambda = \frac{kE}{2(1+\nu)}$, $k = 5/6$ is the shear correction factor and $\mathbf{D}^b$ is the tensor of bending module. The bending ε^b and shear strains ε^s are defined as

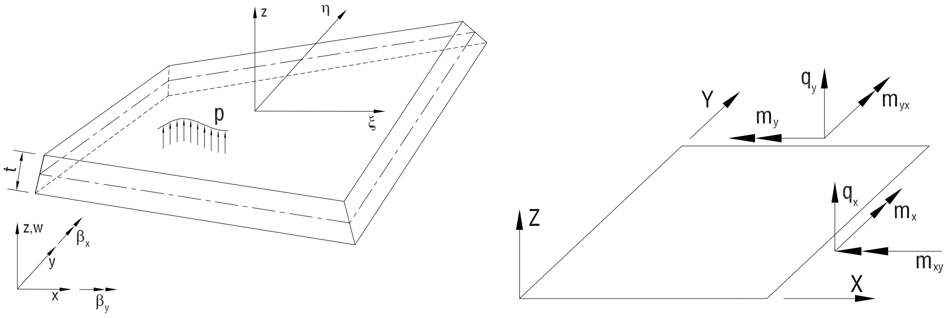

Figure 2.1: Geometry of a typical Mindlin-Reissner plate

$$\varepsilon^b = \mathbf{L}_d \beta \quad , \quad \varepsilon^s = \nabla w + \beta \tag{2.25}$$

where $\nabla = (\partial/\partial x, \partial/\partial y)$ is the gradient vector and $\mathbf{L}_d$ is a differential operator matrix defined by

$$\mathbf{L}_d^T = \begin{bmatrix} \partial/\partial x & 0 & \partial/\partial y \\ 0 & \partial/\partial y & \partial/\partial x \end{bmatrix} \tag{2.26}$$

The weak form of the static equilibrium equations in Eq. (2.24) is as follows

$$\int_\Omega (\delta\varepsilon^b)^T \mathbf{D}^b \varepsilon^b d\Omega + \int_\Omega (\delta\varepsilon^s)^T \mathbf{D}^s \varepsilon^s d\Omega = \int_\Omega \delta\mathbf{u}^T \bar{\mathbf{p}} d\Omega \tag{2.27}$$

where the displacement field is given by $\mathbf{u} = [w, \beta_x, \beta_x]^T$, and the transverse load is redefined by $\bar{\mathbf{p}} = [p, 0, 0]^T$. For the free vibration analysis of a Mindlin-Reissner plate model, a weak form may be derived form the dynamic form of the principle of virtual work under the assumptions of first order shear-deformation plate theory

$$\int_\Omega (\delta\varepsilon^b)^T \mathbf{D}^b \varepsilon^b d\Omega + \int_\Omega (\delta\varepsilon^s)^T \mathbf{D}^s \varepsilon^s d\Omega + \int_\Omega \delta\mathbf{u}^T \mathbf{m}\ddot{\mathbf{u}} d\Omega = 0 \,. \tag{2.28}$$

In the case of in-plane buckling analyses and assuming pre-buckling stresses $\hat{\sigma}_0$, non-linear strains appear and the weak form can be reformulated as (LWNT04)

$$\begin{aligned} &\int_\Omega (\delta\varepsilon^b)^T \mathbf{D}^b \varepsilon^b d\Omega + \int_\Omega (\delta\varepsilon^s)^T \mathbf{D}^s \varepsilon^s d\Omega + t\int_\Omega \nabla^T \delta w \hat{\sigma}_0 \nabla w d\Omega \\ &+ \frac{t^3}{12} \int_\Omega \begin{bmatrix} \nabla^T \delta\beta_x & \nabla^T \delta\beta_y \end{bmatrix} \begin{bmatrix} \hat{\sigma}_0 & 0 \\ 0 & \hat{\sigma}_0 \end{bmatrix} \begin{bmatrix} \nabla\beta_x \\ \nabla\beta_y \end{bmatrix} d\Omega = 0 \,. \end{aligned} \tag{2.29}$$

Eq. (2.29) can be rewritten as:

$$\int_{\Omega}(\delta\varepsilon^{b})^{T}\mathbf{D}^{b}\varepsilon^{b}d\Omega+\int_{\Omega}(\delta\varepsilon^{s})^{T}\mathbf{D}^{s}\varepsilon^{s}d\Omega+\int_{\Omega}(\delta\varepsilon^{g})^{T}\,\tau\varepsilon^{g}d\Omega=0 \tag{2.30}$$

where

$$\varepsilon=\begin{bmatrix}\varepsilon^{b}\\ \varepsilon^{s}\end{bmatrix}=\begin{bmatrix}\beta_{x,x}\\ \beta_{y,y}\\ \beta_{x,y}+\beta_{y,x}\\ \beta_{x}+w_{,x}\\ \beta_{y}+w_{,y}\end{bmatrix},\ \varepsilon^{g}=\begin{bmatrix}w_{x}&0&0\\ w_{y}&0&0\\ 0&\beta_{x,x}&0\\ 0&\beta_{x,y}&0\\ 0&0&\beta_{y,x}\\ 0&0&\beta_{y,y}\end{bmatrix},\ \tau=\begin{bmatrix}t\hat{\sigma}_{0}&0&0\\ 0&\frac{t^{3}}{12}\hat{\sigma}_{0}&0\\ 0&0&\frac{t^{3}}{12}\hat{\sigma}_{0}\end{bmatrix} \tag{2.31}$$

$$\hat{\sigma}_{0}=\begin{bmatrix}\sigma_{x}^{0}&\sigma_{xy}^{0}\\ \sigma_{xy}^{0}&\sigma_{y}^{0}\end{bmatrix},\ \mathbf{D}^{b}=\frac{Et^{3}}{12\,(1-\nu^{2})}\begin{bmatrix}1&\nu&0\\ \nu&1&0\\ 0&0&\frac{1-\nu}{2}\end{bmatrix},\ \mathbf{D}^{s}=k\frac{Et}{2(1+\upsilon)}\begin{bmatrix}1&0\\ 0&1\end{bmatrix}. \tag{2.32}$$

Let us assume that the bounded domain Ω is discretized into *nel* finite elements such that $\Omega=\cup_{e=1}^{nel}\Omega^{e}$ and $\Omega^{i}\neq\Omega^{j}\neq\emptyset$, $i\neq j$. The finite element solution $\mathbf{u}^{h}$ of a displacement model for the Mindlin-Reissner plate is then expressed as:

$$\mathbf{u}^{h}=\sum_{I=1}^{np}\begin{bmatrix}N_{I}(\mathbf{x})&0&0\\ 0&N_{I}(\mathbf{x})&0\\ 0&0&N_{I}(\mathbf{x})\end{bmatrix}\mathbf{d}_{I} \tag{2.33}$$

where np is the total number of nodes $N_{I}(\mathbf{x})$, $\mathbf{d}_{I}=[w_{I}\ \theta_{xI}\ \theta_{yI}]^{T}$ are shape functions and the nodal degrees of freedom of $\mathbf{u}^{h}$ associated to node I, respectively. The bending, shear strains and geometrical strains are written:

$$\varepsilon^{b}=\sum_{I}\mathbf{B}_{I}^{b}\mathbf{d}_{I}\ ,\ \varepsilon^{s}=\sum_{I}\mathbf{B}_{I}^{s}\mathbf{d}_{I}\ ,\ \varepsilon^{g}=\sum_{I}\mathbf{B}_{I}^{g}\mathbf{d}_{I} \tag{2.34}$$

The formulation of a Mindlin-Reissner plate can then be obtained for static analysis,

$$\mathbf{K}\mathbf{u}=\mathbf{f} \tag{2.35}$$

A general solution of such a homogeneous equation can be written as

$$\mathbf{u}=\bar{\mathbf{u}}\exp\left(i\omega t\right) \tag{2.36}$$

where t is indicates time, $\bar{\mathbf{u}}$ is the eigenvector and ω is the natural frequency. The eigenvalue problem is given by

$$\left(\mathbf{K}-\varpi^{2}\mathbf{M}\right)\bar{\mathbf{u}}=0 \tag{2.37}$$

and for the buckling analysis,

$$(\mathbf{K} - \lambda_{cr}\mathbf{K}_g)\,\bar{\mathbf{u}} = 0\,. \tag{2.38}$$

The global stiffness matrix and the load vector

$$\mathbf{K} = \int_{\Omega} \left(\mathbf{B}^b\right)^T \mathbf{D}^b\mathbf{B}^b d\Omega + \int_{\Omega} (\mathbf{B}^s)^T \mathbf{D}^s\mathbf{B}^s d\Omega \ , \qquad \mathbf{f} = \int_{\Omega} p\mathbf{N} d\Omega + \mathbf{f}^b \tag{2.39}$$

in which $\mathbf{f}^b$ is the remaining part of $\mathbf{f}$ subjected to prescribed boundary loads, ϖ is the natural frequency, $\mathbf{M}$ is the global mass matrix.

$$\mathbf{M} = \int_{\Omega} \mathbf{N}^T \mathbf{m}\mathbf{N} d\Omega \quad \text{with} \quad \mathbf{m} = \rho \begin{bmatrix} t & 0 & 0 \\ 0 & \frac{t^3}{12} & 0 \\ 0 & 0 & \frac{t^3}{12} \end{bmatrix} \tag{2.40}$$

The geometrical stiffness matrix is given by

$$\mathbf{K}_g = \int_{\Omega} (\mathbf{B}^g)^T \tau\mathbf{B}^g d\Omega\,. \tag{2.41}$$

Chapter 3

An alternative alpha Finite Element Method for free and forced vibration analysis of solids using triangular element

3.1 Introduction

The analysis of natural frequencies and forced response has played a very important role in the design of structures in mechanical, civil and aerospace engineering applications (Hug87, ZT00). A thorough study of the dynamic behavior of these structures is essential in assessing their full potential. Therefore, it is necessary to develop appropriate models capable of accurately predicting their dynamic characteristics. In practical applications, the lower order linear triangular element is mostly preferred due to its simplicity, efficiency, less demand on the smoothness of the solution, and ease for adaptive mesh refinements for solutions of desired accuracy.

In solving practical engineering problems, numerical methods have become the most widely used tools. The finite element method (FEM) is considered to be a very effective and versatile approach for these problems. A generalized strain smoothing technique was proposed, which relies on the strain smoothing technique (CWYY01). The smoothed FEM results in the application of this strain smoothing idea to the standard finite element method. The smoothed FEM (SFEM) has also been developed for general n-sided polygonal elements (nSFEM) (DLN07), dynamic analysis (DL07, NXNT08, RBZ07), plate and shell analysis (NXRBD08a, NTRNXB08, RAB07b, RA06a, BRZ08) and coupled to partition of unity enrichment (RB05, RB06a, RAB07a). The latter paper also provides a review of strain smoothing in FEM. A general framework for this strain smoothing technique in FEM was proposed in (Liu08). Based on the idea of the node-based smoothed point interpolation method (NS-PIM) and the SFEM, a node-based smoothed finite element method (NS-FEM)(LNTNXL09) for 2D solid mechanics problems has been developed.

The finite element methods with free parameters have been well known via previous contributions in (BF85, Fel94). An alpha finite element method (αFEM) (LNTL08) using triangular and tetrahedral elements were formulated to obtain "exact" or "best possible" solutions for a given problem by scaling the gradient of strains in the natural coordinates and Jacobian matrices with a scaling factor α. The method is not variationally consistent but proven stable and convergent. The αFEM can produce approximate solutions that "very close to exact" solutions in the strain energy for all overestimation problems, and "best" possible solution to underestimation problems.

Recently, Liu *et al* (LNXNTX09) have proposed a superconvergent alpha finite element method (SαFEM) using triangular meshes. In the SαFEM (now AαFEM), an assumed strain field was formulated by adding the averaged nodal strains with an adjustable factor α to the compatible strains. The new Galerkin-like weak form, as simple as the Galerkin weak form, was then obtained for this constructed strain field. It was proven theoretically and numerically that the AαFEM is much more accurate than the original FEM-T3 and even more accurate than the FEM-Q4 when the same sets of nodes are used. The AαFEM can produce both lower and upper bounds to the exact solution in the energy norm for all elasticity problems by properly choosing an α. In addition, a preferable-α approach has also been devised for the AαFEM to produce very accurate solutions for both displacement and energy norms and the superconvergent rate in the energy error norm. Furthermore, a model-based selective scheme is proposed to formulate a combined SαFEM/NS-FEM model that handily overcomes the volumetric locking problems. It is also shown that AαFEM performs excellently for singularity problems (LNXNTX09).

In this chapter, an alternative alpha finite element method is further extended to the free and forced vibration analysis of 2D solids. The AαFEM is based on three-nodes triangular elements and a properly chosen α parameter. The natural frequency and eigenvalue-mode analysis of the free vibration are obtained by solving an eigenvalue problem. In addition, an implicit time integration scheme is used in order to solve the forced vibration system equations. The numerical results demonstrate that the AαFEM is always more accurate than the original FEM-T3, and even more accurate than FEM-Q4. It also gives a good agreement compared to several other methods in the literature.

3.2 Construction of an assumed strain field

The problem domain Ω is partitioned into N_e triangular elements and contains a total of N nodes. The domain, Ω, is then divided into a set of smoothing domains Ω_k by connecting node k to centroid of the surrounding triangles as shown in Fig. 3.1a.

Ω_k is then further divided into M subdomains $\Omega_{k,i}$ as shown in Fig. 3.1b such that $\Omega_k = \bigcup\limits_{i=1}^{M} \Omega_{k,i}$, $\Omega_{k,i} \cap \Omega_{k,j} = \emptyset$, $i \neq j$. The approximation of the displacement field

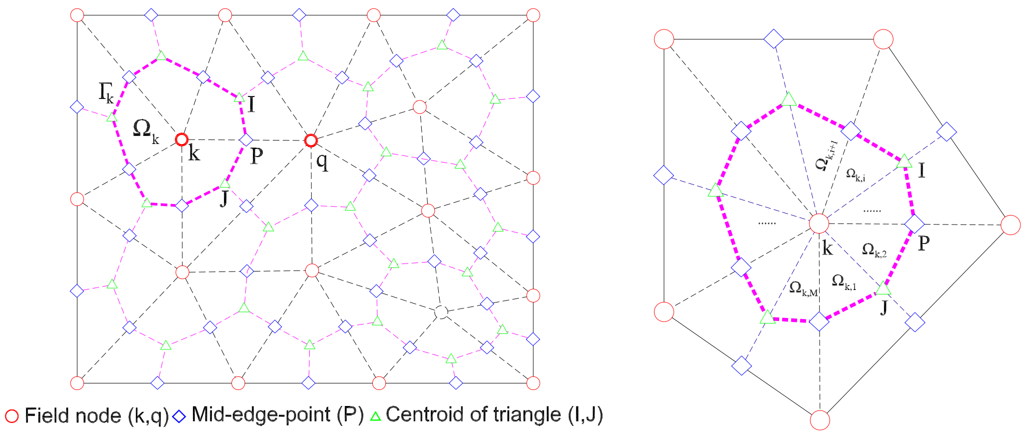

(a) (b)

Figure 3.1: (a) Triangular elements and smoothing cells associated with nodes. (b) Smoothing cell and M triangular sub-domains associated with node k.

$\mathbf{u}^h = (u_x^h, u_y^h)$ of the elasticity problem can then be expressed as

$$\mathbf{u}^h(\mathbf{x}) = \sum_{I=1}^{N} \mathbf{N}_I(\mathbf{x})\,\mathbf{d}_I \tag{3.1}$$

with $\mathbf{d}_i$ being the vector of (unknown) nodal displacements. The compatible strain $\varepsilon_{k,i}$ at any point using the assumed displacement field based on triangular elements. The strain tensor is given by

$$\varepsilon_{k,i} = \nabla_s \mathbf{u}_{k,i}(\mathbf{x}) \ . \tag{3.2}$$

Since the displacement is linear, $\varepsilon_{k,i}$ is constant in $\Omega_{k,i}$ and different from element to element. Such a piecewise constant strain field obviously does not represent well the exact strain field, and should be somehow modified or corrected. To make a proper correction, a smoothed strain for node k is introduced as follows(LNXNTX09):

$$\bar{\varepsilon}_k = \frac{1}{A_k} \int_{\Omega_k} \varepsilon_{k,i}(\mathbf{x}) d\Omega \tag{3.3}$$

The area of the smoothing domain A_k is given by

$$A_k = \int_{\Omega_k} d\Omega = \frac{1}{3} \sum_{i=1}^{N_k^e} A_i^e \tag{3.4}$$

where N_k^e is the number of elements connected to node k and A_i^e is the area of the i^{th} element around node k. The strains ε_k, ε_I at points k, I are then calculated as

$$\begin{aligned} \varepsilon_I &= \varepsilon_P = \varepsilon_{k,i} - \frac{\alpha\sqrt{6}}{3}\left(\bar{\varepsilon}_k - \varepsilon_{k,i}\right) \\ \varepsilon_k &= \alpha\sqrt{6}\bar{\varepsilon}_k + \left(1-\alpha\sqrt{6}\right)\varepsilon_{k,i} - \frac{\alpha\sqrt{6}}{3}\left(\bar{\varepsilon}_k - \varepsilon_{k,i}\right) \end{aligned} \tag{3.5}$$

where α is an adjustable factor. The strain field $\hat{\varepsilon}$ at any point within a sub-triangular domain $\Omega_{k,i}$ is now re-constructed as (LXZNT08, LNXNTX09):

$$\begin{aligned} \hat{\varepsilon}(\mathbf{x}) &= L_1(\mathbf{x})\varepsilon_k + L_2(\mathbf{x})\varepsilon_P + L_3(\mathbf{x})\varepsilon_I \\ &= L_1(\mathbf{x})\left(\alpha\sqrt{6}\bar{\varepsilon}_k + \left(1-\alpha\sqrt{6}\right)\varepsilon_{k,i} - \frac{\sqrt{6}}{3}\alpha\left(\bar{\varepsilon}_k - \varepsilon_{k,i}\right)\right) \\ &+ L_2(\mathbf{x})\left(\varepsilon_{k,i} - \frac{\sqrt{6}}{3}\alpha\left(\bar{\varepsilon}_k - \varepsilon_{k,i}\right)\right) + L_3(\mathbf{x})\left(\varepsilon_{k,i} - \frac{\sqrt{6}}{3}\alpha\left(\bar{\varepsilon}_k - \varepsilon_{k,i}\right)\right) \end{aligned} \tag{3.6}$$

where L_1, L_2, L_3 are the area coordinates for the sub-triangle $\Omega_{k,i}$ which form a partition of unity. Eq. (3.6) can be simplified as

$$\hat{\varepsilon}(\mathbf{x}) = (L_1+L_2+L_3)\varepsilon_{k,i} + \alpha\sqrt{6}L_1(\mathbf{x})\left(\bar{\varepsilon}_k - \varepsilon_{k,i}\right) - (L_1+L_2+L_3)\alpha\frac{\sqrt{6}}{3}\left(\bar{\varepsilon}_k - \varepsilon_{k,i}\right) \tag{3.7}$$

which can be further simplified as

$$\hat{\varepsilon}(\mathbf{x}) = \varepsilon_{k,i} + \alpha\varepsilon_{k,i}^{ad} \tag{3.8}$$

where $\varepsilon_{k,i}$ is constant in $\Omega_{k,i}$ and

$$\varepsilon_{k,i}^{\mathrm{ad}}(\mathbf{x}) = \sqrt{6}\left(\bar{\varepsilon}_k - \varepsilon_{k,i}\right)\left(L_1(\mathbf{x}) - \frac{1}{3}\right) . \tag{3.9}$$

From Eq. (3.9), $\varepsilon_{k,i}^{\mathrm{ad}}$ is the additional strain that is a linear function in $\Omega_{k,i}$. We now prove that the constructed strain field satisfies an orthogonality condition to the constant stress field. Using the formula (ZT00)

$$\int_{\Omega_{k,i}} L_1^p L_2^q L_3^r dA = \frac{p!q!r!}{(p+q+r+2)!}2A_{k,i} \tag{3.10}$$

It is clear that

$$\int_{\Omega_{k,i}} \varepsilon_{k,i}^{\mathrm{ad}} d\Omega = \sqrt{6}\left(\bar{\varepsilon}_k - \varepsilon_{k,i}\right)\int_{\Omega_{k,i}}\left(L_1 - \frac{1}{3}\right)d\Omega = 0 \tag{3.11}$$

which is termed as zero-sum property of the correction strain, which is similar to the orthogonality condition that is used in the stabilization formulation (BB86, BB83, FO04). The zero-sum property results in the following total zero-sum of the additional strain over the entire problem domain:

$$\int_{\Omega_{k,i}} \varepsilon^{\mathrm{ad}} d\Omega = \sum_{k=1}^{N} \sum_{i=1}^{M} \int_{\Omega_{k,i}} \varepsilon^{\mathrm{ad}}_{k,i} d\Omega = 0\ . \tag{3.12}$$

Therefore, we have

$$\int_{\Omega} \hat{\varepsilon} d\Omega = \int_{\Omega} \varepsilon d\Omega + \int_{\Omega} \varepsilon^{\mathrm{ad}} d\Omega = \sum_{k=1}^{N} \sum_{i=1}^{M} \int_{\Omega_{k,i}} \varepsilon_{k,i} d\Omega \tag{3.13}$$

which implies that the strain $\varepsilon_{k,i}$ does not effect the constant stress state that is needed to satisfy a patch test (PT00, SR90), and hence ensures the convergence. Thus a strain field $\hat{\varepsilon}$ based on combining the constant compatible strains ε of the FEM and the node-based smoothed strains $\bar{\varepsilon}$ of the NS-FEM has been carefully reconstructed, so that AαFEM can always pass the standard patch tests ensuring the convergence for any finite $\alpha \in \Re$. In addition, an α is also introduced to regularize the variation of the strain field and results in an effectively softened stiffness matrix.

3.3 Weak form for modified strain field

We use the modified Hellinger-Reissner variational formulation:

$$\sum_{k=1}^{N} \sum_{i=1}^{M} \left[\int_{\Omega_{k,i}} \delta \left(\varepsilon_{k,i} + \alpha \varepsilon^{\mathrm{ad}}_{k,i} \right)^{\mathrm{T}} \mathbf{D} \left(\varepsilon_{k,i} - \alpha \varepsilon^{\mathrm{ad}}_{k,i} \right) d\Omega \right] - \int_{\Omega} \delta \mathbf{u}^{\mathrm{T}} \mathbf{b} d\Omega - \int_{\Gamma_t} \delta \mathbf{u}^{\mathrm{T}} \mathrm{d}\Gamma = 0 \tag{3.14}$$

The Galerkin-like weak form, Eq. (3.14), is an extended form of the standard Galerkin weak formulation to conform the strain field. The Galerkin-like weak form becomes the standard Galerkin weak form as $\varepsilon^{\mathrm{ad}}_{k,i} = 0$. Substituting the approximation, Eq. (3.1), into Eq. (3.14), and using the arbitrariness of the variation, we obtain

$$\hat{\mathbf{K}}^{\mathrm{A}\alpha\mathrm{FEM}}_{\alpha} \hat{\mathbf{d}} = \mathbf{f} \tag{3.15}$$

where $\hat{\mathbf{K}}^{\mathrm{A}\alpha\mathrm{FEM}}_{\alpha}$ is the global stiffness matrix with the scaled gradient strains

$$\begin{aligned} \hat{\mathbf{K}}^{\mathrm{A}\alpha\mathrm{FEM}}_{\alpha} &= \sum_{k=1}^{N} \sum_{i=1}^{M} \int_{\Omega_{k,i}} \mathbf{B}^{\mathrm{T}}_{k,i} \mathbf{D} \mathbf{B}_{k,i} d\Omega - \alpha^2 \sum_{k=1}^{N} \sum_{i=1}^{M} \int_{\Omega_{k,i}} \left(\mathbf{B}^{\mathrm{ad}}_{k,i} \right)^{\mathrm{T}} \mathbf{D} \mathbf{B}^{\mathrm{ad}}_{k,i} d\Omega \\ &= \mathbf{K}^{\mathrm{FEM\text{-}T3}} - \alpha^2 \hat{\mathbf{K}}^{\mathrm{A}\alpha\mathrm{FEM}}_{\mathrm{ad}} \end{aligned} \tag{3.16}$$

and $\mathbf{f}$ is the global force vector given in Eq. (2.39). The $\mathbf{K}^{\mathrm{FEM\text{-}T3}}$ is the global stiffness matrix of the standard FEM (T3). $\hat{\mathbf{K}}^{\mathrm{A}\alpha\mathrm{FEM}}_{\mathrm{ad}}$ is derived from the corrected strain, and hence it is termed as corrected stiffness matrix that helps to reduce the well-known overly-stiff behaviour of the standard FEM. In Eq. (3.16),

$$\mathbf{B}_{k,i}^{\mathrm{ad}} = \sqrt{6}\left(\bar{\mathbf{B}}_k - \mathbf{B}_{k,i}\right)\left(L_1 - \frac{1}{3}\right) \tag{3.17}$$

and $\hat{\mathbf{K}}_{\mathrm{ad}}^{\mathrm{A}\alpha\mathrm{FEM}}$ can be rewritten explicitly as

$$\begin{aligned}\hat{\mathbf{K}}_{\mathrm{ad}}^{\mathrm{A}\alpha\mathrm{FEM}} &= \sum_{k=1}^{N}\sum_{i=1}^{M}\int_{\Omega_{k,i}}\left(\mathbf{B}_{k,i}^{\mathrm{ad}}\right)^{\mathrm{T}}\mathbf{D}\mathbf{B}_{k,i}^{\mathrm{ad}}d\Omega\\ &= 6\sum_{k=1}^{N}\sum_{i=1}^{M}\left(\bar{\mathbf{B}}_k - \mathbf{B}_{k,i}\right)^{\mathrm{T}}\mathbf{D}\left(\bar{\mathbf{B}}_k - \mathbf{B}_{k,i}\right)\int_{\Omega_{k,i}}\left(L_1 - \frac{1}{3}\right)^2 d\Omega\\ &= \frac{1}{3}\sum_{k=1}^{N}\sum_{i=1}^{M}\left(\bar{\mathbf{B}}_k - \mathbf{B}_{k,i}\right)^{\mathrm{T}}\mathbf{D}\left(\bar{\mathbf{B}}_k - \mathbf{B}_{k,i}\right)A_{k,i}\end{aligned} \tag{3.18}$$

where $\bar{\mathbf{B}}_k = \frac{1}{A_k}\sum_{i=1}^{M}\int_{\Omega_{k,i}}\mathbf{B}_{k,i}d\Omega = \frac{1}{A_k}\sum_{i=1}^{M}A_{k,i}\mathbf{B}_{k,i}$ is the nodal strain displacement matrix of node k, $\mathbf{B}_{k,i}$ is the strain displacement matrix of sub-triangular domain i connecting to vertex k, see Fig. 3.1. It is clear that the corrected stiffness matrix $\hat{\mathbf{K}}_{\mathrm{ad}}^{\mathrm{A}\alpha\mathrm{FEM}}$ accounts for the strain gap, Eq. (3.11), between the compatible (element) strains of the FEM and the smoothed nodal strains of the NS-FEM. Note that the present formulation, Eq. (3.16), is always stable for any finite parameters α. Hence, α can be manipulated without affecting the convergence property of the method (LNTL08), i.e. the method converges for any α. Manipulating $\hat{\mathbf{K}}_{\mathrm{ad}}^{\mathrm{A}\alpha\mathrm{FEM}}$ through α can, however, change the convergence rate and the error level of the resulting method. Eq. (3.16) can alternatively be expressed in the following form:

$$\hat{\mathbf{K}}_{\alpha}^{\mathrm{A}\alpha\mathrm{FEM}} = \hat{\mathbf{K}}_{\alpha=0}^{\mathrm{A}\alpha\mathrm{FEM}} - \alpha^2\hat{\mathbf{K}}_{\mathrm{ad}}^{\mathrm{A}\alpha\mathrm{FEM}}\,. \tag{3.19}$$

We note that in the AαFEM is altered only the stiffness matrix. The other quantities: force vector $\mathbf{f}$, mass matrix $\mathbf{M}$ and damping matrix $\mathbf{C}$ remain unchanged.

3.4 Forced and free vibration analysis

From Eq. (3.19), the discretized system of equations in the AαFEM can be expressed

$$\mathbf{M}\ddot{\mathbf{u}} + \mathbf{C}\dot{\mathbf{u}} + \hat{\mathbf{K}}_{\alpha}^{\mathrm{A}\alpha\mathrm{FEM}}\mathbf{u} = \mathbf{f} \tag{3.20}$$

The Rayleigh damping is used where the damping matrix $\mathbf{C}$ is assumed to be a linear combination of $\mathbf{M}$ and $\hat{\mathbf{K}}_{\alpha}^{\mathrm{A}\alpha\mathrm{FEM}}$. I also used the Newmark method (Red93) which is a generation of the linear acceleration method. The latter method assumes that the acceleration varies linearly within the interval $(t, t+\Delta t)$.

$$\ddot{\mathbf{u}} = \ddot{\mathbf{u}}_t + \frac{1}{\Delta t}\left(\ddot{\mathbf{u}}_{t+\Delta t} - \ddot{\mathbf{u}}_t\right)\tau \tag{3.21}$$

$$\dot{\mathbf{u}}_{t+\Delta t} = \dot{\mathbf{u}}_t + \left[(1-\delta)\,\ddot{\mathbf{u}}_t + \delta\ddot{\mathbf{u}}_{t+\Delta t}\right]\Delta t \tag{3.22}$$

$$\mathbf{u}_{t+\Delta t} = \mathbf{u}_t + \dot{\mathbf{u}}\Delta t + \left[\left(\frac{1}{2} - \beta\right)\ddot{\mathbf{u}}_t + \beta\ddot{\mathbf{u}}_{t+\Delta t}\right]\Delta t^2\ . \tag{3.23}$$

The response at $t+\Delta t$ is obtained by evaluating the equation of motion at time $t+\Delta t$. In this chapter, $\delta = 0.5$ and $\beta = 0.25$ are used.

3.5 Numerical results

3.5.1 Static analysis

In this section, I will illustrate a numerical technique to determine an optimal value of α that can produce a nearly exact solution in strain energy. This value will then be used for all the problems in this manuscript.

3.5.1.1 Cantilever beam due to a parabolic traction at the free end

A cantilever beam with length L and height D and unit thickness is studied as a benchmark here. The beam is subjected to a parabolic traction at the free end as shown in Fig. 3.2. The related parameters are taken as length $L = 48m$, height $D = 12m$, Young's module $E = 3.0 \times 10^7 kPa$, Poisson's ratio $\nu = 0.3$, $P = 1000N$. The analytical solution is available and can be found in a textbook by Timoshenko and Goodier (TG70).

$$\begin{aligned} u_x &= \tfrac{Py}{6EI}\left[(6L-3x)\,x + (2+\bar{\nu})\left(y^2 - \tfrac{D^2}{4}\right)\right] \\ u_y &= -\tfrac{Py}{6EI}\left[3\bar{\nu}y^2\,(L-x) + (4+5\bar{\nu})\,\tfrac{D^2x}{4} + (3L-x)\,x^2\right] \end{aligned} \tag{3.24}$$

where the moment of inertia I for a beam with rectangular cross section and unit thickness is given by $I = \frac{D^3}{12}$.

The meshes based on triangular elements are used as shown in Fig. 3.2. The exact strain energy for this problems is 4.4746, that is obtained by $\alpha = 1.4152$ independent of the mesh refinement as shown in Fig. 3.3. The convergence of normalized strain energy with respect to the parameters α are described in Fig. 3.4. As computed, the factor $\alpha = 1.4152$ leads to the highest accuracy compared with the other methods. The solutions in displacement of AαFEM is also compared with those of the FEM-T3, FEM-Q4, NS-FEM-T3(LNTNXL09) and ES-FEM-T3(LNTL09) as given in Fig. 3.5. It is found that the FEM-T3 is very stiff while the NS-FEM-T3 is very soft compared to the exact solution. The AαFEM is stiffer than the NS-FEM-T3 and softer than the FEM-T3, and is very close the exact solution. The AαFEM is clearly a good competitor to the ES-FEM-T3 that was found elsewhere to be one of the most accurate models using linear triangular elements. The AαFEM is also more accurate than the FEM-Q4. From Fig. 3.6 and Fig. 3.7, it is observed that the most accurate methods tested here is the AαFEM.

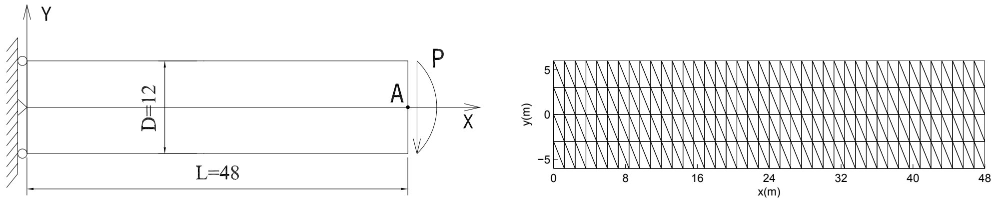

Figure 3.2: A cantilever beam and its meshes.

3.5.1.2 Infinite plate with a circular hole

Fig. 3.8 shows a plate with a circular hole of radius $a = 1$m. The plate is subjected to a unidirectional tensile load of $\sigma = 1.0$N/m at infinity in the x-direction. Due to its symmetry, only the upper right quadrant of the plate is modeled. Plane strain conditions are assumed and $E = 1.0 \times 10^3$ N/m^2, Poisson's ratio $\nu = 0.3$. Symmetric conditions are imposed on the left and bottom edges, and the inner boundary of the hole is traction free. The exact solution of the stress for the corresponding infinite solid is (TG70)

$$\begin{aligned}\sigma_{xx}(r,\theta) &= 1 - \frac{a^2}{r^2}\left[\frac{3}{2}\cos 2\theta + \cos 4\theta\right] + \frac{3a^4}{2r^4}\cos 4\theta \\ \sigma_{yy}(r,\theta) &= -\frac{a^2}{r^2}\left[\frac{1}{2}\cos 2\theta - \cos 4\theta\right] - \frac{3a^4}{2r^4}\cos 4\theta \\ \tau_{xy}(r,\theta) &= -\frac{a^2}{r^2}\left[\frac{1}{2}\sin 2\theta + \sin 4\theta\right] + \frac{3a^4}{2r^4}\sin 4\theta\end{aligned} \tag{3.25}$$

where (r,θ) are the polar coordinates and θ is measured counterclockwise from the positive x-axis. Traction boundary conditions are imposed on the right $(x = 5.0)$ and top $(y = 5.0)$ edges based on the exact solution Eq. (3.25). The displacement components corresponding to the stresses are

$$\begin{aligned}u_1(r,\theta) &= \frac{a}{8\mu}\left[\frac{r}{a}(\kappa+1)\cos\theta + 2\frac{a}{r}\left((1+\kappa)\cos\theta + \cos 3\theta\right) - 2\frac{a^3}{r^3}\cos 3\theta\right] \\ u_2(r,\theta) &= \frac{a}{8\mu}\left[\frac{r}{a}(\kappa-1)\sin\theta + 2\frac{a}{r}\left((1-\kappa)\sin\theta + \sin 3\theta\right) - 2\frac{a^3}{r^3}\sin 3\theta\right]\end{aligned} \tag{3.26}$$

where $\mu = E/(2(1+\nu))$, and $\kappa = 3 - 4\nu$. The mesh with 128 triangular elements is shown in Fig. 3.9. The exact strain energy of the problem is 1.1817717×10^{-2}, the

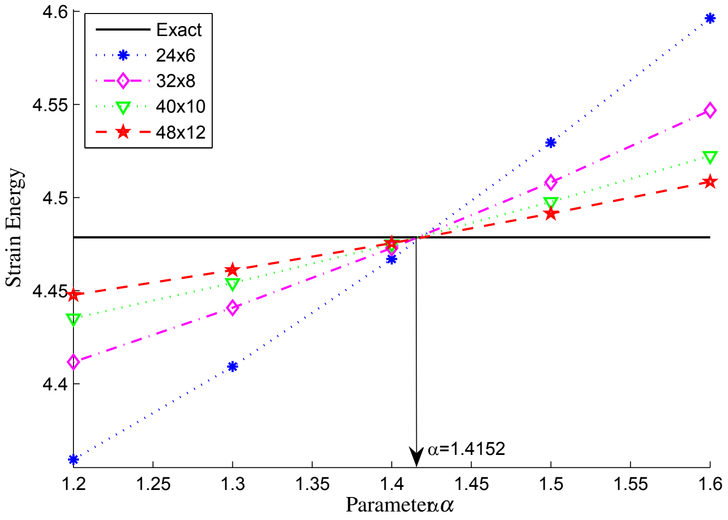

Figure 3.3: Strain energy of the cantilever beam versus parameter α. These series of calculations allow to find an approximatively optimal value for α. This figure also shows that for the range of regular meshes tested, this “optimal” value is mesh dependent (all curves intersect the exact energy line at the same point with meshes of the same aspect ratio). Also notice that the sensitivity to α decreases with mesh refinement (smaller slope) and that the relationship between the strain energy and α being approximately linear, two simulations for two different values of α and a coarse mesh would be sufficient to estimate the optimal value of α. This was also observed in Fig. 3.10.

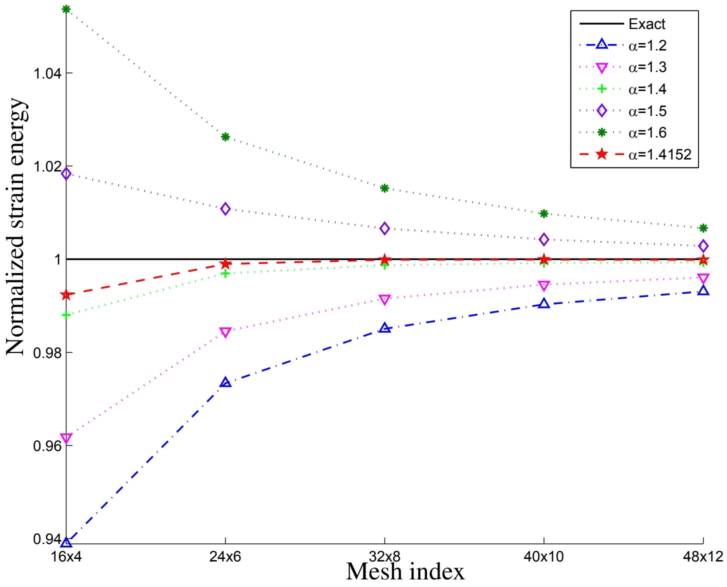

Figure 3.4: Normalized strain energy of the cantilever beam

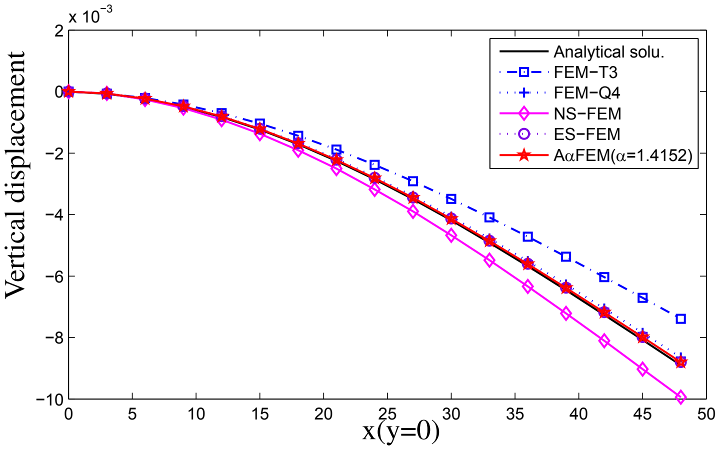

Figure 3.5: Vertical displacement at central line (y = 0) using triangular elements of the cantilever beam

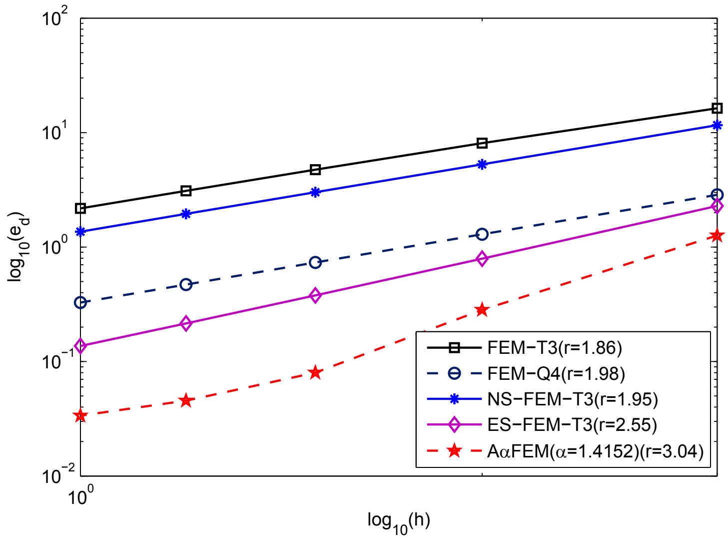

Figure 3.6: Convergence and the estimated rate in the displacement error norm of the cantilever beam. Note that the proposed method, AαFEM outperforms all others and is almost two orders of magnitude more accurate than the FEM-T3.

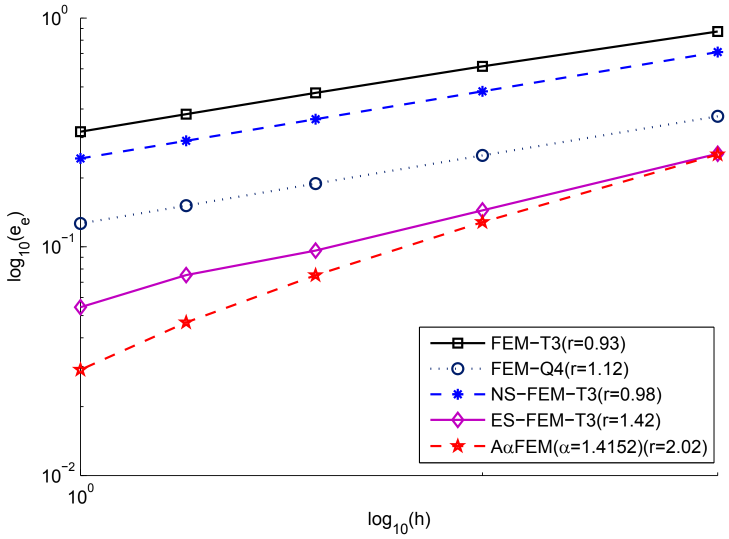

Figure 3.7: Convergence and the estimated rate in the energy error norm of the cantilever beam.

estimated solutions at $\alpha = 1.4156$ for the strain energy are 1.1817966×10^{-2} shown in Fig. 3.10. As resulted in Fig. 3.11 with the parameter $\alpha = 1.4156$, the convergence of strain energy is best compared with other elements. Fig. 3.12 and Fig. 3.13 illustrate the displacements along the bottom and the left boundary of the methods for the mesh with 128 triangular elements. It is shown that the AαFEM is more accurate than FEM-T3, NS-FEM and ES-FEM. Fig. 3.14–Fig. 3.17, in the energy norms.

Remark the performance of the proposed method can be usefully compared with that of the smoothed finite element method (SFEM). Similarly to the SFEM, the proposed method shows different behaviours in the energy and displacement norms. The smoothed FEM, a review of which is presented in (BRNX$^+$10), is superconvergent in the energy norm for the one-subcell version (which suffers from rank deficiency) while this superconvergence is lost for larger numbers of subcells. Stabilization techniques can be devised in the SFEM to combine the strengths of the one-subcell and large-subcell-number methods. In the present method, this rank deficiency is not present. At the cost of a slightly larger bandwidth and a tunable parameter, the AαFEM provides a stable and accurate alternative to standard FEM which can provide both high displacement and stress accuracy and convergence rates.

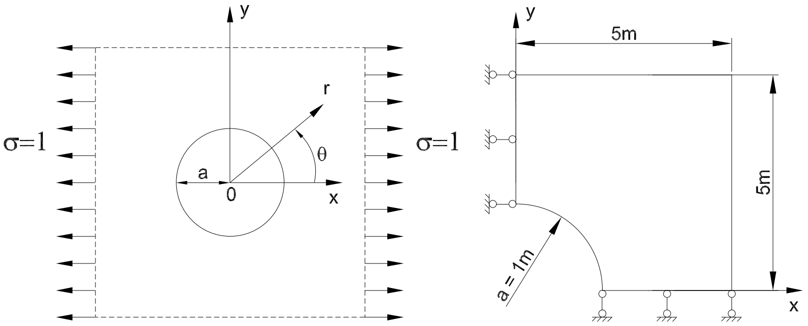

Figure 3.8: Infinite plate with a circular hole and its quarter model

3.5.2 Free and forced vibration analysis

For two problems, we observed that the optimal value of α varies in the interval of $1.4 \div 1.5$. Here, we choose the parameter $\alpha = 1.4156$ for free and force vibration analysis. Although the parameter α chosen may not be optimal for all dynamic problems, the results found are acceptable and more accurate than those of FEM-T3, FEM-Q4 and are a good competitor to serval other methods in the literature.

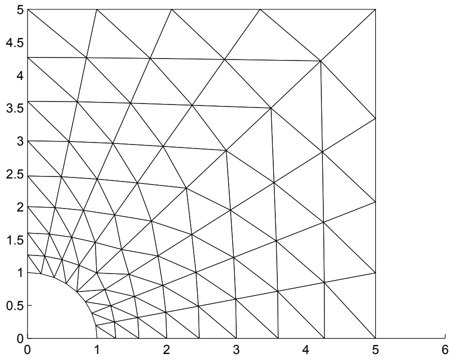

Figure 3.9: Domain discretization using 128 triangular elements for the quarter model of the infinite plate with a circular hole

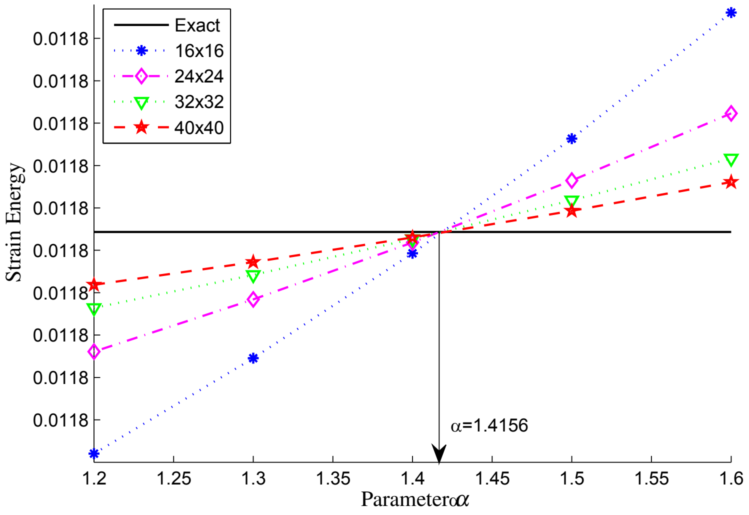

Figure 3.10: Strain energy of the infinite plate with a hole as a function of parameter α. See also Fig. 3.3.

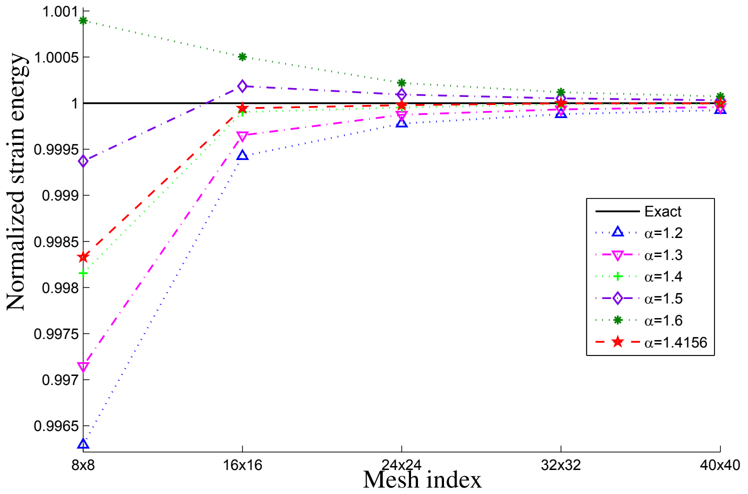

Figure 3.11: Normalized strain energy of the infinite plate with a hole along the bottom boundary for various meshes and values of parameter α. Note that it is possible to obtain overestimation or underestimation of the exact strain energy only by tuning parameter α.

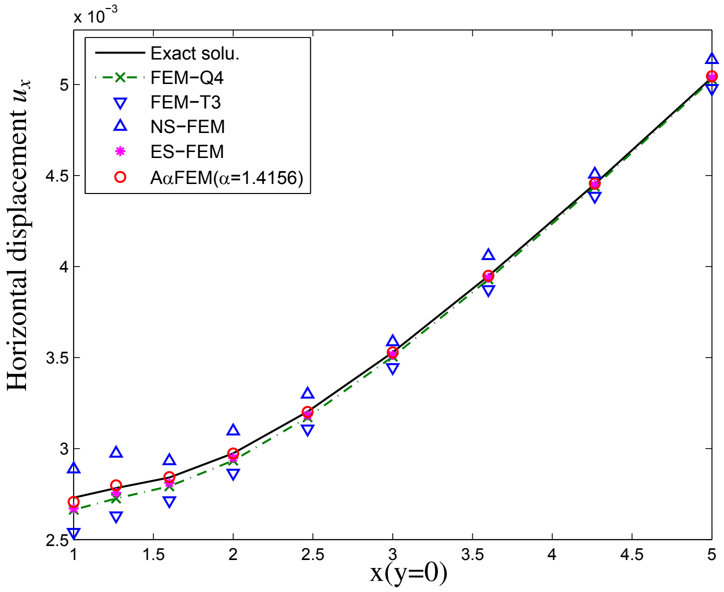

Figure 3.12: Horizontal displacement of the infinite plate with a hole along the bottom boundary

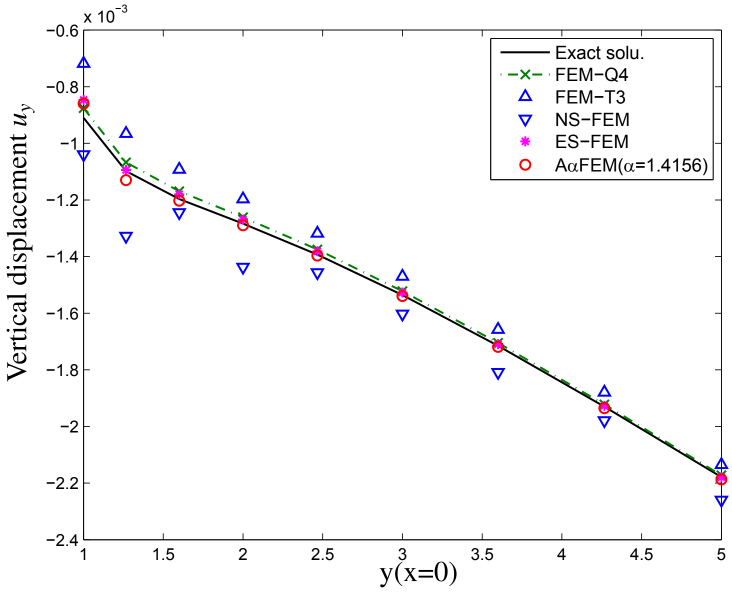

Figure 3.13: Vertical displacement of the infinite plate with a hole along the left boundary.

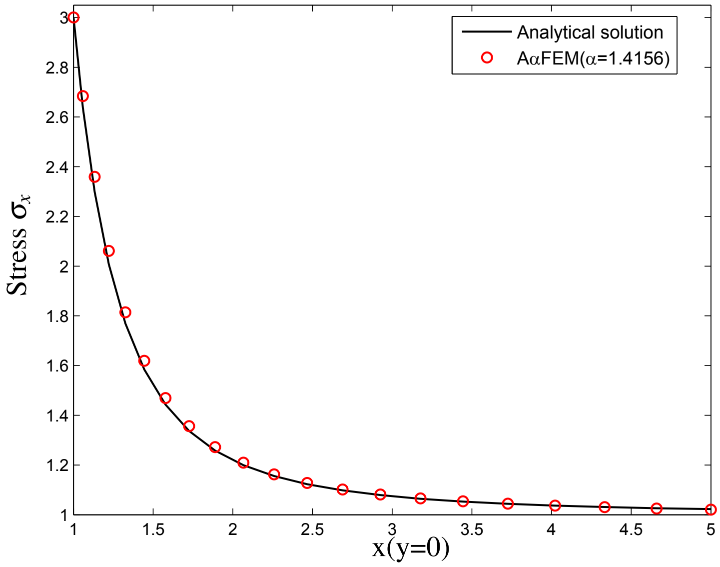

Figure 3.14: Distribution of stress along the left boundary (x = 0) of the infinite plate with a hole subjected to unidirectional tension

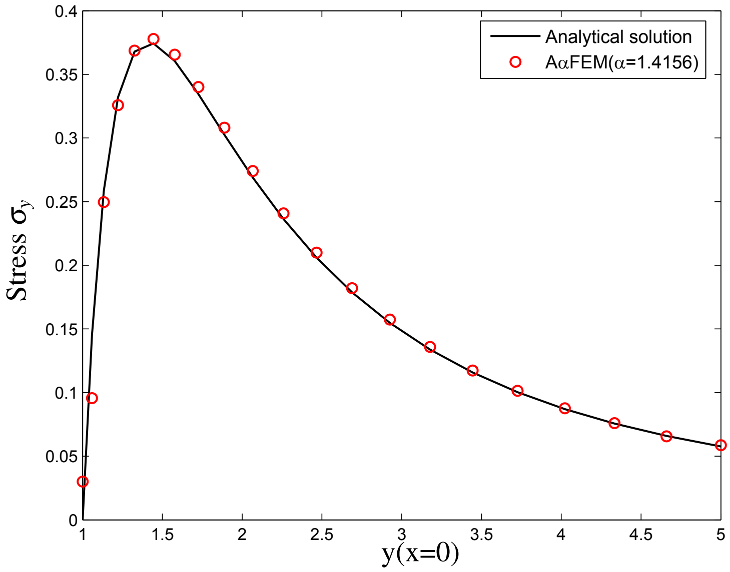

Figure 3.15: Distribution of stress along the bottom boundary (y = 0) of the infinite plate with a hole subjected to unidirectional tension

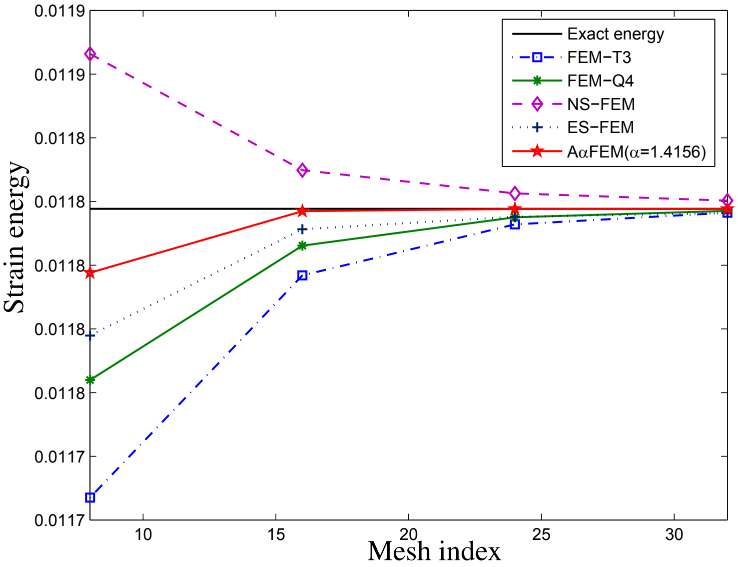

Figure 3.16: Solution bounds of energy for infinite plate with a circular hole.

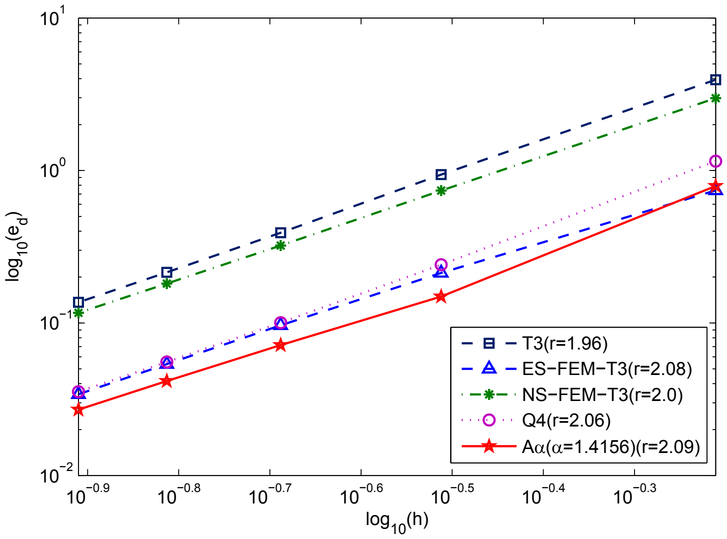

Figure 3.17: Convergence and the estimated rate in the displacement norm of the infinite plate with a circular hole. Note that the proposed method, for this value of α is slightly outperformed by the ES-FEM in terms of displacement accuracy. As shown in Fig. 3.18, this is not the case in the energy norm.

3.5.2.1 Free vibration analysis of a cantilever beam

The free vibration analysis presented for a 2-D cantilever beam as shown in Fig. 3.19. The dimensions of the beam are: length L = 100mm, height D = 10mm, thickness t = 1.0mm, Young's modules $E = 2.1 \times 10^4 kgf/mm^4$, Poisson's ratio $\nu = 0.3$, and mass density $\rho = 8.0 \times 10^{-10} kgfs^2/mm^4$. A plane stress problem is considered.

The first eight eigen-modes of the beam are shown in Fig. 3.20 and results are listed in Tab. 3.1. It is observed that AαFEM converges much faster than the FEM-T3, FEM-Q4 especially for a very coarse mesh (20×2 elements). For 40×4, AαFEM achieves comparable accuracy compared with the corresponding reference solutions. In addition, Tab. 3.2 describes the error of the approximated solution compared with Euler–Bernoulli beam theory. It is clear that the frequency errors of the AαFEM are slightly smaller than those of the other methods.

3.5.2.2 Free vibration analysis of tapered cantilever plate with central circular hole

Consider the tapered cantilever plate with a central circular hole, shown in Fig. 3.21. The following material property parameters are used in the analysis: mass density $\rho = 1$, Young's modulus $E = 1$ and Poisson's ratio $\nu = 0.3$, plane stress condition is

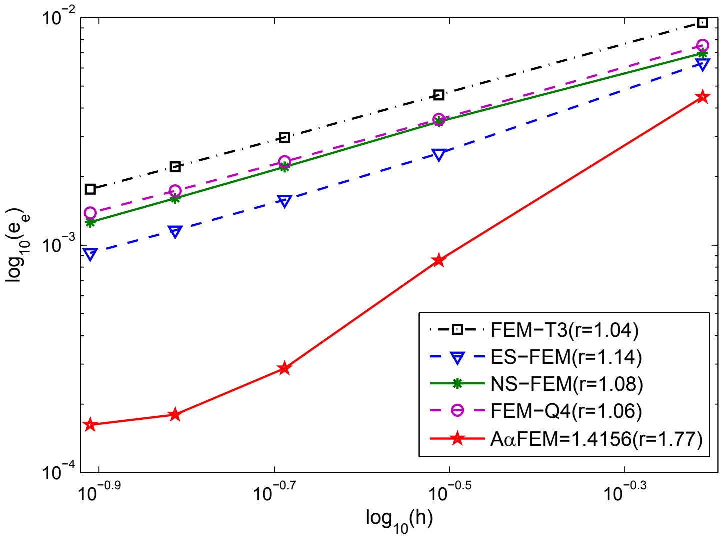

Figure 3.18: Convergence and the estimated rate in the energy norm of the infinite plate with a circular hole. Note the initial (for coarse meshes) superconvergence attenuates and that the “asymptotic” rate of convergence is the same as that of the other method tested.

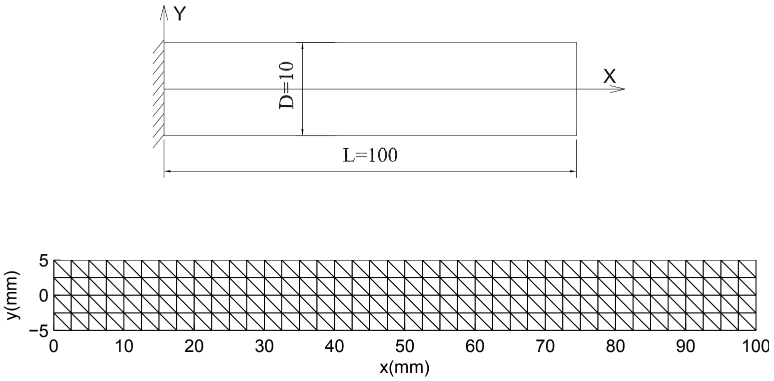

Figure 3.19: A cantilever beam and its mesh

Table 3.1: First eight natural frequencies of a cantilever beam

No.elements	FEM-T3	FEM-Q4	ES-FEM[1]	MLPG[2]	NBNM[3]	$A\alpha$FEM
(20×2)	1119	924	853	824.44	844.19	867.80
	6643	5561	5078	5070.32	5051.21	5228.45
80	12852	13484	12828	12894.73	12827.60	12833.66
triangular	17306	14732	13246	13188.12	13258.21	13858.33
elements	31173	27003	23783	24044.43	23992.82	25366.81
	38686	40502	35784	36596.15	36432.15	38473.60
	47342	41636	38298	38723.90	38436.43	38977.74
	64769	58075	48533	50389.01	49937.19	54022.01
(40×4)	907	879	827	824.44	844.19	827.62
	5431	5267	4950	5070.32	5051.21	4968.00
320	12834	13467	12826	12894.73	12827.60	12826.57
triangular	14286	13863	13006	13188.12	13258.21	13099.22
elements	25949	25193	23554	24044.43	23992.82	23836.27
	38511	38456	35778	36596.15	36432.15	36409.61
	39612	40370	38408	38723.90	38436.43	38453.30
	54647	53043	49029	50389.01	49937.19	50215.89

[1] Edge-based Smoothed Discrete Shear Gap Triangle Element (ES-DSG3)(LNTL09)
[2] Meshless Local Petrov-Galerkin (MLPG) (GL01)
[3] Node-By-Node Method (NBNM)(Nag99)

Table 3.2: Numerical error comparison with Euler–Bernoulli beam natural frequencies

Mode	FEM-T3	FEM-Q4	ES-FEM	MLPG	NBNM	$A\alpha$FEM	Euler beam
1	907	824	827	824	844.19	827.62	827.65
Error(%)	9.594	5.841	-0.072	-0.435	1.959	-0.0036	-
2	5431	4944	4950	5070	5051.21	4968.00	5186.77
Error(%)	4.709	4.681	-4.565	-2.251	-2.683	-4.2178	-

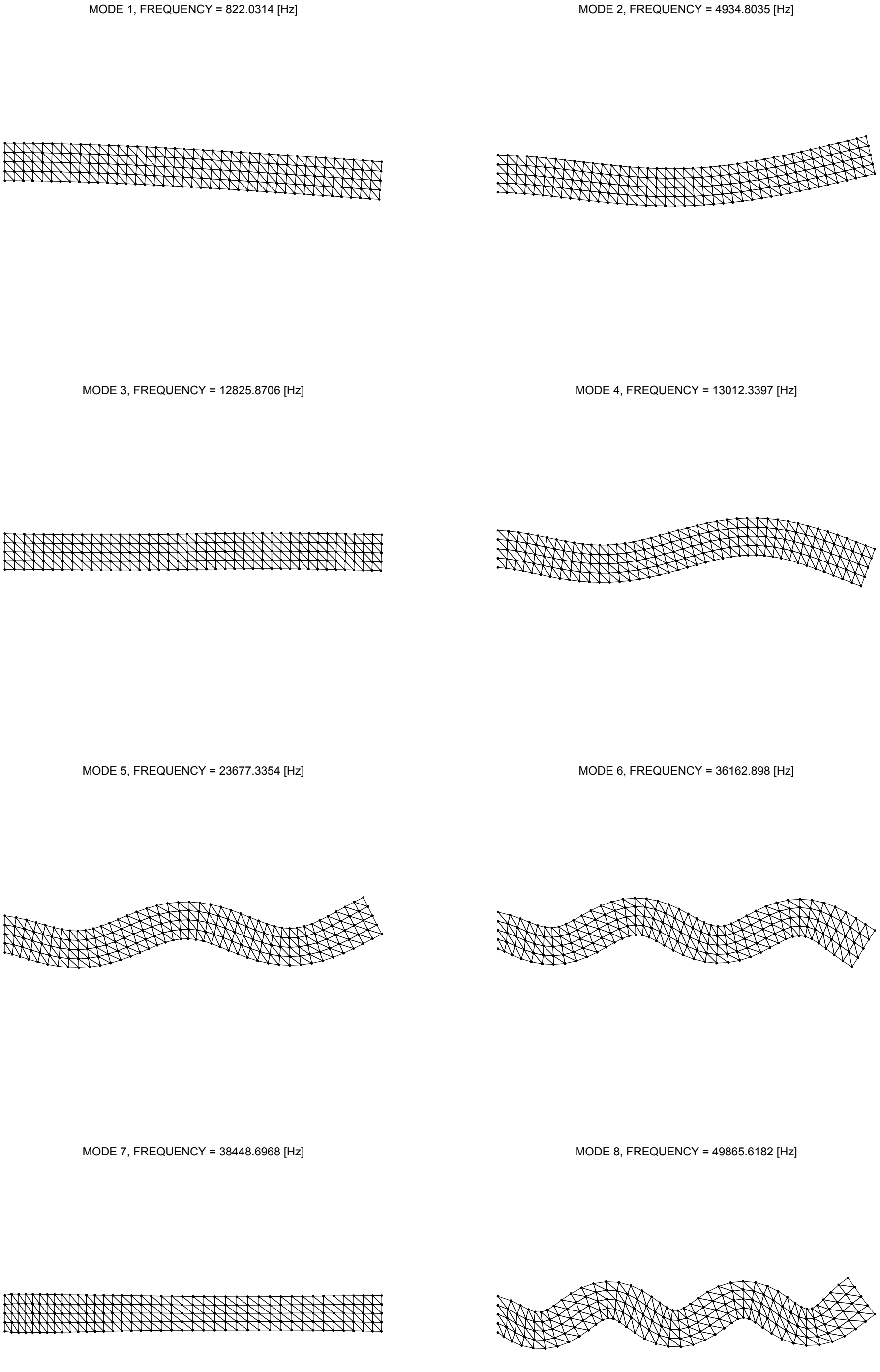

Figure 3.20: First eight modes of a cantilever beam by the $A\alpha$FEM

assumed. Tab. 3.3 shows the numerical error of the AαFEM compared to several other methods. The corresponding mode shapes are shown in Fig. 3.22. The above results show the good performance of the present method. Also, it is found that the AαFEM achieves higher accurate than FEM-T3 as well as reference solutions.

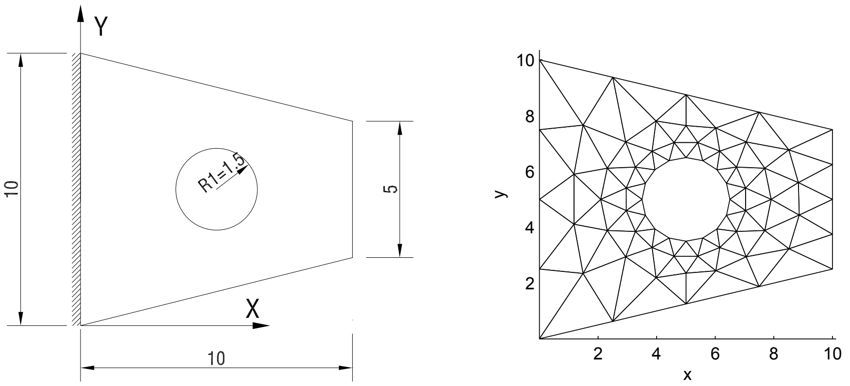

Figure 3.21: Tapered cantilever plate with central circular hole and its meshes

3.5.2.3 Free vibration analysis of a shear wall

A shear wall with four openings (see Fig. 3.23) is analyzed, which has been solved using BEM by Brebbia (BTW84). The bottom edge is fully clamped. Plane stress conditions are considered with $E = 10 \times 10^3 N/m^2$,$\nu = 0.2$,t = 1.0m,$\rho = 1.0 N/m^3$. The natural frequencies of the first 8 modes are calculated and shown in Fig. 3.24 and in Tab. 3.4. The natural frequencies obtained with the AαFEM are lower than those of the FEM-T3 and provide the best results compared to the reference solution provided by Brebbia *et.al.* (BTW84).

3.5.2.4 Free vibration analysis of a connecting rod

A free vibration analysis of a connecting rod as shown in Fig. 3.25 is performed. The plane stress problem is considered with $E = 1.0 \times 10^{10} N/m^2, \nu = 0.3, \rho = 7.8 \times 10^3 kg/m^3$. The nodes on the left inner circumference are fixed in two directions. Again, the AαFEM are always superior to FEM-T3 shown in Tab. 3.5. It is seen that the AαFEM using triangular elements can be applied to the vibration analysis with high reliability. The modes using the present method are also illustrated in Fig. 3.26.

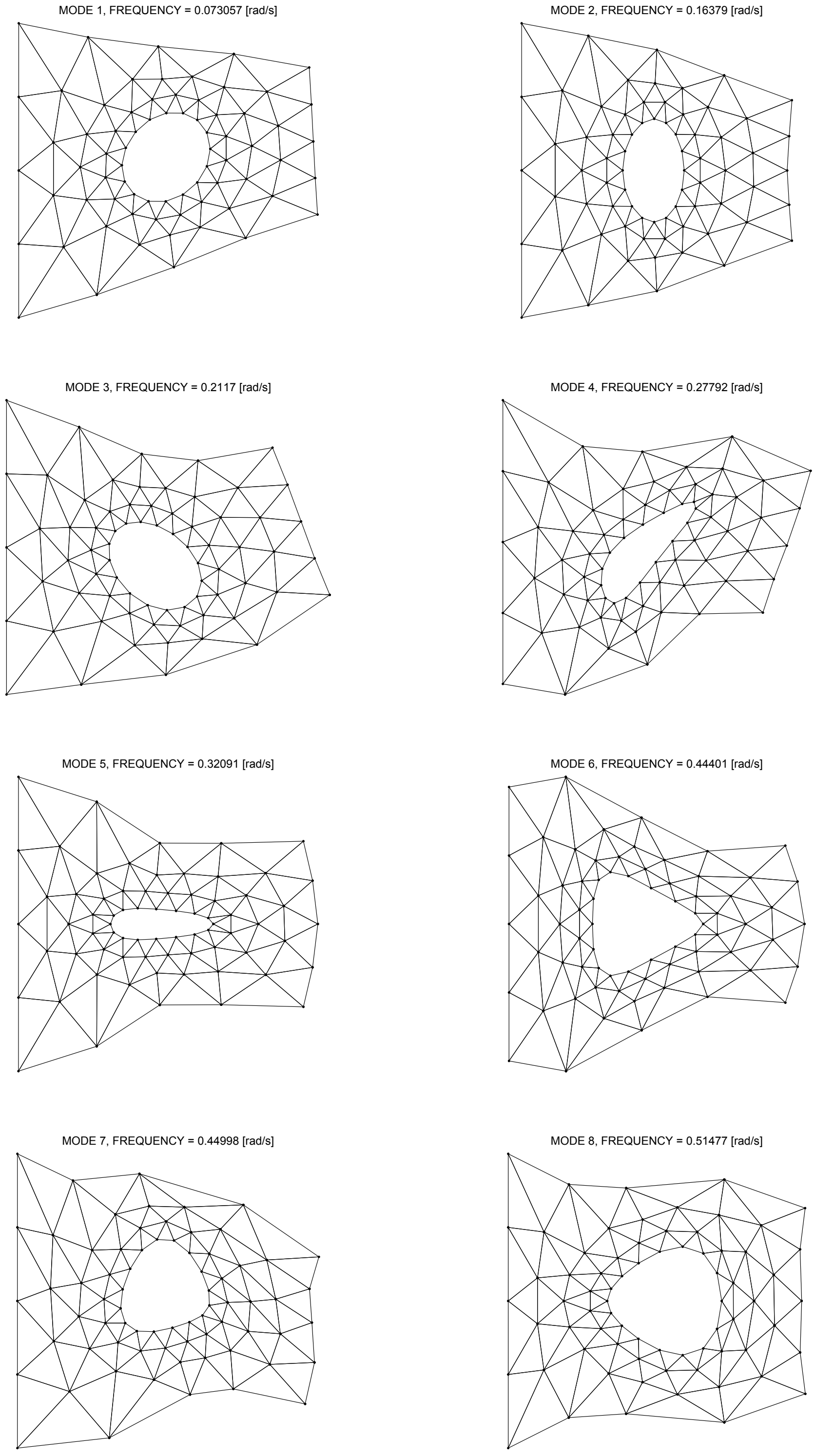

Figure 3.22: First eight modes of the tapered cantilever plate by the $A\alpha$FEM

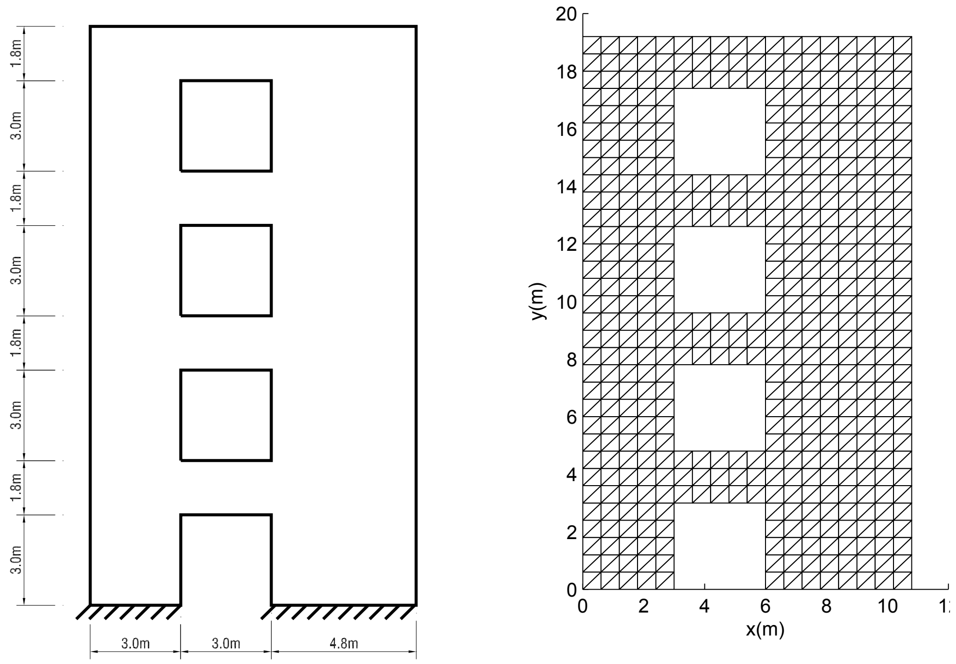

Figure 3.23: A shear wall with four openings and the mesh

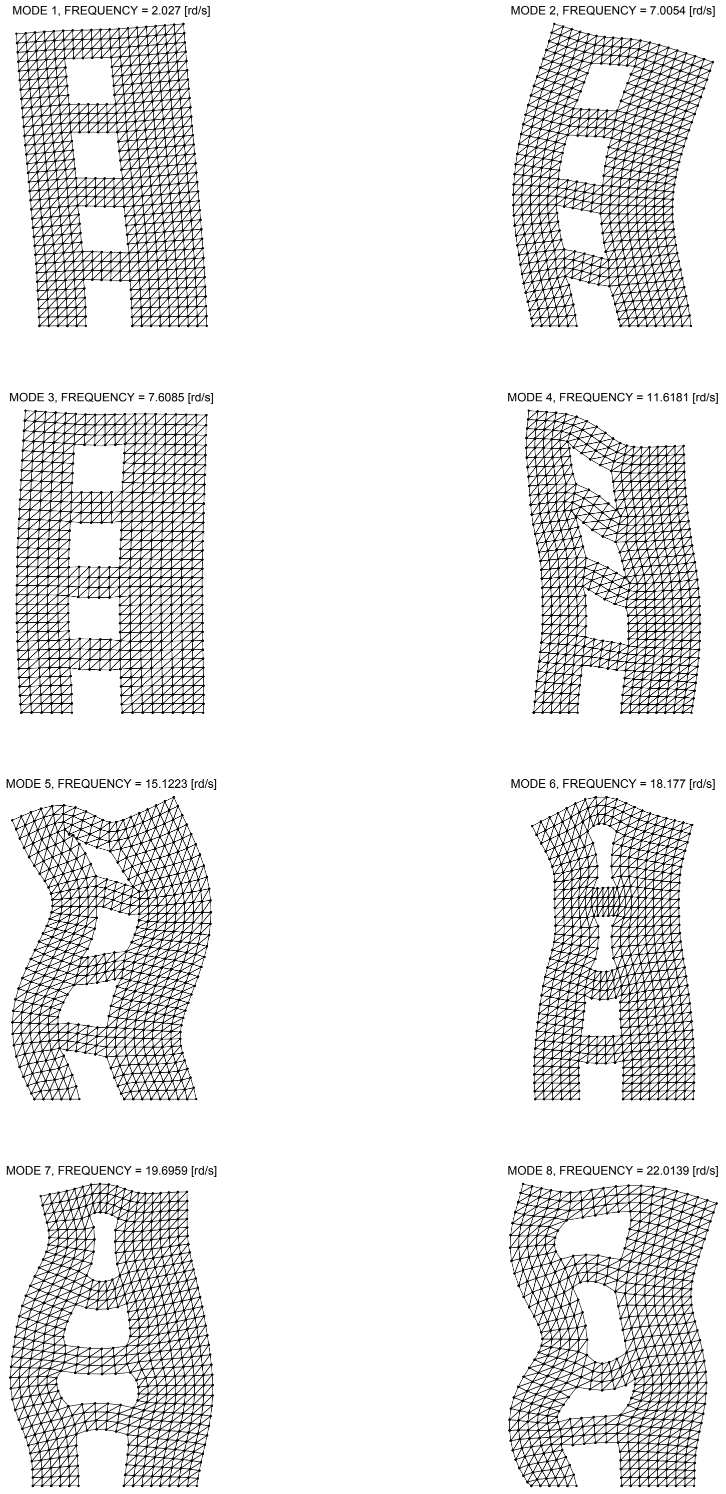

MODE 1, FREQUENCY = 2.027 [rd/s]

MODE 2, FREQUENCY = 7.0054 [rd/s]

MODE 3, FREQUENCY = 7.6085 [rd/s]

MODE 4, FREQUENCY = 11.6181 [rd/s]

MODE 5, FREQUENCY = 15.1223 [rd/s]

MODE 6, FREQUENCY = 18.177 [rd/s]

MODE 7, FREQUENCY = 19.6959 [rd/s]

MODE 8, FREQUENCY = 22.0139 [rd/s]

Figure 3.24: First eight frequencies of the shear wall by the $A\alpha$FEM

Table 3.3: First eight frequencies (rd/s) of the tapered cantilever plate

Mode	FEM-T3	Zhao(ZS96)	AαFEM	Exact solution(ZS95)
Mode 1	0.0773	0.0833	0.0731	0.0744
Error(%)	3.9	11.9624	-1.75	-
Mode 2	0.1699	0.1661	0.1638	0.1648
Error(%)	3.09	0.7888	-0.61	-
Mode 3	0.2223	0.2334	0.2117	0.2055
Error(%)	8.18	13.5766	3.02	-
Mode 4	0.3055	0.3302	0.2779	0.2939
Error(%)	3.95	12.3511	-5.44	-
Mode 5	0.3531	0.3525	0.3209	0.3243
Error(%)	8.88	8.6957	-1.05	-
Mode 6	0.4763	0.4234	0.4441	0.4399
Error(%)	8.27	-3.7509	0.95	-
Mode 7	0.4821	0.4624	0.4499	0.4482
Error(%)	7.56	3.1682	0.38	-
Mode 8	0.5421	0.4805	0.5148	0.4973
Error(%)	9.01	-3.3782	3.52	-

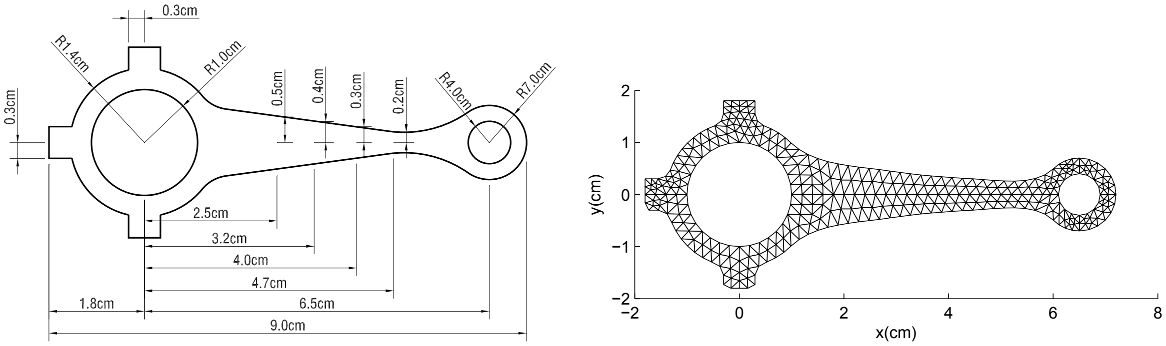

Figure 3.25: Geometric model of an automobile connecting rod and its meshes

Table 3.4: First eight frequencies (rd/s) of a shear wall

No.elements	FEM-T3	ABAQUS	BET[4]	MLPG(GL01)	AαFEM
952 triangular elements	2.146	2.073	2.079	2.069	2.0270
	7.342	7.096	7.181	7.154	7.0054
	7.653	7.625	7.644	7.742	7.6085
	12.601	11.938	11.833	12.163	11.6181
	16.079	15.341	15.947	15.587	15.1223
	18.865	18.345	18.644	18.731	18.1770
	20.525	19.876	20.268	20.573	19.6959
	22.793	22.210	22.765	23.081	22.0139
3808 triangular elements	2.0634	2.073	2.079	2.069	2.0105
	7.0926	7.096	7.181	7.154	6.9554
	7.6206	7.625	7.644	7.742	7.6011
	11.8926	11.938	11.833	12.163	11.4767
	15.3559	15.341	15.947	15.587	14.9788
	18.3444	18.345	18.644	18.731	18.0807
	19.8988	19.876	20.268	20.573	19.5951
	22.2439	22.210	22.765	23.081	21.8834

[4] Boundary Element Techniques (BET) (BTW84)

Table 3.5: First eight natural frequencies (Hz) of a connecting rod

No.elements	FEM-T3	FEM-Q4[5]	FEM-Q8[6]	ES-FEM	$A\alpha$FEM
574 triangular elements	5.454	5.1369	5.1222	5.1368	5.0865
	23.466	22.050	21.840	22.0595	21.8690
	49.803	49.299	49.115	49.3809	49.2016
	55.516	52.232	51.395	52.0420	51.6044
	99.715	93.609	91.787	92.7176	92.3010
	116.243	108.59	106.153	109.5887	107.9777
	147.192	134.64	130.146	132.6795	132.3226
	166.975	159.45	156.142	158.2376	158.0875
2296 triangular elements	5.209	5.124	5.1222	5.1246	5.1082
	22.291	21.909	21.840	21.8805	21.8191
	49.360	49.211	49.115	49.1726	49.1125
	52.592	51.657	51.395	51.5181	51.3580
	94.154	92.390	91.787	91.9305	91.7107
	109.474	107.51	106.153	106.8473	106.3088
	135.321	131.48	130.146	130.5546	130.2115
	160.165	157.51	156.142	156.3497	156.1473

[5] Four Node Quadrilateral Element (FEM-Q4)(Bat96)

[6] Eight Node Hexahedral Element (FEM-Q8)(ZT00)

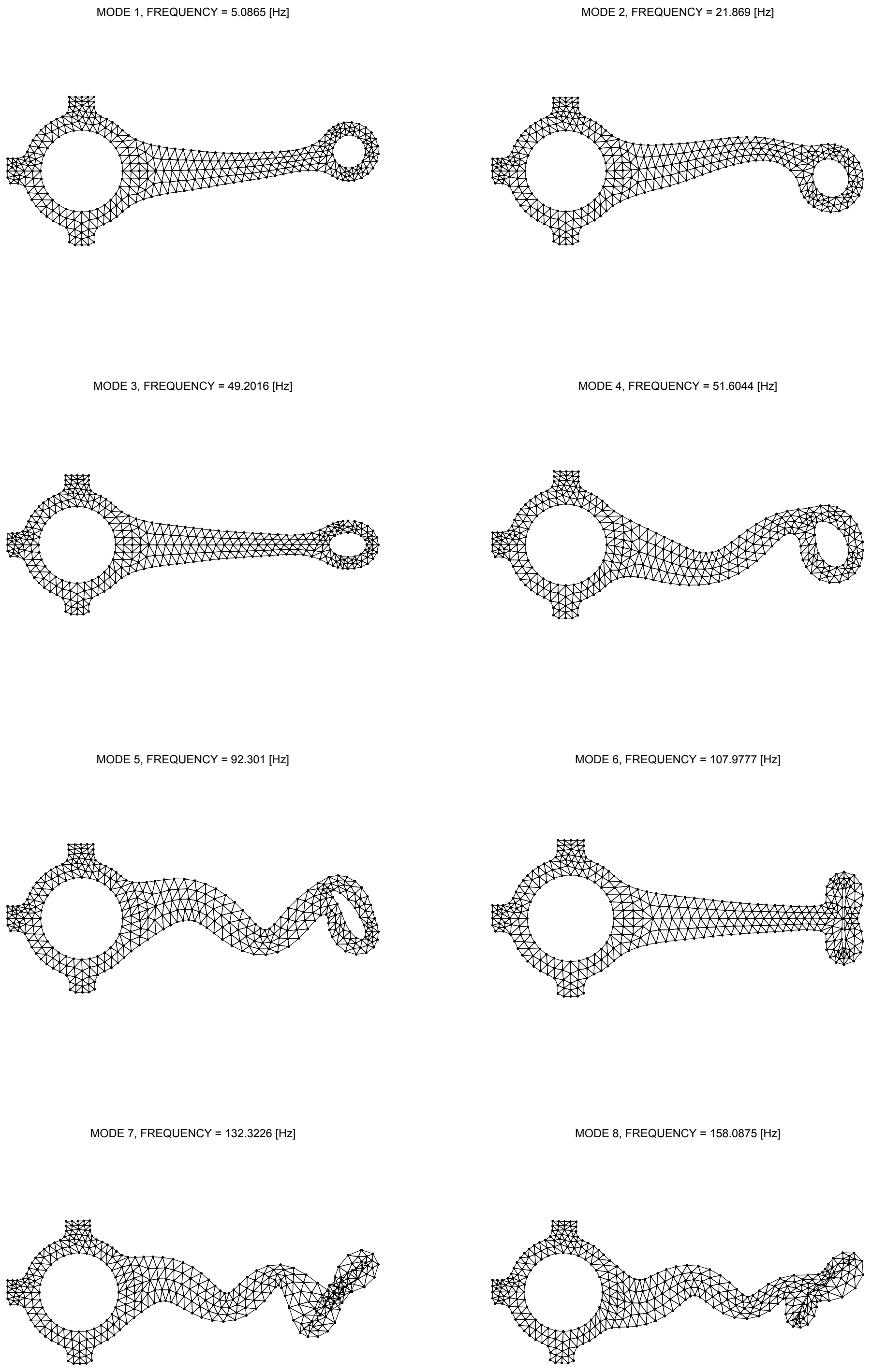

MODE 1, FREQUENCY = 5.0865 [Hz]

MODE 2, FREQUENCY = 21.869 [Hz]

MODE 3, FREQUENCY = 49.2016 [Hz]

MODE 4, FREQUENCY = 51.6044 [Hz]

MODE 5, FREQUENCY = 92.301 [Hz]

MODE 6, FREQUENCY = 107.9777 [Hz]

MODE 7, FREQUENCY = 132.3226 [Hz]

MODE 8, FREQUENCY = 158.0875 [Hz]

Figure 3.26: First eight modes of a connecting rod by the $A\alpha$FEM

3.5.2.5 Free vibration analysis of a machine part

Next, consider the eigenvalue analysis for a machine part designed by CAD as shown in Fig. 3.27. The two-dimensional plane stress problem is assumed with $E = 2.1 \times 10^4 kgf/mm^2, \nu = 0.3, \rho = 8.0 \times 10^{-10} kgfs^2/mm^4, t = 1.0mm.$

The natural frequencies of the first eight modes are presented in Tab. 3.6. The results obtained from the AαFEM agree with the reference solution and are more accurate than the FEM-T3 for the same mesh. The modes calculated using the AαFEM are shown in Fig. 3.28.

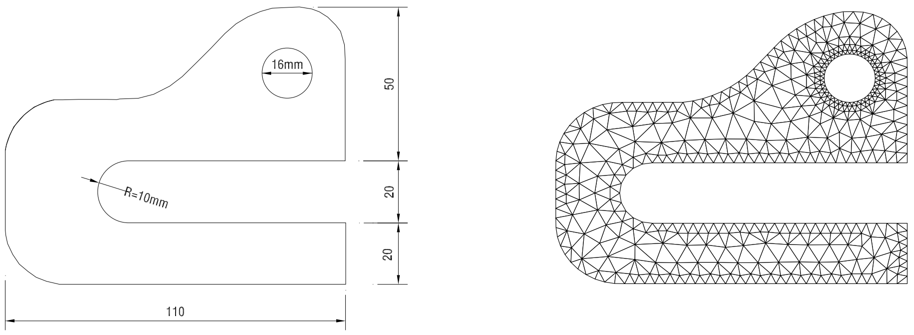

Figure 3.27: A machine part and its meshes

3.5.2.6 Forced vibration analysis of a cantilever beam

Then last example is the cantilever beam is show in Fig. 3.29. This beam is subjected to a tip harmonic loading $P = 1000g(t)$ in the y-direction. Plane strain conditions are assumed with thickness t = 1, Young's modulus $E = 3 \times 10^7$ and Poisson's ratio $\nu = 0.3$. The time step $\Delta t = 1 \times 10^{-3}$ is used. The AαFEM is more accurate than the FEM-T3 and FEM-Q4 for large time steps, as shown in Fig. 3.30 and Fig. 3.31. Of course, this accuracy decreases if the time step is too large (an example for $\Delta t = 5 \times 10^{-2}$ is given in Fig. 3.31), the accuracy of the AαFEM decreases. As shown in Fig. 3.32 the results obtained by the AαFEM without damping (c = 0) are very good. The results with damping (c = 0.4) are very stable as shown in Fig. 3.33.

Table 3.6: First eight natural frequencies (Hz) of a machine part

No.nodes	FEM-T3	FEM(NTV92)	NBNM(Nag99)	$A\alpha$FEM
	954.208	909.09	906.50	899.5509
	1684.134	1639.45	1640.04	1613.7050
637	4602.111	4434.00	4426.57	4372.3597
triangular	10383.386	9944.57	9932.99	9831.4070
elements	11498.753	11209.39	11226.98	11192.9315
	17898.438	17522.44	17516.87	17337.4634
	22907.050	-	-	22376.2442
	24794.438	-	-	24057.6648
	961.745	909.09	906.50	899.3090
	1692.864	1639.45	1640.04	1614.9336
838	4611.028	4434.00	4426.57	4377.1788
triangular	10363.961	9944.57	9932.99	9833.8197
elements	11539.766	11209.39	11226.98	11182.8249
	17961.157	17522.44	17516.87	17349.3836
	22941.550	-	-	22370.2123
	24878.957	-	-	24034.7601

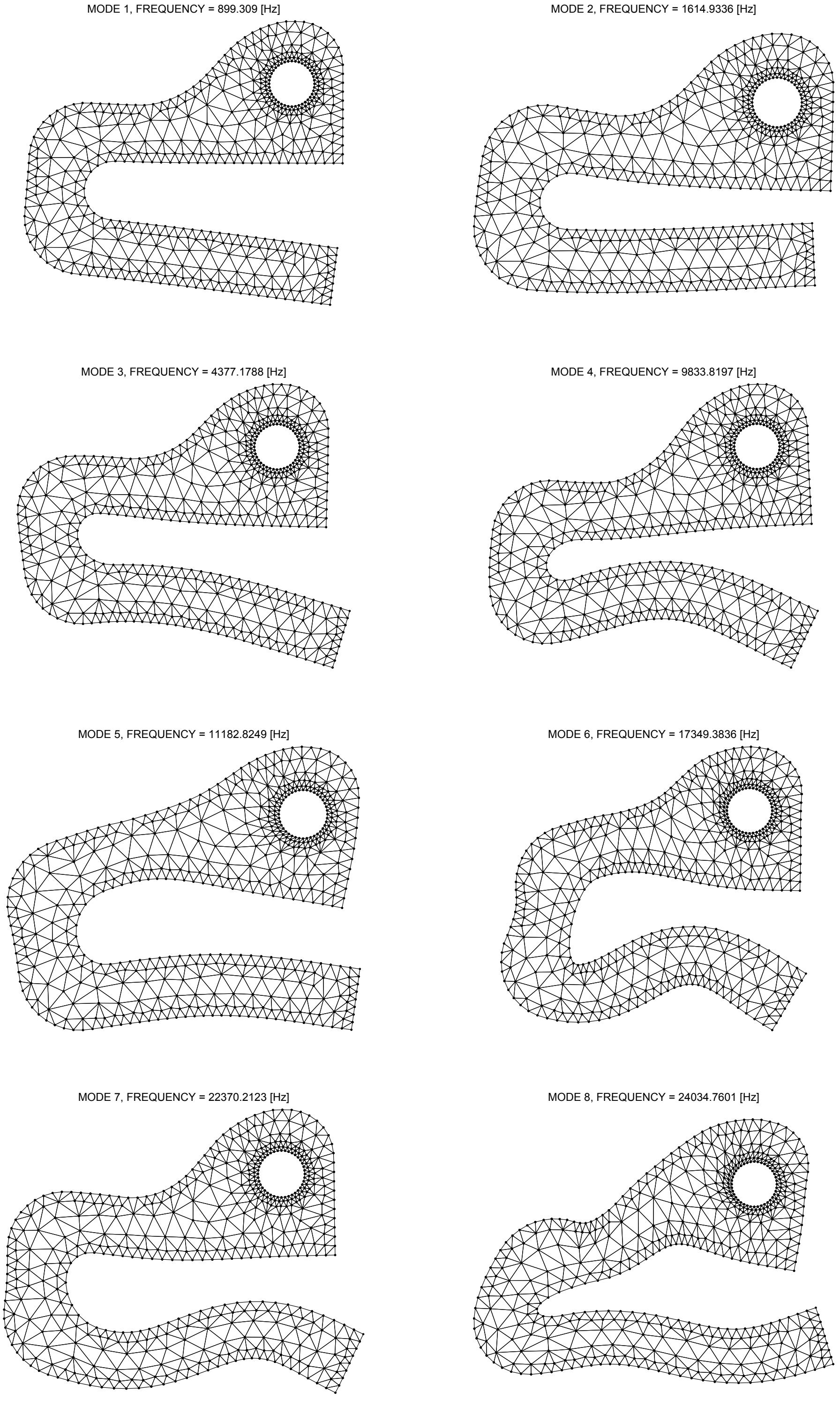

Figure 3.28: First eight modes a machine part by the $A\alpha$FEM

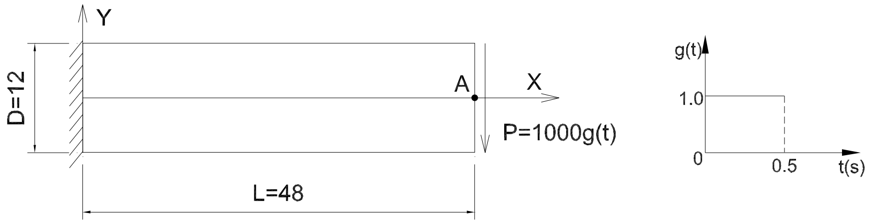

Figure 3.29: Cantilever beam for forced vibration and harmonic loading

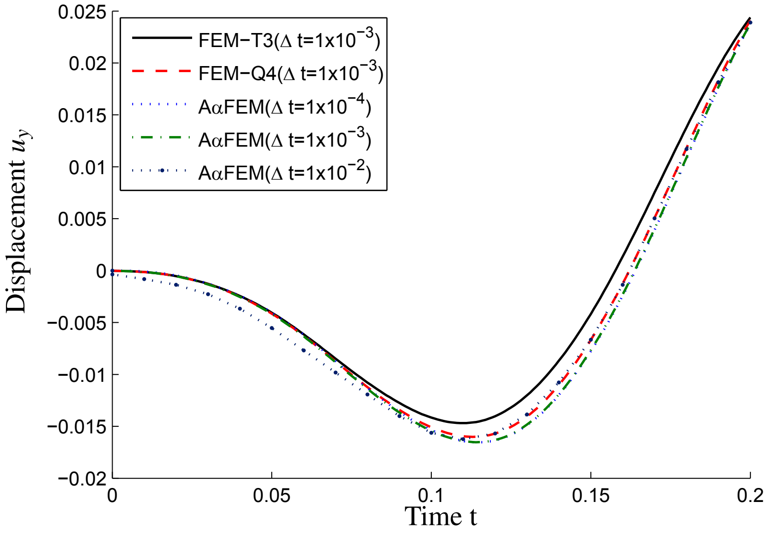

Figure 3.30: Displacement u_y at point A using Newmark method $(\delta = 0.5, \beta = 0.25, g(t) = sin\omega t)$

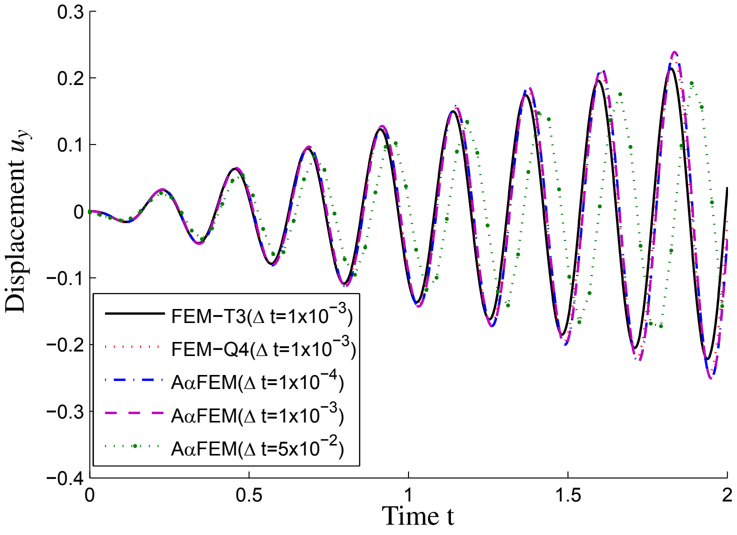

Figure 3.31: Displacement u_y at point A using Newmark method ($\delta = 0.5, \beta = 0.25, g(t) = sin\omega t$)

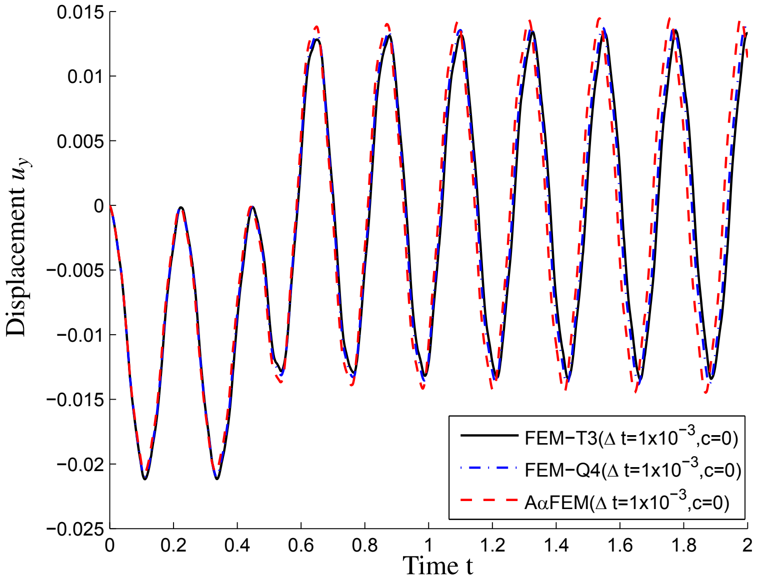

Figure 3.32: Transient displacement u_y at point A using Newmark method ($\delta = 0.5$ *and* $\beta = 0.25$)

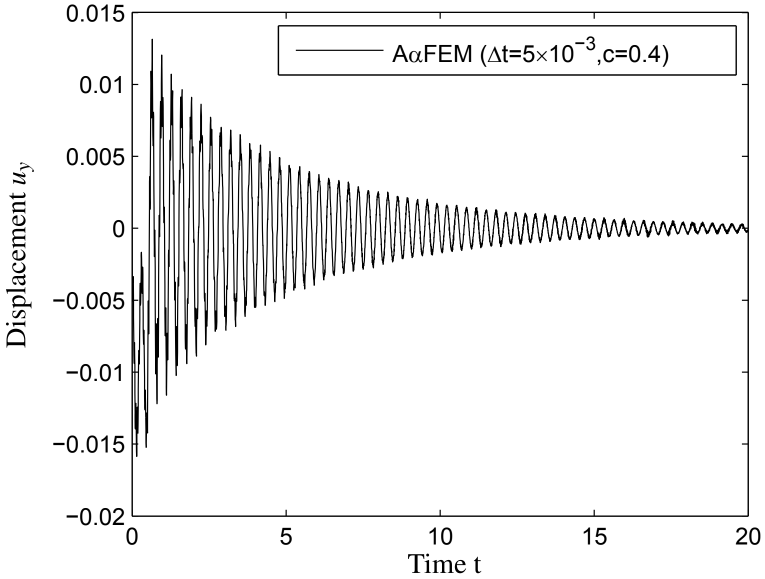

Figure 3.33: Transient displacement u_y at point A using Newmark method ($\delta = 0.5$ *and* $\beta = 0.25$)

3.6 Concluding remarks

The static, free and forced vibration analysis of two dimensional solids have been presented in this chapter. An assumed strain field is carefully constructed based on the piecewise constant strain field of linear triangular FEM models with an adjustable parameter α ($\alpha \in [0, 1.6]$). When $\alpha = 0$, the present element becomes the standard FEM and hence produces a lower bound in the strain energy. For $\alpha = 1.6$, the element becomes the node-based smoothed FEM (NS-FEM) model and leads to an upper bound in the strain energy. For intermediate values of α, the element was shown to underestimate the strain energy. It was also shown that a so-called "optimal" value for α could be easily found such that the exact strain energy is recovered. Through some numerical examples showed, we conclude: (1) The numerical results of the AαFEM using triangular elements are always more accurate than those of FEM-T3 and even more accurate than those of the FEM-Q4 with the same number of nodes. The convergence rates in the energy norm are asymptotically the same as these standard FEM techniques; (2) In the natural frequency and forced vibration analyses, the AαFEM is always stable and gives more accurate results than the corresponding FEM-T3 and FEM-Q4; (3) The AαFEM is easy to implement into a finite element program and triangular meshes are ideal for complicated problem domains.

Chapter 4

An alternative alpha Finite Element Method for Mindlin-Reissner plates analysis with Discrete Shear Gap technique

4.1 Introduction

The finite element analysis of plate structures plays an important role in engineering applications because the plate is one of the most widely used structural components. In practical applications, lower-order Mindlin-Reissner plate elements are preferred due to their simplicity and efficiency. However, these low-order plate elements in the limit of thin plates often suffer from the shear locking phenomenon which has the root of incorrect transverse forces under bending.

Therefore, many formulations have been developed to overcome the shear locking phenomenon and to increase the accuracy and stability of numerical methods such as Mixed formulation/hybrid elements(ZL88, ADB98, Lov98, TA93), the enhanced assumed strain (EAS) method (SR90, SJ99) and the assumed natural strain (ANS) method (dSJVA02, CYM^{+}08). Recently, the Discrete-Shear-Gap (DSG) method (BBR00) which can avoid shear locking was proposed. The DSG is similar to the ANS methods in the aspect of modifying the course of certain strains within the element, but different in that it does not employ collocation points, which makes the DSG method independent of the order and shape of the element.

In this chapter, I further extend the AαFEM to static, free vibration and buckling analyses of Mindlin-Reissner plates using triangular elements only. In the AαFEM for plates, the bending, shearing and geometrical stiffness matrices of the standard FEM formulation are enhanced by additional strain terms with an adjustable parameter

α which results in an effectively softer stiffness formulation compared to the linear triangular element. Transverse shear locking can be avoided through the discrete shear gap (DSG) method. Several numerical examples illustrate the high performance of the Aα-DSG3 formulation compared to other elements from the literature.

4.2 Weak form for modified strain field

We use the modified Hellinger-Reissner variational formulation:

$$\sum_{k=1}^{N}\sum_{i=1}^{M}\left[\int_{\Omega_{k,i}} \delta\left(\varepsilon_{k,i}+\alpha\varepsilon_{k,i}^{\mathrm{add}}\right)^{\mathrm{T}}\mathbf{D}\left(\varepsilon_{k,i}-\alpha\varepsilon_{k,i}^{\mathrm{add}}\right)d\Omega\right]-\int_{\Omega}\delta\mathbf{u}^{\mathrm{T}}\bar{\mathbf{p}}d\Omega-\int_{\Gamma_t}\delta\mathbf{u}^{\mathrm{T}}\bar{\mathbf{t}}d\Gamma=0 \tag{4.1}$$

In the present formulation, the usual compatible strain field is replaced by the modified strain field, Eq. (3.8) and hence the modified Hellinger-Reissner variational principle with the assumed strain vector $\hat{\varepsilon}$ and displacement field $\hat{\mathbf{u}}$ as independent field variables for elasticity problems is given by (PW06)

$$\Pi_{HR}(\hat{\mathbf{u}},\hat{\varepsilon})=-\frac{1}{2}\int_{\Omega}\hat{\varepsilon}^{T}\mathbf{D}\hat{\varepsilon}d\Omega+\int_{\Omega}\hat{\varepsilon}^{T}\mathbf{D}\varepsilon d\Omega-\int_{\Omega}\mathbf{u}^{T}\bar{\mathbf{p}}d\Omega-\int_{\Gamma_t}\mathbf{u}^{T}\bar{\mathbf{t}}d\Gamma \tag{4.2}$$

where the constitutive matrix for linear isotropic elasticity $\mathbf{D}=[\mathbf{D}^{b}\ 0; 0\ \mathbf{D}^{s}]^{T}$, the displacement field is given by $\mathbf{u}=[w,\beta_x,\beta_x]^{T}$, the plate is loaded by a transverse load $\bar{\mathbf{p}}=[p,0,0]^{T}$ and boundary loads $\bar{\mathbf{t}}=[\bar{p},\bar{m}_x,\bar{m}_y]^{T}$.

The strain energy is given by

$$\hat{U}(\hat{\mathbf{u}})=-\frac{1}{2}\int_{\Omega}\hat{\varepsilon}^{T}\mathbf{D}\hat{\varepsilon}d\Omega+\int_{\Omega}\hat{\varepsilon}^{T}\mathbf{D}\varepsilon d\Omega \tag{4.3}$$

which can be rewritten in a summation of integrals over all sub-domain $\Omega_{k,i}$

$$\hat{U}(\hat{\mathbf{u}})=\sum_{k=1}^{N}\sum_{i=1}^{M}\left[-\frac{1}{2}\int_{\Omega_{k,i}}\hat{\varepsilon}_{k,i}^{T}\mathbf{D}\hat{\varepsilon}_{k,i}d\Omega+\int_{\Omega_{k,i}}\hat{\varepsilon}_{k,i}^{T}\mathbf{D}\varepsilon_{k,i}d\Omega\right]=\sum_{k=1}^{N}\sum_{i=1}^{M}\hat{U}_{k,i}(\hat{\mathbf{u}}) \tag{4.4}$$

in which

$$\hat{U}(\hat{\mathbf{u}})=-\frac{1}{2}\int_{\Omega_{k,i}}\hat{\varepsilon}_{k,i}^{T}\mathbf{D}\hat{\varepsilon}_{k,i}d\Omega+\int_{\Omega_{k,i}}\hat{\varepsilon}_{k,i}^{T}\mathbf{D}\varepsilon_{k,i}d\Omega \tag{4.5}$$

Substituting Eq. (**??**) into Eq. (4.5) leads to

$$\begin{aligned}\hat{U}(\hat{\mathbf{u}})&=-\frac{1}{2}\int_{\Omega_{k,i}}\left(\varepsilon_{k,i}+\alpha\varepsilon_{k,i}^{\mathrm{add}}\right)^{T}\mathbf{D}\left(\varepsilon_{k,i}+\alpha\varepsilon_{k,i}^{\mathrm{add}}\right)d\Omega+\int_{\Omega_{k,i}}\left(\varepsilon_{k,i}+\alpha\varepsilon_{k,i}^{\mathrm{add}}\right)^{T}\mathbf{D}\varepsilon_{k,i}\\&=\frac{1}{2}\int_{\Omega_{k,i}}\varepsilon_{k,i}^{T}\mathbf{D}\varepsilon_{k,i}d\Omega-\frac{1}{2}\alpha^{2}\int_{\Omega_{k,i}}\left(\varepsilon_{k,i}^{\mathrm{add}}\right)^{T}\mathbf{D}\varepsilon_{k,i}^{\mathrm{add}}d\Omega\end{aligned} \tag{4.6}$$

Due to the zero-sum property, Eq. (**??**), three terms in the integrals vanish. Hence, the Hellinger-Reissner variational principle reduces to

$$\begin{aligned}\Pi_{HR}\left(\hat{\mathbf{u}}, \varepsilon^{\text{add}}, \alpha\right) = \sum_{k=1}^{N}\sum_{i=1}^{M}\left[\frac{1}{2}\int_{\Omega_{k,i}} \varepsilon_{k,i}^{T}\mathbf{D}\varepsilon_{k,i}d\Omega - \frac{1}{2}\alpha^2\int_{\Omega_{k,i}}\left(\varepsilon_{k,i}^{\text{add}}\right)^{T}\mathbf{D}\varepsilon_{k,i}d\Omega\right] \\ -\int_{\Omega}\mathbf{u}^{T}\bar{\mathbf{p}}d\Omega - \int_{\Gamma_t}\mathbf{u}^{T}\bar{\mathbf{t}}d\Gamma\,.\end{aligned} \tag{4.7}$$

Taking the variation with respect to α, one obtains

$$\delta\Pi_{HR}\left(\hat{\mathbf{u}}, \varepsilon^{\text{add}}, \alpha\right) = -\alpha\sum_{k=1}^{N}\sum_{i=1}^{M}\int_{\Omega_{k,i}}\left(\varepsilon_{k,i}^{\text{add}}\right)^{T}\mathbf{D}\varepsilon_{k,i}^{\text{add}}d\Omega \Rightarrow \alpha = 0 \tag{4.8}$$

Taking the variation with respect to ε^{add}, Eq. (4.7) becomes the total potential energy (Π_{TPE}).

$$\delta_{\varepsilon_{\text{add}}}\Pi_{HR}\left(\hat{\mathbf{u}}, \varepsilon^{\text{add}}, \alpha\right) = -\alpha^2\sum_{k=1}^{N}\sum_{i=1}^{M}\int_{\Omega_{k,i}}\mathbf{D}\varepsilon_{k,i}^{\text{add}}d\Omega \Rightarrow \int_{\Omega_{k,i}}\varepsilon_{k,i}^{\text{add}}d\Omega = 0 \tag{4.9}$$

We next perform variation with respect to $\hat{\mathbf{u}}$ yielding

$$\begin{aligned}\delta_{\hat{\mathbf{u}}}\Pi_{HR}\left(\hat{\mathbf{u}}, \alpha\right) = \sum_{k=1}^{N}\sum_{i=1}^{M}\left[\int_{\Omega_{k,i}}\delta\left(\varepsilon_{k,i} + \alpha\varepsilon_{k,i}^{\text{add}}\right)\mathbf{D}\left(\varepsilon_{k,i} - \alpha\varepsilon_{k,i}^{\text{add}}\right)d\Omega\right] \\ -\int_{\Omega}\delta\mathbf{u}^{T}\bar{\mathbf{p}}d\Omega - \int_{\Gamma_t}\delta\mathbf{u}^{T}\bar{\mathbf{t}}d\Gamma = 0\,.\end{aligned} \tag{4.10}$$

The Galerkin-like weak form Eq. (4.10) is an extended form of the standard Galerkin weak formulation to conform the strain field. The Galerkin-like weak form becomes the standard Galerkin weak form for $\varepsilon_{k,i}^{\text{add}} = 0$. Substituting the approximation Eq. (2.33) into Eq. (4.10), and using the arbitrariness of the variations, we obtain

$$\tilde{\mathbf{K}}^{A\alpha DSG3}\mathbf{d} = \mathbf{f} \tag{4.11}$$

where $\tilde{\mathbf{K}}^{A\alpha DSG3}$ is the element stiffness matrix with the scaled gradient strains

$$\begin{aligned}\tilde{\mathbf{K}}_{k}^{A\alpha DSG3} &= \sum_{k=1}^{N}\sum_{i=1}^{M}\int_{\Omega_{k,i}}\mathbf{B}_{k,i}^{T}\mathbf{D}\mathbf{B}_{k,i}d\Omega - \alpha^2\sum_{k=1}^{N}\sum_{i=1}^{M}\int_{\Omega_{k,i}}\left(\mathbf{B}_{k,i}^{\text{add}}\right)^{T}\mathbf{D}\mathbf{B}_{k,i}^{\text{add}}d\Omega \\ &= \mathbf{K}^{DSG3} - \alpha^2\tilde{\mathbf{K}}_{k}^{\text{add}}\end{aligned} \tag{4.12}$$

where $\mathbf{K}^{\text{DSG3}}$ is the global stiffness matrix of the discrete shear gap. $\tilde{\mathbf{K}}_{k}^{\text{add}}$ is derived from the corrected strain, and hence is coined corrected stiffness matrix and helps reduce the well-known overly-stiff behavior of the discrete shear gap. Defining

$$\mathbf{B}_{k,i}^{\text{add}} = 3\sqrt{2}\left(\bar{\varepsilon}_{k} - \varepsilon_{k,i}\right)\left(L_1 - \frac{1}{3}\right) \tag{4.13}$$

$\tilde{\mathbf{K}}_k^{\text{add}}$ can be rewritten explicitly as

$$\begin{aligned}\tilde{\mathbf{K}}_k^{\text{add}} &= \sum_{k=1}^{N}\sum_{i=1}^{M}\int_{\Omega_{k,i}}(\mathbf{B}_{k,i}^{\text{add}})^T\mathbf{D}\mathbf{B}_{k,i}^{\text{add}}d\Omega \\ &= 18\sum_{k=1}^{N}\sum_{i=1}^{M}(\tilde{\mathbf{B}}_k-\mathbf{B}_{k,i})^T\mathbf{D}(\tilde{\mathbf{B}}_k-\mathbf{B}_{k,i})\int_{\Omega_{k,i}}\left(L_1-\frac{1}{3}\right)^2 d\Omega \\ &= \sum_{k=1}^{N}\sum_{i=1}^{M}(\tilde{\mathbf{B}}_k-\mathbf{B}_{k,i})^T\mathbf{D}(\tilde{\mathbf{B}}_k-\mathbf{B}_{k,i})A_{k,i}\end{aligned} \tag{4.14}$$

Eq. (4.12) can be rewritten as:

$$\tilde{\mathbf{K}}_k^{A\alpha DSG3} = \tilde{\mathbf{K}}_{\alpha=0}^{A\alpha DSG3} - \alpha^2\tilde{\mathbf{K}}_k^{\text{add}}\ . \tag{4.15}$$

Therefore the global stiffness and geometrical stiffness matrices of the Aα-DSG3 element are given by

$$\tilde{\mathbf{K}}^{A\alpha DSG3} = \sum_{k=1}^{N^n}\tilde{\mathbf{K}}_k^{A\alpha DSG3}\ \ ,\ \ \tilde{\mathbf{K}}_g = \sum_{k=1}^{N^n}\tilde{\mathbf{K}}_k^g \tag{4.16}$$

The nodal stiffness matrix $\tilde{\mathbf{K}}_k^{\text{add}}$ and geometrical stiffness matrix $\tilde{\mathbf{K}}_k^g$ are rewritten as

$$\tilde{\mathbf{K}}_k^{\text{add}} = \sum_{k=1}^{N}\sum_{i=1}^{M}\left[\left(\tilde{\mathbf{B}}_k^b-\mathbf{B}_{k,i}^b\right)^T\mathbf{D}^b\left(\tilde{\mathbf{B}}_k^b-\mathbf{B}_{k,i}^b\right)+\left(\tilde{\mathbf{B}}_k^s-\mathbf{B}_{k,i}^s\right)^T\mathbf{D}^s\left(\tilde{\mathbf{B}}_k^s-\mathbf{B}_{k,i}^s\right)\right]A_{k,i} \tag{4.17}$$

$$\tilde{\mathbf{K}}_k^g = \sum_{k=1}^{N}\int_{\Omega_{k,i}}\left(\tilde{\mathbf{B}}^g\right)^T\tau\tilde{\mathbf{B}}^g d\Omega = \sum_{k=1}^{N}\left(\tilde{\mathbf{B}}_k^g\right)^T\tau\tilde{\mathbf{B}}_k^g A_k \tag{4.18}$$

The final formulation for static analysis can be rewritten:

$$\tilde{\mathbf{K}}^{A\alpha DSG3}\mathbf{d} = \mathbf{f} \tag{4.19}$$

for free vibration,

$$\left(\tilde{\mathbf{K}}^{A\alpha DSG3} - \varpi^2\mathbf{M}\right)\mathbf{d} = 0 \tag{4.20}$$

and for the buckling analysis,

$$\left(\tilde{\mathbf{K}}^{A\alpha DSG3} - \lambda_{cr}\tilde{\mathbf{K}}_g\right)\mathbf{d} = 0\ . \tag{4.21}$$

The smoothed gradient matrices through the smoothing domain are given by

$$\tilde{\mathbf{B}}_k^b = \frac{1}{A_k}\sum_{i=1}^{N_k^e}\frac{1}{3}A_i^e\mathbf{B}_i^b\ ,\ \ \tilde{\mathbf{B}}_k^s = \frac{1}{A_k}\sum_{i=1}^{N_k^e}\frac{1}{3}A_i^e\mathbf{B}_i^{sDSG3}\ ,\ \ \tilde{\mathbf{B}}_k^g = \frac{1}{A_k}\sum_{i=1}^{N_k^e}\frac{1}{3}A_i^e\mathbf{B}_i^g \tag{4.22}$$

where $\mathbf{B}_i^b$ is a matrix containing only constants for the three-node standard finite element

$$\mathbf{B}_i^b = \frac{1}{2A_e}\begin{bmatrix} 0 & b-c & 0 & 0 & c & 0 & 0 & -b & 0 \\ 0 & 0 & d-a & 0 & 0 & -d & 0 & 0 & a \\ 0 & d-a & b-c & 0 & -d & c & 0 & a & -b \end{bmatrix} \tag{4.23}$$

and $\mathbf{B}_i^{sDSG3}$ is derived from the discrete shear gap technique (BBR00)

$$\mathbf{B}_i^{sDSG3} = \frac{1}{2A^e}\begin{bmatrix} b-c & A^e & 0 & c & \frac{ac}{2} & \frac{bc}{2} & -b & -\frac{bd}{2} & -\frac{bc}{2} \\ d-a & 0 & A^e & -d & -\frac{ad}{2} & -\frac{bd}{2} & a & \frac{ad}{2} & \frac{ac}{2} \end{bmatrix} \tag{4.24}$$

$\mathbf{B}_i^g$ is obtained from the geometrical strains

$$\mathbf{B}_i^g = \frac{1}{2A^e}\begin{bmatrix} b-c & 0 & 0 & c & 0 & 0 & -b & 0 & 0 \\ d-a & 0 & 0 & -d & 0 & 0 & a & 0 & 0 \\ 0 & b-c & 0 & 0 & c & 0 & 0 & -b & 0 \\ 0 & d-a & 0 & 0 & -d & 0 & 0 & a & 0 \\ 0 & 0 & b-c & 0 & 0 & c & 0 & 0 & -b \\ 0 & 0 & d-a & 0 & 0 & -d & 0 & 0 & a \end{bmatrix} \tag{4.25}$$

with $a = x_2 - x_1, b = y_2 - y_1, c = y_3 - y_1, d = x_3 - x_1$ and A^e is the area of the triangular element, see Fig. 4.1.

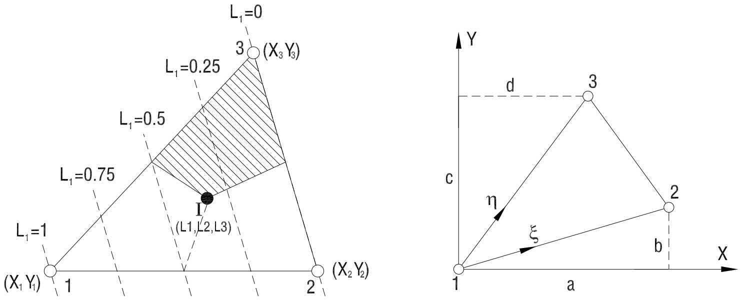

Figure 4.1: Area coordinates and three node triangle element

Since only linear triangular elements are used to obtain stiffness matrices, the finite Reissner-Mindlin plate-bending element approximation is simply interpolated using the linear basis functions for both deflection and rotations without any additional variables. Hence, the bending strains are constant and unchanged from the standard finite elements while the transverse shear strains contain linear interpolated functions. Applying the Discrete Shear Gaps (DSG) (BBR00), the shear strains γ^h become constant and aims to avoid shear locking problem. Thus, strains $\varepsilon = [\varepsilon^b \quad \varepsilon^s \quad \varepsilon^g]^T$ are always constant on the element.

4.3 Numerical results

In the following, the performance of the proposed element (Aα-DSG3) is compared to several elements from the literature, summarized in Tab. 4.1. Static, buckling and free vibration analyses of square, rectangular, circular and triangular plates are considered.

Table 4.1: Summary elements

MITC4	Four node Mixed Interpolation of Tensorial Component (BD85)
MIN3	Three node Mindlin (TH85)
DSG3	Discrete Shear Gap Triangle Element (BBR00)
ES-DSG3	Edge-based Smoothed Discrete Shear Gap Triangle Element (NXLCHNT10)
Q4BL	Quadrilateral Bubble Linked (ZXZ$^+$93)
DKMQ	Discrete Kirchhoff Mindlin Quadrilateral (Kat93)
ANS4	Four node Assumed Natural Strain (Lee04)
ANS9	Nine node Assumed Natural Strain (LH01)
RPIM	Radial Point Interpolation Method (LC04)
Pb-2 Ritz	Two-dimensional polynomial function Rayleigh-Ritz method (KKAb96)
NBNM	Node-By-Node method (Nag99)

4.3.1 Static analysis

4.3.1.1 Patch test

The patch test is introduced to examine the convergence of finite elements. It is checked if the element is able to reproduce a constant distribution of all quantities for arbitrary meshes. A rectangular plate is modeled by several triangular elements as shown in Fig. 4.2. The boundary deflection is assumed to be $w = (1+x+2y+x^2+xy+y^2)/2$. It is found that the A$\alpha$-DSG3 element passes the constant bending patch test within machine precision.

Table 4.2: Patch test

Element	w_5	θ_{x5}	θ_{y5}	m_{x5}	m_{x5}	m_{xy5}
MIN3	0.6422	1.1300	-0.6400	-0.0111	-0.0111	-0.0033
DSG3	0.6422	1.1300	-0.6400	-0.0111	-0.0111	-0.0033
Aα-DSG3	0.6422	1.1300	-0.6400	-0.0111	-0.0111	-0.0033

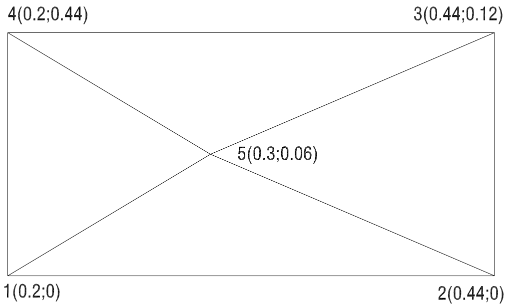

Figure 4.2: Patch test of the element (E = 100000; ν = 0.25; t = 0.01)

4.3.1.2 Square plates

Consider the model of a square plate (length L, thickness t) with clamped and simply supported boundary conditions, respectively, subjected to a uniform load $p = 1$ as shown in Fig. 4.3. The material parameters are: Young's modulus $E = 1092000$ and Poisson's ratio $\nu = 0.3$. Uniform meshes N×N with $N = 2, 4, 8, 16, 32$ are used and symmetry conditions are employed.

The first step is the selection of the "optimal" value of α for this particular problem. This is done by plotting the strain energy versus α for a sequence of meshes with different fineness. As shown in Fig. 4.4, the curves obtained intersect at one point corresponding to the exact energy (known in this particular case). The corresponding value of α is called α_{exact} and for this problem, $\alpha_{exact} = 0.9483$.[1]

Remark: the dependence of the strain energy plotted in Fig. 4.4 on α decreases with mesh refinement, as was also the case in linear flexural analysis of continuum (NTRHXB10).

Remark: for values of α approximately α_{exact}, the mesh density does not influence the results significantly. Once the optimal α has been determined, coarse meshes are sufficient. This is a useful property if a large number of analyses with different loading conditions must be performed on the same structure.

The Aα-DSG3 for $\alpha_{exact} = 0.9483$ leads to improved results compared to all other elements considered in Fig. 4.4 and Fig. 4.5, both in terms of strain energy, displacement and moment accuracy. The MITC4 (four-noded quadrilateral (BD85)) is clearly the best competitor and, for an extremely coarse 2×2 mesh, surpasses the proposed element in terms of displacement accuracy. In terms of gradient accuracy and strain energy however, the proposed element outperforms all others, including the DSG3 and MIN3 (TH85).

---

[1] The reference energy was obtained from (TA93) as 8.5105×10^3.

For a simply clamped plate, the exact strain energy is 1.9456×10^4(TA93), the estimated strain energy at the intersection of the strain energy curves is 1.9478×10^4 and is obtained for $\alpha_{exact} = 0.8372$ and strain energy error, as shown in Fig. 4.6. The convergence of the normalized deflection and moment at the center as a function of $t/L = 0.001$ shown in Fig. 4.7. The Aα-DSG3 is clearly a good competitor to the ES-DSG3 (NXLCHNT10) that was found recently to be one of the most accurate 3-noded triangular plate elements. These results also show that the proposed element is free of shear locking in the thin plate limit.

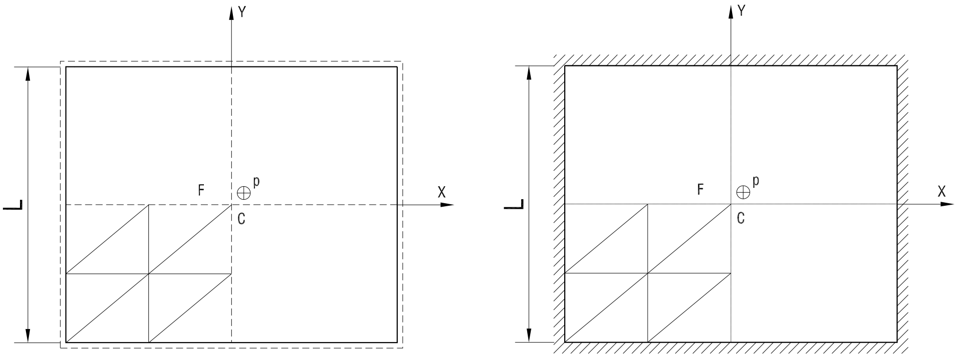

Figure 4.3: Simply supported and full clamped plate.

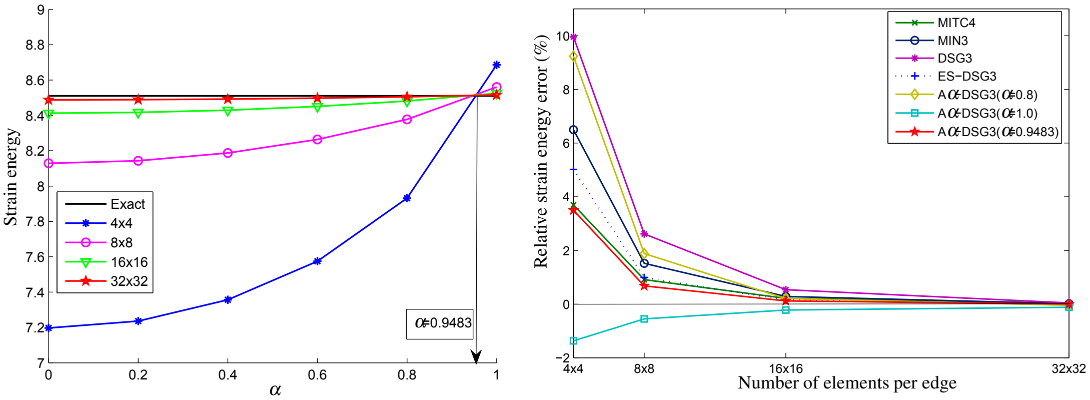

Figure 4.4: Strain energy versus parameter α and the error in strain energy of simply supported plate (t/L=0.01).

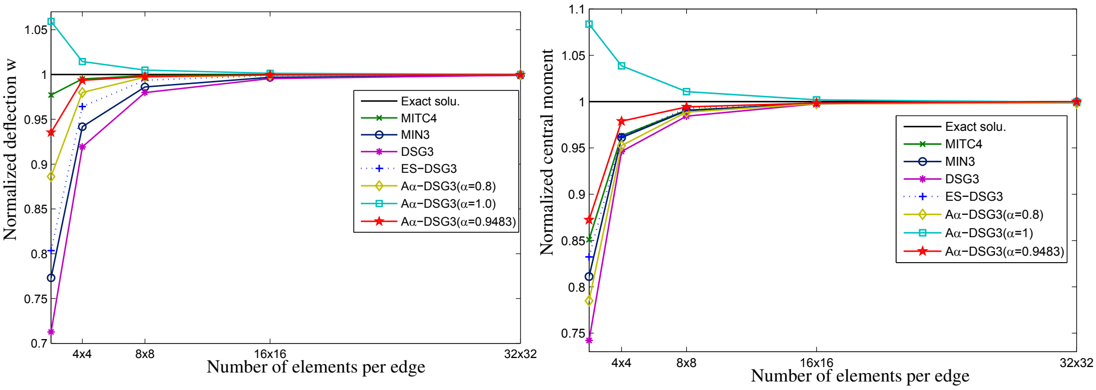

Figure 4.5: Normal deflection and moment of simply supported plate ($t/L = 0.01$).

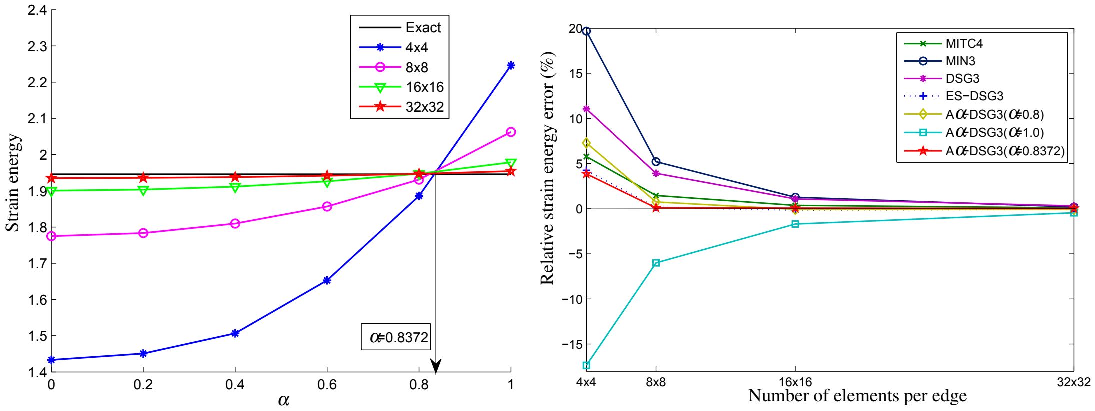

Figure 4.6: Strain energy versus parameter α and the error in strain energy of clamped plate plate (t/L=0.001).

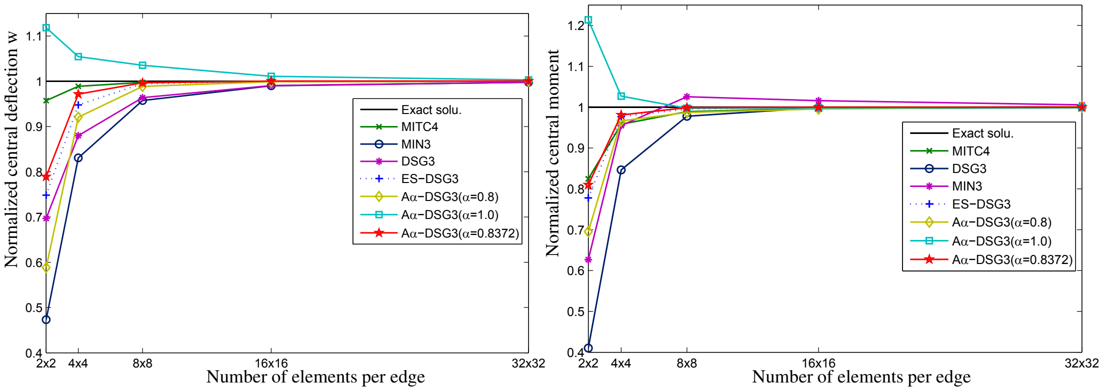

Figure 4.7: Normal deflection and moment of clamped plate plate (t/L=0.001).

4.3.1.3 Skew plate subjected to a uniform load

Let us consider a rhombic plate subjected to a uniform load $p = 1$ as shown in Fig. 4.8. This plate was originally studied by Morley (Mor63). Geometry and material parameters are length $L = 100$, thickness $t = 0.1$, Young's modulus $E = 10.92$ and Poisson's ratio $\nu = 0.3$.

The estimated strain energy at the intersection of the strain energy curves is 3.5438 and is reached for $\alpha_{exact} = 0.8221$ as shown in Fig. 4.9. The values of the Max & Min principle moments at the central point with $\alpha_{exact} = 0.8221$ are given in Fig. 4.10. The Aα-DSG3 shows remarkably good performance compared to the DSG3, MITC4, ES-DSG3 elements and a list of other elements (CLYC06).

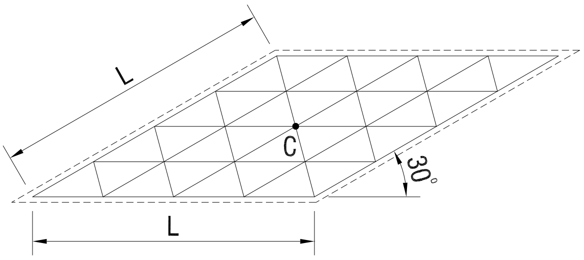

Figure 4.8: A simply supported skew Morley's model.

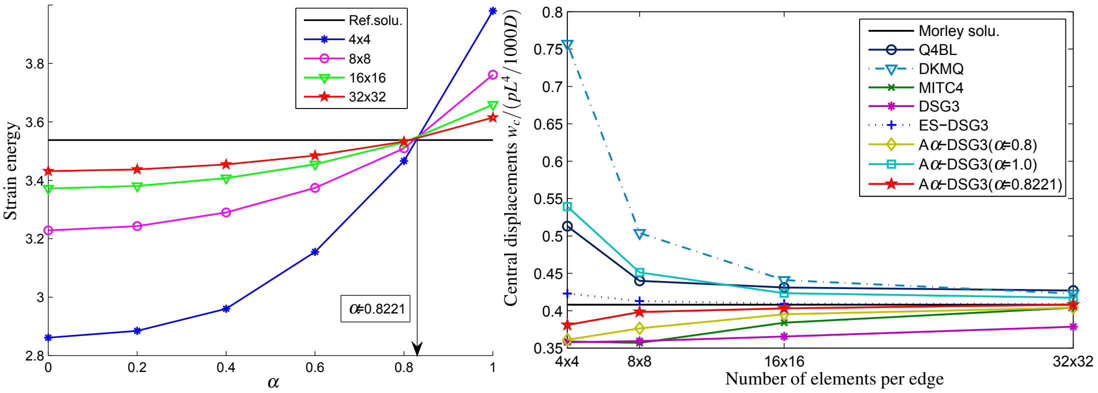

Figure 4.9: Strain energy versus parameter α and normal deflection of the supported skew plate.

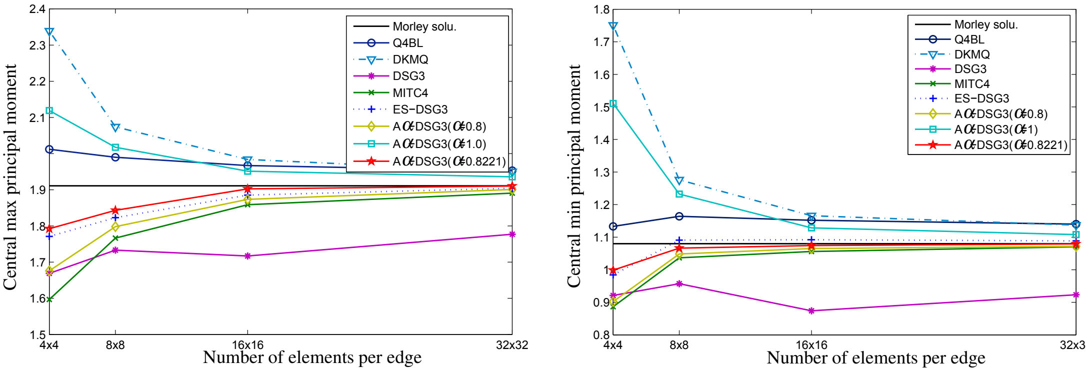

Figure 4.10: Morley plates central principle moment $M_{max}/(pL^2/100)$ and $M_{min}/(pL^2/100)$.

4.3.2 Free vibration of plates

For free vibration and buckling plate analysis, we observed that the optimal value of α varies in the interval of $[0.8 \div 1.0]$. Here, we choose the parameter $\alpha = 0.9$. Although the parameter α chosen may not be optimal for all problems, the results found are more accurate than serval other methods in the literature.

In this section, I examine the accuracy and efficiency of the Aα-DSG3 element for analyzing natural frequencies of plates. The plate may have free (F), simply (S) supported or clamped (C) edges. A non-dimensional frequency parameter ϖ is often used for the presentation of the results for regular meshes.

4.3.2.1 Square plates

We consider square plates of length a, width b and thickness t as shown in Fig. 4.11. The material parameters are Young's modulus $E = 2.0 \times 10^{11}$, Poisson's ratio $\nu = 0.3$ and the density mass $\rho = 8000$. The plate is modeled with uniform meshes of 16 elements per side are shown in Fig. 4.11. A non-dimensional frequency parameter $\varpi = (\omega^2 \rho a^4 t/D)^{1/4}$ is used, where $D = Et^3/(12(1-\nu^2))$ is the flexural rigidity of the plate. Thin and thick plates (SSSS) corresponding to length-to-width ratios, $a/b = 1$ and thickness-to-length $t/a = 0.005$ and $t/a = 0.1$ are considered in this problem.

The convergence of computed frequencies of SSSS and CCCC plates is shown in Fig. 4.12. Our element outperforms the DSG3 element. In the case of thin and thick plates (CCCC) the result are shown in Fig. 4.13. The Aα-DSG3 element outperforms both the DSG3 and ES-DSG3 elements. We also consider the five sets of various boundary conditions in this example: SSSF, SFSF, CCCF, CFCF, and CFSF. The first four lowest frequencies are presented in Tab. 4.3.

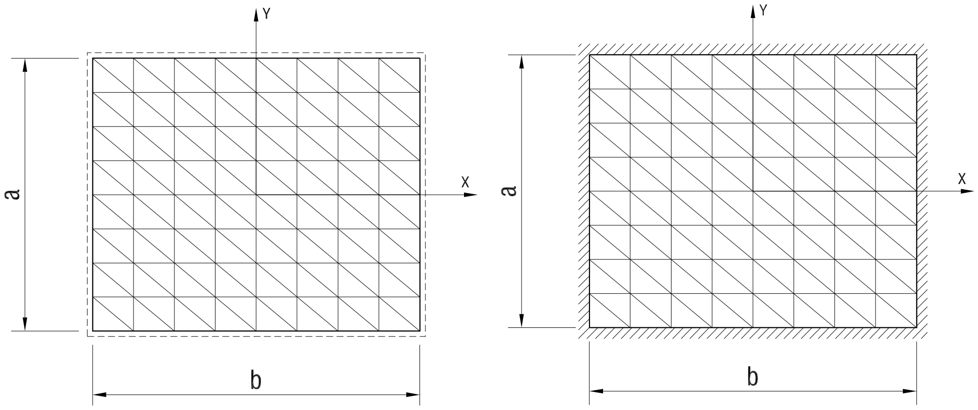

Figure 4.11: Supported and clamped plate

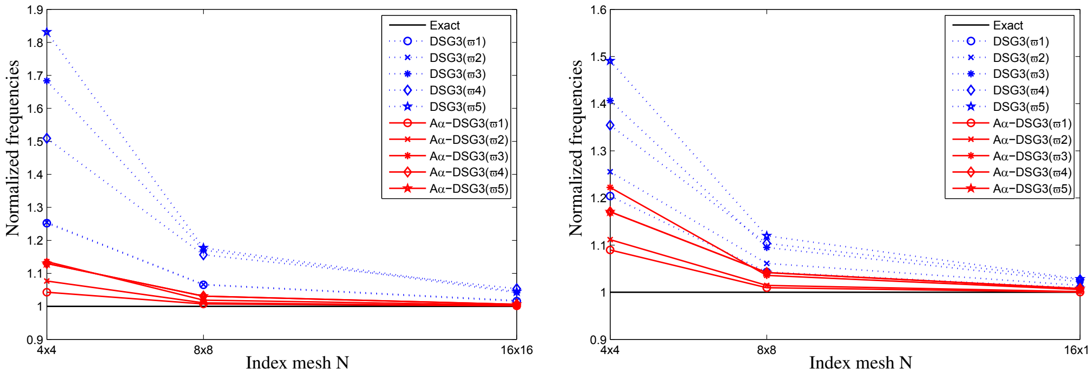

Figure 4.12: Convergence of normalized frequency of SSSS and CCCC plate with a/b = 1; t/a = 0.005.

Table 4.3: A non-dimensional frequency parameter $\varpi = \omega a^2 \sqrt{\rho t/D}$ of a square plate $(t/a = 0.005)$ with various boundary conditions

Plate type	Mode	Methods			
		DSG3	ES-DSG3	Present	Exact(?)
SSSF	1	11.7720	11.6831	11.6851	11.685
	2	28.3759	27.8382	27.7362	27.756
	3	41.9628	41.4312	41.3646	41.197
	4	61.5092	59.6720	59.4379	59.066
SFSF	1	9.6673	9.6425	9.634	9.631
	2	16.3522	16.1239	16.1305	16.135
	3	37.6792	36.9054	36.8071	36.726
	4	39.5026	39.2167	39.092	38.945
CCCF	1	24.2848	23.8947	24.0025	24.020
	2	41.7698	40.1998	40.0401	40.039
	3	65.0068	63.5127	63.5079	63.493
	4	80.9461	77.8776	77.6198	76.761
CFCF	1	22.3437	22.1715	22.238	22.272
	2	27.1814	26.4259	26.5397	26.529
	3	45.8829	43.9273	43.7792	43.664
	4	62.5225	62.9466	63.1078	64.466
CFSF	1	15.2788	15.2035	15.2357	15.285
	2	21.0199	20.5856	20.6477	20.673
	3	41.1975	39.9697	39.8558	39.882
	4	50.3328	49.7767	49.118	49.500

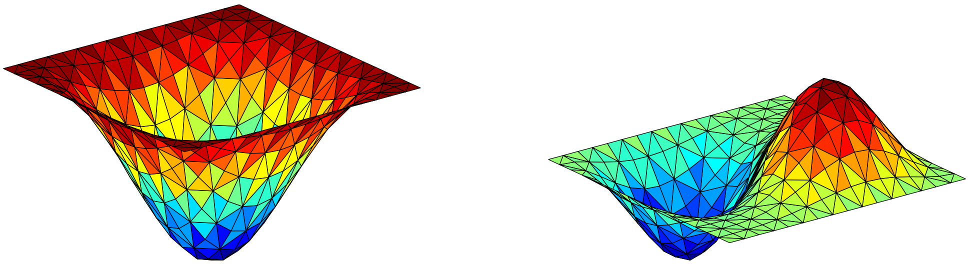

(a) Mode 1 (b) Mode 2

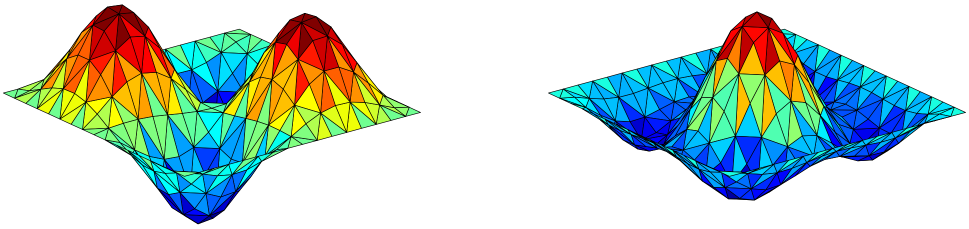

(c) Mode 3 (d) Mode 4

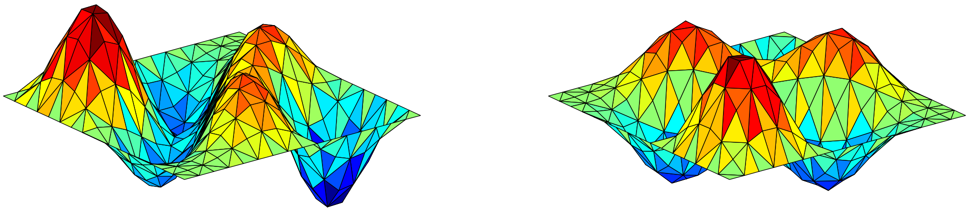

(e) Mode 5 (f) Mode 6

Figure 4.13: The first six mode shapes of CCCC plate using the $A\alpha$-DSG3 with $t/a = 0.005$.

4.3.2.2 Circle plates

In this example, a circular plate with clamped boundary is studied as shown in Fig. 4.14. The material parameters are Young's modulus $E = 2.0 \times 10^{11}$, Poisson's ratio $\nu = 0.3$, radius $R = 5$ and mass density $\rho = 8000$. The plate is discretized with 848 triangular elements with 460 nodes. Two thickness-span ratios $h/2 \times R = 0.01$ and 0.1 are considered.

The first six mode shapes of the circular plate using the Aα-DSG3 are plotted in Fig. 4.15. The frequencies obtained from our element are closer to the analytical solutions in references compared to the DSG3 element and is a good competitor to quadrilateral plate elements such as the Assumed Natural Strain solutions (ANS4) and the higher order Assumed Natural Strain solutions (ANS9) shown in Tab. 4.4. In case of the thickness-span ratio $h/2 \times R = 0.1$, the Aα-DSG3 results also agree well with the ANS4 element with 432 quadrilateral elements presented in Tab. 4.5.

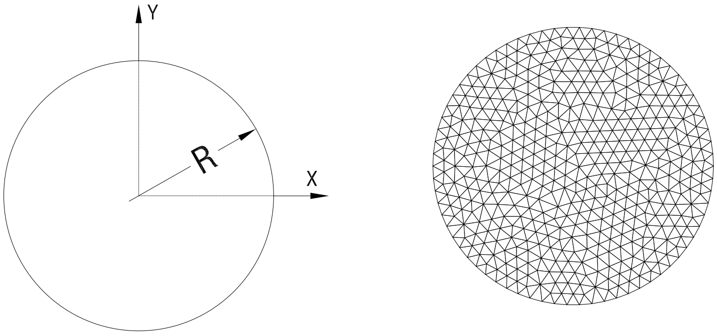

Figure 4.14: The circle plates and initial mesh

4.3.2.3 Triangular plates

Let us consider cantilever (CFF) triangular plates with various shape geometries, see Fig. 4.16. The material parameters are Young's modulus $E = 2.0 \times 10^{11}$, Poisson's ratio $\nu = 0.3$ and mass density $\rho = 8000$. A non-dimensional frequency parameter $\varpi = \omega a^2 (\rho t/D)^{1/2}/\pi$ of triangular square plates with the aspect ratio $t/a = 0.001$ and 0.2 is calculated. The mesh of 744 triangular elements with 423 nodes is used to analyze the convergence for modes via various skew angles such as $\varphi^o = 0^o, 15^o, 30^o, 45^o, 60^o$.

The first six modes of the thin triangular plate ($t/a = 0.001$) are shown in Tab. 4.6. The Aα-DSG3 element is also compared to the MITC4 element and two other well-known numerical methods such as the Rayleigh-Ritz method (MLH92). The frequencies of the Aα-DSG3 are often bounded by these reference models. Note that our method is simply based on the formulation of three-node triangular elements without

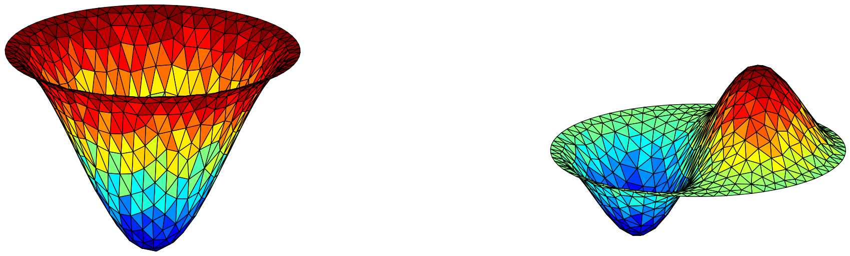

(a) Mode 1 (b) Mode 2

(c) Mode 3 (d) Mode 4

(e) Mode 5 (f) Mode 6

Figure 4.15: The first six mode shapes of the clamped circle plate using the $A\alpha$-DSG3.

Table 4.4: The parameterized natural frequencies $\varpi = \omega a^2 \sqrt{\rho t/D}$ of a clamped circular plate with $t/2*R = 0.01$

Mode	Methods					
	DSG3	ES-DSG3	Present	ANS4[7]	ANS9[8]	Exact (Lei69)
1	10.2941	10.2402	10.2363	10.2572	10.2129	10.2158
2	21.6504	21.3966	21.3121	21.4981	21.2311	21.2600
3	21.6599	21.4096	21.2788	21.4981	21.2311	21.2600
4	35.9885	35.3012	35.0255	35.3941	34.7816	34.8800
5	35.9981	35.3277	35.4113	35.5173	34.7915	34.8800
6	41.1864	40.3671	40.2645	40.8975	39.6766	39.7710
7	53.4374	52.0138	51.1476	52.2054	50.8348	51.0400
8	53.5173	52.1013	51.1876	52.2054	50.8348	51.0400
9	64.2317	62.3053	61.0122	63.2397	60.6761	60.8200
10	64.4073	62.4665	61.1281	63.2397	60.6761	60.8200
11	74.2254	71.6554	70.6303	71.7426	69.3028	69.6659
12	74.3270	71.7269	70.8946	72.0375	69.3379	69.6659
13	91.4366	87.7019	85.8113	88.1498	84.2999	84.5800
14	91.5328	87.7861	85.9978	89.3007	84.3835	84.5800

[7] Four node Assumed Natural Strain (ANS4)(Lee04)

[8] Nine node Assumed Natural Strain (ANS9)(LH01)

Table 4.5: The parameterized natural frequencies $\varpi = \omega a^2 \sqrt{\rho t/D}$ of a clamped circular plate with t/2*R=0.1

Mode	Methods				
	DSG3	ES-DSG3	Present	ANS4	Exact(Lei69)
1	9.3012	9.2527	9.2502	9.2605	9.240
2	18.0038	17.8372	17.8308	17.9469	17.834
3	18.0098	17.8428	17.8375	17.9469	17.834
4	27.6010	27.2344	27.2248	27.0345	27.214
5	27.6082	27.2391	27.2273	27.6566	27.214
6	30.9865	30.5173	30.3818	30.3221	30.211
7	37.9464	37.2817	37.1889	37.2579	37.109
8	37.9817	37.3128	37.2297	37.2579	37.109
9	43.9528	43.0626	42.4781	43.2702	42.409
10	44.0324	43.1328	42.4573	43.2702	42.409
11	48.9624	47.8823	47.4465	47.7074	47.340
12	48.9793	47.8976	47.5786	47.8028	47.340
13	57.2487	55.7747	55.2053	56.0625	54.557
14	57.2776	55.8052	55.2727	57.1311	54.557

adding any additional DOFs. The results for a thick plate are shown in Tab. 4.7. The mode shapes of free vibration of cantilever triangular square plates are illustrated in Fig. 4.17 .

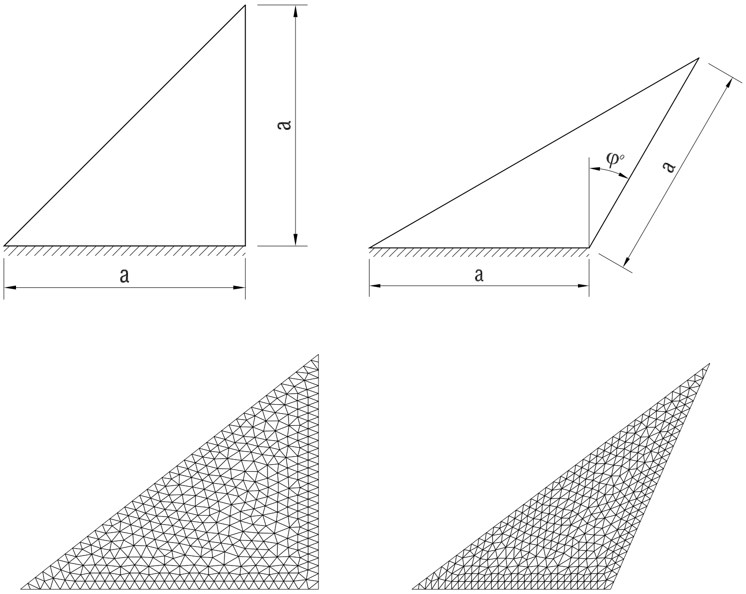

Figure 4.16: A triangular cantilever plates and mesh.

4.3.2.4 Free vibration analysis of the machine part

In this problem, we analyze the natural frequencies and shape modes for the machine part as shown in Fig. 4.18. The numerical parameters are given as $E = 2.1 \times 10^4 kgf/mm^2, \nu = 0.3, \rho = 8.0 \times 10^{-10} kgfs^2/mm^4, t = 1.0mm$.

The natural frequencies of the first six modes are presented in Tab. 4.8. It is clear that the method present always produces more accurate results than the DSG3 element. Also, the results obtained from the Aα-DSG3 show a very good agreement with the reference solution. The first six modes using the Aα-DSG3 are described in Fig. 4.19.

4.3.3 Buckling of plates

In the following examples, we choose the parameter $\alpha = 0.9$, the buckling load factor is defined as $K = \lambda_{cr} b^2/(\pi^2 D)$ where b is the edge width of the plate, λ_{cr} the critical buckling load. The material parameters are Young's modulus $E = 2.0 \times 10^{11}$, Poisson's ratio $\nu = 0.3$.

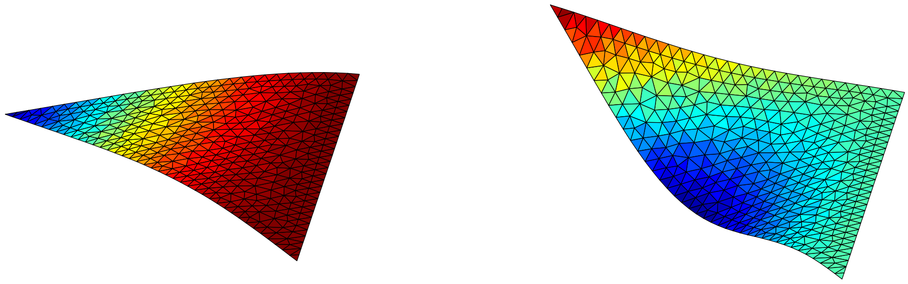

(a) Mode 1 (b) Mode 2

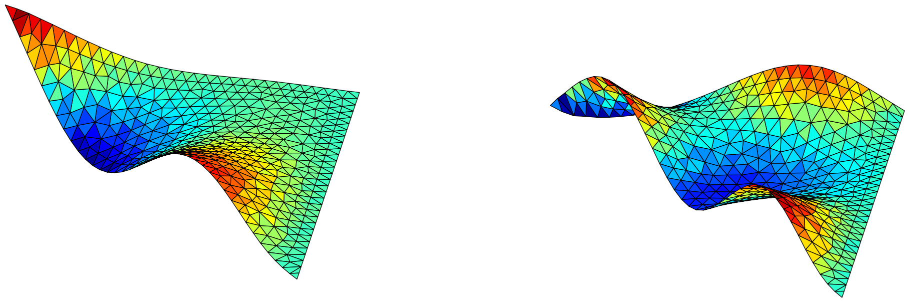

(c) Mode 3 (d) Mode 4

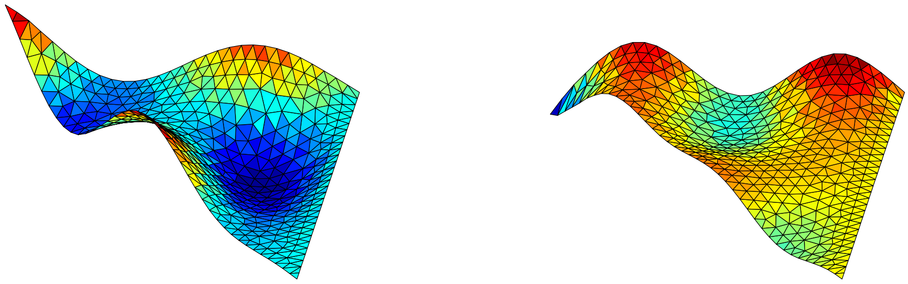

(e) Mode 5 (f) Mode 6

Figure 4.17: The first six mode shapes of triangular plates with t/a=0.001

Table 4.6: The parameterized natural frequencies $\varpi = \omega a^2(\rho t/D)^{1/2}/\pi$ of triangular platess with $t/b = 0.001$

φ^o	Mode	Methods				
		DSG3	ES-DSG3	Present	ANS4	Ref.[9]
0^o	1	0.6252	0.6242	0.6248	0.624	0.625
	2	2.3890	2.3789	2.3776	2.379	2.377
	3	3.3404	3.3159	3.3139	3.317	3.310
	4	5.7589	5.7124	5.7033	5.724	5.689
	5	7.8723	7.7919	7.7727	7.794	7.743
	6	10.3026	10.1547	10.1316	10.200	-
15^o	1	0.5855	0.5840	0.5847	0.583	0.586
	2	2.1926	2.1833	2.1822	2.181	2.182
	3	3.4528	3.4163	3.4153	3.413	3.412
	4	5.3481	5.3020	5.296	5.303	5.279
	5	7.3996	7.3112	7.2939	7.289	7.263
	6	10.2498	10.0779	10.0601	10.095	-
30^o	1	0.5798	0.5766	0.5779	0.575	0.578
	2	2.1880	2.1778	2.1780	2.174	2.178
	3	3.7157	3.6539	3.6543	3.638	3.657
	4	5.5983	5.5361	5.5330	5.534	5.518
	5	7.2814	7.1628	7.1496	7.139	7.109
	6	10.7753	10.5108	10.4989	10.477	-
45^o	1	0.6006	0.5923	0.5926	0.588	0.593
	2	2.3564	2.3359	2.3350	2.324	2.335
	3	4.2795	4.1699	4.1778	4.126	4.222
	4	6.5930	6.4424	6.4544	6.381	6.487
	5	7.8615	7.6658	7.6224	7.614	7.609
	6	11.7850	11.3496	11.3123	11.224	-
60^o	1	0.6497	0.6261	0.6288	0.613	0.636
	2	2.7022	2.6101	2.6153	2.564	2.618
	3	5.6491	5.4283	5.4580	5.353	5.521
	4	8.3505	7.7333	7.8264	7.460	8.254
	5	10.7757	10.3756	10.3883	10.306	10.395
	6	14.6003	13.3296	13.3254	12.942	-

[9] Reference solution(MLH92)

Table 4.7: The parameterized natural frequencies $\varpi = \omega a^2(\rho t/D)^{1/2}/\pi$ of a triangular plates with $t/b = 0.2$

φ^o	Mode	Methods				
		DSG3	ES-DSG3	Present	ANS4	Ref.[9]
	1	0.5830	0.5823	0.5819	0.582	0.582
	2	1.9101	1.9040	1.9007	1.915	1.900
0^o	3	2.4176	2.4083	2.4082	2.428	2.408
	4	3.9772	3.9559	3.9432	3.984	3.936
	5	5.0265	4.9954	4.9948	5.018	-
	6	5.9521	5.8994	5.8997	5.944	-
	1	0.5449	0.5441	0.5440	0.545	0.544
	2	1.7803	1.7749	1.7718	1.764	1.771
15^o	3	2.3959	2.3854	2.3859	2.420	2.386
	4	3.6668	3.6467	3.6354	3.608	3.628
	5	4.8504	4.8208	4.8212	4.820	-
	6	5.6057	5.5385	5.5074	5.431	-
	1	0.5339	0.5328	0.5332	0.532	0.533
	2	1.7815	1.7754	1.7722	1.773	1.772
30^o	3	2.4356	2.4206	2.414	2.437	2.419
	4	3.6085	3.5842	3.5735	3.591	3.565
	5	4.7829	4.7444	4.7241	4.765	-
	6	5.4532	5.3377	5.3057	5.323	-
	1	0.5412	0.5391	0.5402	0.541	0.540
	2	1.8977	1.8882	1.8845	1.884	1.885
45^o	3	2.5304	2.5004	2.4937	2.518	2.489
	4	3.7518	3.7035	3.6946	3.748	3.674
	5	4.8188	4.6800	4.6632	4.740	-
	6	5.4304	5.2256	5.2132	5.292	-
	1	0.5634	0.5588	0.5577	0.559	0.559
	2	2.0837	2.0623	2.0586	2.095	2.059
60^o	3	2.5355	2.4356	2.4055	2.483	2.396
	4	4.0862	3.8009	3.7622	3.910	3.590
	5	4.6612	4.3393	4.3687	4.517	-
	6	5.9782	5.5835	5.658	5.763	-

[9] Reference solution(MLH92)

Table 4.8: Natural frequency of the machine part

Methods	Mode					
	1	2	3	4	5	6
DSG3	52.5925	72.5096	259.6188	525.8082	816.6085	894.7389
Present	50.8872	71.8003	255.7298	518.9853	788.5719	880.7170
NBNM	50.94	72.41	256.36	518.29	781.00	874.50

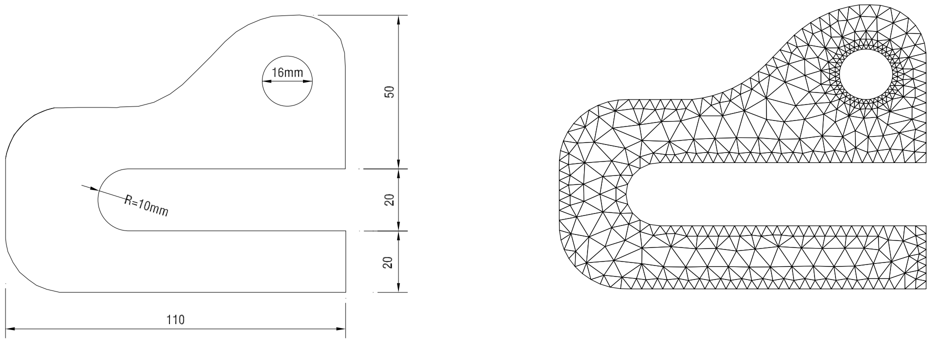

Figure 4.18: The machine part and mesh

4.3.3.1 Simply supported rectangular plates subjected to uniaxial compression

Let us first consider a plate with length a, width b and thickness t subjected to uniaxial compression. Simply supported (SSSS) and clamped (CCCC) boundary conditions are assumed. The geometry and a typical mesh of the plate are shown in Fig. 4.20.

Tab. 4.9 gives the convergence of the buckling load factor corresponding to meshes with triangular elements. Fig. 4.21 plots the convergence of the normalized buckling load K^h/K_{exact} of the square plate with thickness ratio $t/b = 0.01$, where K^h is the numerical buckling load and K_{exact} is the analytical buckling load (TG70). The convergence rate provided by the Aα-DSG3 is higher than that of the DSG3 and some other methods from the literature, see Tab. 4.10.

Next, we consider the buckling load factors of SSSS, CCCC, CFCF plates with thickness-to-width ratios $t/b = 0.05$; 0.1. The results compare well with several other methods shown in Tab. 4.11.

We also consider simply supported plates with various thickness-to-width ratios, $t/b = 0.05$; 0.1; 0.2 and length-to-width ratios, $a/b = 0.5$; 1.0; 1.5; 2.0; 2.5. The axial buckling modes and buckling load of simply-supported rectangular plates with thickness-to-width ratios $t/b = 0.01$ and various length-to-width ratios, $a/b = 1.0$; 1.5; 2.0; 2.5 are shown in Fig. 4.22 and Tab. 4.12.

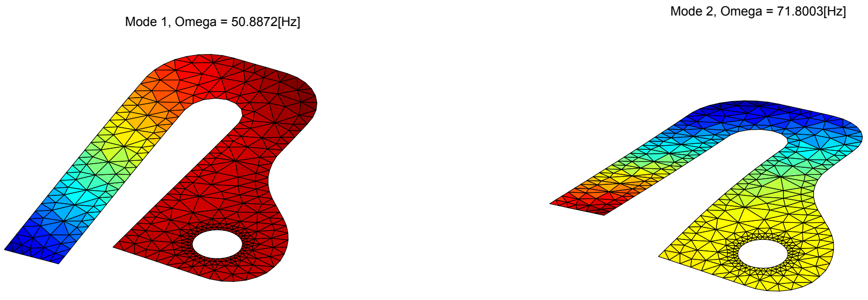

(a) Mode 1 (b) Mode 2

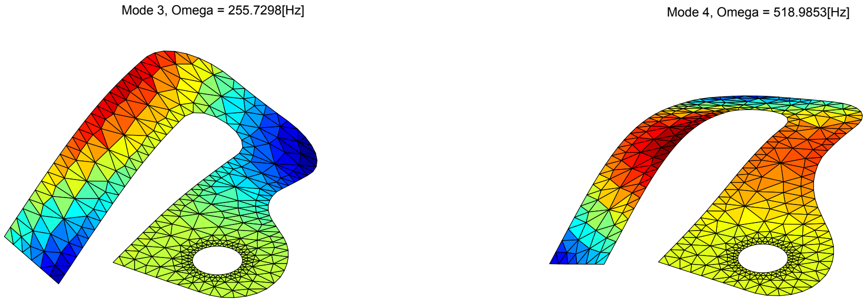

(c) Mode 3 (d) Mode 4

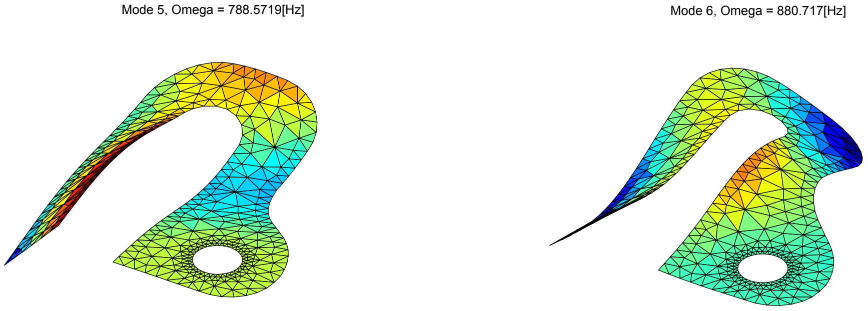

(e) Mode 5 (f) Mode 6

Figure 4.19: The first six mode shapes of the machine part.

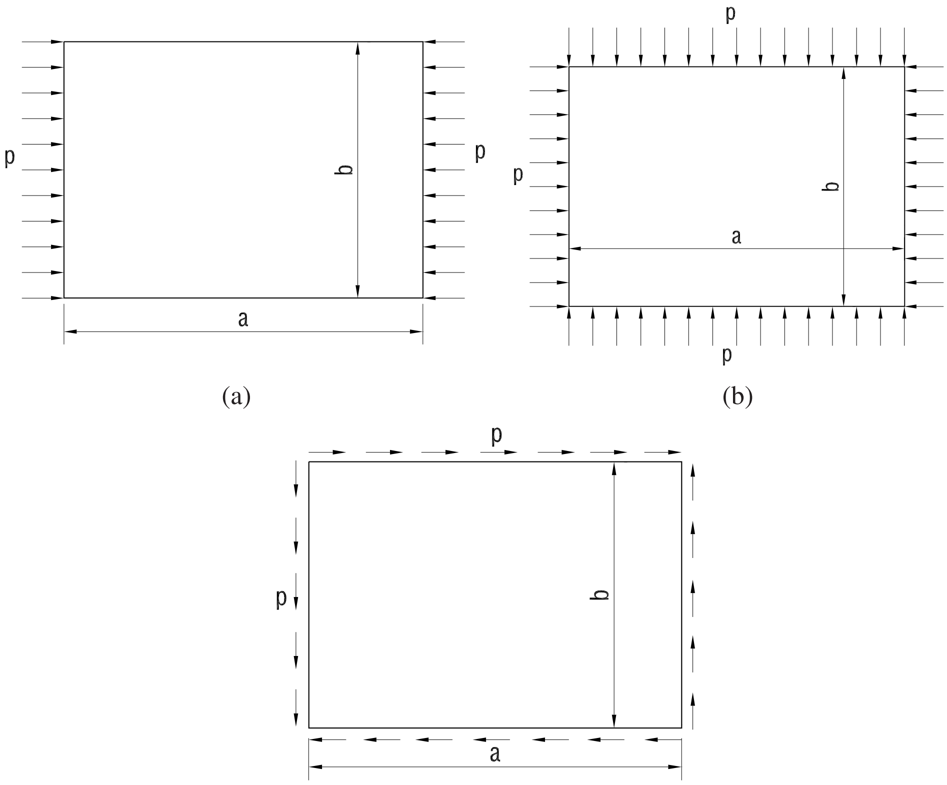

(a)

(b)

(c)

Figure 4.20: Rectangular plates: (a) Axial compression, (b) Biaxial compression, (c) Shear in-plane.

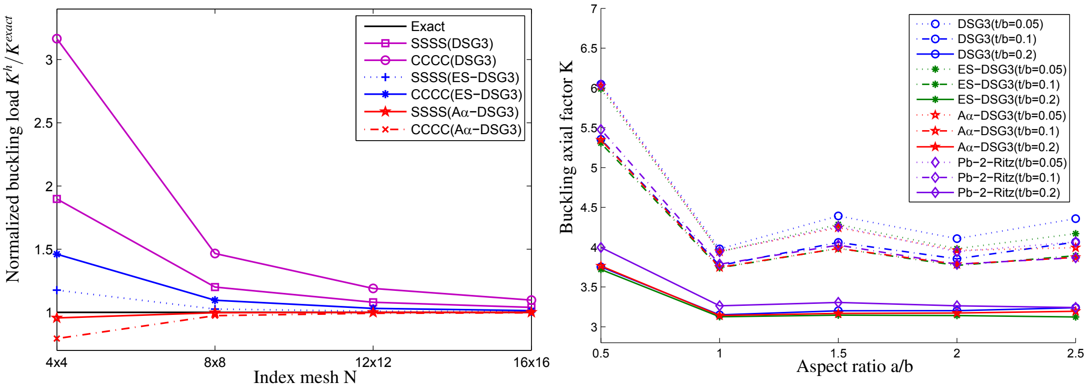

Figure 4.21: Normalized buckling load and convergence of axial buckling.

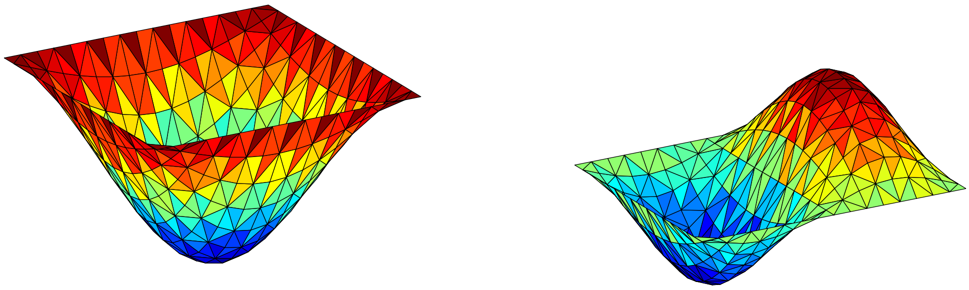

(a) a/b=1 (b) a/b=1.5

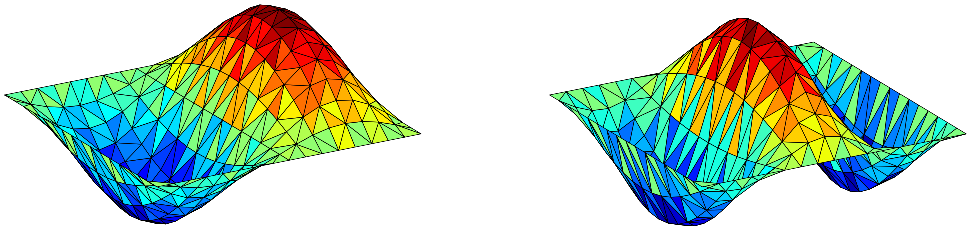

(c) a/b=2 (d) a/b=2.5

Figure 4.22: Axial buckling modes of simply-supported rectangular plates with thickness-to-width ratios t/b = 0.01 and various length-to-width ratios a/b =1; 1.5; 2.0; 2.5

Table 4.9: The axial buckling load factors K_b along the x-axis of rectangular plates with length-to-width ratios $a/b = 1$ and thickness-to-width ratios $t/b = 0.01$

Plates type	Methods	Index mesh			
		4×4	8×8	12×12	16 × 16
SSSS	DSG3	7.5891	4.8013	4.3200	4.1590
	ES-DSG3	4.7023	4.1060	4.0368	4.0170
	Aα-DSG3	3.8236	3.9882	4.0003	4.0008
CCCC	DSG3	31.8770	14.7592	11.9823	11.0446
	ES-DSG3	14.7104	11.0428	10.3881	10.2106
	Aα-DSG3	7.9868	9.8106	9.9968	10.0331

Table 4.10: The axial buckling load factors K_b along the x-axis of rectangular plates with length-to-width ratios $a/b = 1$ and thickness-to-width ratios $t/b = 0.01$

Plates	Methods						
type	DSG3	ES-DSG3	Present	Liew	Ansys	Tham[10]	Timoshenko[11]
SSSS	4.1590	4.0170	4.0008	3.9700	4.0634	4.00	4.00
(%)	3.97%	0.4%	0.02%	-0.75%	1.85%	-	-
CCCC	11.0446	10.2106	10.0331	10.1501	10.1889	10.08	10.07
(%)	9.68%	1.4%	-0.36%	0.8%	1.18%	0.1%	-

[10] Reference solution (TS90)

[11] Reference solution (TG70)

Table 4.11: The axial buckling load factors K_b along the x axis of rectangular plates with various length-to-width ratios $a/b = 1$ and various thickness-to-width ratios

t/b	Plates	Methods				
	type	DSG3	ES-DSG3	Present	RPIM(LC04)	Ritz(KXWL93)
0.05	SSSS	3.9786	3.9412	3.9446	3.9464	3.9444
	CCCC	9.8284	9.5426	9.5535	9.5819	9.5586
	CFCF	3.8365	3.7654	3.8017	3.8187	3.8005
0.1	SSSS	3.7692	3.7702	3.7771	3.7853	3.7873
	CCCC	8.2670	8.2674	8.2873	8.2931	8.2921
	CFCF	3.4594	3.4966	3.4978	3.5138	3.5077

Table 4.12: The axial buckling load factors K_b along the x-axis of rectangular plates with various length-to-width ratios and various thickness-to-width ratios

a/b	t/b	Methods				
		DSG3	ES-DSG3	Present	Meshfree(LWNT04)	Ritz(KXWL93)
0.5	0.05	6.0478	5.9873	6.0237	6.0405	6.0372
	0.1	5.3555	5.3064	5.3472	5.3116	5.4777
	0.2	3.7524	3.7200	3.7642	3.7157	3.9963
1.0	0.05	3.9786	3.9412	3.9449	3.9293	3.9444
	0.1	3.7692	3.7402	3.7465	3.7270	3.7865
	0.2	3.1493	3.1263	3.1420	3.1471	3.2637
1.5	0.05	4.3930	4.2852	4.2450	4.2116	4.2570
	0.1	4.0604	3.9844	3.9640	3.8982	4.0250
	0.2	3.2014	3.1461	3.1680	3.1032	3.3048
2.0	0.05	4.1070	3.9811	3.9594	3.8657	3.9444
	0.1	3.8539	3.7711	3.7855	3.6797	3.7865
	0.2	3.2023	3.1415	3.1733	3.0783	3.2637
2.5	0.05	4.3577	4.1691	3.9938	3.9600	4.0645
	0.1	4.0644	3.8924	3.8508	3.7311	3.8683
	0.2	3.2393	3.1234	3.1950	3.0306	3.2421

4.3.3.2 Simply supported rectangular plates subjected to biaxial compression

Consider the square plate subjected to biaxial compression shown in Fig. 4.20. Tab. 4.13 gives the shear buckling factor of the square plate subjected to biaxial compression with three essential boundary conditions (SSSS, CCCC, SCSC). The Aα-DSG3 element matches well with the analytical solution (TG70).

Table 4.13: The biaxial buckling load factors K of rectangular plates with length to width ratios a/b=1, thickness to width ratios t/b=0.01 and various boundary conditions

Plates type	Methods				
	DSG3	ES-DSG3	Present	Tham(TS90)	Timoshenko(TG70)
SSSS	2.0549	2.0023	2.0021	2.00	2.00
CCCC	5.6419	5.3200	5.3113	5.61	5.31
SCSC	4.0108	3.8332	3.8339	3.83	3.83

4.3.3.3 Simply supported rectangular plates subjected to in-plane pure shear

Finally, consider the simply supported plate subjected to in-plane shear shown in Fig. 4.20. The shear buckling load factors K of this plate are calculated using a

16×16 mesh. The shear buckling factors with thickness-to-width ratio, $t/b = 0.001$ and length-to-width ratios, $a/b = 1.0; 2.0; 3.0; 4.0$ are listed in Tab. 4.14. The Aα-DSG3 element agrees well with the exact solution. Fig. 4.23 shows the convergence of the shear buckling load. Fig. 4.24 presents the shear buckling modes of simply-supported rectangular plates with thickness-to-width ratios $t/b = 0.01$ and various length-to-width ratios, $a/b = 1.0; 2.0; 3.0; 4.0$. The results are given in Tab. 4.15. The Aα-DSG3 element agrees well with the analytical solution.

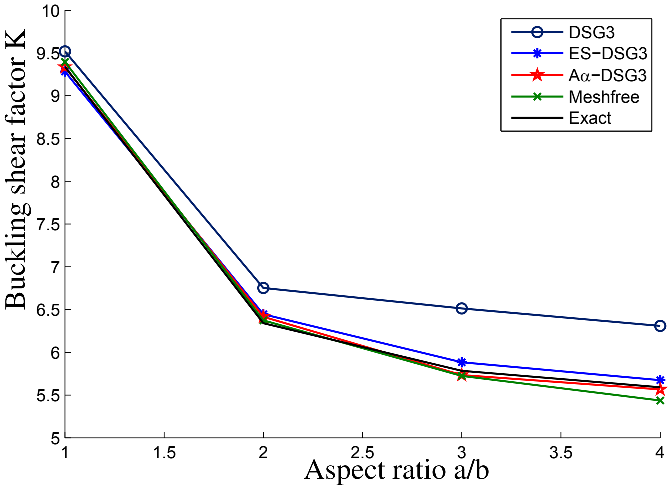

Figure 4.23: Normalized shear buckling load K^h/K_{exact} of a square plate with t/b=0.01.

Table 4.14: The shear buckling load factors K of simply supported rectangular plates with various length-to-width ratios, choose $t/b = 0.01$

a/b	Methods				
	DSG3	ES-DSG3	Present	Meshfree(LWNT04)	Exact (AHB00)
1.0	9.5195	9.2830	9.3351	9.3962	9.34
2.0	6.7523	6.4455	6.3853	6.3741	6.34
3.0	6.5129	5.8830	5.7143	5.7232	5.784
4.0	6.3093	5.6732	5.5466	5.4367	5.59

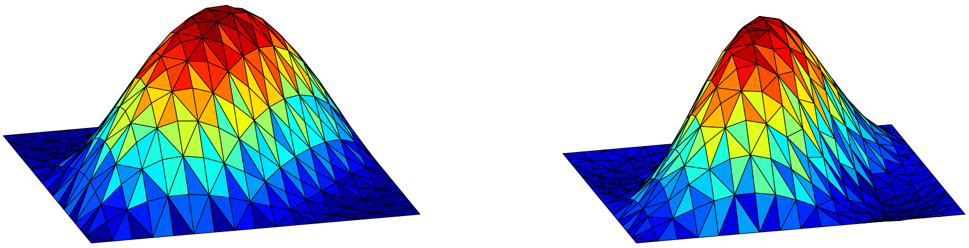

(a) a/b=1 (b) a/b=2

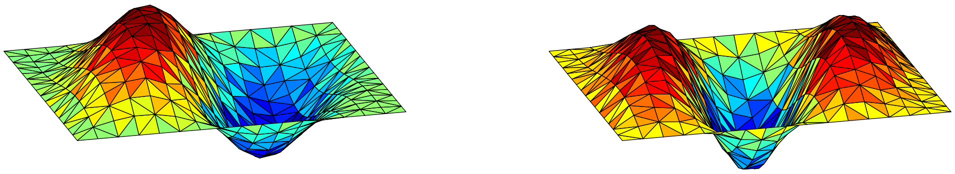

(c) a/b=3 (d) a/b=4

Figure 4.24: Shear buckling mode of simply supported rectangular plates with various length-to-width ratios.

Table 4.15: The shear buckling load factors K of rectangular plates with length-to-width ratios a/b=1, thickness-to-width ratios t/b=0.01 and various boundary condition

Plates	Methods				
type	DSG3	ES-DSG3	Present	Tham(TS90)	Timoshenko(TG70)
SSSS	9.5195	9.2830	9.3351	9.40	9.33
CCCC	15.6397	14.6591	14.6628	14.58	14.66
SCSC	13.1652	12.5533	12.5605	12.58	12.58

4.4 Concluding remarks

In this chapter, we extended previous works on the α finite element method from 3-nodes triangular continuum elements to 3-nodes triangular plate elements and analyzed the behavior of the resulting element, named Aα-DSG3, in solving static, free vibration and buckling problems. The basic idea behind this element formulation is to approximate displacements and rotations as in the standard finite element method, but to construct the bending, geometrical and shear strains using node-based smoothing domains.

The Aα-DSG3 is equipped with an adjustable factor α ($\alpha \in [0,1]$). When $\alpha = 0$, the present element becomes the standard Discrete Shear Gap (DSG) element and hence produces a lower bound in the strain energy. For $\alpha = 1$, the element becomes the node-based smoothed DSG model and leads to an upper bound in the strain energy. For intermediate values of α, the element was shown to underestimate the strain energy. It was also shown that a so-called “optimal” value for α could be easily found such that the “sufficiently exact” strain energy can be recovered.

Chapter 5

Isogeometric Analysis

In this chapter, the Computer Aided Design (CAD) basic geometry is reviewed for the development into the Isogeometric Analysis (IgA) method. The first part gives a short overview of the general Bézier function which is called a Bernstein blending function, and that has basis function properties. The next part introduces a B-spline basis functions and it is extended to B-spline surfaces and solids. The difference parametric mapping in finite element method and isogeometric analysis is introduced at last part.

5.1 Bézier basis function

A Bézier curve is widely used in geometric modeling. The tensor product of bidirectional Bézier curves allows to constitute Bézier surfaces. The Bézier function represents a parametric functions and is written as follows

$$\mathbf{C}(\xi) = \sum_{i=1}^{n} B_{p,i}(\xi)\mathbf{P}_i \ ; \qquad \xi \in [0,1] \tag{5.1}$$

where $\mathbf{P}_i$ are the control points, n is the number of control points. The polynomial degree is related to the number of control points by: $p = n - 1$. The Bernstein polynomials B_i^p of degree p are given by

$$B_i^p(\xi) = \frac{n!}{i!\,(n-i)!}\xi_i(1-\xi)^{n-i} \tag{5.2}$$

The Bernstein functions have the following important properties (PT97):

- Partition of unity: $\sum_{i=1}^{n} B_{p,i}(\xi) = 1 \quad \forall \xi \in [0,1]$
- Point wise non-negative: $B_{p,i}(\xi) \geqslant 0 \quad \forall \xi \in [0,1]$

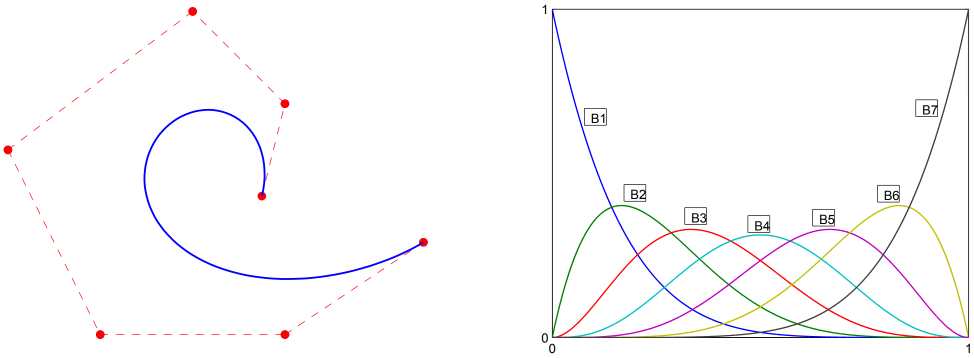

(a) (b)

Figure 5.1: (a) Bézier curve. (b) Bézier basis function.

- Endpoint interpolation: $\mathbf{C}(0) = \sum_{i=1}^{n} B_{p,i}(0)\mathbf{P}_i = \mathbf{P}_0$; $\mathbf{C}(1) = \sum_{i=1}^{n} B_{p,i}(1)\mathbf{P}_i = \mathbf{P}_n$
- Symmetry: $B_{p,i}(\xi) = B_{p,p-i+1}(1-\xi) \quad \forall \xi \in [0,1]$
- Linear independent: $\sum_{i=1}^{n} c_i B_{p,i}(\xi) = 0 \Leftrightarrow c_i = 0,\ \forall i = 1, n$.

The de Casteljau's algorithm (PT97) is frequently used to evaluate the Bernstein polynomials or to find a point on the Bézier curve for a given parameter value. It can also be used to create new Bézier curves from the original Bézier curve by curve subdivision at an arbitrary parameter value. By applying de Casteljau's algorithm, new control points $\mathbf{P}_{i,j}$ are also evaluated by the following form

$$\mathbf{P}_{i,j} = (1-\xi)\mathbf{P}_{i-1,j} + \xi\mathbf{P}_{i-1,j+1} \qquad \left\{ \begin{array}{c} i = 1,2,..,n \\ j = 0,1,...,n-i \end{array} \right. \tag{5.3}$$

A short review of subdividing a given Bézier curve into two new Bézier sub-curves at the parameter value, $\xi = 0.4$ see in Fig. 5.2a. Without the loss of generality, a set of seven control points $\{\mathbf{P}_{00}...\mathbf{P}_{06}\}$ are given. The $\mathbf{P}_{10}$ is in the leg of $\mathbf{P}_{00}$ and $\mathbf{P}_{01}$, $\mathbf{P}_{11}$ is in the leg of $\mathbf{P}_{01}$ and $\mathbf{P}_{02}$,..., and $\mathbf{P}_{15}$ is in the leg of $\mathbf{P}_{05}$ and $\mathbf{P}_{06}$. The triangular table of control points generated by the de Casteljau's algorithm is shown in Fig. 5.2b which describes all intermediate steps using the de Casteljau's algorithm to evaluate the point $\mathbf{P}\xi = \mathbf{P}_{60}$ on the curve. The original Bézier curve is subdivided into two pieces, each of which is a new Bézier curve belonging to half of the original Bézier curve. Also, their corresponding control points are obtained. It is known that we can modify a part of the original Bézier curve (i.e, the left piece or the right one of the original Bézier curve) while the other one is still unchanged. Applying this feature to graphical models, Deng *et al.* (DCL^{+}08) have recently used it to modify the basis functions for the PHT-spline. More details on the construction of the PHT-spline will be given in section 6.3. A Bézier surface is defined as

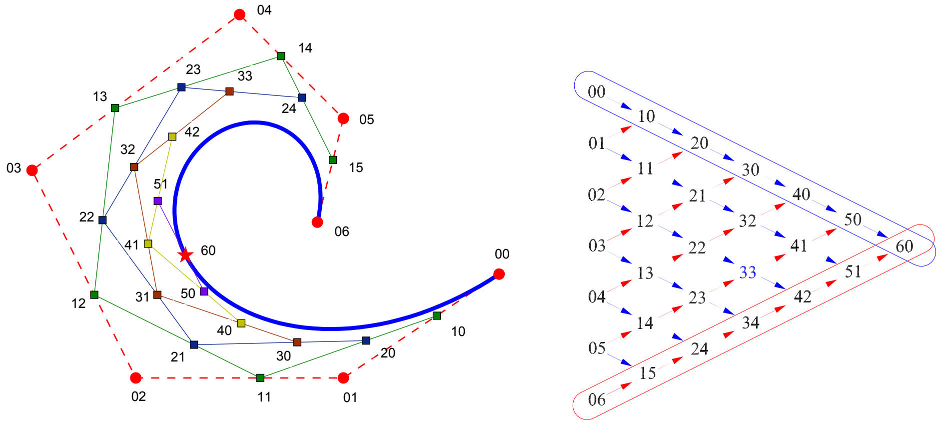

(a) (b)

Figure 5.2: Subdivision of the Bézier curve using de Casteljau's algorithm at the parameter $\xi = 0.4$

$$\mathbf{S}(\xi,\eta) = \sum_{i=1}^{n}\sum_{j=1}^{m} B_{i,p}(\xi)B_{j,q}(\eta)\mathbf{P}_{i,j}\ . \tag{5.4}$$

A three-dimensional solid based on the tensor product of Bézier basis functions in three parametric dimensions.

$$\mathbf{S}(\xi,\eta,\gamma) = \sum_{i=1}^{n}\sum_{j=1}^{m}\sum_{k=1}^{l} B_{i,p}(\xi)B_{j,q}(\eta)B_{k,r}(\gamma)\mathbf{P}_{i,j,k}\ . \tag{5.5}$$

The drawbacks of Bézier curves are an increasing number of control points the polynomial degree increased. For example Bézier curves in Fig. 5.1 performed that the relate the polynomial degree and the number of control points ($p = n-1 = 6$). However, the computation of higher degree Bézier curves are inefficient and can result in numerical instabilities. The global support of the basis functions is a problem for geometric modeling, because it means that any modification of a control point has influence on the whole curve and no local changes can be made to the curve. Another drawback is the fact that no points of reduced continuity, such as kinks, can be inserted inside the curve. Spline basis functions outlined in the next section can be overcome these drawbacks.

5.2 B-Splines basis function

Let $\Xi = \left[\xi_1, \xi_2, ..., \xi_{n+p+1}\right]$ be a nondecreasing sequence of parameter values, $\xi_i \leq \xi_{i+1}, i = 1, ..., n+p$; ξ_i are called knots, and Ξ is the set of coordinates in the parametric space. If all knots are equally spaced then the knot vector is called uniform. Otherwise, it is called non-uniform knots vector. When the first and the last knots are repeated by $p+1$ times, the knots are called open. A knot value can appear more than once and is then called a multiple knot. A B-Spline basis function is C^{∞} continuous inside a knot span and C^{p-1} continuous at a single knot. At a knot of multiplicity k, the continuity is C^{p-k}. The B-spline basis functions $N_{i,p}(\xi)$ of order $p = 0$ (piece-wise constant) are defined recursively on the corresponding knot vector given by:

$$N_{i,0}(\xi) = \begin{cases} 1 \text{ if } \xi_i \leq \xi \leq \xi_{i+1} \\ 0 \quad \text{otherwise} \end{cases} \tag{5.6}$$

For $p \geqslant 1$, we obtain

$$N_{i,p}(\xi) = \frac{\xi - \xi_i}{\xi_{i+p} - \xi_i} N_{i,p-1}(\xi) + \frac{\xi_{i+p+1} - \xi}{\xi_{i+p+1} - \xi_{i+1}} N_{i+1,p-1}(\xi) \,. \tag{5.7}$$

The B-splines basis functions $N_{i,p}$ possess the important properties such as non-negativity, local support, partition of unity and linear independency. There are several types of knot vectors. In this study, we only present non-periodic knot vectors which have the form:

$$\Xi = \left[\underbrace{0, ..., 0}_{p+1}, \xi_{p+1}, ..., \xi_{m-p-1}, \underbrace{1, ..., 1}_{p+1}\right] \,. \tag{5.8}$$

The B-spline curves are defined as follows:

$$\mathbf{C}(\xi) = \sum_{i=1}^{m} N_{i,p}(\xi)\mathbf{P}_i \tag{5.9}$$

The B-splines surfaces are defined by the tensor product of basis functions with parameters Ξ and are expressed as follows:

$$\mathbf{S}(\xi, \eta) = \sum_{i=1}^{n}\sum_{j=1}^{m} N_{i,p}(\xi) M_{j,q}(\eta)\mathbf{P}_{i,j} \,, \tag{5.10}$$

where $\mathbf{P}_{i,j}$ are the bidirectional control net, $N_{i,p}(\xi)$ and $M_{j,q}(\eta)$ are the B-spline basis functions defined on the knot vectors over an $n \times m$ net of control points $\mathbf{P}_{i,j}$. An example of a quadratic B-splines surface with three elements are illustrated in Fig. 5.4.

The B-splines solid is based on the tensor product of B-Splines basis functions in

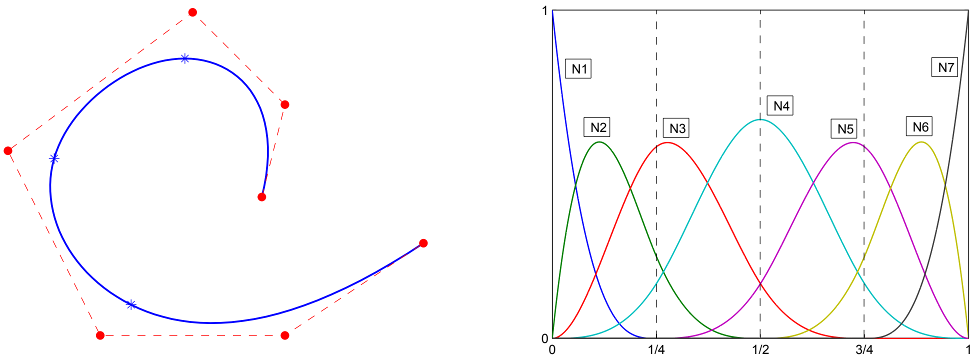

(a)

(b)

Figure 5.3: (a) B-spline curves. (b) Cubic B-spline basis function with open knot vector $\Xi = [0,0,0,0,1/4,1/2,3/4,1,1,1,1]$.

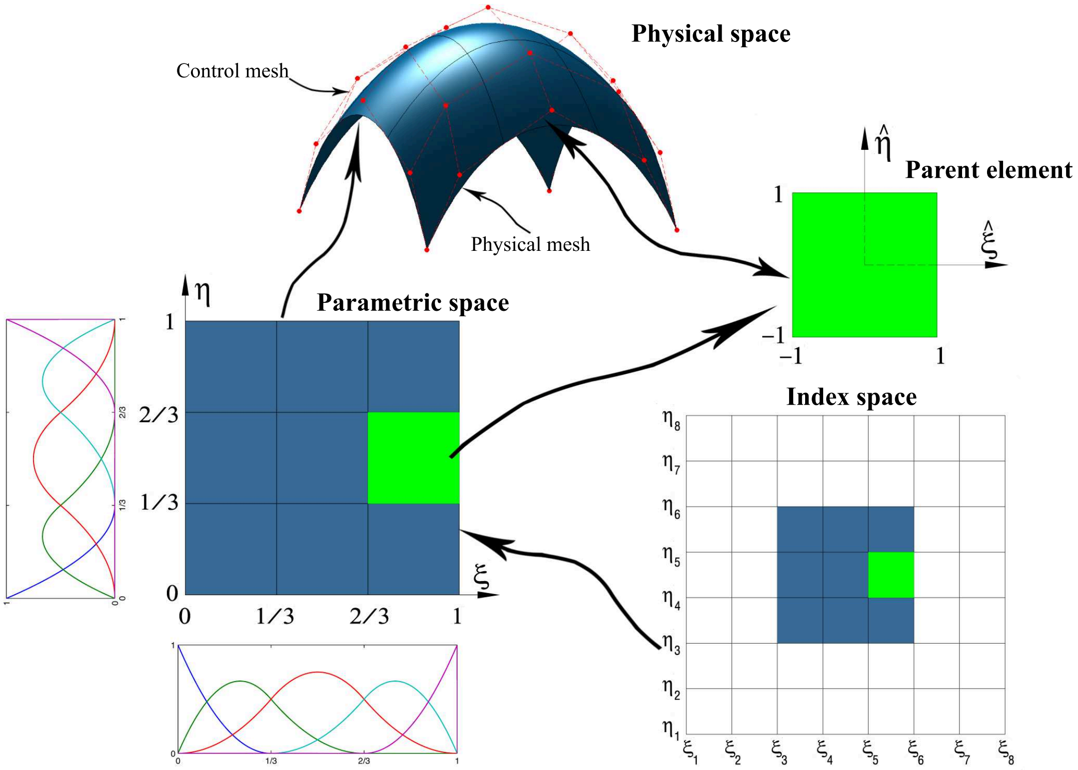

Figure 5.4: Parametric and physical space with quadratic B-splines.

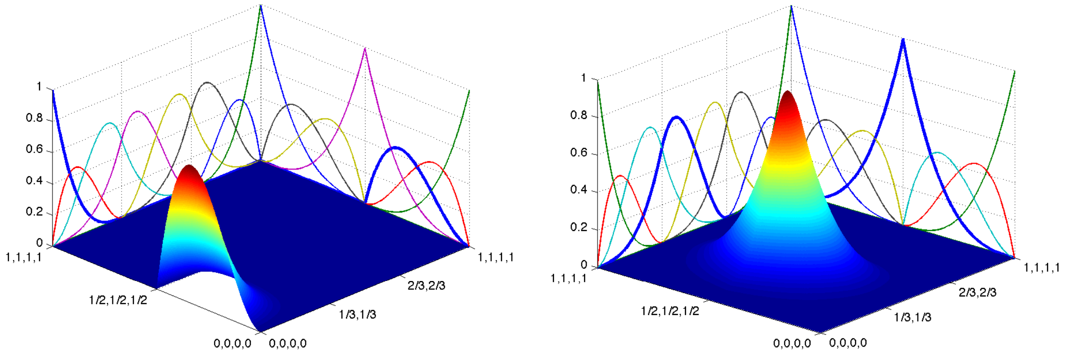

(a) (b)

Figure 5.5: A bivariate cubic B-spline basis functions with knot vector $\Xi_1 = [0,0,0,0,1/3,1/3,2/3,2/3,1,1,1,1]$ and $\Xi_2 = [0,0,0,0,1/2,1/2,1/2,1,1,1,1]$. (a) B-spline basis functions with $N_{1,3}$. (b) B-spline basis functions with $N_{4,4}$.

three parametric dimensions

$$\mathbf{S}(\xi,\eta,\gamma) = \sum_{i=1}^{n}\sum_{j=1}^{m}\sum_{k=1}^{l} N_{i,p}(\xi)\,M_{j,q}(\eta)\,L_{k,r}(\gamma)\,\mathbf{P}_{i,j,k} \tag{5.11}$$

where $\mathbf{P}_{i,j,k}$ are the tri-directional control net; $N_{i,p}(\xi), M_{j,q}(\eta), L_{k,r}(\gamma)$ are the B-splines basis functions. A NURBS solid is defined as:

$$\mathbf{S}(\xi,\eta,\gamma) = \sum_{i=1}^{n}\sum_{j=1}^{m}\sum_{k=1}^{l} \mathbf{R}_{i,j,k}^{p,q,r}(\xi,\eta,\gamma)\,\mathbf{P}_{i,j,k} \tag{5.12}$$

with the basis functions

$$\mathbf{R}_{i,j,k}^{p,q,r}(\xi,\eta,\gamma) = \frac{N_{i,p}(\xi)\,M_{j,q}(\eta)\,L_{k,r}(\gamma)\,w_{i,j,k}}{\sum\limits_{i=1}^{n}\sum\limits_{j=1}^{m}\sum\limits_{k=1}^{l} N_{i,p}(\xi)\,M_{j,q}(\eta)\,L_{k,r}(\gamma)\,w_{i,j,k}} \tag{5.13}$$

where w are the weights.

Chapter 6

Isogeometric analysis using rational splines over hierarchical T-meshes for two-dimensional elastic solids

6.1 Introduction

Isogeometric analysis was introduced by (HCB05) in order to improve and accelerate numerical analysis and to closely link Computer Aided Design (CAD) and Computer Aided Engineering (CAE). The basic idea is to use CAD basis functions in the context of numerical analysis. While the finite element method is most popular in CAE, the most common CAD basis functions are NURBS. Therefore, most studies in the context of isogeometric analysis focus on NUBRS-based isogeometric finite element formulations (EB10, HÖ3, SFMH08, SR08, SDR04).

One major advantage of CAD basis functions (e.g. NURBS) over finite elements is their ability to describe a larger class of geometric objects, e.g. conic geometries. However, the requirements on basis functions in CAE are higher than in CAD.

Besides their potential to unify CAD and CAE and therefore to reduce computational cost, NURBS-based isogeometric finite element formulations have other advantages over (Lagrange) polynomial based Finite Elements (FEs):

- For many examples (see e.g. the results in (BCC$^+$10, ABC$^+$08, BCHZ08, CRBH06, WFC08, HRS08)), it was found that NURBS-based isogeometric FEs give more accurate results than their traditional FE-counterparts. This was devoted to the higher smoothness and continuity of the isogeometric basis functions. Higher continuous formulations do not lead to jump in derivatives, e.g. in the strain field and stress field in mechanical analysis, inherent to C^0 continuous FE formulations.

- The higher continuity of the isogeometric formulation can also be exploited in a different context, e.g. for thin plates and thin shells (DBH10, KBLW09) or for gradient based constitutive models. We note that any order of continuity-even C^{-1} -can be created in NURBS basis functions through a simple procedure, i.e. knot insertion.
- Initial studies (DBH10) conjecture that isogeometric FEs based on NURBS show less sensitivity with respect to excessive mesh distortion as compared to Lagrange polynomial based FEs making them particularly attractive for problems with large deformations such as shear band formation, sheet metal stamping or crashworthiness etc. (though mesh distortion can also be a consequence of poor mesh generation); this was again attributed to higher-order and higher-continuity of the approximation.
- It was found that the natural eigenfrequencies of higher order NURBS-based isogeometric FEs are much lower compared to higher order Lagrange polynomial based FEs (CHR07). This is particularly advantageous for explicit time integration where the stable time step is inversely proportional to the maximum eigenfrequency.
- Besides the conventional h-refinement and p-refinement, NURBS-based isogeometric FEs offer a more flexible k-refinement. The k-refinement is ideally suited for higher-order approximations. It maintains the polynomial degree and the higher-order continuity under refinement. (TCB05, HRS08) showed many examples demonstrating the superiority of the k-refinement over the p-refinement.

However, NURBS also have certain drawbacks in the context of numerical analysis:

- Due to the tensor-product form of NURBS, their control points are required to lie in a structured grid (e.g. in a rectangle in 2D). This leads to an excessive overhead of control points with increasing refinement. (CHR07, FB98) proposed a local refinement strategy, Fig. 6.1, but constraint equations require increasing complexity and implementational effort. Moreover, refinement still propagates through a given patch.
- Another disadvantage of NURBS is that they usually achieve only C^0 continuity across patch boundaries. However, when two NURBS surfaces do not share a common boundary, they cannot even achieve C^0 continuity without disturbing at least one of the surfaces. Note, that (Lagrange) polynomial based FEs also possess only C^0 continuity.

- Probably the most striking drawback is that NURBS based geometries often suffer from gaps and overlaps that are unacceptable for analysis and require "repairing".

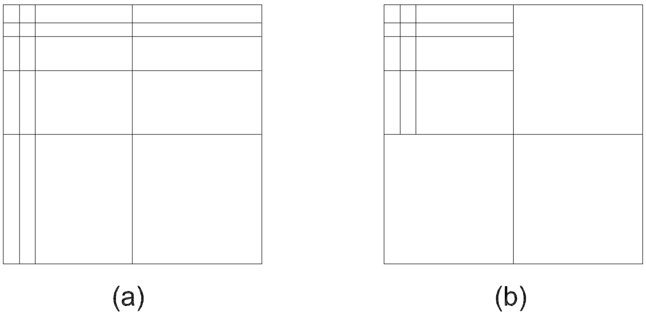

Figure 6.1: (a) Tensor product global refinement and (b) An illustration of local refinement (HCB05).

Sederberg (SZBA03, SCF$^+$04) recently developed the T-spline in order to eliminate or at least alleviate some of the above mentioned drawbacks of NURBS. (BCS09) showed that T-splines inherit some of the basic properties of NURBS mentioned above.

1. T-splines are capable of joining objects without gaps.
2. T-splines are capable of preserving higher continuity globally, i.e. everywhere.
3. T-splines are better suited for local refinement that is a key ingredient of an effective numerical method.

T-splines are meanwhile already available in commercial CAD software such as Maya or Rhino .

However, though T-splines allow for local adaptive refinement, the complexity of knot insertion under adaptive refinement is complex, particularly in 3D. Moreover, (BCS09) showed that linear independence of the basis functions is not guaranteed for generic T-meshes.

Recently, the polynomial splines over hierarchical T-meshes (PHT-spline) (DCL$^+$08, LDC07, LDC10) that inherits all above mentioned properties of NURBS (Non-negativity, partition of unity, linear independence of the basis functions and local support) while maintaining the advantages. The conversion between NURBS and PHT-splines is simple and very fast, while conversion between NURBS and T-splines is a bottleneck of T-splines in practical applications.

From a linear algebra point of view, the NURBS space and T-spline space is a subspace of the PHT-spline space. Or to be more precise: When we form a new T-mesh (see Fig. 6.2) from a given T-spline mesh such that in the new T-mesh, a T-spline function is a single polynomial over each cell, then we can say that the T-spline space is a subspace of the PHT-space. Therefore, besides being polynomial over each cell, the PHT-spline inherits basically all benefits of the T-spline, e.g. the ability to exactly represent conic sections, free gaps, handle trimming curves, etc. Moreover, the piecewise polynomial approach facilitates adaptive refinement strategies. Local refinement algorithms are relatively simple while the complexity of knot insertion with T-splines might be high, particularly in 3D. Note that adaptive FEs are defined over hierarchical T-meshes and therefore, efficient refinement strategies can be adopted from the FE literature (RB04b, RB06b, RB07a, RS08, RZBNX08). Compared with T-splines and hierarchical B-splines, PHT-splines are only C^1 continuous though extensions of the PHT-spline to higher order continuous formulations seem possible. However, since PHT-splines are polynomial, they cannot exactly represent common engineering shapes of conic sections such as circles, spheres, ellipsoids, etc. Therefore, I employed rational splines over hierarchical T-meshes (RHT-splines) for numerical analysis.

In this chapter, isogeometric analysis based on RHT-spline basis functions for two-dimensional problems is proposed. The key feature of the proposed method is its simplicity. It does not require the set-up of an additional mesh, nor additional nodes and local refinement can be readily implemented through the refinement of geometric models using RHT-splines.

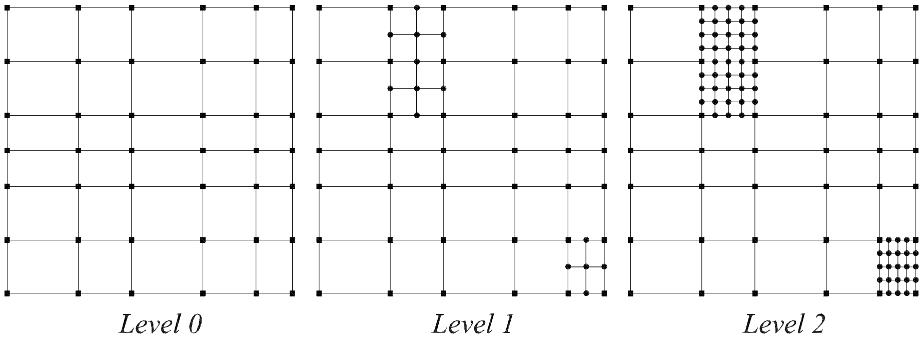

Figure 6.2: An illustration of T-meshes.

6.2 Rational splines over hierarchical T-meshes

6.2.1 2D T-meshes

A T-mesh is a mesh based on rectangular grids that allow T-junctions (Sed). In T-meshes, the end points of each grid line must lie on two other grid lines, and each cell or facet in the grid is formed by a quadrilateral. Fig. 6.3 illustrates a typical T-mesh. A vertex of the T-mesh is assigned to each grid point. If a vertex is inside the domain, it is called an interior vertex. Otherwise, it is called a boundary vertex.

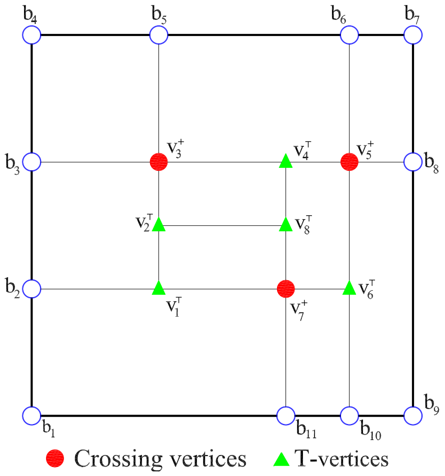

Figure 6.3: An illustration of boundary, crossing and T-junctional vertices: b_i are boundary vertices, v_i^+ are crossing vertices and v_i^T are T-junctional vertices.

6.2.2 Hierarchical T-meshes

A hierarchical T-mesh can be considered as a special form of T-mesh, which has a natural level structure. One is also used widely in many research areas such as computational methods, computer science, and so on. Hierarchical T-mesh is initiated from a TP mesh which is assumed to be a level-0 as shown in Fig. 6.2. If a level-k mesh is given, then the level $(k+1)$ mesh is obtained by subdividing some of the cells in level-k. Each cell is subdivided into four subcells by connecting the middle points of the opposite edges in the cell.

6.2.3 A dimension formula

As pointed out in (DCF06), polynomial spline functions over T-meshes has the advantages such as the simplification of local refinement strategy, the use of piecewise polynomials, and the utilization of hierarchical structures. Herein two important issues are addressed to be the dimension formula of spline function spaces and the construction of basis functions of splines over hierarchical T-meshes. Let $\mathscr{T}$ be the T-mesh, $\mathscr{H}$ be the cells in $\mathscr{T}$, $\Omega \subset \mathbb{R}^2$ be the region occupied by $\mathscr{T}$. Then we write:

$$\mathscr{S}(p,q,\alpha,\beta,\mathscr{T}) = \left\{ s(x,y) \in C^{\alpha,\beta}(\Omega) | s(x,y)|_{\phi} \in \mathbb{P}_{pq} \text{ for any } \phi \in \mathscr{H} \right\} \tag{6.1}$$

where the space, $\mathbb{P}_{pq}$, consists of all the bi-degree (p,q) polynomials and the space, $C^{\alpha,\beta}$, consists of all the continuously bivariate functions up to order α in the x direction and order β in the y direction. The dimension formula of the spline space $\mathscr{S}(p,q,\alpha,\beta,\mathscr{T})$ when $p \geq 2\alpha+1$ and $q \geq 2\beta+1$ has already been proved in (DCF06). For a C^1-continuous cubic spline, where every interior knots is of multiplicity two, the evaluation of the dimension formula is reduced to the following form

$$\dim \mathscr{S}(3,3,1,1,\mathscr{T}) = 4(V^b + V^+) \tag{6.2}$$

where V^b, V^+ are boundary vertices, and interior crossing vertices, respectively. For example, we have $V^b = 11$ and $V^+ = 3$ as illustrated in Fig. 6.3. The dimension formula is

$$\dim \mathscr{S}(3,3,1,1,\mathscr{T}) = 4(11+3) = 56 \tag{6.3}$$

Eq. (6.2) shows the number of basis functions corresponding to boundary and crossing vertices which need to be constructed. It is also implied that each boundary vertex or each crossing vertex is connected by four basis functions. After obtaining the dimensional formula, the task in the next section will show how to construct basis functions of splines over hierarchical T-meshes.

6.3 RHT-spline basis functions

6.3.1 Definition of knot vectors

Let us consider a knot vector with multiplicity of two defined as

$$\Xi = \{\xi_0,\xi_0,\xi_1,\xi_1,\xi_2,\xi_2,\xi_3,\xi_3,\ldots,\xi_{m-2},\xi_{m-2},\xi_{m-1},\xi_{m-1},\xi_m,\xi_m\} \tag{6.4}$$

such that $\xi_i < \xi_{i+1},\ \ 1 \leq i \leq m-2$, and $\xi_0 = \xi_1$ and $\xi_{m-1} = \xi_m$. The set in Eq. (6.4) can be rearranged as:

$$\Xi = \left\{ \underbrace{\xi_0,\xi_0,\xi_1,\xi_1}_{p+1}, \underbrace{\xi_2,\xi_2}_{k=2}, \ldots, \xi_{m-2},\xi_{m-2}, \underbrace{\xi_{m-1},\xi_{m-1},\xi_m,\xi_m}_{p+1} \right\}. \tag{6.5}$$

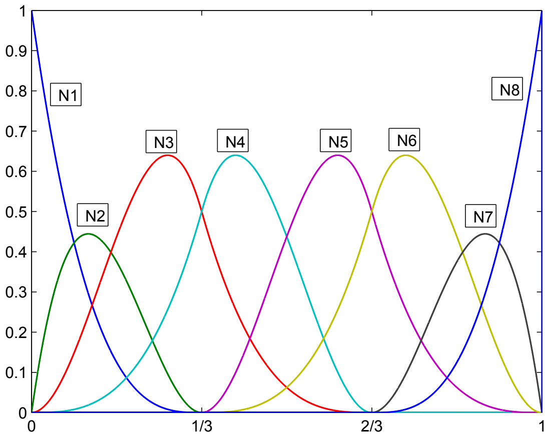

Figure 6.4: This figure illustrates cubic B-spline basis functions with multiplicity two of interior knots, i.e, only C^1-continuity: $\Xi = \{0,0,0,0,\frac{1}{3},\frac{1}{3},\frac{2}{3},\frac{2}{3},1,1,1,1\}$

As already mentioned in (DCL$^+$08), the construction of RHT-spline basis functions is initiated from C^1 continuous cubic B-splines. Eq. (6.5) implies that cubic B-splines (p = 3) are $C^{p-k} = C^1$-continuous at every interior knots Fig. 6.4.

It is seen that, for the line case, only two B-spline basis functions in $[\xi_{i-1},\xi_{i+1}]$ are nonzero at each interior knot ξ_i. These two basis functions are incorporated with knot vectors $[\xi_{i-1},\xi_{i-1},\xi_i,\xi_i,\xi_{i+1}]$ and $[\xi_{i-1},\xi_i,\xi_i,\xi_{i+1},\xi_{i+1}]$ (see in Fig. 6.5). This property also is satisfied by any B-spline basis function of degree $p \geq 3$. In addition, every interior knot is of multiplicity two, the derivatives of the basis functions also vanish at ξ_i. Extending this fact further to the surface case, there are four B-spline basis functions in $[\xi_{i-1},\xi_{i+1}] \times [\eta_{i-1},\eta_{i+1}]$ that are nonzero at each interior vertex (ξ_i,η_i).

6.3.2 Modification of the basis functions at level k

Following Deng *et al.* (DCL$^+$08), a basis function is represented by specifying its 16 Bézier ordinates in every cell within the support of the basis function as depicted in Fig. 6.6a. A set of new Bézier ordinates is then generated by applying de Casteljau algorithm, see Figs. 6.6b,c.

Suppose, among all the cells at level k, the cells $\theta_i^k, i = 1,\ldots,C_k$ are subdivided. For each i, if the basis function $b_i^k(\xi,\eta)$ does not vanish in some cells of θ_i^k (see Fig. 6.7). Then we subdivide $b_i^k(\xi,\eta)$ into these cells at level $k+1$ according to Eqs. (5.3).

Recall that the RHT-spline is constructed from cubic B-spline basis functions. Therefore, there are 16 control points required to exactly interpolate the surface re-

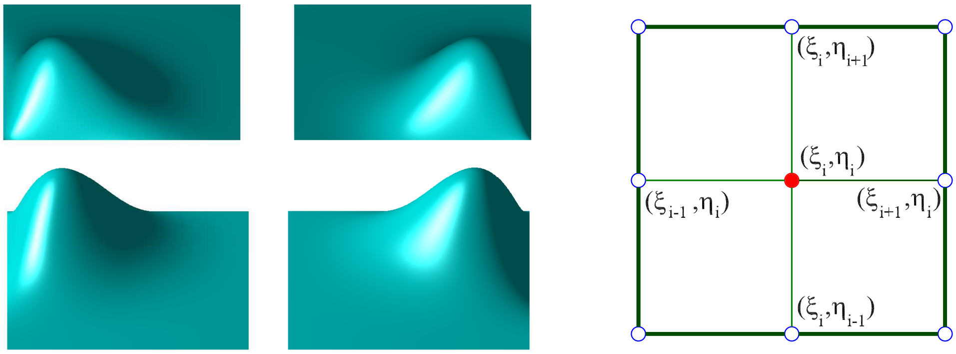

Figure 6.5: Four basis functions associated with (ξ_i, η_i) and their support

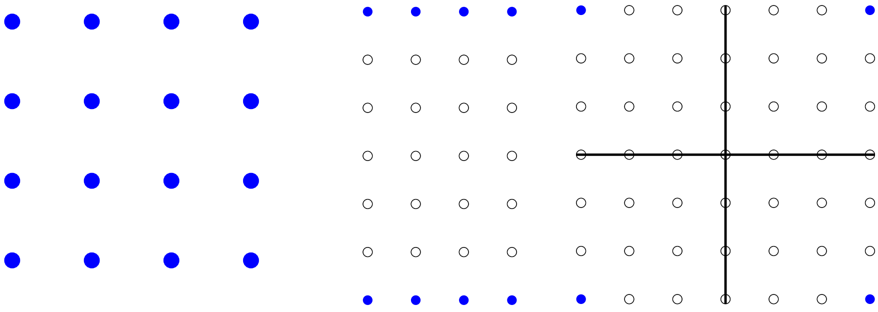

(a) (b) (c)

Figure 6.6: 16 basis function values of a basis function $b_i^k(\xi, \eta)$: (a) It is considered as the given 16 Bézier ordinates, (b) Eq. (5.3) (or the de Casteljau algorithm) is then applied to each of the four columns of $b_i^k(\xi, \eta)$, (c) The de Casteljau algorithm is then applied to each of the seven rows of $b_i^k(\xi, \eta)$.

stricted to each local “element”. Hence, there are 16 shape functions with respect to these 16 control points (or 16 basis functions) presented in that element. Since the RHT-spline is based on the knot vector in Eqs. (6.5), there are four basis functions at each vertex (ξ_i, η_i) in the surface case.

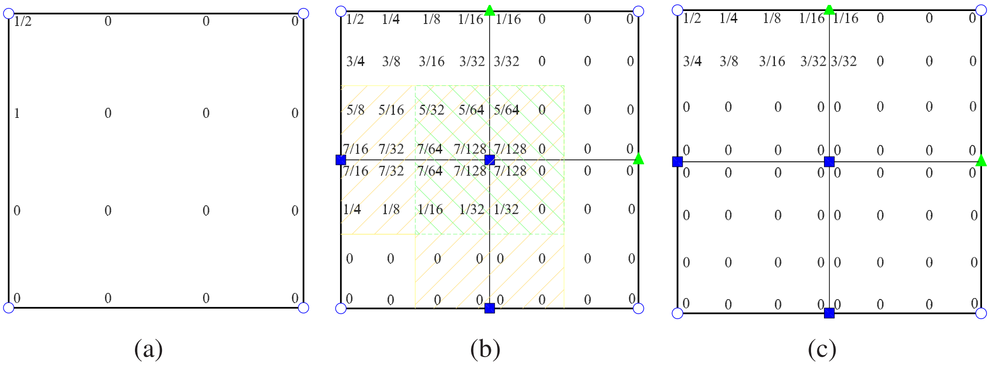

Figure 6.7: Modification of a basis function : apply Eqs. (5.3) to each of the seven rows of four Bézier ordinates, to obtain seven new Bézier ordinates. (a) A basis function $b_i^k(\xi,\eta)$ is considered as the given Bézier ordinates. (b) $b_i^k(\xi,\eta)$ is subdivided into four sub-cells. The square shaped vertices are new basis vertices. (c) The Bézier ordinates around the new basis vertices are reset to zero (DCL⁺08).

It is clear that only Bézier ordinates are changed after its subdivision into four subcells while the function $b_i^k(\xi,\eta)$ has not changed, but is now defined over the mesh $\mathscr{T}_{k+1}$.

6.3.3 Modification of the basis functions at level $k+1$

In the following, we illustrate a simple way to modify a basis function at level k. Now we describe the details of constructing the basis functions at level $k+1$. Let consider a new basis vertex (ξ_i, η_i) and its neighboring cells. The basis functions are associated with the new basis vertices as $\{\tilde{b}_i^{k+1}(\xi,\eta)\}_{i=1}^{4V_{k+1}}$ (see Fig. 6.8). The four basis functions associated with (ξ_i, η_i) are defined to be $M_{ik}^3(s)N_{il}^3(t)$, $k,l = 1,2$ where $M_{i1}^3(\xi), M_{i2}^3(\xi)$, $N_{i1}^3(\eta), N_{i2}^3(\eta)$ are the cubic B-spline basis functions associated with the knot vectors $(\xi_{i-1}, \xi_{i-1}, \xi_i, \xi_i, \xi_{i+1})$, $(\xi_{i-1}, \xi_i, \xi_i, \xi_{i+1}, \xi_{i+1})$, respectively. If (ξ_i, η_i) is a boundary vertex, then either $\xi_{i-1} = \xi_i$, $\xi_{i+1} = \xi_i$ or $\eta_{i-1} = \eta_i$, $\eta_{i+1} = \eta_i$. These four basis functions are in $\mathscr{S}(3,3,1,1,\mathscr{T}_{k+1})$ and they have the same support $[\xi_{i-1}, \xi_{i+1}] \times [\eta_{i-1}, \eta_{i+1}]$. Note that from the previous construction process, $\mathscr{S}_1(\xi,\eta) = \sum_{i=1}^{4V_{k+1}} \tilde{b}_i^{k+1}(\xi,\eta)$ and $\mathscr{S}_2(\xi,\eta) = \sum_{i=1}^{n_k} \bar{b}_i^k(\xi,\eta)$ are linearly independent as proven in (DCL⁺08).

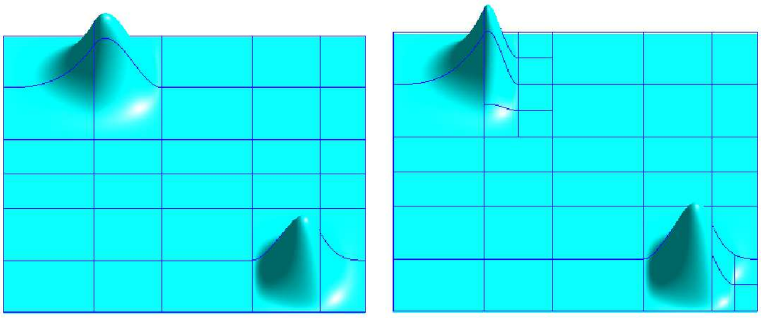

Figure 6.8: Modification of a basis function at level k and $k+1$.

6.3.4 Properties of the basis functions

It was found that the RHT-basis functions built in the previous section subsection have the following properties (DCL+08):

- Partition of unity: For $\mathscr{S}_1(\xi,\eta)$, the Bézier ordinates attached to the new basis vertices are equal to unit whereas all the others are equal to zero; and $\mathscr{S}_2(\xi,\eta)$ also have the same properties as $\mathscr{S}_1(\xi,\eta)$. Hence, we have $\mathscr{S}_1(\xi,\eta)+\mathscr{S}_2(\xi,\eta)=1$.
- Non-negativity: $\forall i,\ b_i(\xi,\eta)\geqslant 0$.
- Local support : $\forall i,\ b_i(\xi,\eta)$ has a support as minimal as possible.
- Linear independent.

Let $\mathscr{T}$ be a hierarchical T-mesh, and $b_i(\xi,\eta)$, $i=1,2...n$ be the basis functions. Then, the polynomial spline surface over $\mathscr{T}$ is defined by:

$$\mathbf{S}(\xi,\eta)=\sum_{i=1}^{n}\mathbf{R}_i(\xi,\eta)\mathbf{P}_i \quad ; \quad \mathbf{R}_i=\frac{w_i b_i(\xi,\eta)}{\sum_{i=1}^{nml} w_i b_i(\xi,\eta)} \tag{6.6}$$

where $\mathbf{P}_i$ are the control points; w_i are the weights; b_i are RHT-spline basis functions.

RHT-splines surfaces not only inherit all properties of B-spline and NURBS surfaces, but also, more importantly, allow us to manipulate efficiently local refinement. In addition, it is in fact that RHT splines can also be considered as a special type of Hermitian interpolation splines over T-meshes (SCM08). Note that in case of objects including conic sections, the initial NURBS basis (level 0) should be chosen to represent exactly the geometry entire and a rational form of RHT splines should be therefore recommended. In the following, we focus on an alternative to NURBS-based isogeometric finite elements using the polynomial splines over hierarchical T-meshes for two-dimensional solid mechanics problems. Note that when we consider rational form as its homogeneous one, there is not any difference between polynomial form and rational form. This is because polynomial curve is a curve with RHT bases and control points in R^2, while rational form is with RHT bases and control points in R^3. In RHT approach, if the geometry contains conic sections, the initial basis (level 0) based on NURBS needs to be employed. From this initial basis, the process of the refinement is started. At refinement step, new basis functions over T-meshes are created by using above mentioned procedures. During the process of the refinement, the exact geometry is always maintained. Therefore, communication with CAD is avoided.

6.4 Numerical results

In this section, four numerical examples are presented to demonstrate the performance of my method. Note that with the geometry including conic sections such circles, I use the original NURBS form at level 0. The results of the present formulation will be compared with those of the standard FEM using cubic quadrilateral elements (FEM-Q16) and the original cubic C^1 continuous NURBS finite element approach. The energy error norm is defined by

$$\left\|\mathbf{u}-\mathbf{u}^h\right\|_E=\left(\frac{1}{2}\int_\Omega\left(\sigma-\sigma^h\right)^T\mathbf{D}^{-1}\left(\sigma-\sigma^h\right)\mathrm{d}\Omega\right)^{1/2} \tag{6.7}$$

where $\mathbf{u}$ and σ represent the analytical displacement and stress solutions, respectively, whereas all approximate values are denoted by the superscript h. It was shown in (CHB09) that a priori error estimate can be derived as in the standard FEM, i.e,

$$\left\|\mathbf{u}-\mathbf{u}^h\right\|_{H^1(\Omega)}\leq C_2h^p \tag{6.8}$$

where h is assumed to be a uniform mesh refinement. Therefore the energy error norm can be obtained through the equivalence of H^1-norm as follows

$$\left\|\mathbf{u}-\mathbf{u}^h\right\|_E=\left(\frac{1}{2}\times a(\mathbf{u}-\mathbf{u}^h,\mathbf{u}-\mathbf{u}^h)\right)^{1/2}\leq C_3\left\|\mathbf{u}-\mathbf{u}^h\right\|_{H^1(\Omega)}\leq C_2C_3h^p\equiv Ch^p \tag{6.9}$$

It is seen from numerical results below that the isogeometric finite element model using RHT-spline basis functions can produce an optimal order of convergence of the a prior error estimate as given in Eqs. (6.9).

6.4.0.1 Cantilever beam subjected to a parabolic traction at the free end

A cantilever beam with length L and height D and unit thickness is studied as a benchmark here. The beam is subjected to a parabolic traction at the free end as shown in Fig. 6.9. The parameters are: length $L = 48m$, height $D = 12m$, Young's module $E = 3.0 \times 10^7 kPa$, Poisson's ratio $\nu = 0.3$, $P = 1000N$. The analytical solution is available and can be found in a textbook by Timoshenko and Goodier (TG70).

$$\begin{aligned} u_x &= \tfrac{Py}{6\bar{E}I}\left[(6L-3x)x+(2+\bar{\nu})\left(y^2-\tfrac{D^2}{4}\right)\right] \\ u_y &= -\tfrac{Py}{6\bar{E}I}\left[3\bar{\nu}y^2(L-x)+(4+5\bar{\nu})\tfrac{D^2x}{4}+(3L-x)x^2\right] \end{aligned} \tag{6.10}$$

where the moment of inertia I for a beam with rectangular cross section and unit thickness is given by $I = \frac{D^3}{12}$ and

$$\bar{E} = \left\{ \begin{array}{c} E \\ E/(1-\nu^2) \end{array} \right. , \quad \bar{\nu} = \left\{ \begin{array}{cc} \nu & \text{for plane stress} \\ \nu/(1-\nu) & \text{for plane strain} \end{array} \right. \tag{6.11}$$

The stresses corresponding to the displacements Eqs. (6.10) are

$$\sigma_{xx} = \frac{P(L-x)y}{I}; \quad \tau_{xy} = -\frac{P}{2I}\left(\frac{D^2}{4}-y^2\right); \quad \sigma_{yy} = 0\,. \tag{6.12}$$

The normalized strain energies and the energy error norms of the methods are computed for various grid densities and shown in Fig. 6.10 and Fig. 6.11, respectively. It is observed that the RHT-splines exhibits a superconvergence in the energy error norm of the same order as that provided by the NURBS-based isogeometric analysis. However, the errors of the RHT-splines are smaller than those of the traditional FEM-Q16 and the NURBS-based isogeometric analysis. The contour plot of displacement and stress components are shown in Fig. 6.12.

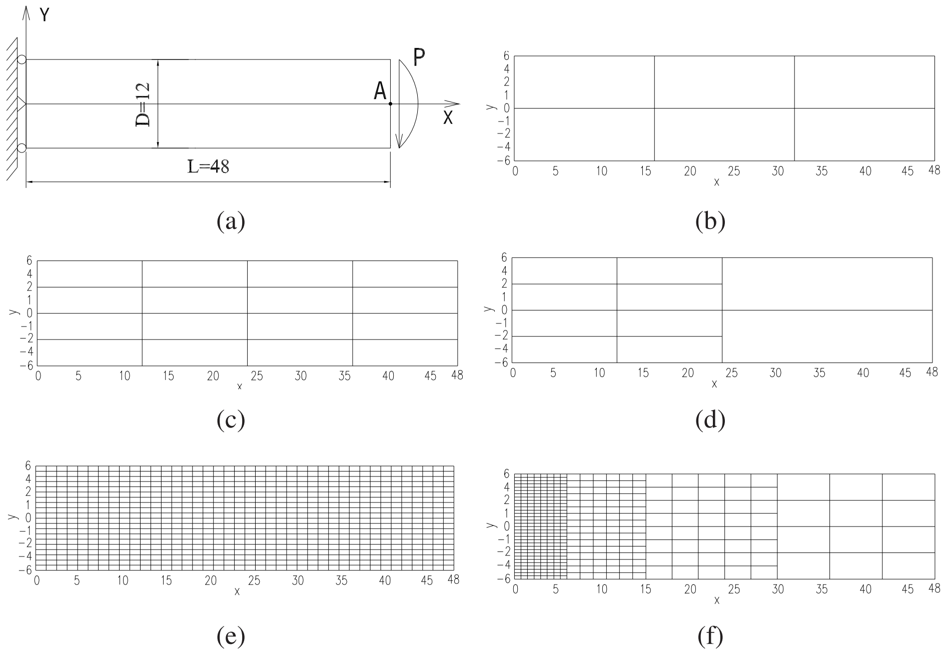

(a) (b)

(c) (d)

(e) (f)

Figure 6.9: A cantilever beam and meshes: a) A cantilever beam with parameters; b) A uniformly coarse mesh used for both NURBS and RHT-splines at level 0; Slightly finer meshes: c) NURBS and d) RHT-splines; Fine meshes: e) NURBS and f) RHT-splines.

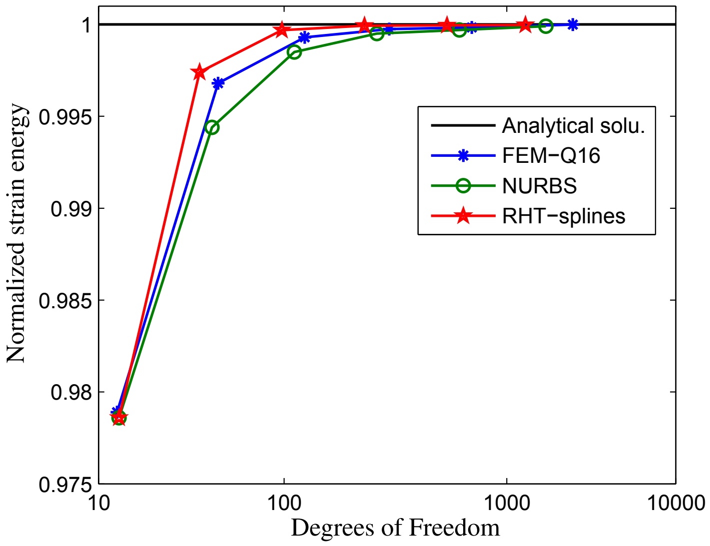

Figure 6.10: Normalized strain energy of the cantilever beam.

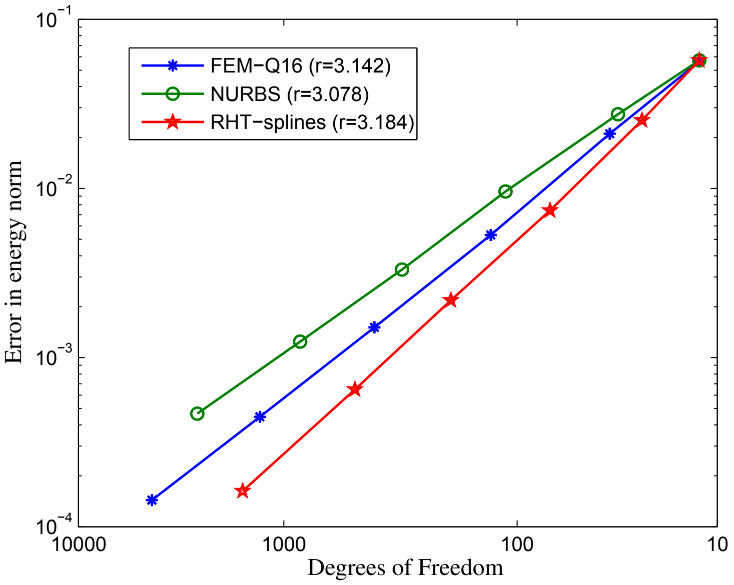

Figure 6.11: Error in energy norm of the cantilever beam.

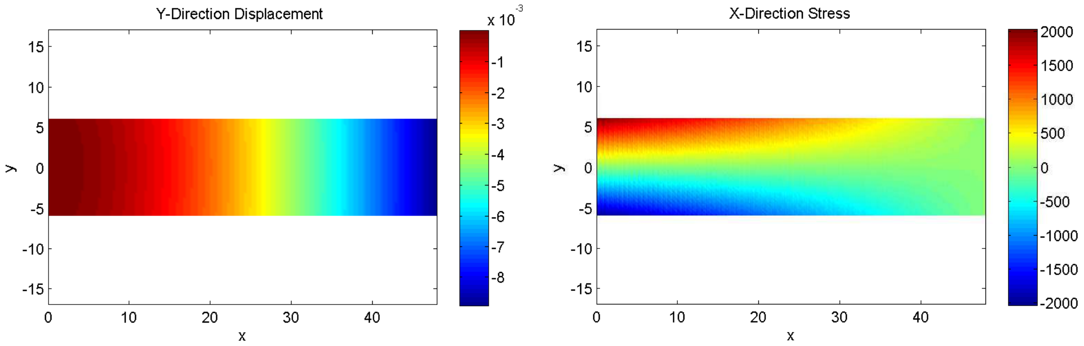

Figure 6.12: Contour plots of displacement and stress component of the cantilever beam.

6.4.0.2 Infinite plate with a circular hole

Next, we consider a plate with a hole. The exact solution for an infinite plate with a hole of radius a centered at its origin, subjected to a constant tension in the x-direction at infinity (see Fig. 6.13), is given by:

$$\begin{aligned}
\sigma_{rr}(r,\theta) &= \frac{T_x}{2}\left(1-\frac{R^2}{r^2}\right)+\frac{T_x}{2}\left(1-4\frac{R^2}{r^2}+3\frac{R^4}{r^4}\right)\cos 2\theta \\
\sigma_{\theta\theta}(r,\theta) &= \frac{T_x}{2}\left(1+\frac{R^2}{r^2}\right)-\frac{T_x}{2}\left(1+3\frac{R^4}{r^4}\right)\cos 2\theta \\
\sigma_{r\theta}(r,\theta) &= -\frac{T_x}{2}\left(1+2\frac{R^2}{r^2}-3\frac{R^4}{r^4}\right)\sin 2\theta\ .
\end{aligned} \tag{6.13}$$

The normalized strain energies and the energy error norms of the methods are depicted in Fig. 6.14 and Fig. 6.15, respectively. The most accurate results are obtained with the RHT-splines formulation. In terms of convergence rate, it is seen that the convergence rate of the RHT-splines are higher than that of the FEM-16 (r=3.196) and the NURBS analysis (r=3.152). The contour plot of displacement and stress components are shown in Fig. 6.16.

6.4.0.3 A hollow cylinder subjected to inner pressure: a plane stress problem

Fig. 6.17 shows a hollow cylinder and the discretizations of the domain, with internal radius a = 0.3m, external radius b = 0.5m, subjected to an internal pressure $p = 3\times 10^4 kN/m^2$. Because of the axis-symmetry of the problem, only the upper right quadrant of the cylinder is modeled. Plane stress conditions are assumed with Young's modulus $E = 3\times 10^7 kN/m^2$ and Poisson ratio $\nu = 0.25$. Symmetry conditions are imposed on the left and bottom edges, and the outer boundary is traction free. The exact solution for the stress components (TG70) as

$$\sigma_r(r) = \frac{a^2 p}{b^2-a^2}\left(1-\frac{b^2}{r^2}\right)\ ;\ \sigma_\phi(r) = \frac{a^2 p}{b^2-a^2}\left(1+\frac{b^2}{r^2}\right)\ ;\ \sigma_{r\phi}=0 \tag{6.14}$$

whereas the radial and the tangential exact displacements are given by

$$u_r(r) = \frac{a^2 pr}{E(b^2-a^2)}\left\{1-\upsilon+\frac{b^2}{r^2}(1+\upsilon)\right\}\quad ;\quad u_\phi = 0\ . \tag{6.15}$$

Fig. 6.18 and Fig. 6.19 present the normalized strain energies and the energy error norms, respectively. It is seen that the convergence rate of the RHT-splines are higher than that other methods. More important, the RHT-spline can produce the smallest error. Fig. 6.20 shows contour plots of different stress components.

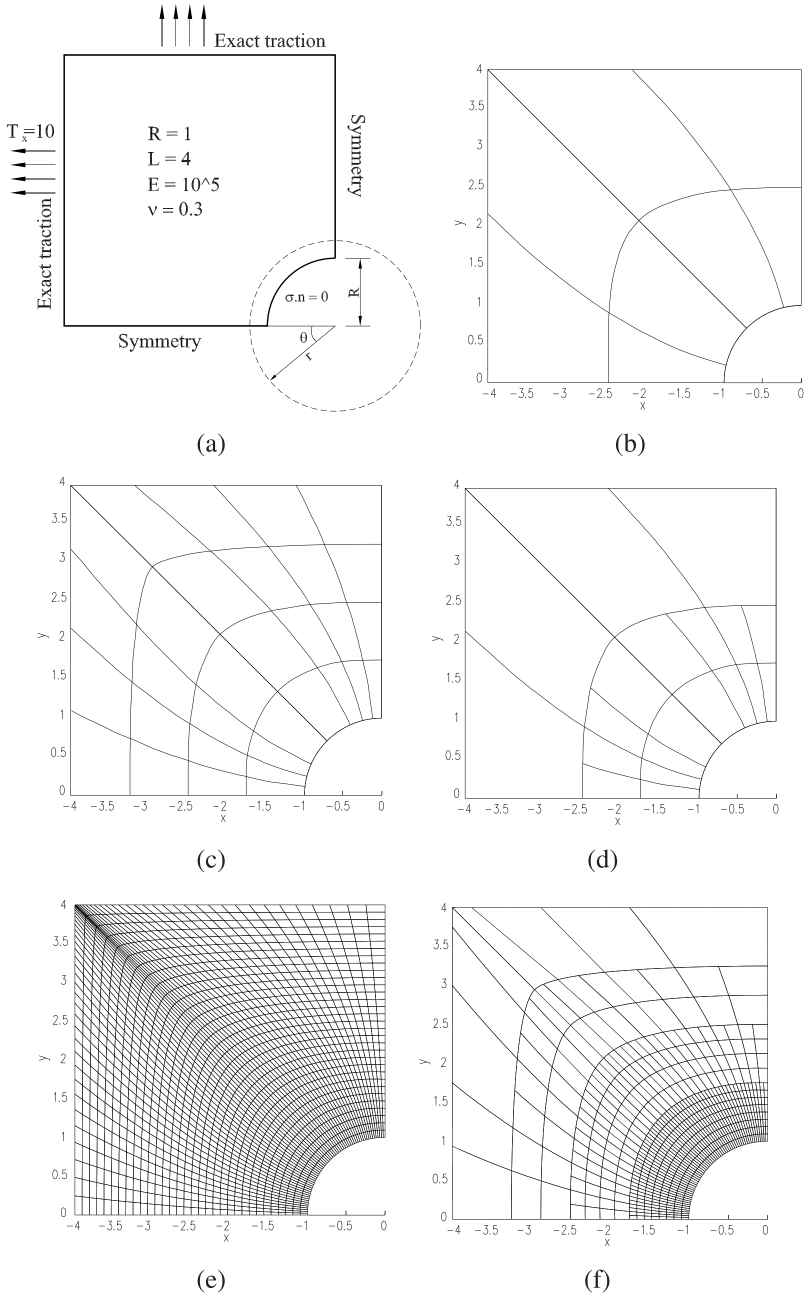

Figure 6.13: The elastic plate with circular hole and meshes: a) The elastic plate with circular hole with parameters; b) A uniformly coarse mesh used for both NURBS and RHT-splines at level 0; Slightly finer meshes: c) NURBS and d) RHT-splines; Fine meshes: e) NURBS and f) RHT-splines.

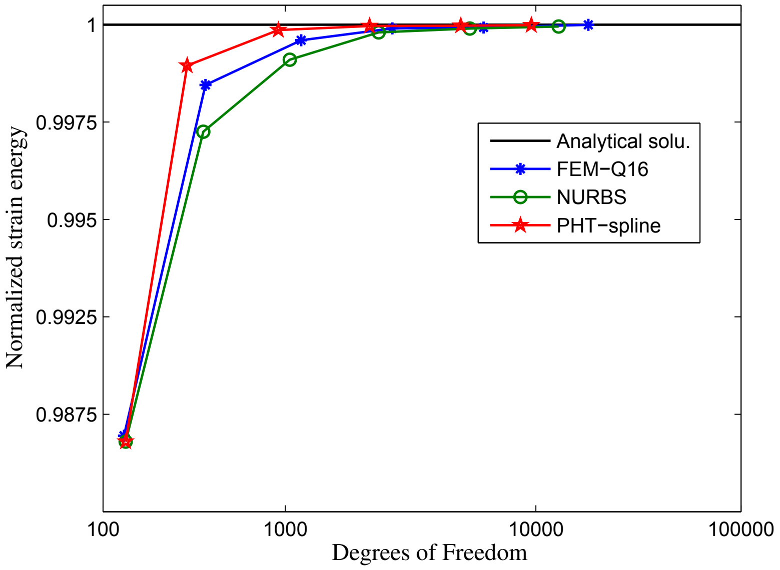

Figure 6.14: Normalized strain energy of the infinite plate with a hole.

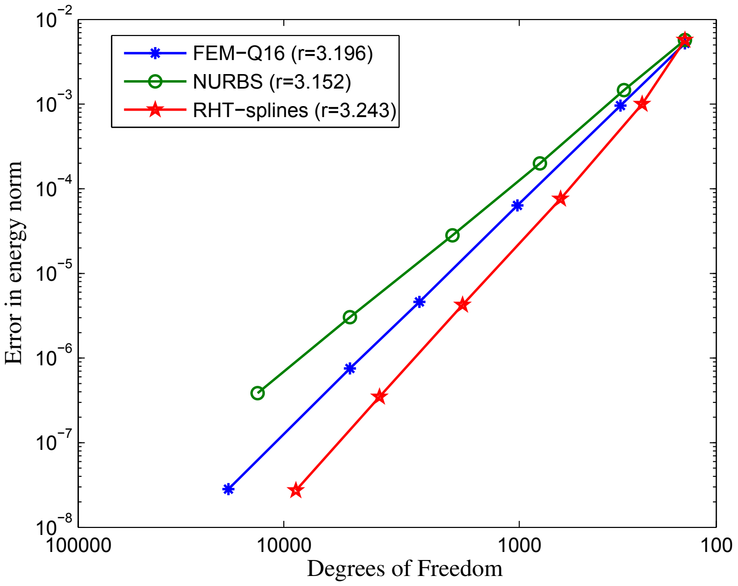

Figure 6.15: The estimated rate in energy norm of the plate with a hole.

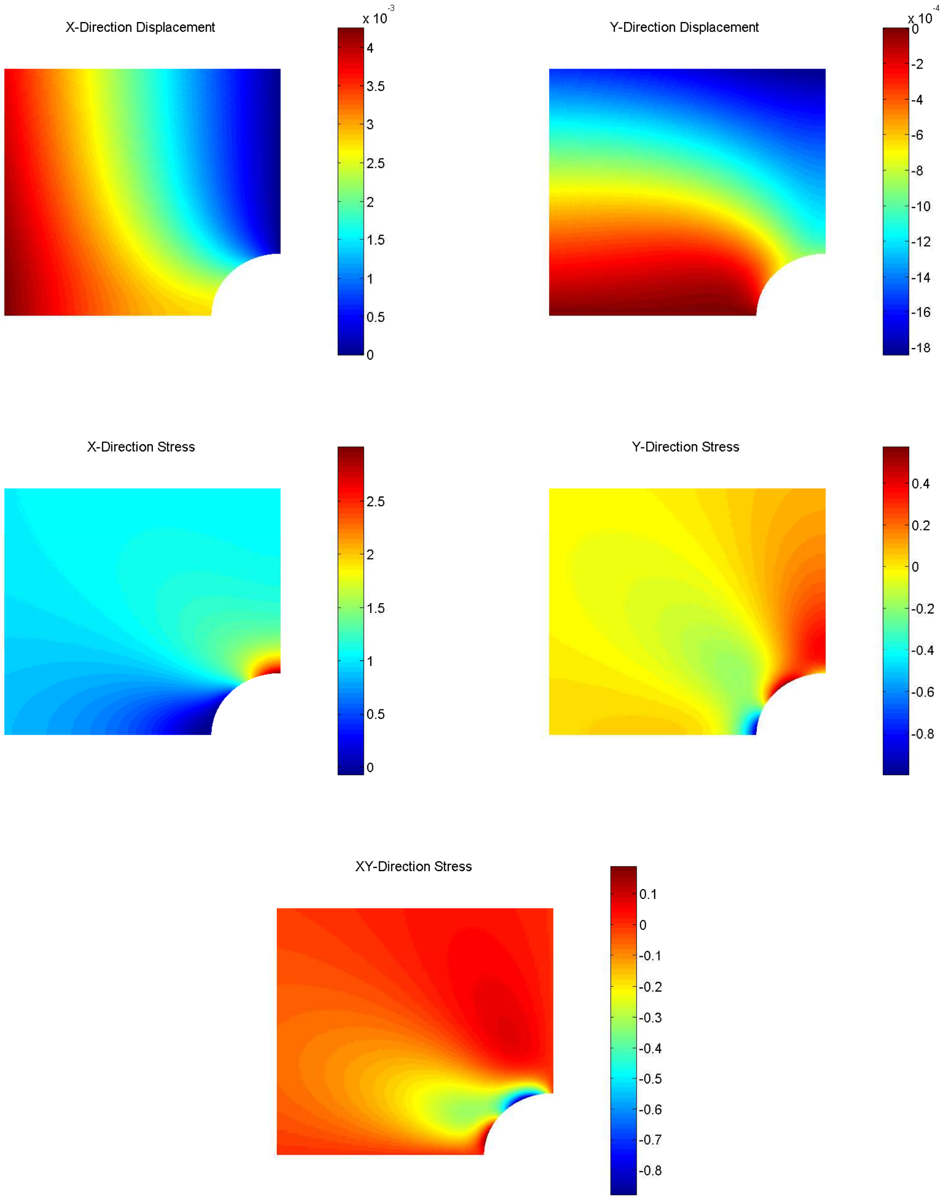

Figure 6.16: Contour plots of displacement and stress components of the plate hole.

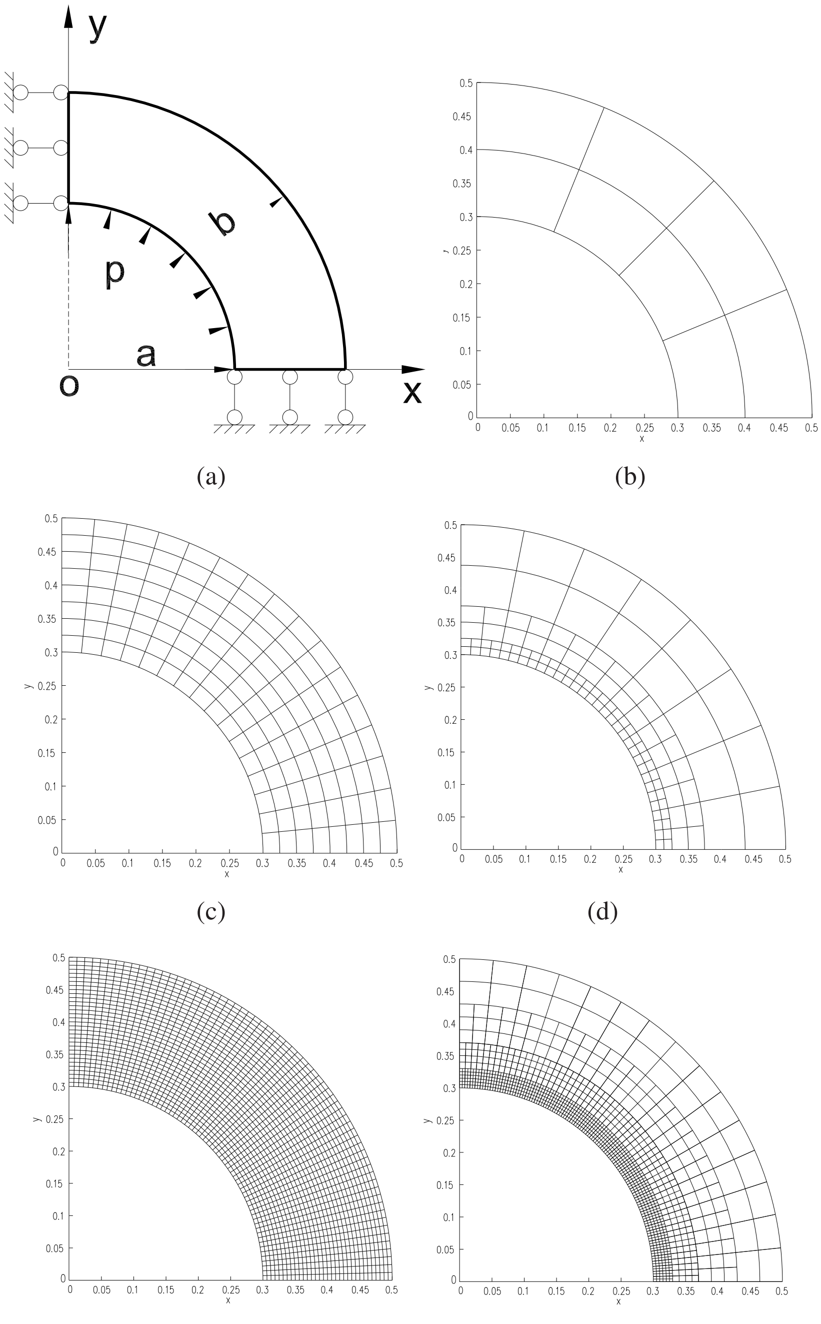

(a) (b)

(c) (d)

(e) (f)

Figure 6.17: A hollow cylinder subjected to inner pressure and domain discretization: a) A hollow cylinder; b) A uniformly coarse mesh used for both NURBS and RHT-splines at level 0; Slightly finer meshes: c) NURBS and d) RHT-splines; Fine meshes: e) NURBS and f) RHT-splines.

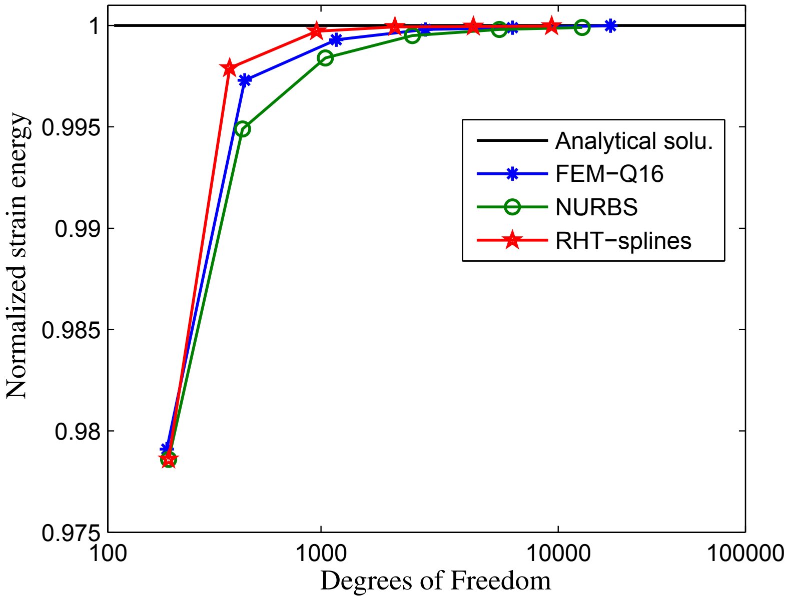

Figure 6.18: Normalized strain energy of the hollow cylinder.

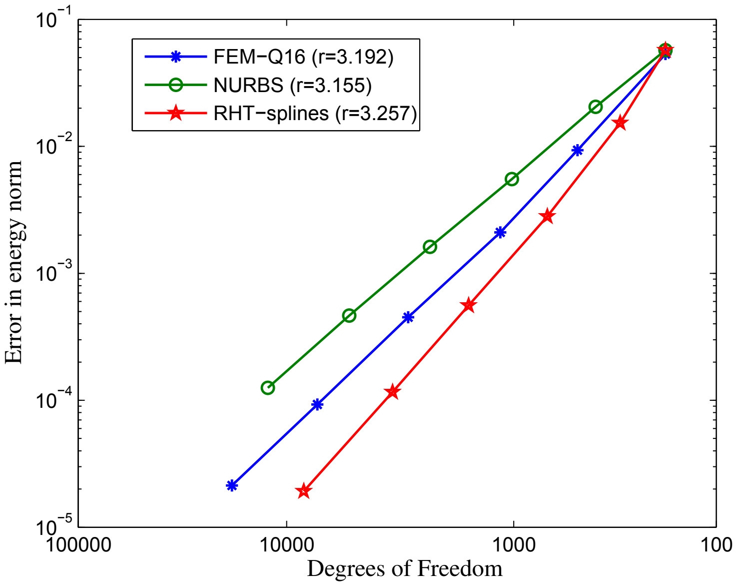

Figure 6.19: The estimated rate in energy norm of a hollow cylinder.

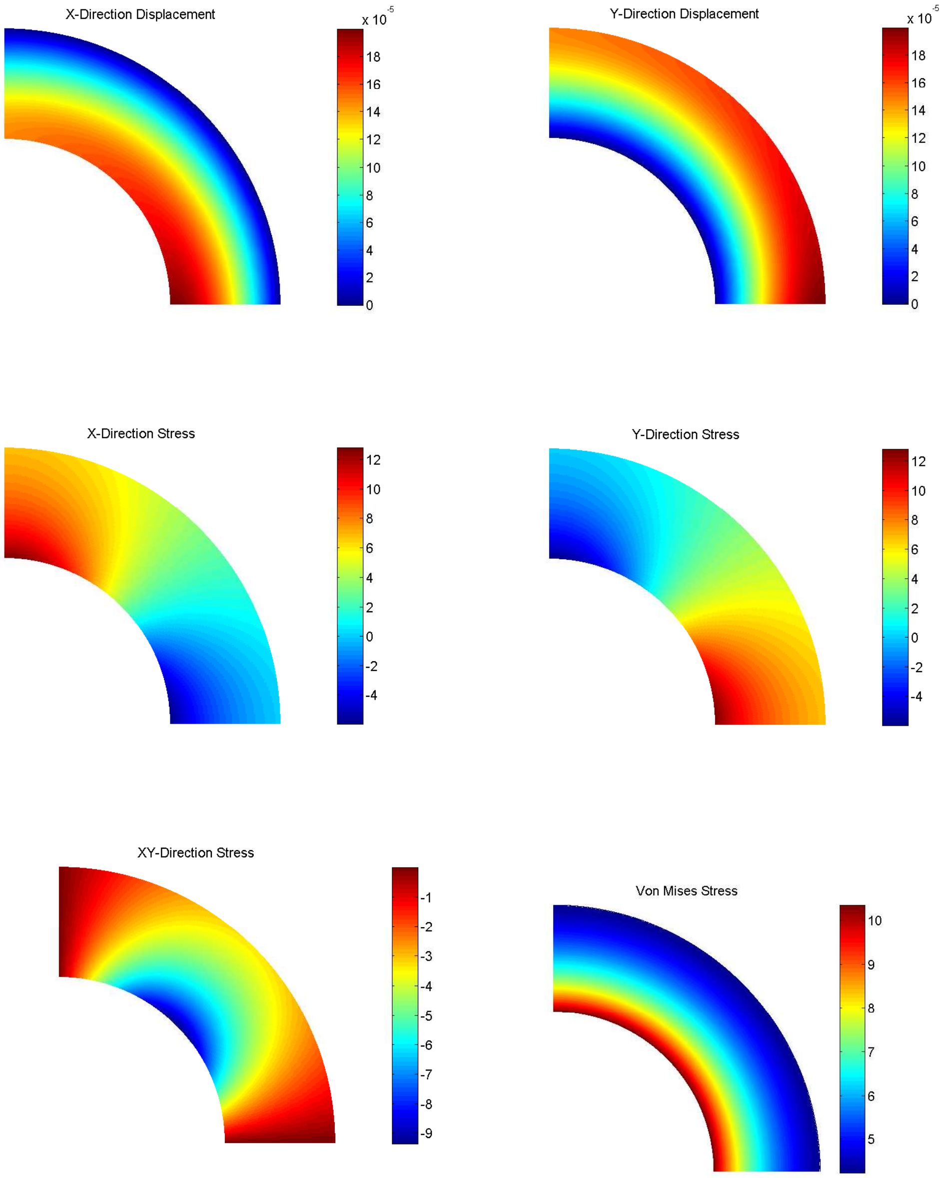

Figure 6.20: Contour plots of displacement and stress components of a hollow cylinder.

6.4.0.4 L-shaped panel subjected traction

Our last example is an L-shaped panel under plane stress condition as shown in Fig. 6.21. The parameters of the structure are $E = 1.0, \nu = 0.3, t = 1$. In this problem, the re-entrant corner causes a stress singularity. Therefore, we refined the mesh in the vicinity of the singularity. The normalized strain energy versus the number of degrees of freedom is shown in Fig. 6.22. The most accurate results are obtained with the RHT-splines. For example, an error of below 2% is obtained with approximately 5800 degrees of freedom (DOFs)for FEM-Q16 formulation while only 2600 DOFs elements are needed for the RHT-spline formulation. The error in the energy norm for different mesh refinements is shown in Fig. 6.23. Contour plots for this problem are given in Fig. 6.24.

6.5 Concluding remarks

Isogeometric analysis based on RHT-splines with applications to solids in two dimensions are presented. The RHT-spline basis functions fulfill all important properties in the context of numerical analysis, i.e. non-negativity, partition of unity, linear independent and local support. Moreover, the RHT-spline formulation facilitates adaptive refinement that is cumbersome for NURBS or even T-spline based FE formulations.

In this chapter four numerical examples are presented: the cantilever beam, the plate with a hole, a hollow cylinder under internal pressure and a L-shaped panel under traction boundary conditions; a singularity is present for the latter example at the re-entrant corner. For these problems, we showed that the convergence rate of the RHT-spline is higher than that of the FEM-Q16 and the NURBS while the total error is lower. It is clear that the RHT-spline is superior to the FEM-Q16 and the NURBS for all problem tested. Moreover, RHT-splines allow for simpler (adaptive) mesh refinement. The main drawback of the RHT-spline is that it can achieve only C^1 continuity which is nonetheless usually sufficient for most problems in solid and structural mechanics. In conclusion, we believe the isogeometric analysis using RHT-splines holds significant potential in computer-aided engineering and is a desirable alternative to the current isogeometric analysis using B-splines and NURBS.

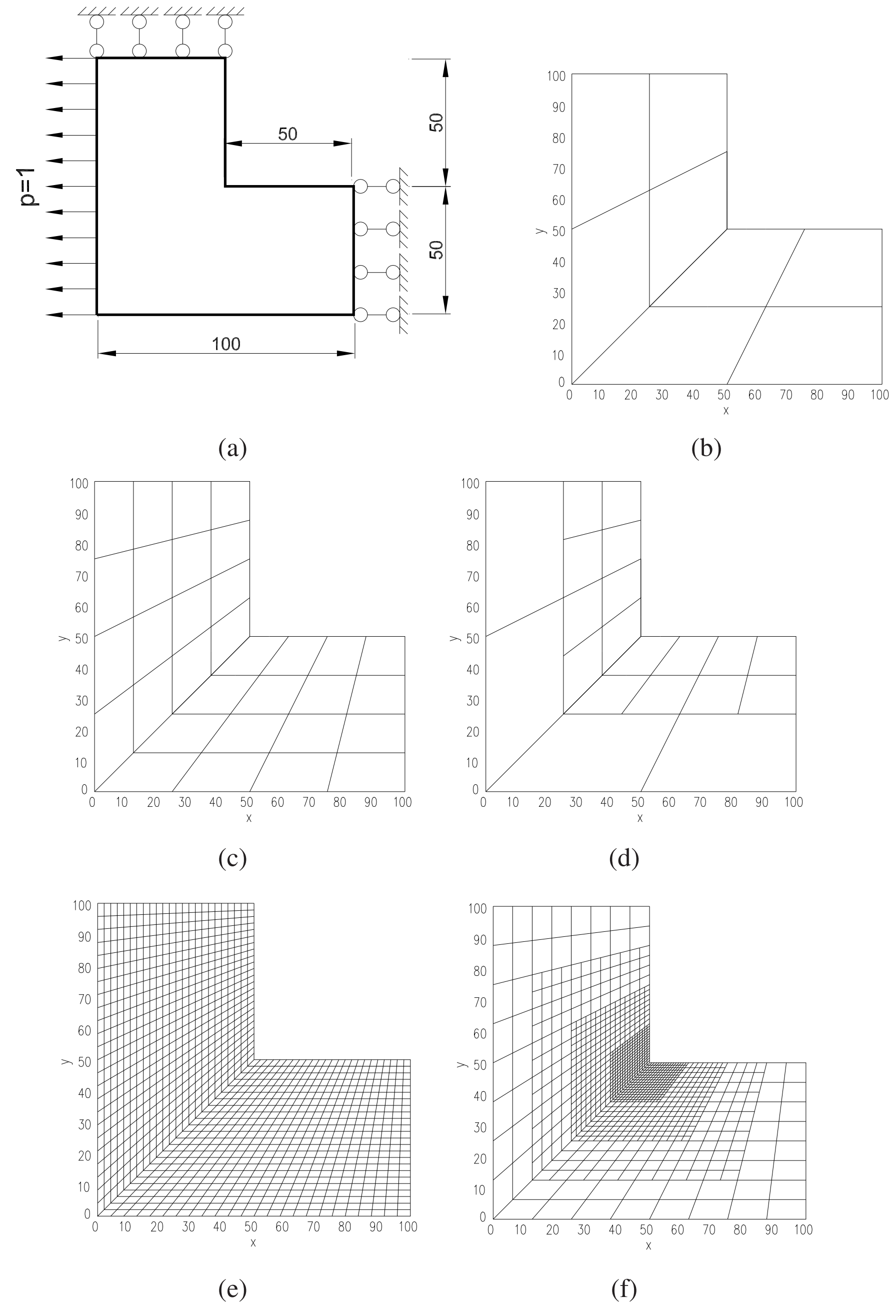

(a) (b)

(c) (d)

(e) (f)

Figure 6.21: L-shaped panel problem setting: a) L-shaped panel problem; b) A uniformly coarse mesh used for both NURBS and RHT-splines at level 0; Slightly finer meshes: c) NURBS and d) RHT-splines; Fine meshes: e) NURBS and f) RHT-splines.

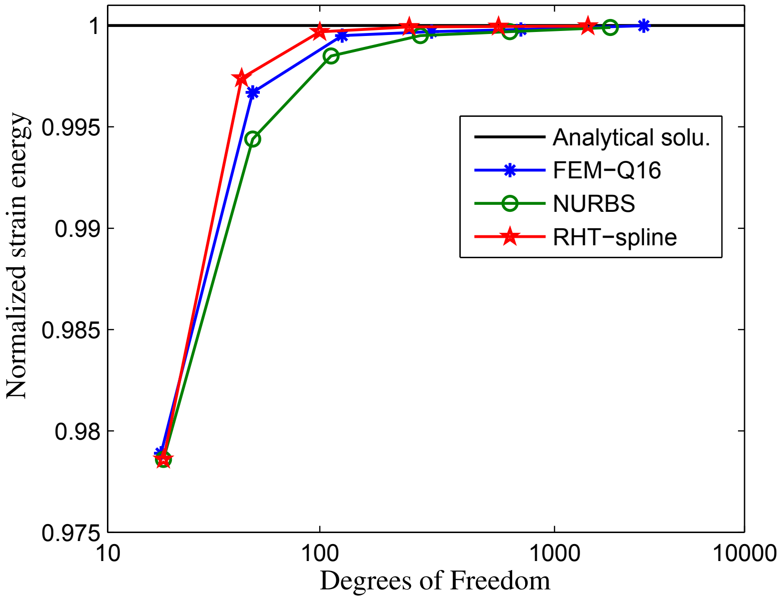

Figure 6.22: Normalized strain energy versus number of DOFs of the L-shape panel.

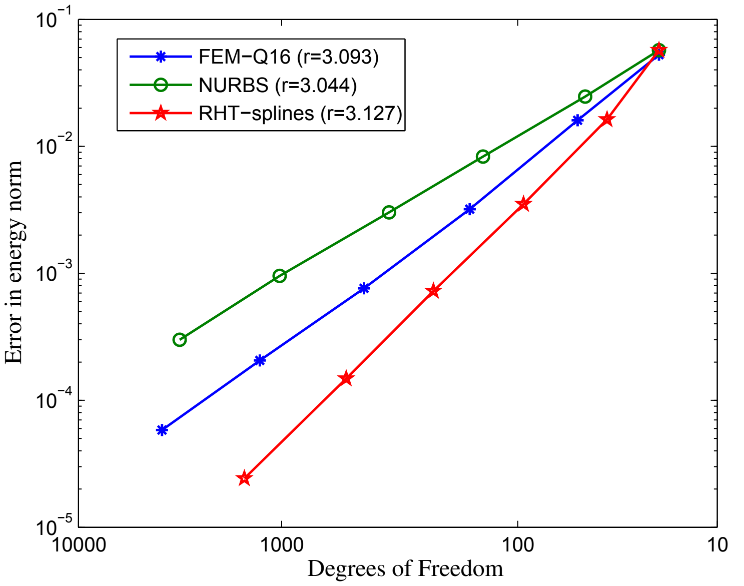

Figure 6.23: Error in the energy norm for the L-shape problem.

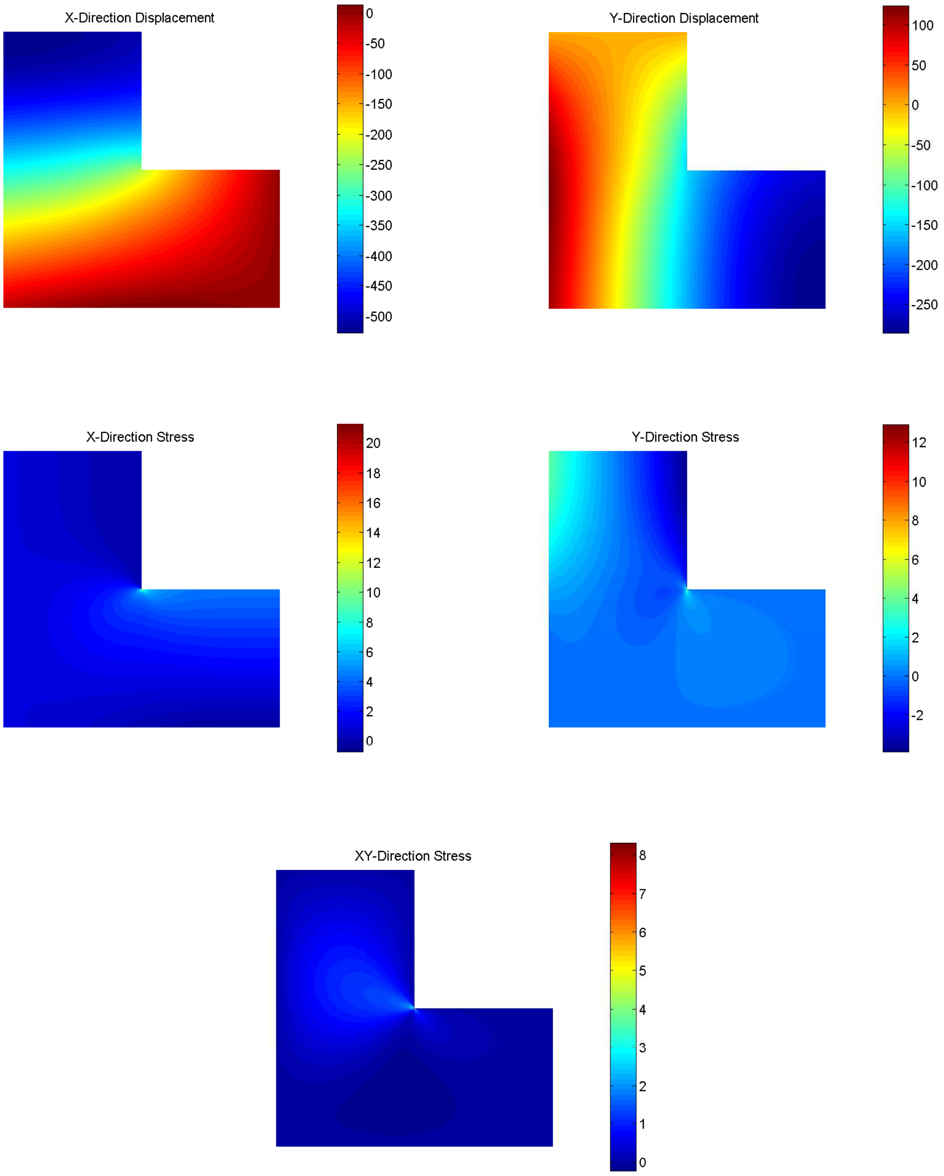

Figure 6.24: Contour plots of displacement and stress components for the L-shape problem.

Chapter 7

An adaptive three-dimensional RHT-spline formulation in linear elasto-statics and elasto-dynamics

7.1 Introduction

Isogeometric analysis (IGA) was introduced by Hughes et al. (HCB05) in order to unify Computer Aided Design (CAD) and Computer Aided Engineering (CAE). Non Uniform Rational B-Splines (NURBS) are classically used in CAD though they have certain drawbacks in numerical analysis. One drawback is related to adaptive h-refinement that is complex for NURBS-based isogeometric approaches. Recent approaches in IGA exploit different basis functions such as T-splines (SCF$^+$04, BCC$^+$10, DJS10), polycube splines (WHL$^+$08), Locally Refined (LR) splines (DS10), polynomial splines over hierarchical T-meshes (PHT-splines) (Den) and among others (SDS$^+$12, VGJS12, KJZ12, GJS12).

The RHT-splines inherits all important properties of NURBS such as linear independence of the basis functions, partition of unity, non-negativity and local support (CHR07, BCS09, LDC07, LDC10). In contrast to NURBS, RHT-splines have the capability of joining geometric objects without gaps, preserving higher order continuity everywhere and allow for simple and effective h-refinement strategies. From a linear algebra point of view, the NURBS space is a subspace of the RHT-splines space. Moreover, local refinement algorithms are relatively simple while the complexity of knot insertion with T-splines might be high, particularly in 3D.

In this chapter, the RHT-splines 2D formulation is extened to 3D for problems in elasto-statics *and* elasto-dynamics. In order to drive the adaptive h-refinement the stress recovery technique in isogeometric analysis is presented. The idea from Superconvergent Patch Recovery (SPR) technique proposed by Zienkiewicz *et.al.* (OZ92a, OZ92b) is employed. The procedure is a least squares fitting of finite element solutions over a local patch of elements at pre-selected points, where the rate of convergence is higher than the global rate. The patch in SPR comprises elements that are assembled around a central corner node. In isogeometric analysis the recovered stress components are considered at an imaginary solid. This imaginary solid is constructed by the same RHT-splines basis functions which are used for the approximation of the unknown displacement field. It was show by Hassani *et.al.*(HGT12), that for NURBS-based IGA the Gauss points of the knot elements are used as superconvergent points.

7.2 Rational splines over 3D hierarchical T-meshes

7.2.1 3D T-meshes

In 2D, a T-mesh is a mesh based on rectangular grids that allows T-junctions (Sed). In T-meshes, the end points of each grid line must lie on two other grid lines, and each cell or facet in the grid is formed by a quadrilateral. A 3D T-mesh is a partition of a cuboid domain $\Omega \in \mathbb{R}^3$ such that each cell is a smaller cuboid (see in Fig. 7.1). A vertex of the T-mesh is assigned to each grid point. If a vertex is inside the domain, it is called an interior vertex. Otherwise, it is called a boundary vertex.

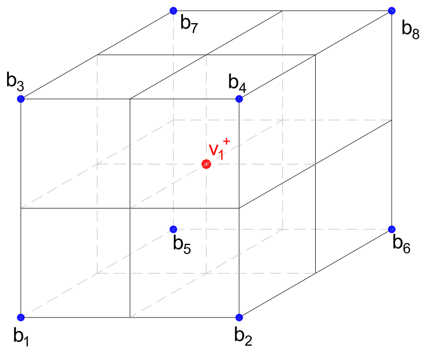

Figure 7.1: An illustration a typical 3D T-mesh with boundary vertices ($b_i = 8$) and crossing vertices ($v_i^+ = 1$).

7.2.2 Hierarchical T-meshes

A hierarchical T-mesh can be considered as a special form of tensor product splines with a natural level structure (PT97, Sed, Den). Hierarchical T-meshes are constructed from a tensor product (TP) mesh starting from level-0 ($\mathscr{T}_0$). At level k ($\mathscr{T}_k$), some cuboids are subdivided equally by three planes into eight sub-cuboids which are labeled as cuboid of level $(k+1)$. An example of a hierarchical T-mesh is shown in Fig. 7.2.

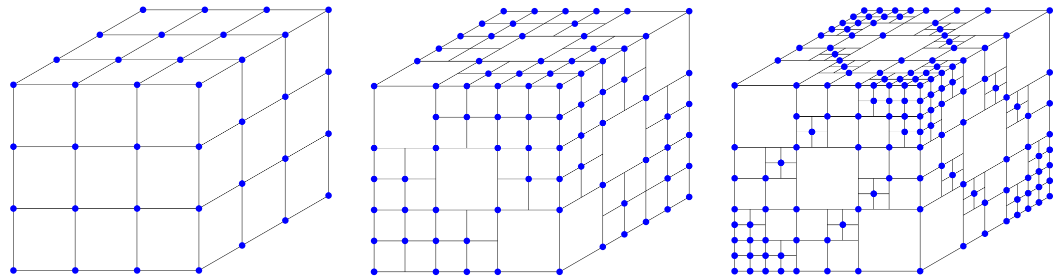
(a) Level 0 (b) Level 1 (c) Level 2

Figure 7.2: A hierachical over 3D T-mesh.

7.2.3 A dimension formula

A 3D T-mesh is a natural generalization of 2D T-mesh. Let $\mathscr{T}$ be the T-mesh, $\mathscr{H}$ be the cells in $\mathscr{T}$, and $\Omega \subset \mathbb{R}^3$ be the region occupied by $\mathscr{T}$. Then, when $p \geq 2\alpha+1$; $q \geq 2\beta+1$ and $r \geq 2\gamma+1$ the dimension formula can be defined as:

$$\mathscr{S}(p,q,r,\alpha,\beta,\gamma,\mathscr{T}) = \left\{ s(x,y,z) \in C^{\alpha,\beta,\gamma}(\Omega) | s(x,y,z)|_{\phi} \in \mathbb{P}_{pqr} \text{ for any } \phi \in \mathscr{H} \right\} \tag{7.1}$$

where the space $\mathbb{P}_{pqr}$ consists of all the tri-degree (p,q,r) polynomials and the space $C^{\alpha,\beta,\gamma}$ consists of continuously trivariate functions of α,β,γ in the x,y,z direction, respectively. For a C^1-continuous cubic spline, where every interior knots is of multiplicity two, the evaluation of the dimension formula is reduced to

$$\dim \mathscr{S}(3,3,3,1,1,1,\mathscr{T}) = 8(V^b + V^+) \tag{7.2}$$

where V^b, V^+ are boundary vertices and interior crossing vertices, respectively. Eq. (7.2) shows the number of basis functions corresponding to boundary and crossing vertices which need to be constructed. It is also implied that each boundary vertex or each crossing vertex is connected by eight basis functions. More details for construction of dimension formula can be found in (DCF06, WYJ$^+$11, LDC06).

In order to define the RHT-spline solid, let $b_i(\xi,\eta,\gamma)$ be a hierarchical T-mesh $\mathscr{T}$, and $\mathbf{P}_i$ be the corresponding control points. The RHT-spline solid is computed by

$$\mathbf{S}(\xi,\eta,\gamma) = \sum_{i=1}^{nml} \mathbf{R}_i(\xi,\eta,\gamma)\mathbf{P}_i \quad ; \quad \mathbf{R}_i = \frac{w_i b_i(\xi,\eta,\gamma)}{\sum_{i=1}^{nml} w_i b_i(\xi,\eta,\gamma)} \tag{7.3}$$

To parameterize the physical domain Ω by a global geometry function $G:\Omega_0=[0,1]^2\rightarrow\Omega$ and $(\xi,\eta,\gamma)\in\Omega_0\rightarrow(x,y,z)\in\Omega$, the domain Ω is modeled by tri-cubic NURBS functions:

$$G(\xi,\eta,\gamma)=\sum_{i=1}^{nml}\mathbf{R}_i(\xi,\eta,\gamma)\,\mathbf{P}_i, \tag{7.4}$$

The RHT-spline basis functions are identical to the NURBS basis functions at level 0. The global geometry function is constructed from the parametric domain Ω_0 which remains unchanged after refinement. This geometry function can be exactly represented with RHT-spline basis functions at any level k. The geometry of the RHT-spline solid at level k can be represented by

$$G(\xi,\eta,\gamma)=\sum_{i=1}^{nml_k}\mathbf{R}_i^k(\xi,\eta,\gamma)\,\mathbf{P}_i^k, \tag{7.5}$$

where $\mathbf{R}_i$ are RHT-spline basis function given in Eq. (7.3). Let us define the linear operator

$$\mathscr{L}b(\xi,\eta,\gamma)=\left(b,b_\xi,b_\eta,b_\gamma,b_{\xi\eta},b_{\eta\gamma},b_{\xi\gamma},b_{\xi\eta\gamma}\right) \tag{7.6}$$

For any fixed basis vertex (ξ_0,η_0,γ_0), eight basis functions with indices $j=1,..,8$ are associated

$$\mathscr{L}G(\xi_0,\eta_0,\gamma_0)=\sum_{s=1}^{N}\mathbf{C}_s\mathscr{L}b_s(\xi_0,\eta_0,\gamma_0)=\sum_{j=1}^{8}\mathbf{C}_j\mathscr{L}b_j(\xi_0,\eta_0,\gamma_0)=\mathbf{C}\cdot\mathbf{B} \tag{7.7}$$

where $\mathbf{B}=(\mathscr{L}b_i^1(\xi_0,\eta_0,\gamma_0),\mathscr{L}b_i^2(\xi_0,\eta_0,\gamma_0),...,\mathscr{L}b_i^7(\xi_0,\eta_0,\gamma_0),\mathscr{L}b_i^8(\xi_0,\eta_0,\gamma_0))$ is a 8×8 matrix, and $\mathbf{C}=(C_i^1,C_i^2,...,C_i^7,C_i^8)$ is a 1×8 matrix. From Eq. (7.7) we obtained

$$\mathbf{C}=\mathscr{L}G(\xi_0,\eta_0,\gamma_0)\cdot\mathbf{B}^{-1} \tag{7.8}$$

The RHT-splines solid at level $k+1$ can be described as

$$G^{k+1}(\xi,\eta,\gamma)=\sum_{i=1}^{nml_{k+1}}\mathbf{R}_i^{k+1}(\xi,\eta,\gamma)\mathbf{P}_i^{k+1} \tag{7.9}$$

The RHT-splines basis functions at level $k+1$ is given

$$\mathbf{R}_i^{k+1}(\xi,\eta,\gamma)=\frac{w_i^{k+1}b_i^{k+1}(\xi,\eta,\gamma)}{\sum\limits_{i=1}^{nml_{k+1}}w_i^{k+1}b_i^{k+1}(\xi,\eta,\gamma)} \tag{7.10}$$

7.3 Stress recovery in isogeometric analysis

In isogeometric analysis, the recovered stress components are considered at an imaginary solid. This imaginary solid is constructed by the same IGA basis functions which are used for the approximation of the displacement field. The imaginary solid will be fitted to these optimal sampling points in a least square sense for the recovered stress components. Therefore, we take advantage of the RHT-spline solid generation with the same control points. By minimizing a discrete L_2 norm between the obtained stresses and the recovered stresses at the Gauss points. The unknown coordinates of the control points in the imaginary solid are obtained. An example for imaginary solid in three-dimensions is shown in Fig. 7.3.

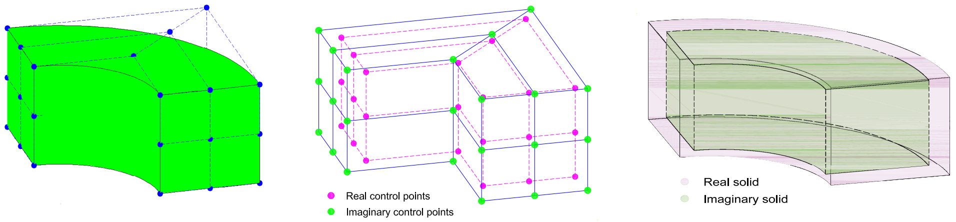

Figure 7.3: An example regarding imaginary solid in three dimensional.

The recovered stress components can be constructed by using the RHT-splines basis functions follow

$$\sigma_\alpha^* = \sum_{i=1}^{n} \sum_{j=1}^{m} \sum_{k=1}^{l} \mathbf{R}_{i,j,k}(u,v,w)\left(\mathbf{P}_{i,j,k}\right)_\alpha \tag{7.11}$$

where σ_α^* are stress components ($\alpha = xx, yy, zz, xy, yz, zx$); $\mathbf{R}_{i,j,k}$ are the RHT-splines basis function and $\mathbf{P}_{i,j,k}$ are the coordinates of control points.

$$\mathbf{R} = \begin{bmatrix} R_1(u_1,v_1,w_1) & R_2(u_1,v_1,w_1) & \dots & R_{nml}(u_1,v_1,w_1) \\ R_1(u_2,v_2,w_2) & R_2(u_2,v_2,w_2) & \dots & R_{nml}(u_2,v_2,w_2) \\ \dots & \dots & \dots & \dots \\ R_1(u_{nml},v_{nml},w_{nml}) & R_2(u_{nml},v_{nml},w_{nml}) & \dots & R_{nml}(u_{nml},v_{nml},w_{nml}) \end{bmatrix} \tag{7.12}$$

$$\mathbf{P}_\alpha = \begin{bmatrix} (P_1(u_1,v_1,w_1))_\alpha & (P_2(u_1,v_1,w_1))_\alpha & \dots & (P_{nml}(u_1,v_1,w_1))_\alpha \\ (P_1(u_2,v_2,w_2))_\alpha & (P_2(u_2,v_2,w_2))_\alpha & \dots & (P_{nml}(u_2,v_2,w_2))_\alpha \\ \dots & \dots & \dots & \dots \\ (P_1(u_{nml},v_{nml},w_{nml}))_\alpha & (P_2(u_{nml},v_{nml},w_{nml}))_\alpha & \dots & (P_{nml}(u_{nml},v_{nml},w_{nml}))_\alpha \end{bmatrix} \tag{7.13}$$

Eq. (7.11) can be rewritten in matrix form as:

$$\sigma_{\alpha}^{*} = \mathbf{R}^{T}\mathbf{P}_{\alpha} \tag{7.14}$$

We minimize discrete a norm $F(\mathbf{P}_{\alpha})$ of the difference between the new field and the values at superconvergence points with respect to $\mathbf{P}_{\alpha}$ as follows

$$F(\mathbf{P}_{\alpha}) = \sum_{i=1}^{g_x}\sum_{j=1}^{g_y}\sum_{k=1}^{g_z}\left(\sigma_{\alpha_{i,j,k}}^{*} - \sigma_{\alpha_{i,j,k}}^{h}\right)^{2} \tag{7.15}$$

where σ_{α}^{h} are the stress components obtained from the numerical analysis; g_x, g_y, g_z are the number of the Gauss points in the x, y, z-directions of the patch, respectively.

Substituting Eq. (7.14) into Eq. (7.15), we obtained

$$F(\mathbf{P}_{\alpha}) = \sum_{g=1}^{G}\left(\mathbf{R}_{g}^{T}\mathbf{P}_{\alpha} - \sigma_{\alpha_g}^{h}\right)^{2} \tag{7.16}$$

where G is the number of Gauss points inside the patch

The minimization condition of $F(\mathbf{P}_{\alpha})$ requires its first derivative to be zero

$$\frac{\partial F(\mathbf{P}_{\alpha})}{\partial (P_i)_{\alpha}} = 0 \tag{7.17}$$

Yielding

$$\mathbf{A}\mathbf{P}_{\alpha} = \mathbf{C} \quad \Rightarrow \quad \mathbf{P}_{\alpha} = \mathbf{A}^{-1}\mathbf{C} \tag{7.18}$$

with

$$\mathbf{A} = \sum_{i=1}^{G}\mathbf{R}_{i}^{T}\mathbf{R}_{i}\mathbf{P}_{\alpha_i} \quad ; \quad \mathbf{C} = \sum_{i=1}^{G}\mathbf{R}_{i}\sigma_{\alpha_i}^{h} \tag{7.19}$$

The error in the energy norm and the approximate the energy norm is

$$\|e\| = \left[\int_{\Omega}\left(\sigma - \sigma^{h}\right)^{T}\mathbf{D}\left(\sigma - \sigma^{h}\right)d\Omega\right]^{1/2} \tag{7.20}$$

$$\|e^{*}\| = \left[\int_{\Omega}\left(\sigma^{*} - \sigma^{h}\right)^{T}\mathbf{D}\left(\sigma^{*} - \sigma^{h}\right)d\Omega\right]^{1/2} \tag{7.21}$$

where σ is the exact stress, σ^{*} is the recovered stress, σ^{h} is the stress obtained from RHT-splines formulation.

The quality and accuracy of an error estimate is measured by its effective index (ZTZ05)

$$\theta = \frac{\|e^{*}\|}{\|e\|} \tag{7.22}$$

7.4 Numerical example

7.4.1 Static analysis

The RHT-splines results are compared with those of the cubic NURBS approach. At level 0, both NURBS and RHT-splines share a uniformly coarse mesh for the initial step. Both meshes are refined; while the RHT-splines formulation allows for local refinement, the refinement for the NURBS-formulation crosses the entire patch. For the error estimate the rate (r) is refered to degree of freedom.

7.4.1.1 Three dimension Lame problem

The first example is a hollow sphere of internal radius $a = 1m$ and external radius $b = 2m$, subjected to an internal pressure $P = 1N/m^2$ as illustrated in Fig. 7.4a. Only one eighth of the geometry is modelled and symmetry conditions are imposed on the three planes of symmetry. The parameters are Young's modulus $E = 1kPa$ and Poisson ratio $\nu = 0.3$. The exact solution in polar coordinates is available in Timoshenko *et. al.* (TG70):

$$u_r = \frac{\mathrm{P}a^3 r}{E\left(b^3-a^3\right)}\left[(1-2\upsilon)+(1+\upsilon)\frac{b^3}{2r^3}\right] \quad ; \quad \sigma_r = \frac{Pa^3\left(b^3-r^3\right)}{r^3\left(a^3-b^3\right)} \quad ; \quad \sigma_\theta = \frac{Pa^3\left(b^3+2r^3\right)}{2r^3\left(b^3-a^3\right)} \tag{7.23}$$

where r is the radial distance from the centroid of the sphere to the point of interest in the sphere.

Fig. 7.4 shows the discretization of the cylinder for NURBS and RHT-splines. The contour plot of the radial displacement and the deformed configuration are shown in Fig. 7.5. The computed radial displacement and the tangential stresses along the x-axis are presented in Fig. 7.6. The numerical results match with the analytical solution well. Fig. 7.7 presents the error in the displacement and the error in the energy norms. The effectivity index according to Eq. (7.22) is 0.837 for this problem. The convergence rate in the energy error norm of the proposed method $(r = 3.6275)$ is higher than the convergence rate of the NURBS $(r = 3.0153)$ based formulation with the same polynomial degree (p=3).

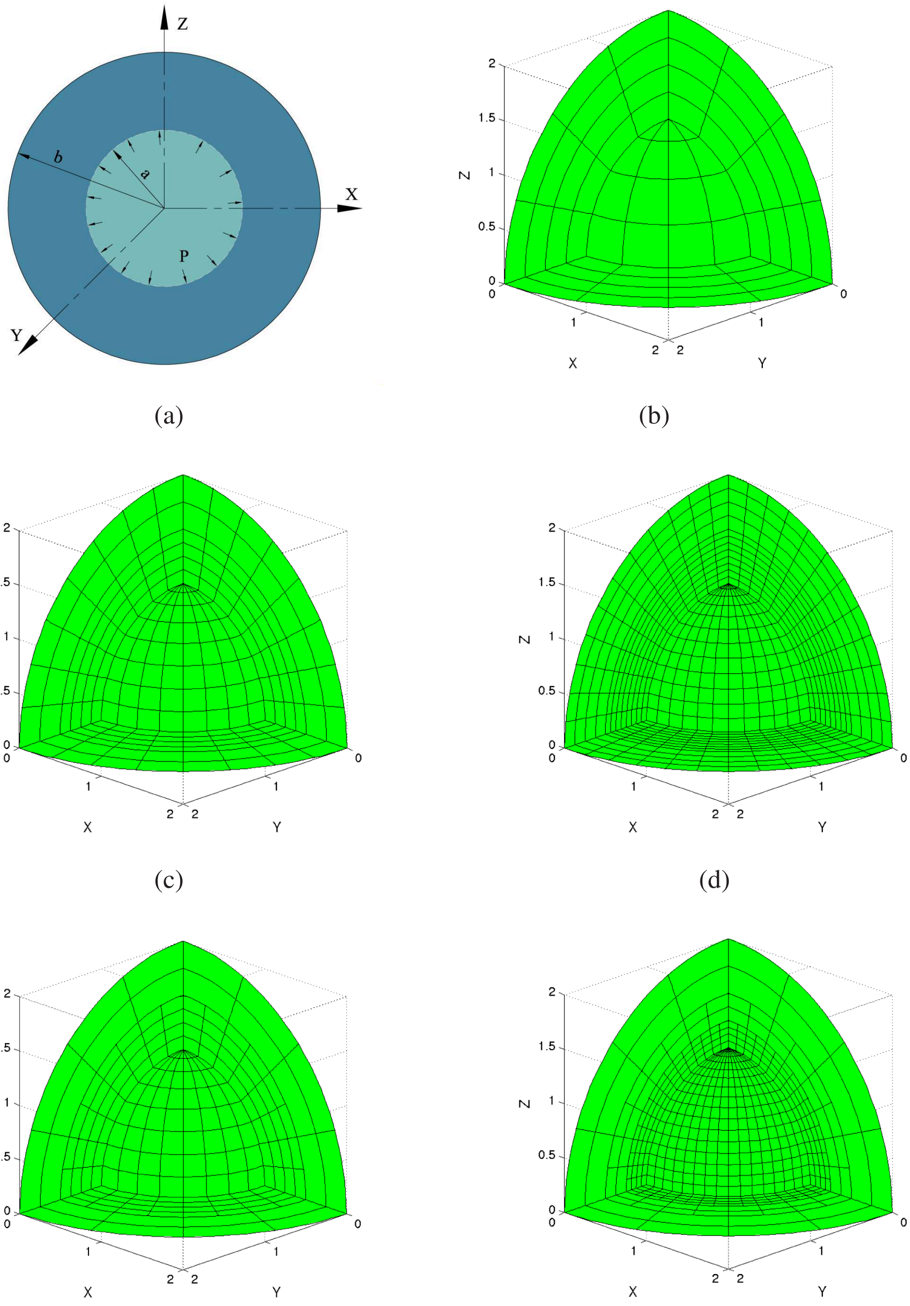

(a)

(b)

(c)

(d)

(e)

(f)

Figure 7.4: (a) Hollow sphere model. (b) A uniformly coarse mesh used for both NURBS and RHT-splines. (c),(d) Non uniform NURBS refinements. (e),(f) RHT-splines after 1 and 2 refinements.

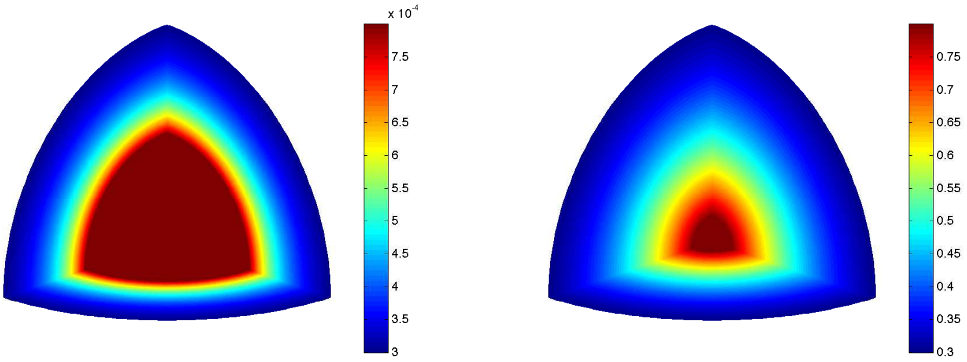

(a) (b)

Figure 7.5: (a) Contour plot of displacement. (b) Deformed configuration (scaling factor = 1×10^3).

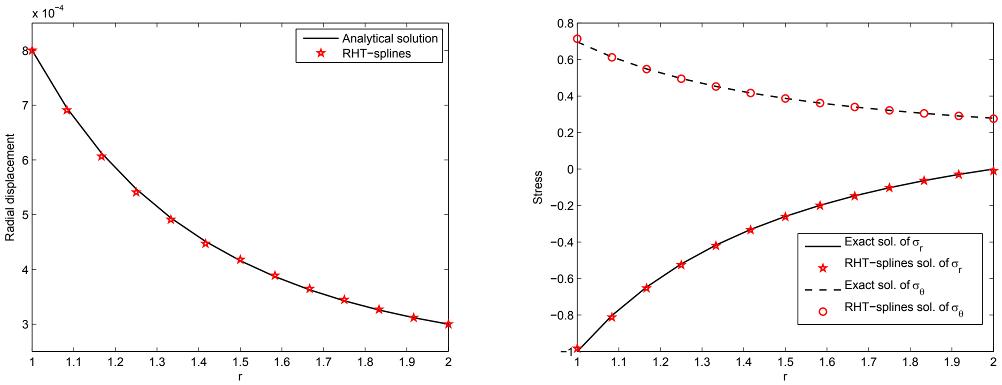

(a) (b)

Figure 7.6: (a) Distribution of the radial displacement. (b) Tangential stresses along the x-axis.

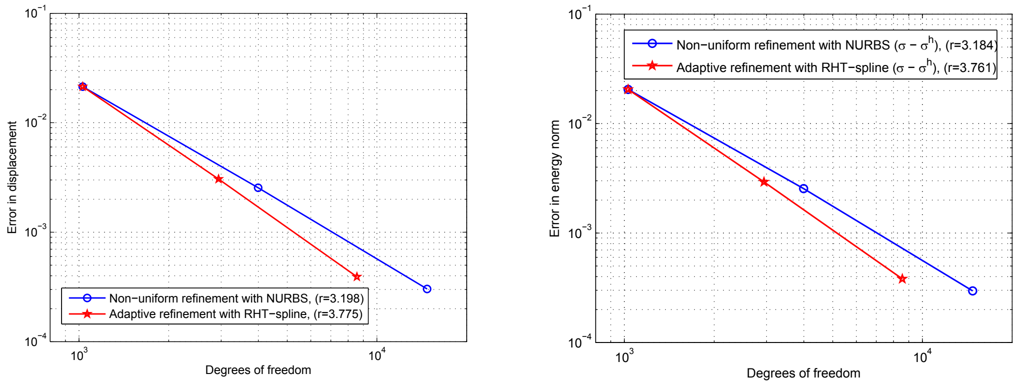

(a) (b)

Figure 7.7: (a) Convergence rate in displacement of hollow sphere. (b) Convergence rate in energy norm.

7.4.1.2 Pinched Cylinder

The cylindrical shell with rigid end diaphragm is subjected to a point load at the center of the cylindrical surface as shown in Fig. 7.11a. The related parameters (NTRHXB08) are: cylinder length $L = 600$; radius $R = 300$; thickness $t = 3$; Young's modulus $E = 3 \times 10^6$; and Poisson's ratio $\nu = 0.3$. Due to its symmetry, only one-eighth of the cylinder is modelled. The expected deflection at point A is 1.8248×10^{-5} (BSL$^+$85).

The initial mesh and the mesh after 3 refinement steps are shown in Fig. 7.11. The contour plot of the radial displacement at the loading point are shown in Fig. 7.8. Fig. 7.9 shows the error in the displacement directly under load. Note that the reference solution is based on shell theory while we employ a 3D continuum approach. The error in the approximate energy norm according to Eq. (7.21) is illustrated in Fig. 7.10.

7.4.1.3 Solid "horseshoe" subjected to equal and opposite in-plane flat edge displacements

Next, we consider the horseshoe problem, Fig. 7.12a. The parameters are Young's modulus $E = 7.5 \times 10^7$; and Poisson's ratio $\nu = 0.25$.

The initial mesh and the mesh after 2 refinement steps are shown in Fig. 7.12. The contour plot of the displacement and the deformed configuration are shown in Fig. 7.13. The error in the approximate energy norm is shown in Fig. 7.14.

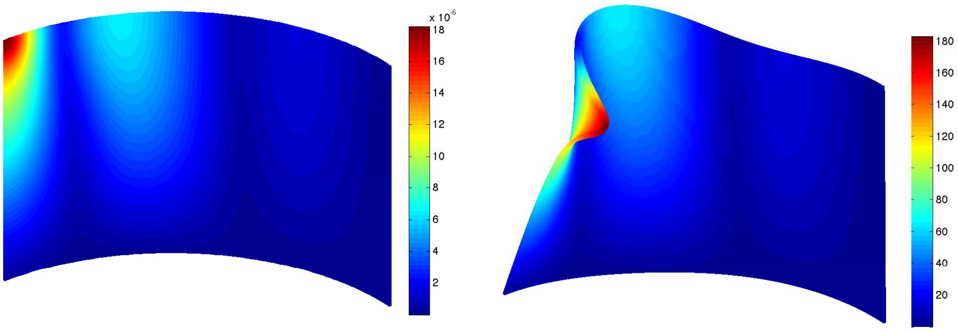

Figure 7.8: Contour plot of displacement and deformed configuration (scaling factor $= 1 \times 10^7$).

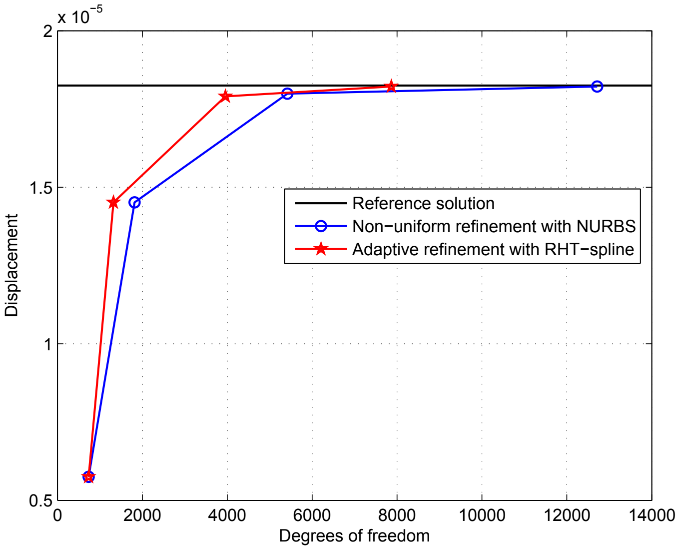

Figure 7.9: Convergence in displacement of pinched cylinder.

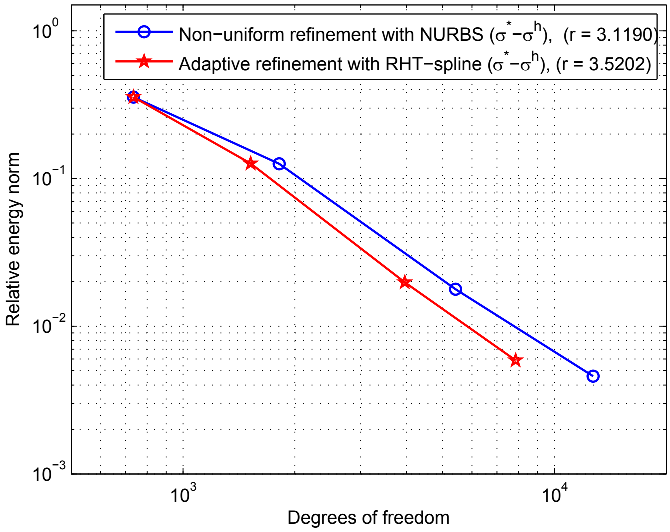

Figure 7.10: Relative in the energy norm error.

Table 7.1: Natural frequency of a cantilevered rectangular plate

Methods	Modes					
	1	2	3	4	5	6
Ref. solution(Nag99)	84.05	525.88	1469.99	1557.09	2874.13	4694.48
RHT-splines	84.326	527.642	1471.134	1574.465	2901.321	4732.816

7.4.2 Free vibration analysis

In this section, we examine the accuracy and efficiency of the RHT-splines for analyzing natural frequencies of plates. The plate may have simply (S) supported or clamped (C) edges.

7.4.2.1 Free vibration analysis of a cantilevered rectangular plate

The free vibration analysis is presented for a rectangular plate as shown in Fig. 7.15a. The parameters (NTRHXB10) are: length $L = 100mm$, height $D = 10mm$, thickness $t = 1.0mm$, Young's modulus $E = 2.1\times10^4 kgf/mm^4$, Poisson's ratio $\nu = 0.3$, and mass density $\rho = 8.0\times10^{-10} kgfs^2/mm^4$. The meshes are shown in Fig. 7.15b,c,d.

The first six shape modes of the free vibration of the plate are plotted in Fig. 7.16 and the results are listed in Tab. 7.1. The frequencies obtained from proposed method are close to the reference solution (Nag99).

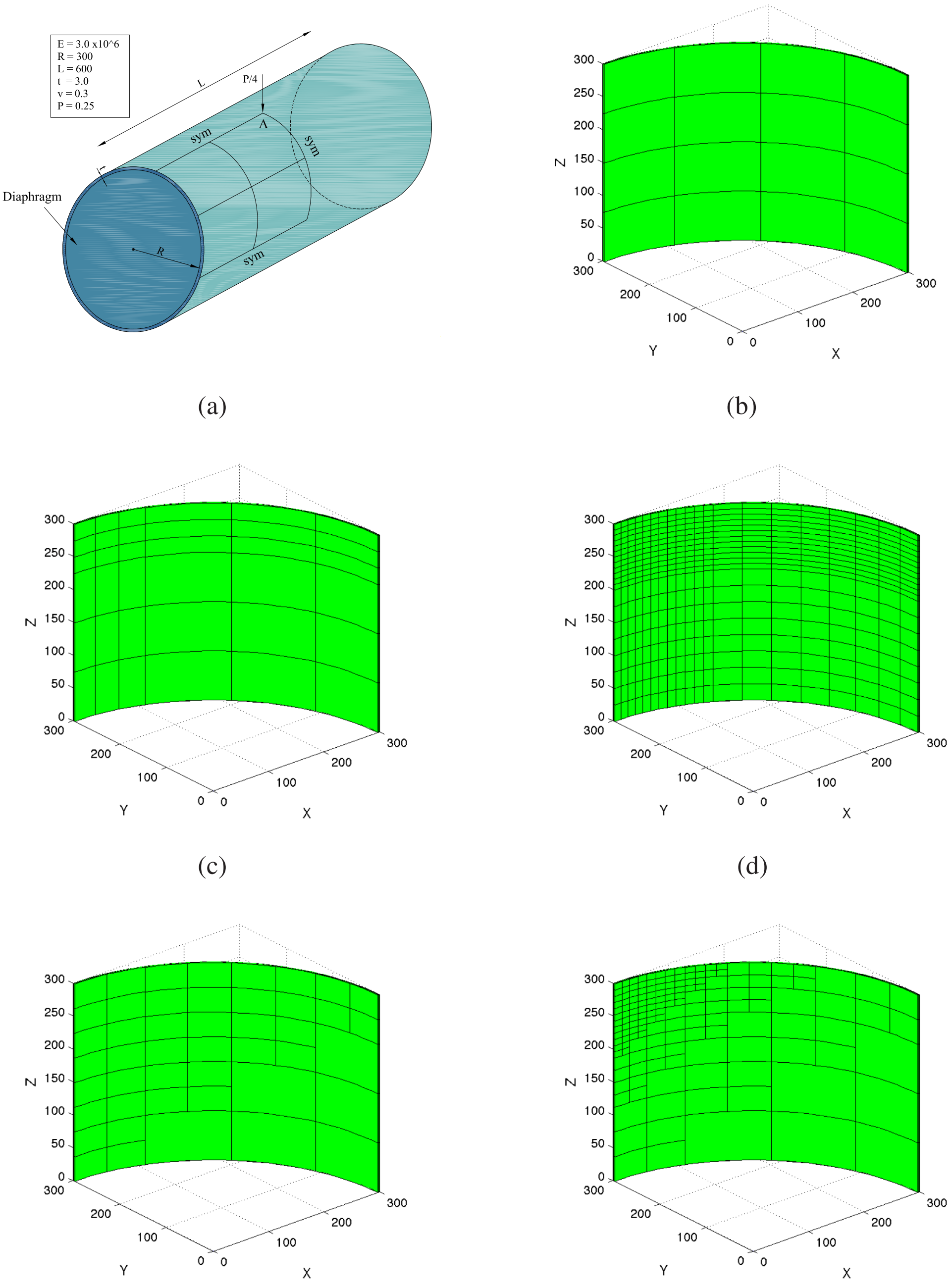

(a) (b)

(c) (d)

(e) (f)

Figure 7.11: (a) Pinched cylinder model. (b) A uniformly coarse mesh used for both NURBS and RHT-splines. (c),(d) Non uniform NURBS refinements. (e),(f) RHT-splines after 1 and 3 refinements.

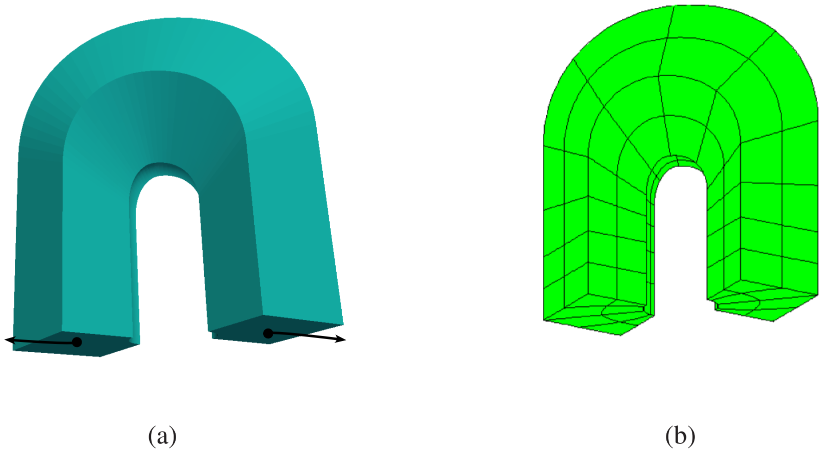
(a) (b)

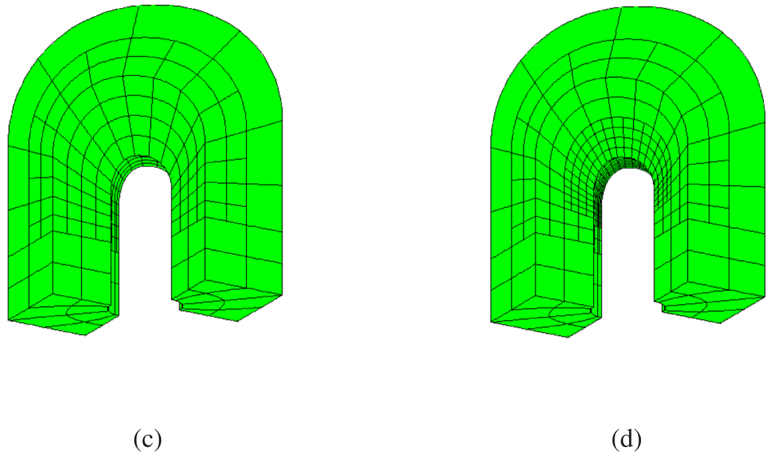
(c) (d)

Figure 7.12: (a) A horseshoe geometry. (b)(c)(d) The RHT-splines refinement steps at level $0, 1, 2$, respectively.

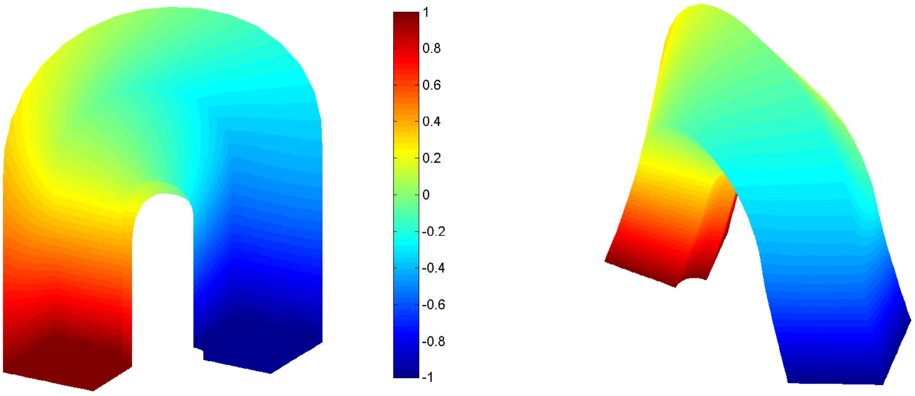

Figure 7.13: Contour plot of displacement and deformed configuration.

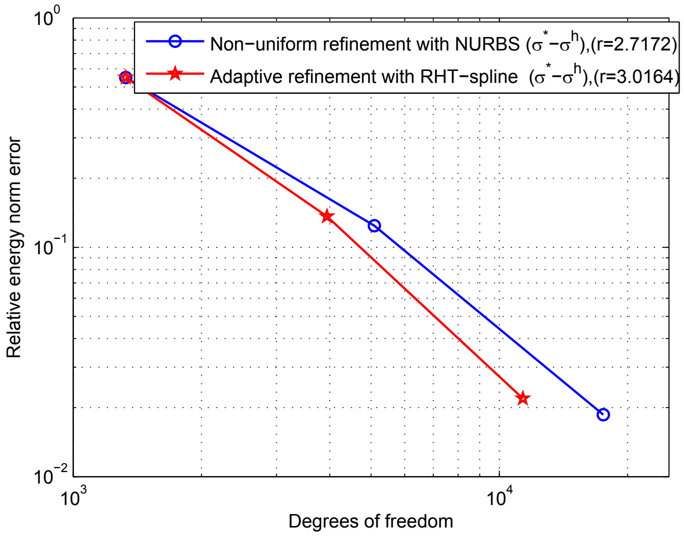

Figure 7.14: Relative in the energy norm error.

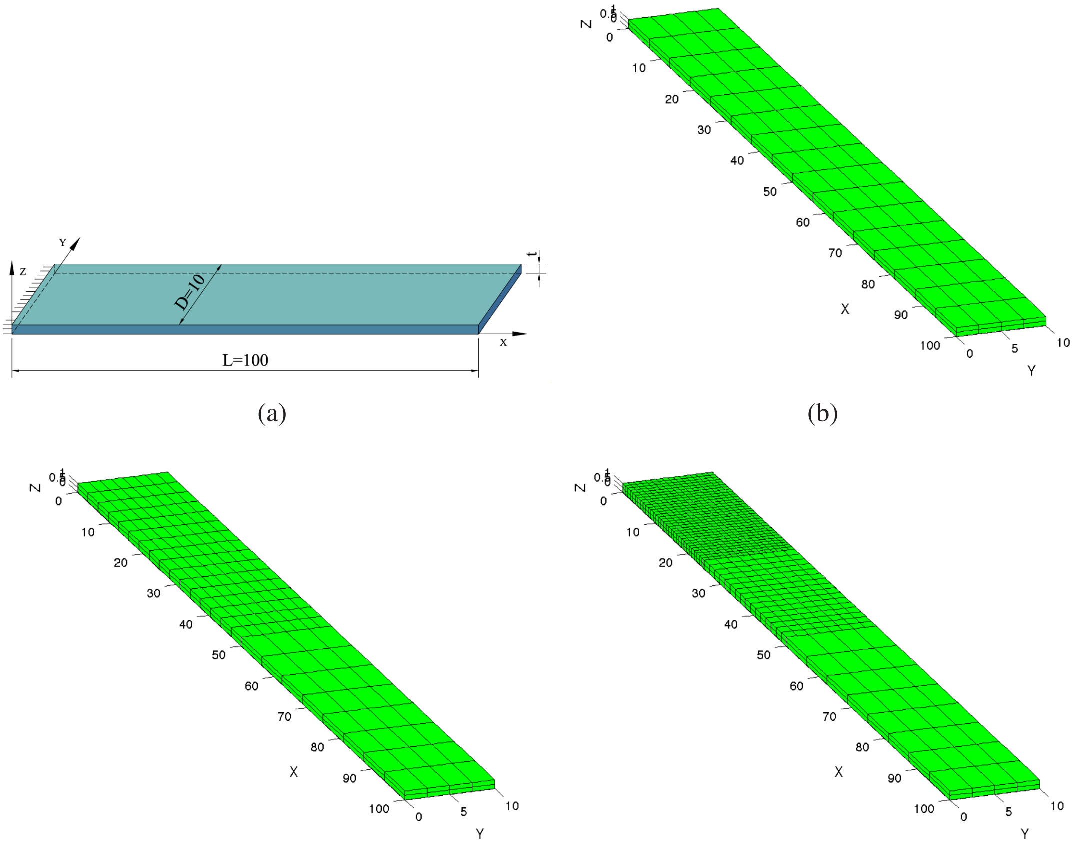

Figure 7.15: (a) A cantilevered rectangular plate model. (b),(c),(d) RHT-splines refinement mesh at level 0, level 1 and level 2.

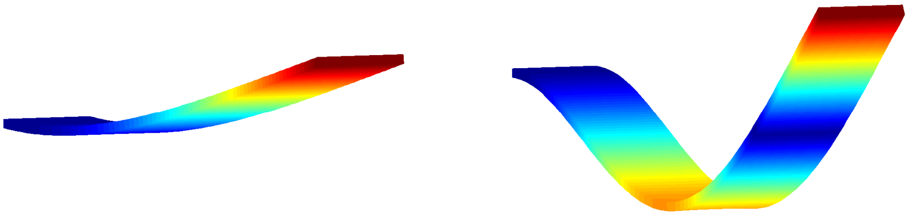

(a) Mode 1 (b) Mode 2

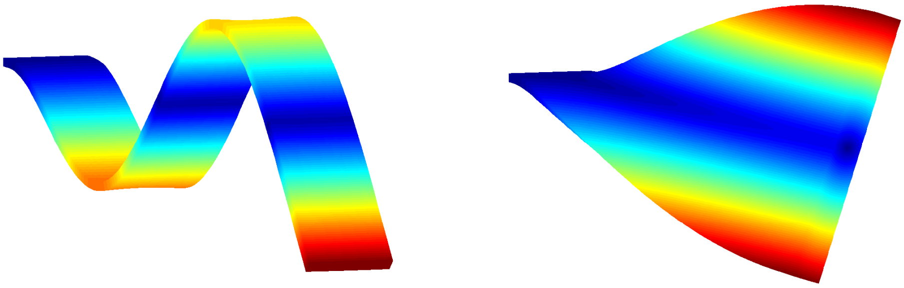

(c) Mode 3 (d) Mode 4

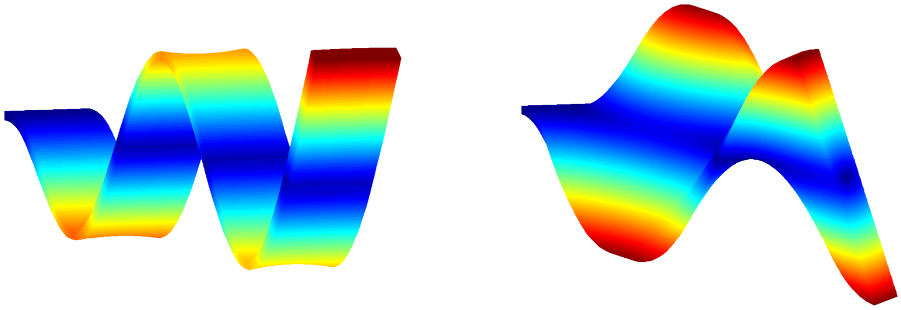

(e) Mode 5 (f) Mode 6

Figure 7.16: The first six shape modes of a cantilevered rectangular plate.

Table 7.2: A non-dimensional frequency parameter $\varpi = \left(\omega^2 \rho a^4 t/D\right)^{1/4}$ of SSSS plate (a/b=1)

t/b	Methods	Modes					
		1	2	3	4	5	6
0.1	Exact (ADK87)	4.37	6.74	6.74	8.35	9.22	9.22
	NURBS	4.3803	6.7885	6.7894	8.4736	9.3645	9.3687
	RHT-splines	4.3812	6.7912	6.7956	8.4961	9.3932	9.3973

7.4.2.2 Free vibration analysis of square plate

The next example is a square plate of length a, width b and thickness t as shown in Fig. 7.17. The parameters (NTRHXB11, TNXNT+12) are Young's modulus $E = 2.0 \times 10^{11}$, Poisson's ratio $\nu = 0.3$ and mass density $\rho = 8000$. A non-dimensional frequency parameter $\varpi = (\omega^2 \rho a^4 t/D)^{1/4}$ is used, where $D = Et^3/(12(1-\nu^2))$ is the flexural rigidity of the plate. Thin and thick plates corresponding to length-to-width ratios of $a/b = 1$ and thickness-to-length ratio of $t/a = 0.1$ are considered.

An initial mesh and the mesh after 2 refinement steps are shown in Fig. 7.18. The first six shape modes of the clamped plate using the RHT-splines are plotted in Fig. 7.19. The error in the first six frequencies are shown in Fig. 7.21 as well as in Tab. 7.2 and Tab. 7.3. The RHT-splines results are compared with the results of NURBS based on uniform and global refinement. It can be seen the convergence rate in the eigenfrequencies of RHT-splines is faster than NURBS.

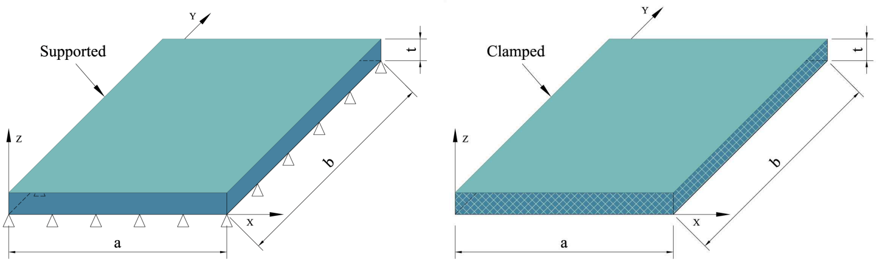

(a) (b)

Figure 7.17: (a) Square plates with four simply-supported edges (SSSS). (b) Square plates with four clamped edges (CCCC).

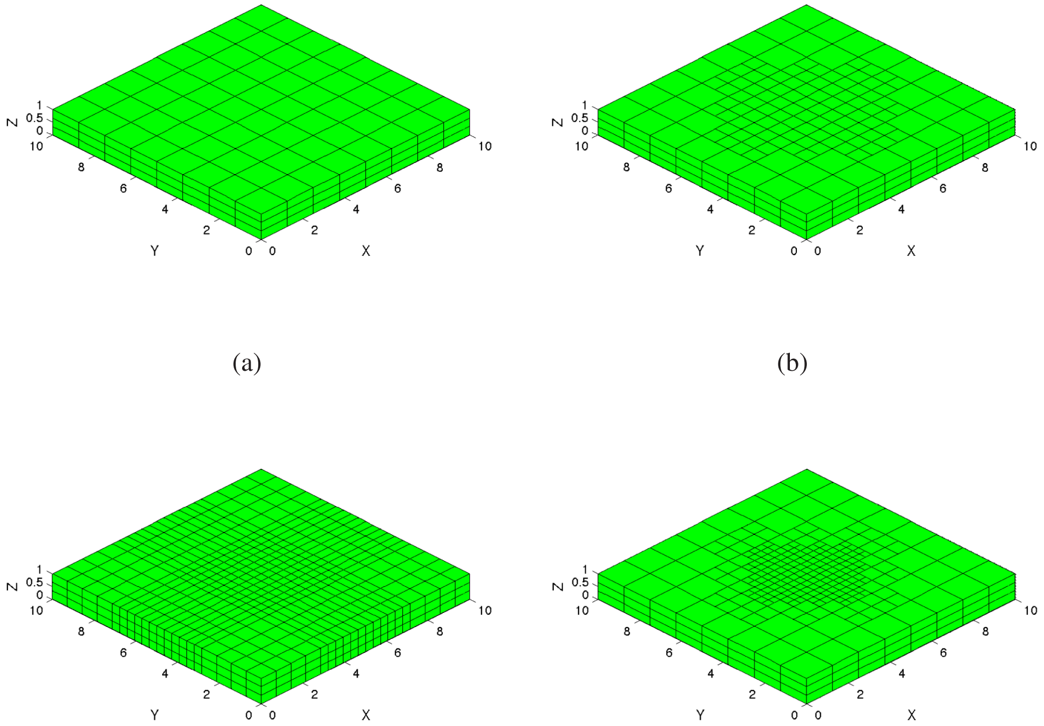

(a) (b)

(c) (d)

Figure 7.18: The meshes of square plate. (a) NURBS and RHT-splines coarse meshes. (b) RHT-splines after 1 refinement. (c) Non uniform NURBS refinement. (d) RHT-splines after 2 refinements.

Table 7.3: A non-dimensional frequency parameter $\varpi = \left(\omega^2 \rho a^4 t/D\right)^{1/4}$ of CCCC plate (a/b=1)

t/b	Methods	Modes					
		1	2	3	4	5	6
0.1	Exact (ADK87)	5.71	7.88	7.88	9.33	10.13	10.18
	NURBS	5.7232	7.9204	7.9227	9.4468	10.2623	10.3115
	RHT-splines	5.7263	7.9283	7.9297	9.4485	10.2958	10.3224

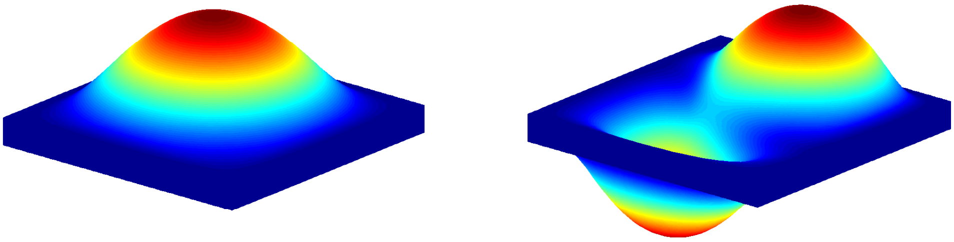

(a) Mode 1 (b) Mode 2

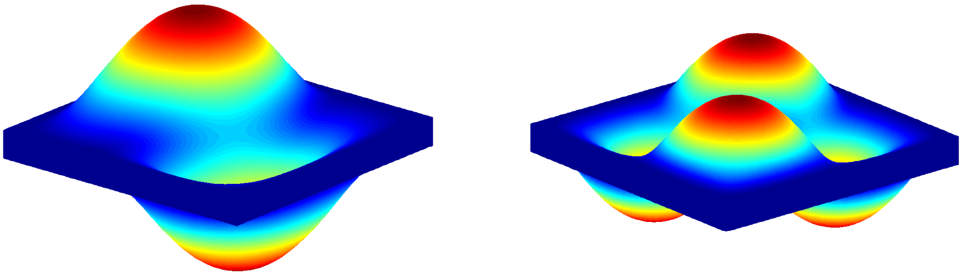

(c) Mode 3 (d) Mode 4

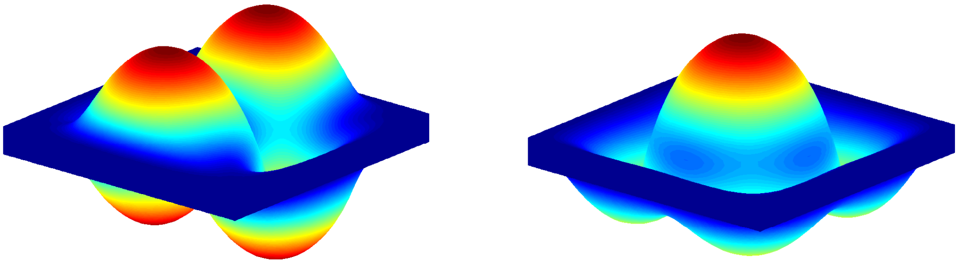

(e) Mode 5 (f) Mode 6

Figure 7.19: The first six shape modes of square with four clamped plate using the RHT-splines.

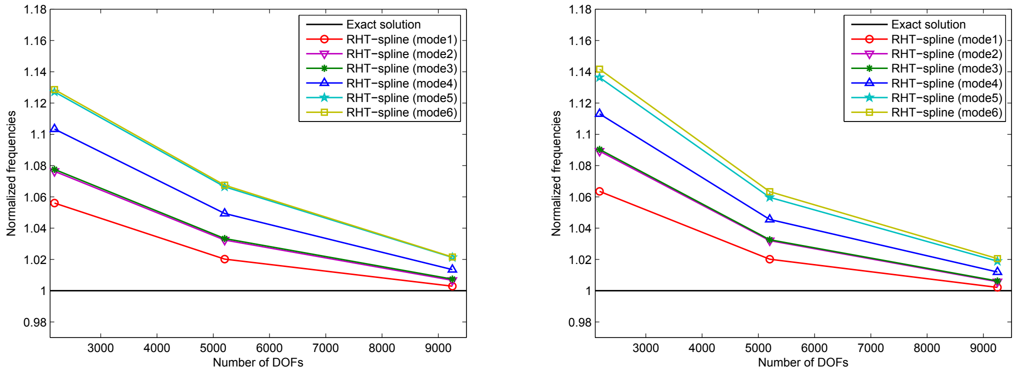

(a)

(b)

Figure 7.20: Convergence of normalized frequencies ϖ^h/ϖ_{exact}. (a) SSSS plate. (b) CCCC plate.

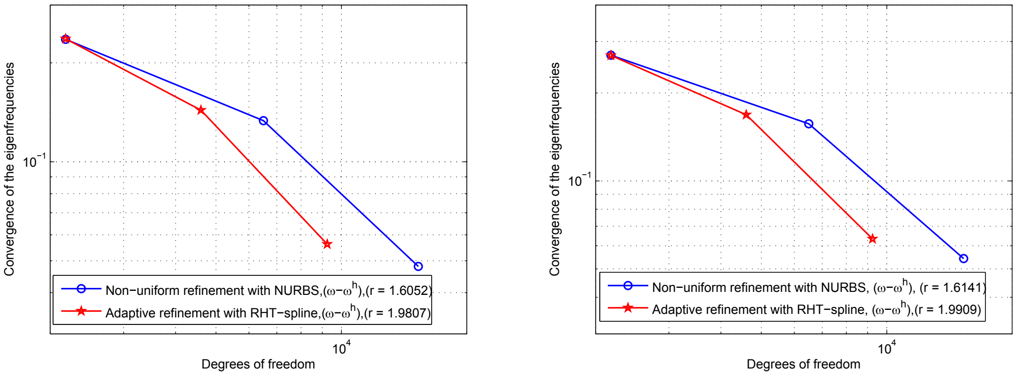

(a)

(b)

Figure 7.21: Convergence rates in the eigenfrequencies of mode 1. (a) SSSS plate. (b) CCCC plate.

7.5 Conclusion

We presented an isogeometric analysis based on RHT-splines for three-dimensional problems in elasto-statics and elasto-dynamics. The RHT-splines is a piecewise tricubic rational over 3D hierarchical T-meshes. The idea is based on rational splines and exploits the flexibility of T-meshes for local refinement. The shape functions satisfy important properties such as non-negativity, local support and partition of unity. The RHT-splines inherits all properties of B-spline, NURBS and allows for efficient local refinement. We also presented stress recovery approach in isogeometric analysis to drive the adaptive h-refinement procedure. Therefore, an imaginary solid is defined. This imaginary solid is constructed by the same the RHT-splines basis functions which are used for approximation of the displacement field. Numerical studied showed the high accuracy of the proposed method. A good agreement was achieved between the numerical and analytical results for both static and free vibration problems.

Chapter 8

Rotation free isogeometric thin shell analysis using RHT-splines

8.1 Introduction

The shell structures are used for wide range of application in engineering design, e.g. for car bodies in automotive industry, light weight component in aero space structures. Shell elements can also be classified according to the thickness of the shell and the curvature of the mid-surface (BBWR04). Depending on the thickness, shell elements can be categorized into thin plate/shell elements (WC08, KB96, BD83, COS00, MRA11, NR08, RGSB10) and thick plate/shell elements (WC04, CW06, UO10, NXRBD08b, NTRHXB10, NTRHXB11, NTRNXB08). Thin shell elements are based on the Kirchhoff-Love theory (TWK59) in which transverse shear deformations are negligible. The thin shell element also requires C^1 displacement continuity which is difficult to achieve for free-form geometries when using Lagrange polynomials as basis functions. Thick shell elements are based on Reissner-Mindlin theory which require only C^0 continuity for the deflection and rotation fields. Especially the development of thick shell elements suffers from one intrinsic difficulty locking, i.e. the presence of “artificial” stresses. It is well known that low-order finite elements are more prone to locking phenomena and that locking can often be alleviated by the use of higher order elements.

Using higher continuous formulations in the context of thin shell analysis based on Kirchhoff-Love theory avoids the use of rotational degrees of freedom or discretization of the director field. A formulation that just discretizes the mid-surface position and automatically fulfills the Kirchhoff-Love constraint by using a higher continuous formulation was first proposed in the context of meshfree methods by (RA06b, RAB07c). In the context of isogeometric analysis based on NURBS, such approaches have been presented by (DBH10, BBHH11, KBLW09, KBH$^+$10). Shell analysis based on T-splines were proposed by (UY09).

In this chapter, I exploit a novel basis based on the rational splines over hierarchical T-meshes for thin shell structures with single patch and multi-patches analysis. The key feature of the proposed method is its simplicity. It does not require the set-up of an additional mesh, nor additional nodes and local refinement can be readily implemented through the refinement of geometric models using RHT-splines. It employs Kirchhoff-Love theory in pristine form avoiding the need to introduce rotation DOFs due to the C^1 continuity of the RHT-splines.

8.2 Thin shell model

In this section, the basic equations of the thin shell theory is introduced. The transverse shear deformation is ignored and the shell director remains normal to the middle surface in the deformed configuration. Therefore, the description of the shell can be reduced to the description of its middle surface. The Greek indices $\alpha = 1,2$ refer to quantities curvilinear coordinate system.

8.2.1 Kinematics of the shell

The deformation of a thin shell can be fully described by the deformation of its mid-surface, which is a two-dimensional surface embedded in the dimensional. The mapping of shell middle surface is parameterized using coordinates $\xi, \eta \in \mathscr{A} \subset \mathbb{R}^2$. The position vector of a material point in the reference geometry is given by

$$\mathbf{x}_0(\xi,\eta,\zeta) = \varphi_0(\xi,\eta) + \zeta \mathbf{t}_0(\xi,\eta) \tag{8.1}$$

and similar for the deformed geometry

$$\mathbf{x}(\xi,\eta,\zeta) = \varphi(\xi,\eta) + \zeta \mathbf{t}(\xi,\eta) \tag{8.2}$$

where $\zeta \in [-0.5h, 0.5h]$ is the through-thickness coordinate with h is the shell thickness and $\mathbf{t}$ is the shell normal. The functions $\varphi_0(\xi,\eta)$ and $\varphi(\xi,\eta)$ provide a parametric representation of the middle surface of the shell in the reference and deformed configurations, respectively. The area element of the middle surface is computed as $d\Omega_0 = \bar{j}_0 d\xi d\eta$ where $\bar{j}_0 = ||\varphi^0_{,1} \times \varphi^0_{,2}||$. The notation ξ, η and ζ for the local coordinates are abbreviated for the purpose of index notation and summation convention into $\xi^\alpha(\xi^1 = \xi, \xi^2 = \eta)$ and $\xi^3 = \zeta$ (see Fig. 8.1). The Kirchhoff-Love hypothesis is imposed by requiring that $\mathbf{t}_0, \mathbf{t}$ are perpendicular to $\varphi^0_\alpha, \varphi_\alpha$

$$\mathbf{t}_0 = \frac{\varphi^0_{,1} \times \varphi^0_{,2}}{\left\| \varphi^0_{,1} \times \varphi^0_{,2} \right\|} \quad ; \quad \mathbf{t} = \frac{\varphi_{,1} \times \varphi_{,2}}{\left\| \varphi_{,1} \times \varphi_{,2} \right\|} \tag{8.3}$$

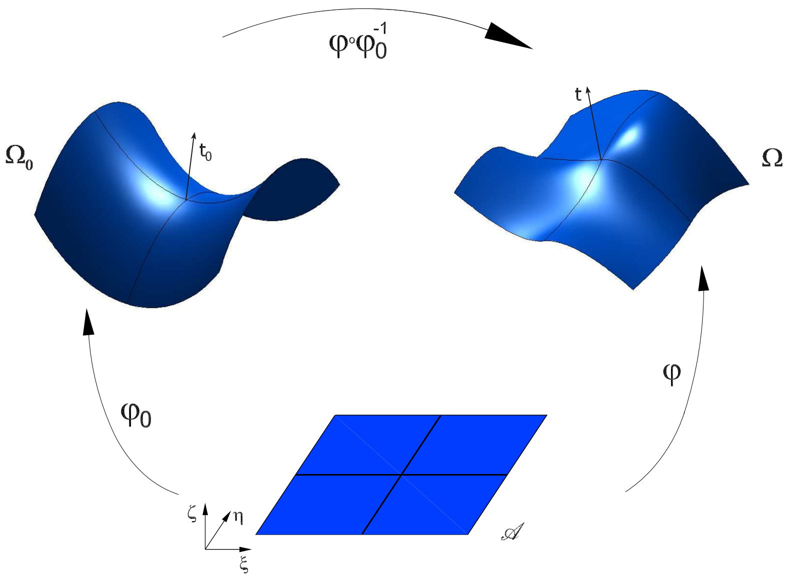

Figure 8.1: Shell geometry in the reference and the deformed configurations.

$$\varphi^0_{,\alpha} \cdot \mathbf{t}_0 = 0 \quad ; \quad |\mathbf{t}_0| = 1 \quad ; \quad \mathbf{t}_0 \cdot \mathbf{t}_{0,\alpha} = 0 \, . \tag{8.4}$$

The deformation gradient is given by

$$\mathbf{F} = \nabla \mathbf{x} \cdot (\nabla \mathbf{x}_0)^{-1} \tag{8.5}$$

with the tangent map

$$\nabla \mathbf{x} = \begin{bmatrix} \frac{\partial x_1}{\partial \xi_1} & \frac{\partial x_1}{\partial \xi_2} & \frac{\partial x_1}{\partial \xi_3} \\ \frac{\partial x_2}{\partial \xi_1} & \frac{\partial x_2}{\partial \xi_2} & \frac{\partial x_2}{\partial \xi_3} \\ \frac{\partial x_3}{\partial \xi_1} & \frac{\partial x_3}{\partial \xi_2} & \frac{\partial x_3}{\partial \xi_3} \end{bmatrix} . \tag{8.6}$$

We also define the covariant base vectors as

$$\begin{aligned} \mathbf{g}_\alpha &= \frac{\partial \mathbf{x}}{\partial \xi^\alpha} = \varphi_{,\alpha} + \xi^3 \mathbf{t}_\alpha \quad ; \quad \mathbf{g}_3 = \frac{\partial \mathbf{x}}{\partial \xi^3} = \mathbf{t} \\ \mathbf{g}^0_\alpha &= \frac{\partial \mathbf{x}_0}{\partial \xi^\alpha} = \varphi^0_{,\alpha} + \xi^3 \mathbf{t}^0_\alpha \quad ; \quad \mathbf{g}^0_3 = \frac{\partial \mathbf{x}_0}{\partial \xi^3} = \mathbf{t}_0 \, . \end{aligned} \tag{8.7}$$

The Green-Lagrange strain tensor is given by

$$\mathbf{E} = \frac{1}{2} \left(\mathbf{F}^T \mathbf{F} - \mathbf{I} \right) \tag{8.8}$$

where **F** is the deformation gradient and **I** is the identity tensor. The strain is decomposed into a constant part due to membrane action and a linear part due to bending. The covariant strain coefficients is given by:

$$E_{\alpha\beta} = \varepsilon_{\alpha\beta} + \xi^3 \kappa_{\alpha\beta} = \frac{1}{2}\left(g_{\alpha\beta} - g^0_{\alpha\beta}\right) + \xi^3 \left(k_{\alpha\beta} - k^0_{\alpha\beta}\right) \tag{8.9}$$

In Eq. (8.9), the covariant metric tensor and the curvature tensors of the surface are given by

$$g_{\alpha\beta} = \mathbf{g}_{,\alpha} \cdot \mathbf{g}_{,\beta} = \mathbf{x}_{,\alpha} \cdot \mathbf{x}_{,\beta} \quad ; \quad g^0_{\alpha\beta} = \mathbf{g}^0_{,\alpha} \cdot \mathbf{g}^0_{,\beta} = \mathbf{x}^0_{,\alpha} \cdot \mathbf{x}^0_{,\beta} \tag{8.10}$$

$$k_{\alpha\beta} = -\mathbf{g}_{\alpha,\beta} \cdot \mathbf{t} \quad ; \quad k^0_{\alpha\beta} = -\mathbf{g}^0_{\alpha,\beta} \cdot \mathbf{t}^0 \, . \tag{8.11}$$

8.2.2 Equilibrium deformations of thin shells

The principle of virtual work is expressed as

$$\delta\Pi = \delta\Pi_{\text{int}} + \delta\Pi_{ext} = 0 \, . \tag{8.12}$$

The internal virtual work, which can be presented in terms of integrals over the parametric space $\mathscr{A}$ are as follows:

$$\delta\Pi_{\text{int}} = -\int_{\Omega_0} (\sigma \cdot \delta\mathbf{E})\, \mathrm{d}\Omega_0 = -\int_{\mathscr{A}} (\mathbf{n} \cdot \delta\varepsilon + \mathbf{m} \cdot \delta\kappa)\, \bar{j}_0 \mathrm{d}\xi^1 \mathrm{d}\xi^2 \tag{8.13}$$

The stress tensor can be written in Voigt notation as

$$\sigma = \begin{bmatrix} \sigma_{11} \\ \sigma_{22} \\ \sigma_{12} \end{bmatrix} = \frac{E}{1-\nu^2} \begin{bmatrix} 1 & \nu & 0 \\ \nu & 1 & 0 \\ 0 & 0 & (1-\nu)/2 \end{bmatrix} \begin{bmatrix} E_{11} \\ E_{22} \\ 2E_{12} \end{bmatrix} \tag{8.14}$$

where $\sigma_{\alpha\beta}$ and $E_{\alpha\beta}$ are the strains; E is the Young's modulus and ν the Poisson's ratio Separating the stresses into a membrane and a bending stress and integrating through the thickness h, which can be interpreted as force and moment resultants.

$$\mathbf{n} = \begin{bmatrix} n_{11} \\ n_{22} \\ n_{12} \end{bmatrix} = \frac{Eh}{1-\nu^2} \begin{bmatrix} 1 & \nu & 0 \\ \nu & 1 & 0 \\ 0 & 0 & (1-\nu)/2 \end{bmatrix} \begin{bmatrix} \varepsilon_{11} \\ \varepsilon_{22} \\ 2\varepsilon_{12} \end{bmatrix} \tag{8.15}$$

$$\mathbf{m} = \begin{bmatrix} m_{11} \\ m_{22} \\ m_{12} \end{bmatrix} = \frac{Eh^3}{12(1-\nu^2)} \begin{bmatrix} 1 & \nu & 0 \\ \nu & 1 & 0 \\ 0 & 0 & (1-\nu)/2 \end{bmatrix} \begin{bmatrix} \kappa_{11} \\ \kappa_{22} \\ 2\kappa_{12} \end{bmatrix} \tag{8.16}$$

For thin shell theory, the three-dimensional continuum description is reduced to that of the shell mid-surface, and the transverse normal stress is neglected. Furthermore, the Kirchhoff-Love theory is assumed that the shell cross-sections remain normal to its mid-surface in the deformed configuration, which implies that the strain is assumed to be linear through the thickness and the transverse shear strains are zero. The internal energy density can be integrated through-the-thickness, resulting in an internal energy density per unit area.

8.2.3 Galerkin discretization

The undeformed shell surface is defined in terms of basis functions

$$\varphi_0(\xi^1,\xi^2) = \sum_{i=1}^{n} R_i\left(\xi^1,\xi^2\right)\mathbf{P}^i\,. \tag{8.17}$$

The displacement field $\mathbf{u}$ is discretized as

$$\mathbf{u}(\xi^1,\xi^2) = \sum_{i=1}^{n} R_i(\xi^1,\xi^2)\mathbf{u}^i\,. \tag{8.18}$$

The membrane strain and the bending strain in Voigt notation can then be computed as

$$\varepsilon(\xi^1,\xi^2) = \sum_{i=1}^{n}\mathbf{B}_n^i(\xi^1,\xi^2)\mathbf{u}^i \quad ; \quad \kappa(\xi^1,\xi^2) = \sum_{i=1}^{n}\mathbf{B}_m^i(\xi^1,\xi^2)\mathbf{u}^i\,. \tag{8.19}$$

The membrane and bending strain matrices take the form

$$\mathbf{B}_n^i = \begin{bmatrix} b^i_{,1}\varphi^0_{,1}\cdot\mathbf{e}_1 & b^i_{,1}\varphi^0_{,1}\cdot\mathbf{e}_2 & b^i_{,1}\varphi^0_{,1}\cdot\mathbf{e}_3 \\ b^i_{,2}\varphi^0_{,2}\cdot\mathbf{e}_1 & b^i_{,2}\varphi^0_{,2}\cdot\mathbf{e}_1 & b^i_{,2}\varphi^0_{,2}\cdot\mathbf{e}_3 \\ (b^i_{,2}\varphi^0_{,1}+b^i_{,1}\varphi_{,2}{}^0)\cdot\mathbf{e}_1 & (b^i_{,2}\varphi^0_{,1}+b^i_{,1}\varphi^0_{,2})\cdot\mathbf{e}_2 & (b^i_{,2}\varphi^0_{,1}+b^i_{,1}\varphi^0_{,2})\cdot\mathbf{e}_3 \end{bmatrix} \tag{8.20}$$

$$\mathbf{B}_m^i = \begin{bmatrix} \mathbf{B}^i_{m11}\cdot\mathbf{e}_1 & \mathbf{B}^i_{m11}\cdot\mathbf{e}_2 & \mathbf{B}^i_{m11}\cdot\mathbf{e}_3 \\ \mathbf{B}^i_{m22}\cdot\mathbf{e}_1 & \mathbf{B}^i_{m22}\cdot\mathbf{e}_2 & \mathbf{B}^i_{m22}\cdot\mathbf{e}_3 \\ 2\mathbf{B}^i_{m12}\cdot\mathbf{e}_1 & 2\mathbf{B}^i_{m12}\cdot\mathbf{e}_2 & 2\mathbf{B}^i_{m12}\cdot\mathbf{e}_3 \end{bmatrix} \tag{8.21}$$

in which

$$\begin{aligned} \mathbf{B}^i_{m\alpha\beta} &= \varphi^0_{,\alpha\beta}\cdot\mathbf{t}_0\frac{1}{\bar{j}_0}\left[b^i_{,1}\left(\varphi^0_{,2}\times\mathbf{t}_0\right)-b^i_{,2}\left(\varphi^0_{,1}\times\mathbf{t}_0\right)\right] \\ &\quad+\frac{1}{\bar{j}_0}\left[b^i_{,1}\left(\varphi^0_{,\alpha\beta}\times\varphi^0_{,2}\right)-b^i_{,2}\left(\varphi^0_{,\alpha\beta}\times\varphi^0_{,1}\right)\right]-b^i_{,\alpha\beta}\cdot\mathbf{t}_0 \end{aligned} \tag{8.22}$$

and where $(\mathbf{e}_1,\mathbf{e}_2,\mathbf{e}_3)$ are the basis vectors of an orthonormal coordinate system. Combining simultaneously membrane and bending actions, we write a linear system for the vector of nodal unknowns $\mathbf{u}$

$$\mathbf{K}\mathbf{u} = \mathbf{f}\,. \tag{8.23}$$

The assembly of an element membrane and bending stiffness into the global stiffness matrix **K** can finally be written as

$$\mathbf{K}^{ij} = \int_{\mathscr{A}} \left(h \left(\mathbf{B}_n^i\right)^T \mathbf{D}\mathbf{B}_n^j + \frac{h^3}{12} \left(\mathbf{B}_m^i\right)^T \mathbf{D}\mathbf{B}_m^j \right) \bar{j}_0 \mathrm{d}\xi^1 \mathrm{d}\xi^2 \tag{8.24}$$

The force contribution of the i^{th} node is

$$\mathbf{f}_i = \int_{\mathscr{A}} \mathbf{q} b_i \bar{j}_0 \mathrm{d}\xi^1 \mathrm{d}\xi^2 + \int_{\partial\mathscr{A}} \mathbf{p} b_i \|\varphi^0_{,t}\| \mathrm{d}l_\xi \tag{8.25}$$

where **q** is the body force per unit area and **p** are the forces per unit length on the boundary of the middle surface.
During the element assembly, Eq. (8.24) is computed for all pairs of element basis functions i, j for all elements and added to the global stiffness matrix **K** as described above.

8.3 RHT-splines with multi-patches

8.3.1 Continuity conditions for RHT-splines surface

Consider the two bi-cubic polynomials, $W_1(x,y)$ and $W_2(x,y)$, defined by over two adjacent domains $[x_0,x_1] \times [y_0,y_1]$ and $[x_1,x_2] \times [y_0,y_1]$, respectively. They are presented in the Bézier form with Bézier ordinates $b^1_{i,k}$ and $b^2_{i,k}$, respectively and form C^1-continuity through their common boundary following:

$$\frac{b^1_{3,i} - b^1_{2,i}}{x_1 - x_0} = \frac{b^2_{1,i} - b^2_{0,i}}{x_2 - x_1} \qquad (i = 0,..,3)\ . \tag{8.26}$$

In order to achieve the two bi-cubic polynomials with C^1 continuity, we introduce the following addition:

$$\frac{\partial}{\partial x} W_1 = p(y) \frac{\partial}{\partial x} W_2 + q(y) \frac{\partial}{\partial y} W_1 \qquad (y \in [y_0,y_1]) \tag{8.27}$$

for $x = x_1$ and some functions $p(y)$ and $q(y)$, and the connecting functions are $p(x)$ and $q(x)$ (with $p(x) > 0$).
From Eq. (8.27), we can choose the functions p, q are $p(x) = 1$ and $q(x) = \alpha x + \beta(1 - x)$, a linear function of x. The following are stilcient conditions for **S** to be C^1.

$$\begin{aligned}
p_{0,1} - q_{0,0} &= q_{0,0} - r_{0,1} + \alpha(q_{0,0} - q_{1,0}) \\
p_{1,1} - q_{1,0} &= q_{1,0} - r_{1,1} + \tfrac{2}{3}\alpha(q_{1,0} - q_{2,0}) + \tfrac{1}{3}\beta(q_{0,0} - q_{1,0}) \\
p_{2,1} - q_{2,0} &= q_{2,0} - r_{2,1} + \tfrac{1}{3}\alpha(q_{2,0} - q_{3,0}) + \tfrac{2}{3}\beta(q_{1,0} - q_{2,0}) \\
p_{3,1} - q_{3,0} &= q_{3,0} - r_{3,1} + \beta(q_{2,0} - q_{3,0})
\end{aligned} \tag{8.28}$$

where α, β are constants. In order to generate a piecewise bicubic surface that is C^1, we set $p(x) = 1$ and $q(x) = \alpha(1-x)^2$, this would automatically force $q(x,0)$ to be quadratic, then the conditions are:

$$\begin{aligned}
&p_{0,1} - q_{0,0} = q_{0,0} - r_{0,1} + \alpha(q_{0,0} - q_{1,0}) \\
&p_{1,1} - q_{1,0} = q_{1,0} - r_{1,1} + \tfrac{2}{3}\alpha(q_{1,0} - q_{2,0}) - \tfrac{1}{3}\alpha(q_{0,0} - q_{1,0}) \\
&p_{1,1} - q_{1,0} = q_{1,0} - r_{1,1} + \tfrac{1}{3}\alpha(q_{2,0} - q_{3,0}) \\
&p_{2,1} - q_{2,0} = q_{2,0} - r_{2,1} \\
&p_{3,1} - q_{3,0} = q_{3,0} - r_{3,1}\ .
\end{aligned} \tag{8.29}$$

Next, we consider two vertices A, B on the boundary lines of two RHT-splines surfaces $\mathbf{S}^1(\xi,\eta)$ and $\mathbf{S}^2(\xi,\eta)$ over the T-meshes $\mathscr{T}_1$ and $\mathscr{T}_2$ as shown in Fig. 8.2. In case of point B which is not a basis vertex, the geometry information is formed by its neighbor basis vertex in $\mathscr{T}_2$. The knot line segments are inserted in $\mathscr{T}_1$ and $\mathscr{T}_2$ when they are through the boundary basis vertices of two meshes. The C^1-continuity conditions through the common boundary are given as :

$$\mathbf{S}^1_{\xi}(A) = \mathbf{S}^2_{\eta}(B) \quad ; \quad \mathbf{S}^1_{\xi\eta}(A) = -\mathbf{S}^2_{\xi\eta}(B) \tag{8.30}$$

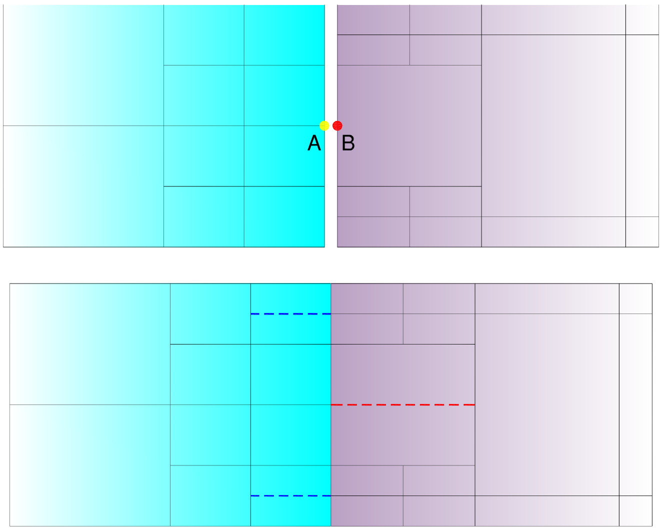

Figure 8.2: Continuity condition for surface over T-mesh

8.3.2 Connecting surface multi-patches

These are the main steps of connecting surface multi-patches algorithm:

- Step 1: Determining the common parameter domains The common parameter boundary domains of two patches are extracted at this step. As an example shown in Fig. 8.3, two curve segments (AB and CD) were determined on each boundary. Then, they will be mapped back to the parameter domains.

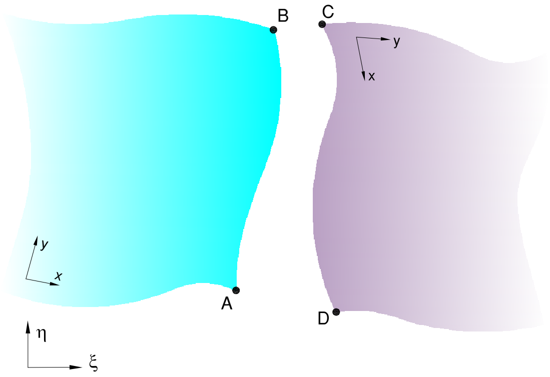

Figure 8.3: Common boundary

- Step 2: Reparameterization of surfaces The reparameterization of two surfaces along with the common boundary curve are presented on this step. The geometry information at the surface $\mathbf{S}^2$ is f, f_x, f_y, f_{xy}. Then it will be transformed into $h, h_\xi, h_\eta, h_{\xi\eta}$ (see in Fig. 8.3) such that

  $$h = f \;\;;\;\; h_\xi = f_x \;\;;\;\; h_\eta = -f_y \;\;;\;\; h_{\xi\eta} = -f_{xy}$$

  Describe the linear reparameterization form $f(x) = ax + b$ along the common boundary that has the similar coincident parameter (for example: the parameter at point A, D and B, C have the same knot values).

- Step 3: Combining the boundary information Insert some knot segments into T-mesh. The geometric information at these basis vertices is evaluated by the average of the geometric information at two basis vertices on the common boundary. The new geometric information at A and B should be f, f_x, f_y, f_{xy} and $f, -f_x, f_y, -f_{xy}$, respectively.

  $$f = \frac{f_1+f_2}{2} \;\;;\;\; f_\xi = \frac{f_x^1+f_y^2}{2} \;\;;\;\; f_\eta = \frac{f_x^1-f_y^2}{2} \;\;;\;\; f_{\xi\eta} = \frac{f_{xy}^1-f_{xy}^2}{2}$$

- Step 4: Interpolation of the geometry information

8.4 Numerical results

In this section, we show the performance of the proposed method through three benchmark problems coming from the so-called shell obstacle course (BSL+85): the Scordelis-Lo roof, the hemispherical shell and the pinched cylinder with diaphragms. These problems were often used to asses the elements' robustness and accuracy under complex strain states. The present results are compared with those of the original cubic NURBS approach. At level 0, both NURBS and RHT-splines share a uniformly coarse mesh for the initial step. At each refinement step, NURBS still handles a uniform mesh based on tensor-product form while RHT-splines uses a hierarchical T-mesh framework. For the convergence in strain energy, we use the relative error in strain energy $(E-E_h)/E$ versus the number of DOFs, where E_h is the strain energy calculated using by NURBS and RHT-splines and E is the "exact" strain energy calculated using a fine mesh of higher order NURBS approximation (p=9).

8.4.1 Single patch analysis

8.4.1.1 Scordelis - Lo roof

Consider a cylindrical concrete shell roof with self-weight $(g = 90/area)$ where two curved edges are supported by rigid diaphragms and the other two edges are free see Fig. 8.4.In our calculations, the given data is assumed as follows: the length of the cylinder $L = 50$; its radius $R = 25$; the thickness $h = 0.25$; the Young's modulus $E = 4.32 \times 10^8$; and the Poisson's ratio $\nu = 0.0$. The reference value for the mid-side vertical displacement is 0.3024 (BSL+85, MH85).

For the parameters above a maximal value of the vertical displacement at the mid-point of the side edge using the PHT approach is approximate $u = 0.3006$, that is lower than the reference value $u_{ref} = 0.3024$ given in (BSL+85) about 0.6%. The reason for the different results is the different treatment of shear deformations in the respective formulations: In the reference solution, it was taken a shear-deformable theory while the present method is based on Kirchhoff-Love theory which neglects transverse shear deformations. The results displacement convergence of the methods are shown in Fig. 8.5. It is observed that the RHT-splines exhibits the higher accuracy than the NURBS-based approach when the same order approximation used. Strain energy and energy error norm of the methods are computed for various grid densities and shown in Fig. 8.6,Fig. 8.7, respectively. Contour plot of the vertical displacement and deformed configuration are displayed in Fig. 8.8 and the force and moment resultants are presented in Fig. 8.9.

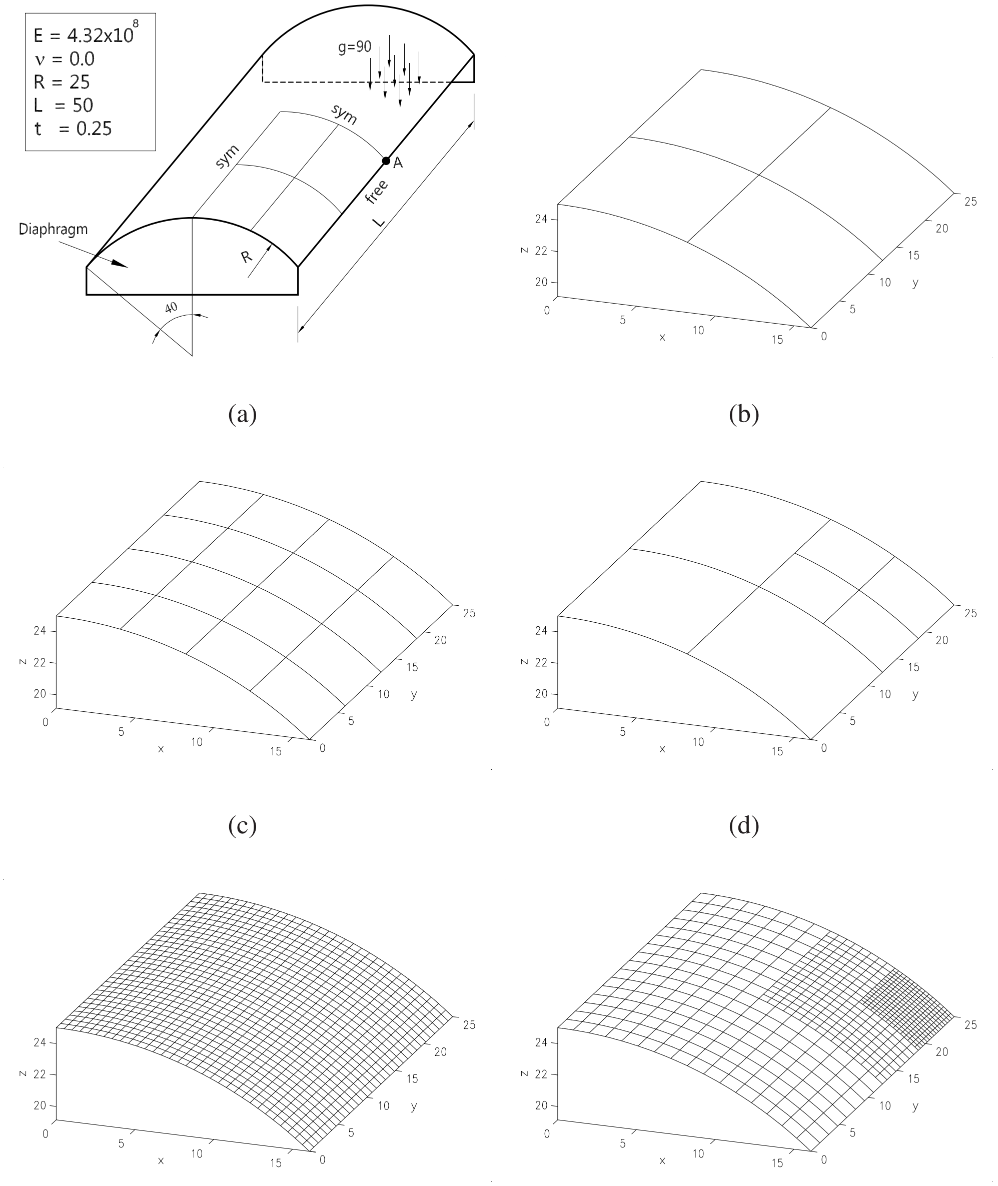

(a) (b)

(c) (d)

(e) (f)

Figure 8.4: The Scordelis-Lo roof and meshes: a) The Scordelis-Lo roof; b) A uniformly coarse mesh used for both NURBS and RHT-splines at level 0; Slightly finer meshes: c) NURBS and d) RHT-splines; Fine meshes: e) NURBS and f) RHT-splines.

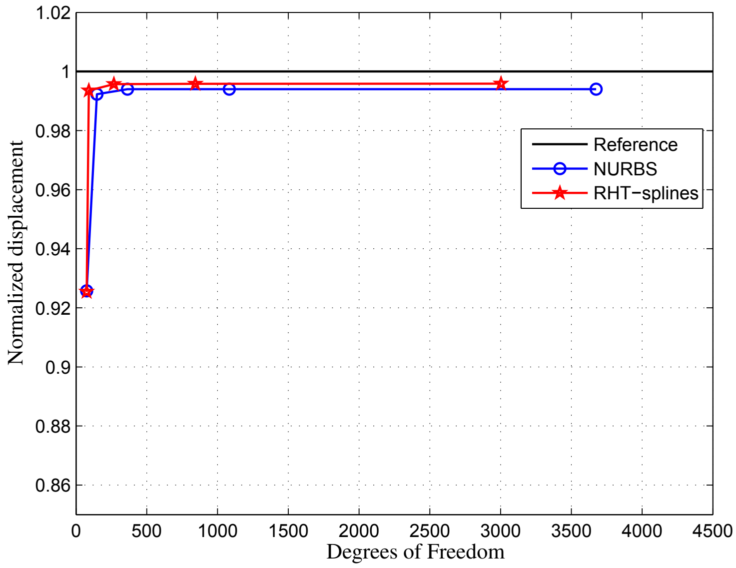

Figure 8.5: Convergence in displacement of the Scordelis–Lo roof.

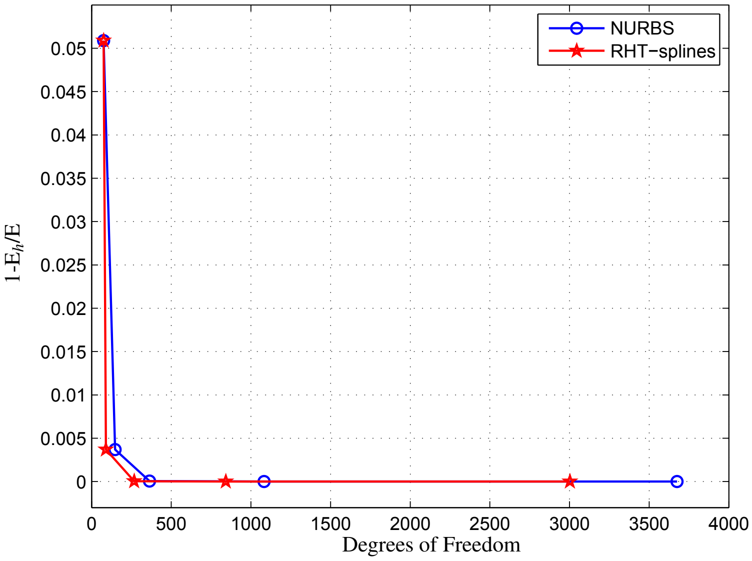

Figure 8.6: Convergence of strain energy of the Scordelis-Lo roof.

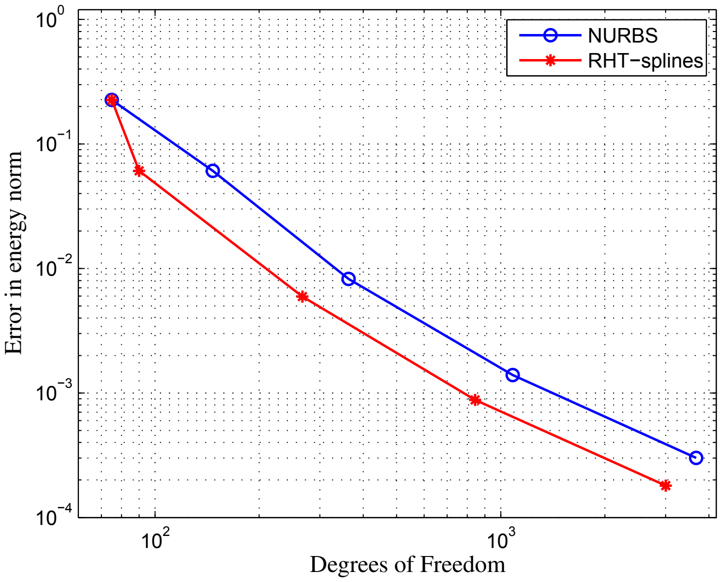

Figure 8.7: Error in energy norm of the Scordelis-Lo roof.

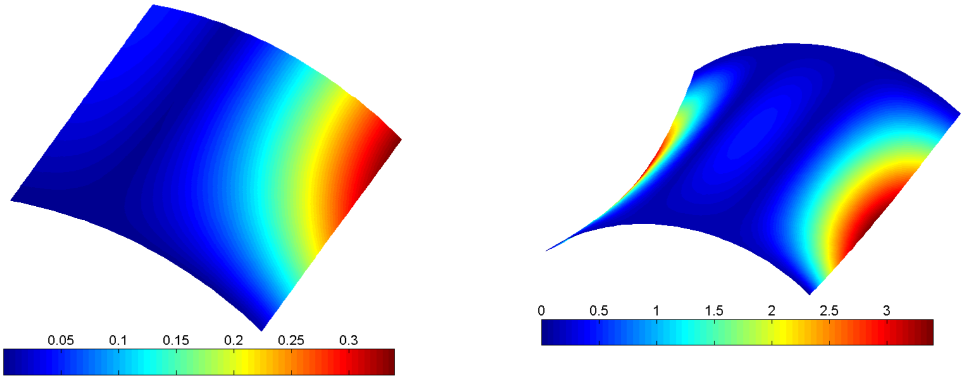

Figure 8.8: Contour plots of the vertical displacement at A point and deformed configuration (scaling factor = 10) of the Scordelis-Lo roof.

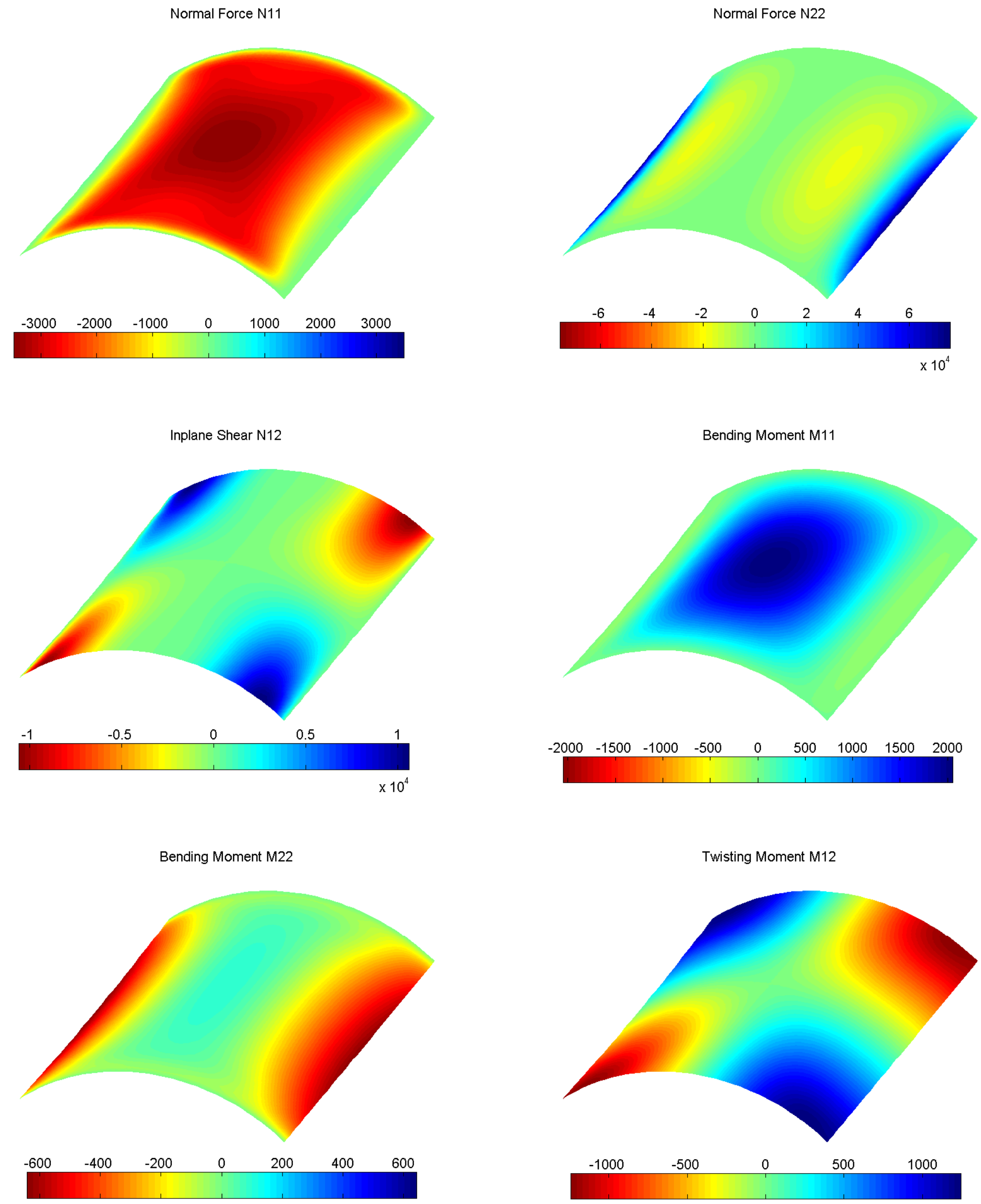

Figure 8.9: Contour plot of the force and moment resultants of the Scordelis-Lo roof.

8.4.1.2 Pinched cylinder with diaphragm

A cylindrical shell with rigid end diaphragm is subjected to a point load at the center of the cylindrical surface. The related parameters are taken as: length of the cylinder $L = 600$; radius $R = 300$; thickness $t = 3$; Young's modulus $E = 3 \times 10^6$; and Poisson's ratio $\nu = 0.3$. Due to its symmetry, only one octant of the cylinder as shown in Fig. 8.11 is modeled for the computation. The expected deflection under a concentrated load is 1.8248×10^{-5} (BSL+85).

Convergence of the normalized radial displacement at the loading point is depicted in Fig. 8.10. Convergence of strain energy versus the number of degrees of freedom is shown in Fig. 8.23. The error in the energy norm for different mesh refinements is depicted in Fig. 8.13. The RHT-splines is clearly superior to the NURBS approach. Fig. 8.21 illustrates contour plots of displacements for the an eighth and the full model of the cylinder.

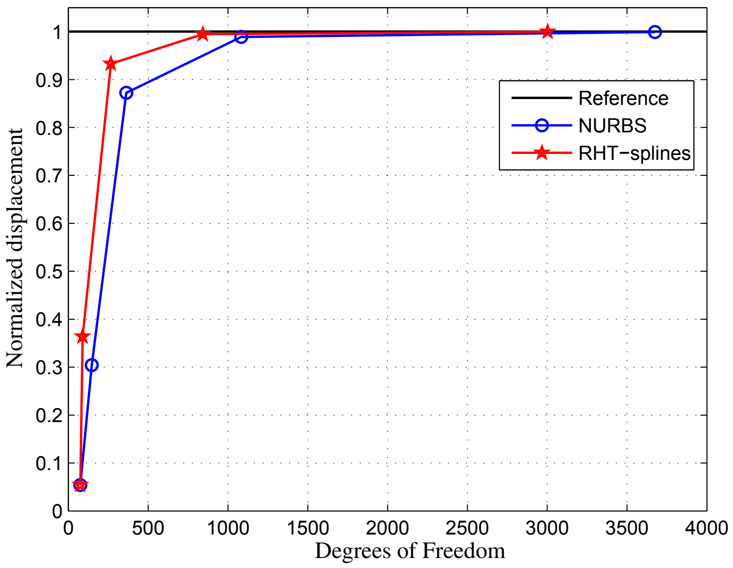

Figure 8.10: Convergence in displacement of pinched cylinder.

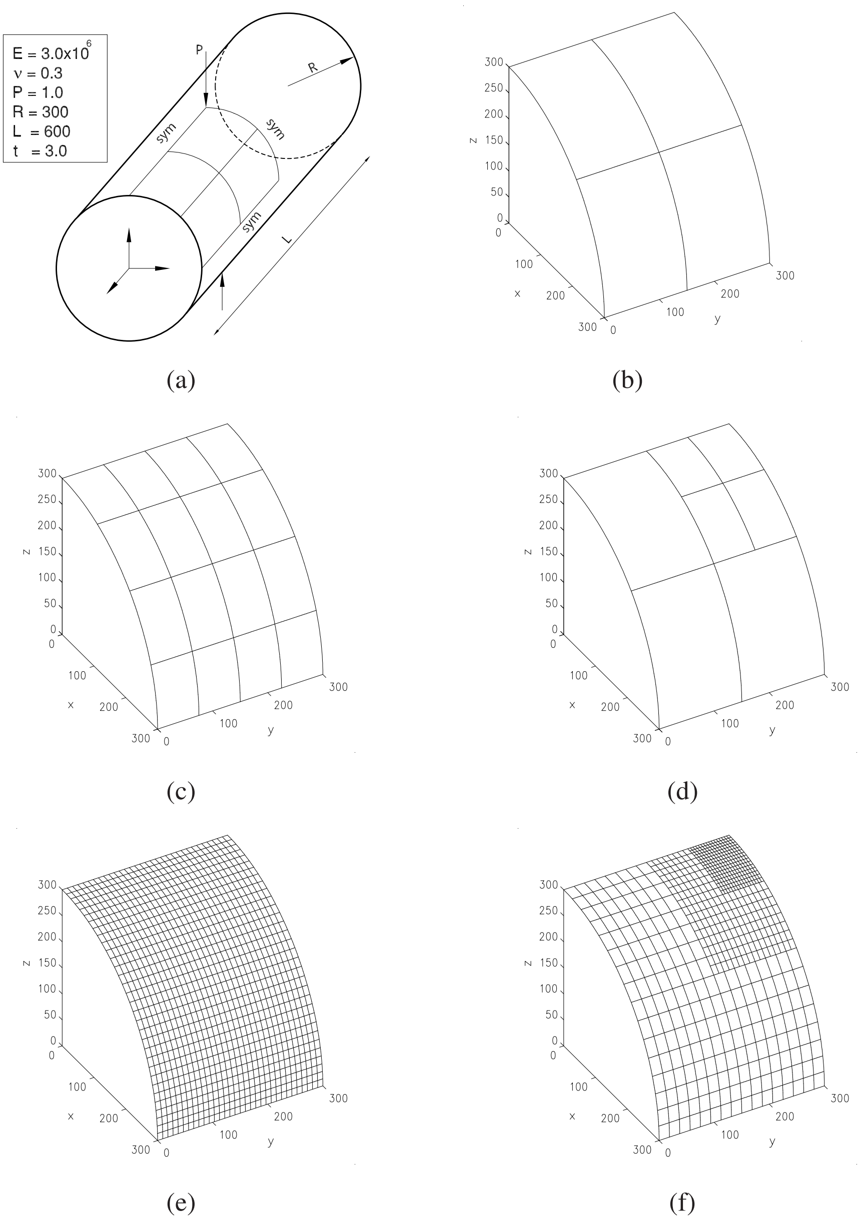

(a) (b)

(c) (d)

(e) (f)

Figure 8.11: Pinched cylinder with diaphragms boundary conditions and meshes: a) A pinched cylinder; b) A uniformly coarse mesh used for both NURBS and RHT-splines at level 0; Slightly finer meshes: c) NURBS and d) RHT-splines; Fine meshes: e) NURBS and f) RHT-splines.

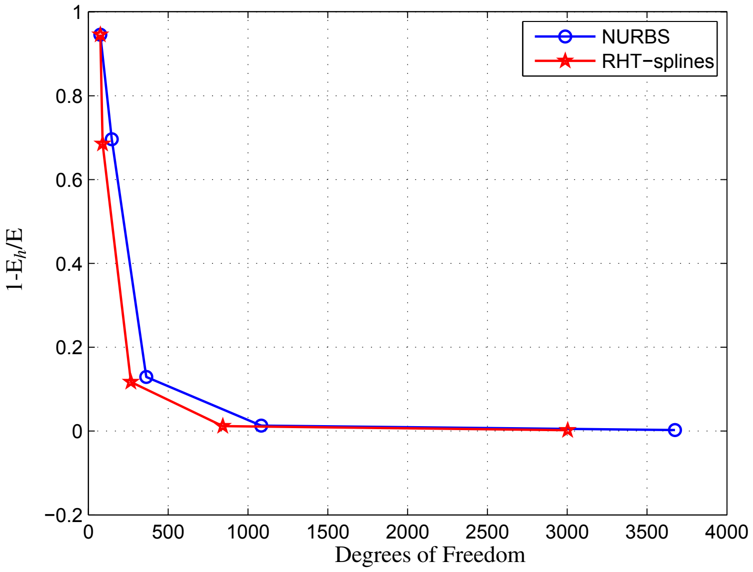

Figure 8.12: Convergence of strain energy of pinched cylinder.

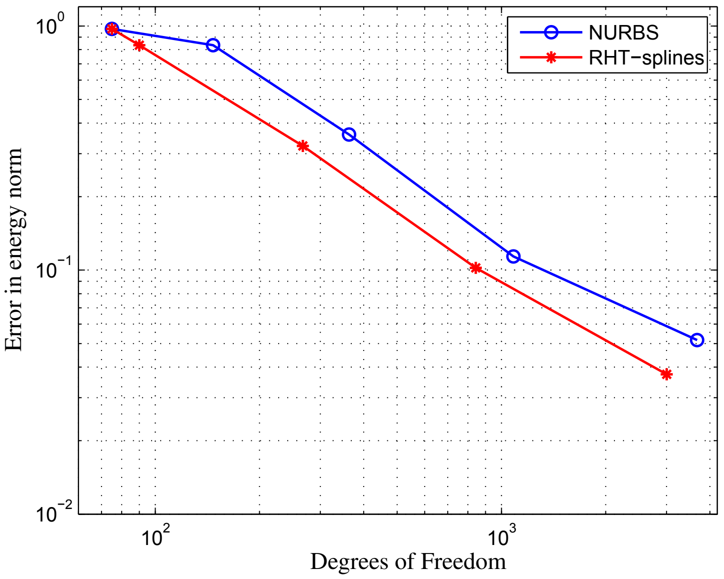

Figure 8.13: Error in energy norm of pinched cylinder.

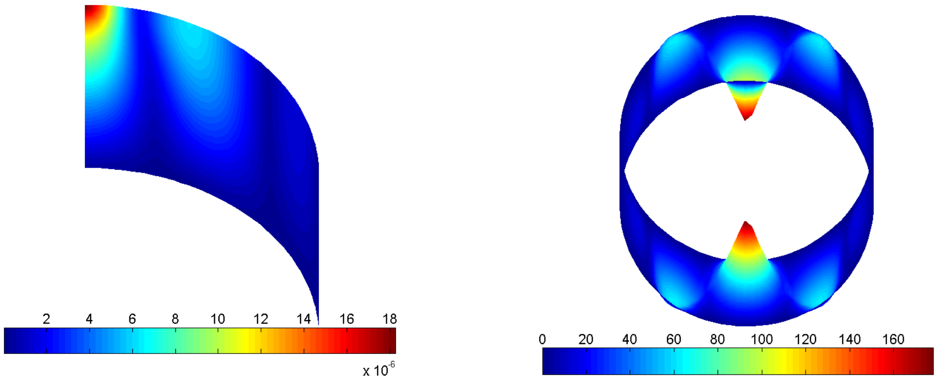

Figure 8.14: Contour plots of displacement under point load and deformed configuration (scaling factor = 1×10^7) of pinched cylinder.

8.4.1.3 Hemispherical shell

Let us consider a pinched hemisphere shell subjected to two opposite point loads $F = 2.0$. The bottom circumferential edge of the hemisphere is free (see in Fig. 8.15). The parameters are given as follows: Young's modulus $E = 6.825 \times 10^7$, Poisson's ratio $\nu = 0.3$, radius $R = 10.0$ and the thickness of the shell $t = 0.04$. Due to its symmetry, only one quarter of geometry is modeled. The reference value of the radial displacement under the point loads is 0.0924 (BSL$^+$85).

Convergence of the radial displacement under the applied loads is shown in Fig. 8.16. Also, Fig. 8.17 and Fig. 8.18 present the convergence of strain energy and the energy error norm, respectively. It is again seen that the RHT-splines produce more accurate solution than the NURBS model. Fig. 8.19 shows contour plots and deformed configuration of displacement component for both the quarter and full models.

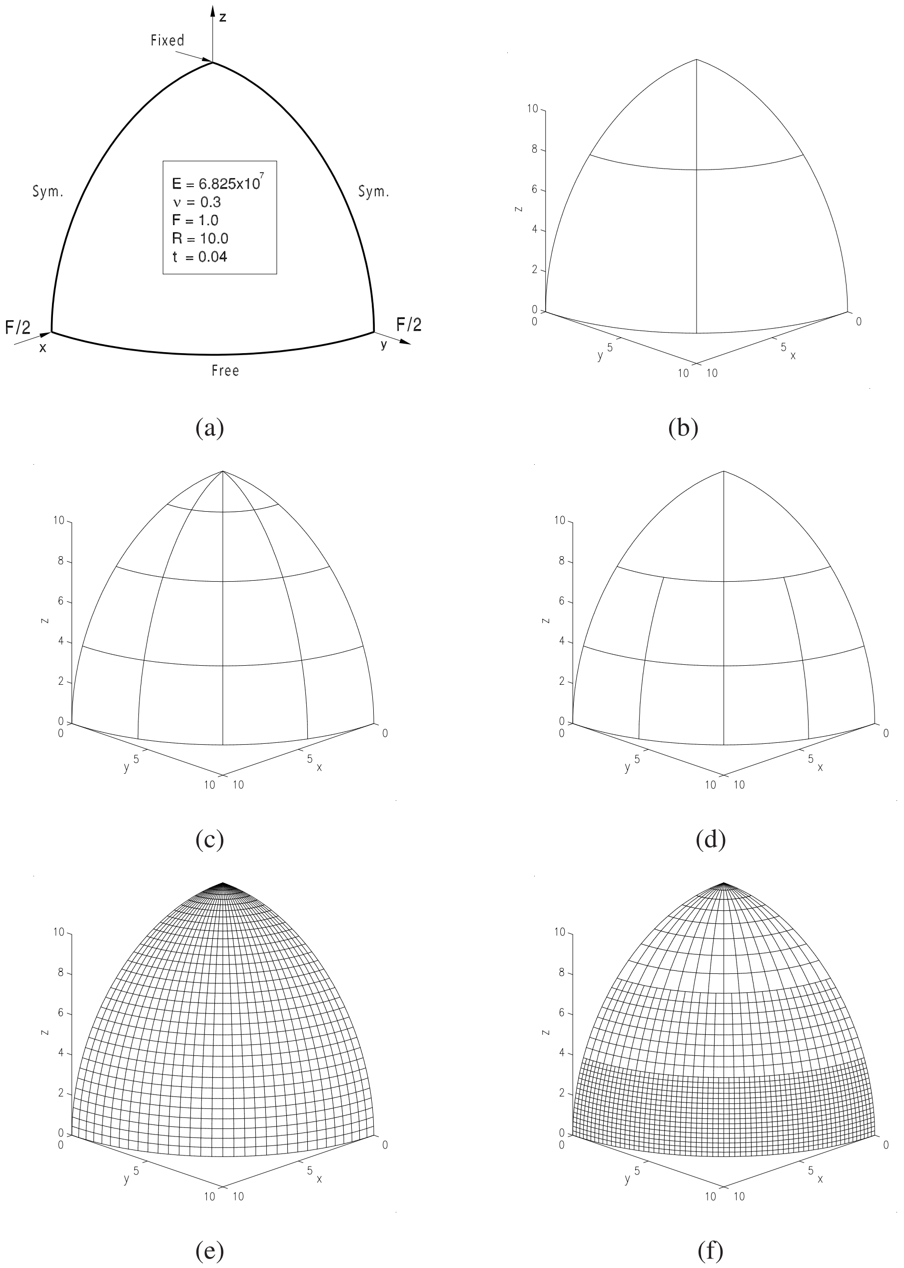

(a) (b)

(c) (d)

(e) (f)

Figure 8.15: Hemispherical shell at point loads and meshes: a) A hemispherical shell; b) A uniformly coarse mesh used for both NURBS and RHT-splines at level 0; Slightly finer meshes: c) NURBS and d) RHT-splines; Fine meshes: e) NURBS and f) RHT-splines.

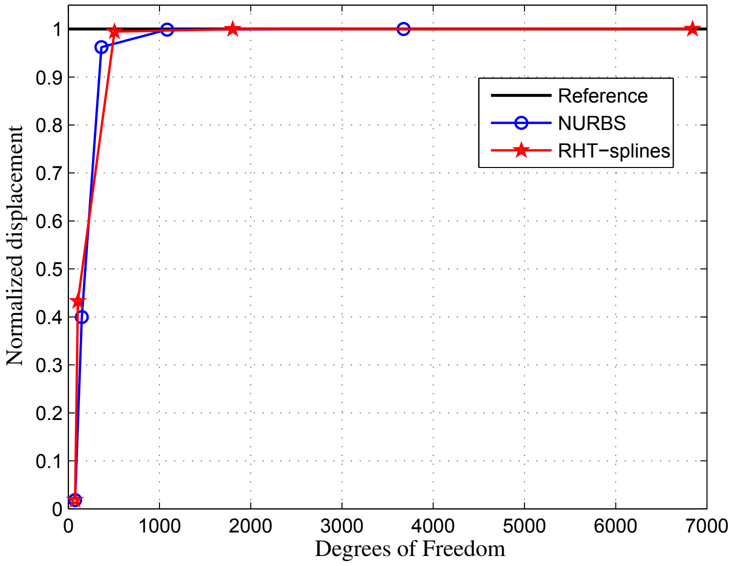

Figure 8.16: Convergence of the normalized displacements of a hemispherical shell.

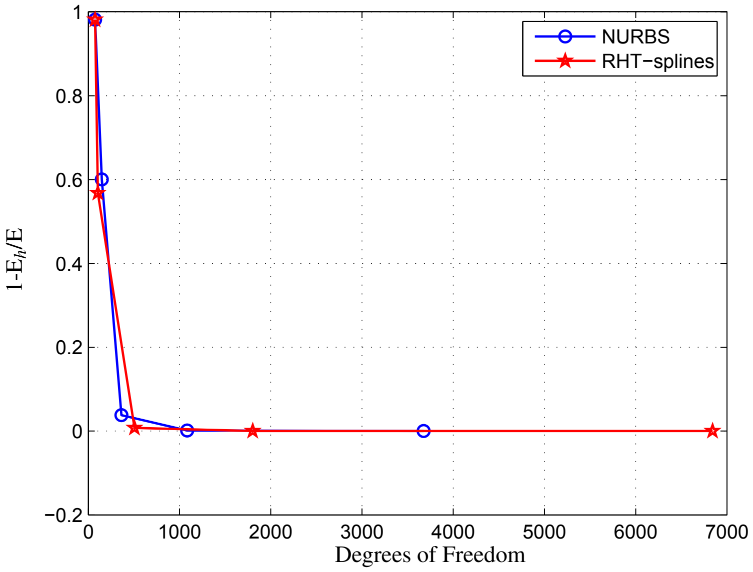

Figure 8.17: Convergence of strain energy of a hemispherical shell.

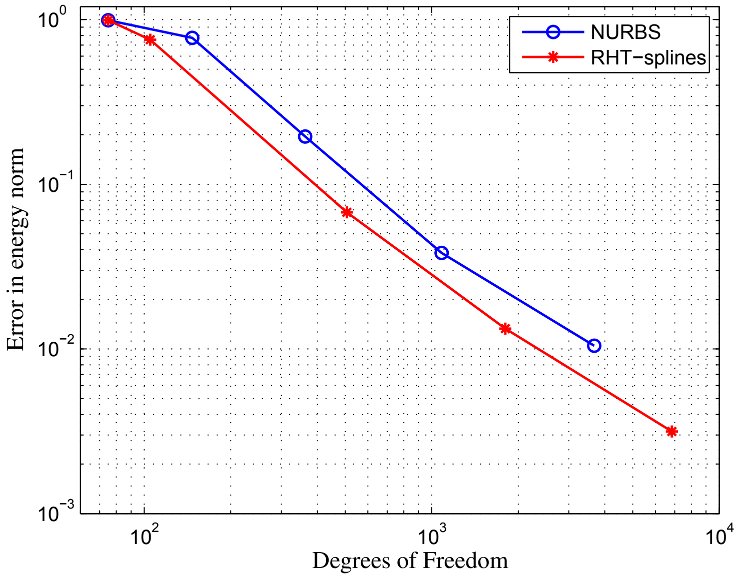

Figure 8.18: Error in energy norm of a hemispherical shell.

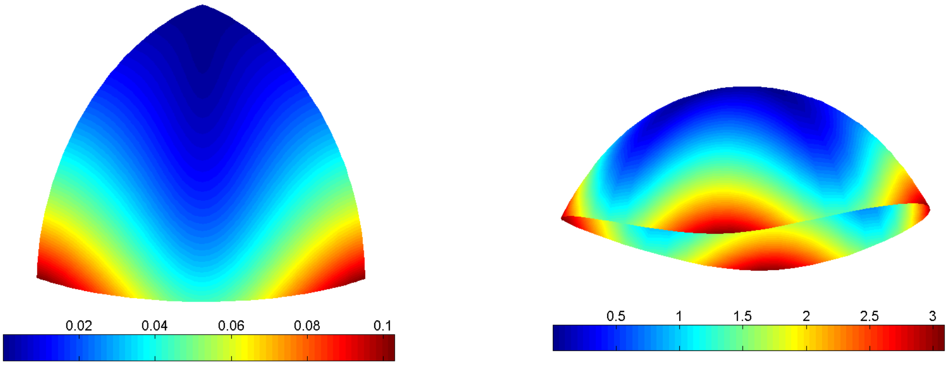

Figure 8.19: Contour plots of displacement at point loads and deformed configuration (scaling factor = 30) of a hemispherical shell.

8.4.2 Multi-patches analysis

8.4.2.1 Pinched Cylinder

A cylindrical shell with rigid end diaphragm is subjected to a point load at the center of the cylindrical surface. The related parameters are taken as: length of the cylinder $L = 600$; radius $R = 300$; thickness $t = 3$; Young's modulus $E = 3 \times 10^6$; and Poisson's ratio $\nu = 0.3$. The expected deflection under a concentrated load is 1.8248×10^{-5} (BSL+85).

The geometry of cynlinder is subdivided into four patches and the meshes are shown in Fig. 8.20. An illustrates contour plots of displacements force and moment resultants of the pinched cylinder for a half model by coupling four patches are shown Fig. 8.21. Convergence of displacement and the energy at the loading point is depicted in Fig. 8.22, Fig. 8.23.

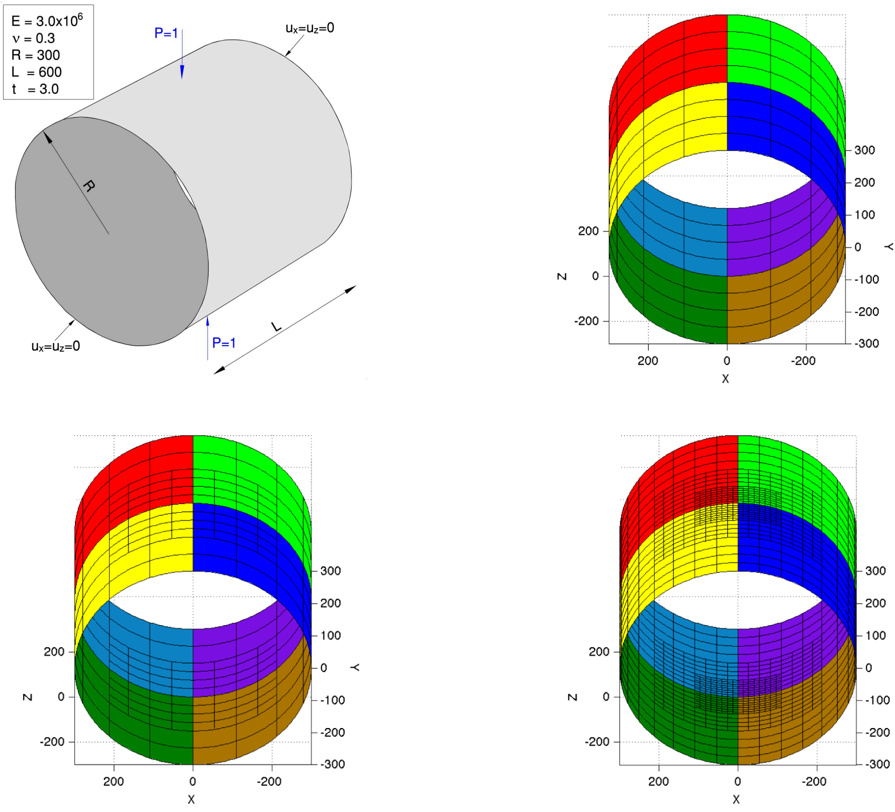

Figure 8.20: Pinched cylinder is subdivided into 8-patches and meshes.

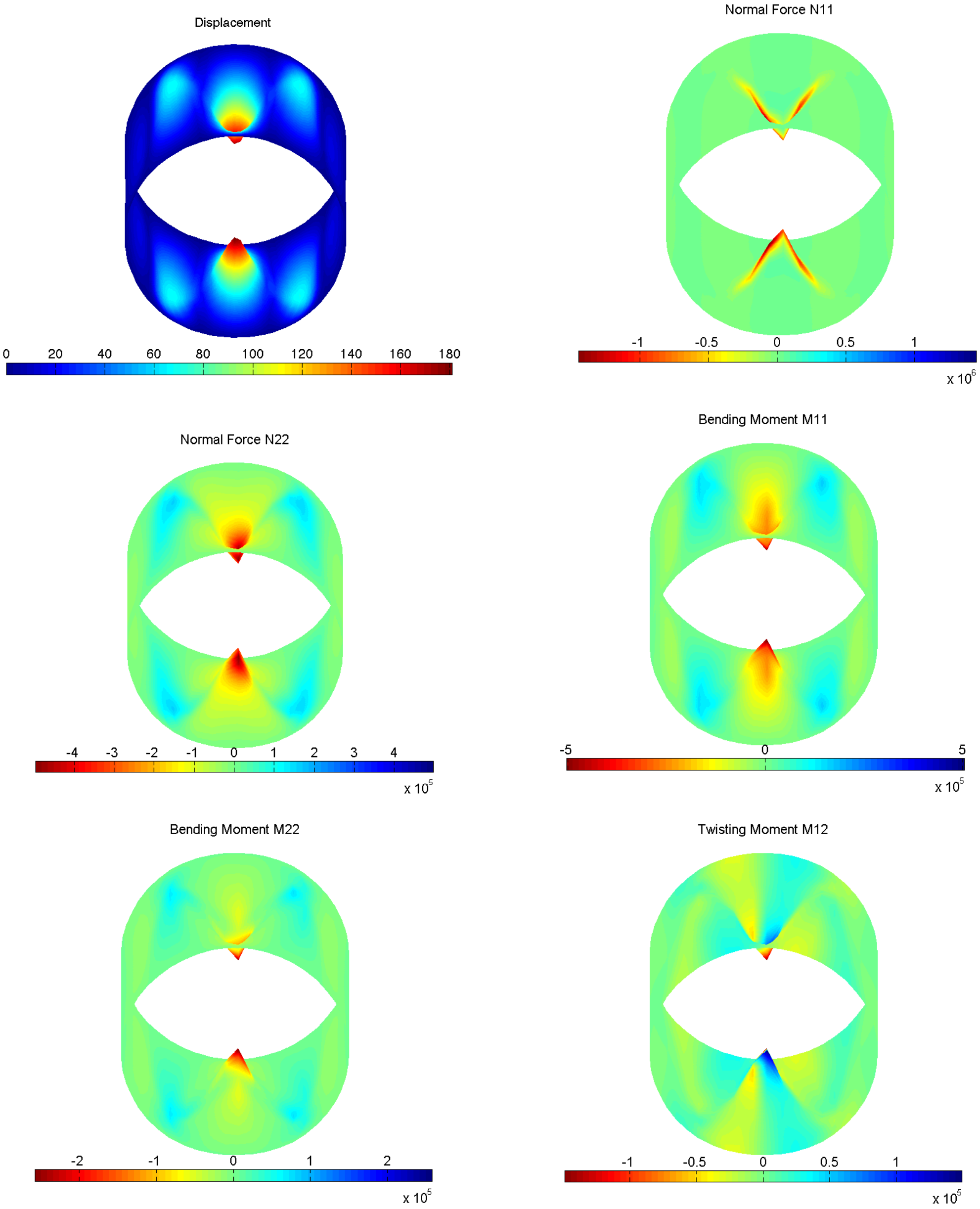
Displacement

Normal Force N11

Normal Force N22

Bending Moment M11

Bending Moment M22

Twisting Moment M12

Figure 8.21: Contour plots of displacement, force and moment resultants on deformed configuration (scaling factor = 1×10^{7}).

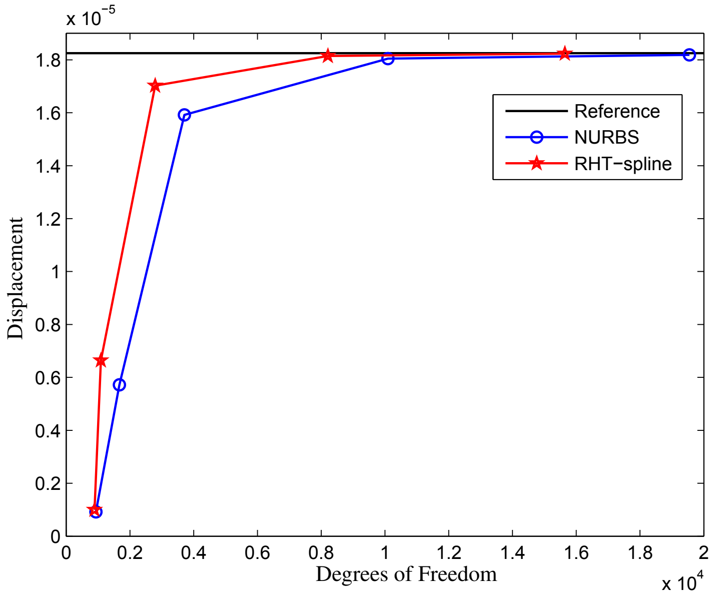

Figure 8.22: Convergence in displacement of the pinched cylinder with multi-patches analysis.

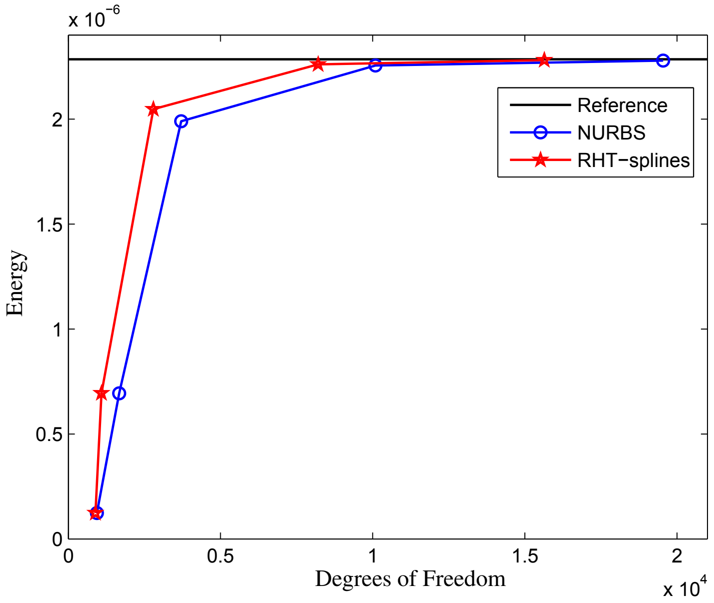

Figure 8.23: Energy convergence of the pinched cylinder with multi-patches analysis.

8.4.2.2 A wind turbine rotor

We consider a wind turbine rotor with gravity loading ($g = 9.81m/s^2$) which is presented in Fig. 8.24a. For this example, we used isotropic material with the parameters follow: Young's modulus $E = 19 \times 10^9$, Poisson's ratio $\nu = 0.29$, and the thickness of the wind turbine rotor are shown in Fig. 8.24b.

The geometry of this problem is subdivided into sixteen patches and the meshes are shown in Fig. 8.25. For this example, we used the different parameters mesh on patches and these are refined from the tip to roof. Contour plots of the displacement and and deformed configuration are displayed in Fig. 8.26. Convergence of displacement under the gravity loading is presented in Fig. 8.28. The good performance of the method is confirmed by complex geometry problem. Maximum displacement at the tip of the blade using the RHT approach is $u = 3.05$m, while the reference value is $u_{ref} = 3.03$m (from Prof. Y. Bazilevs's group) and the error is 0.66%.

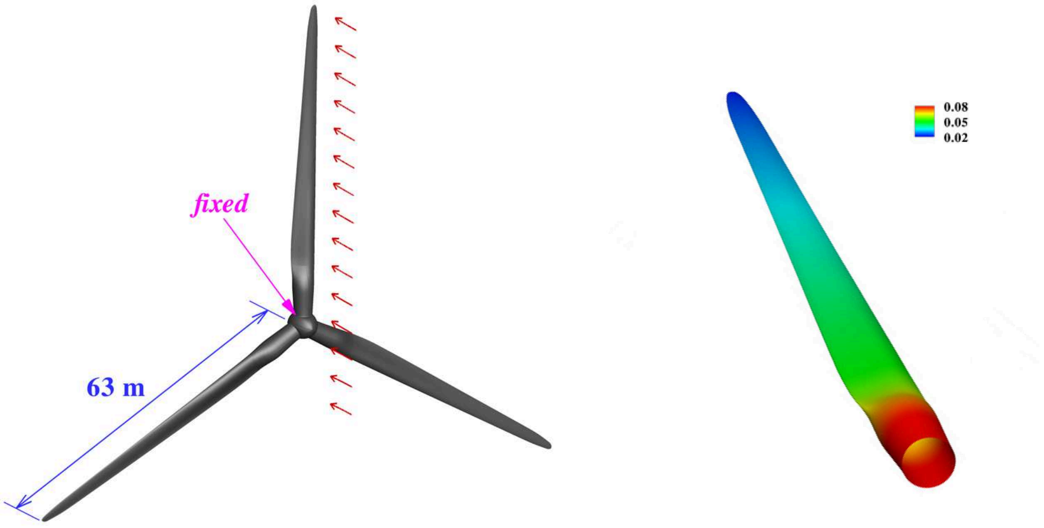

(a) (b)

Figure 8.24: (a) The wind turbine rotor. (b) Blade thickness distribution.

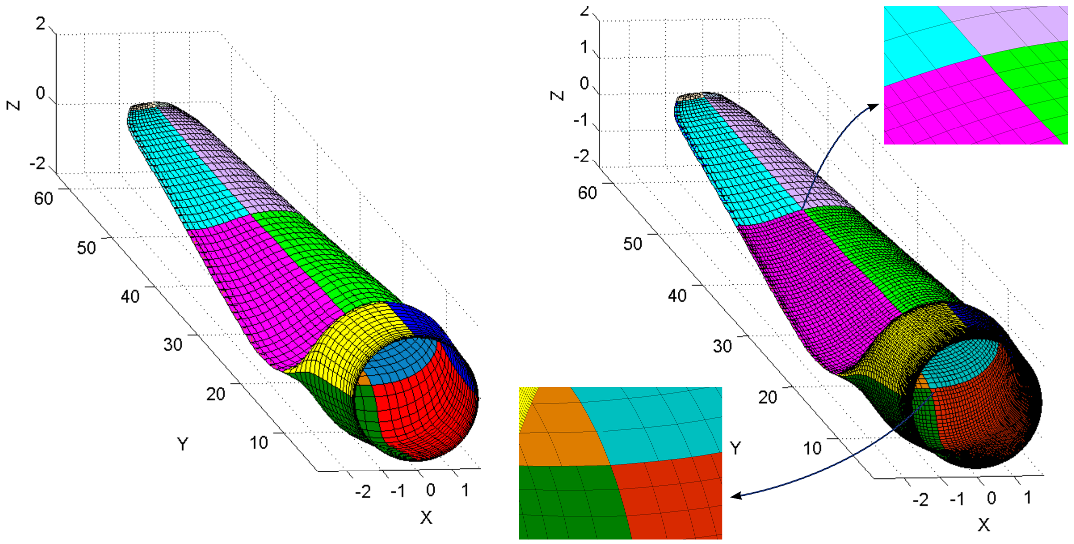

Figure 8.25: The wind turbine blade is subdivided into 16-patches with coarse mesh and refinement meshes.

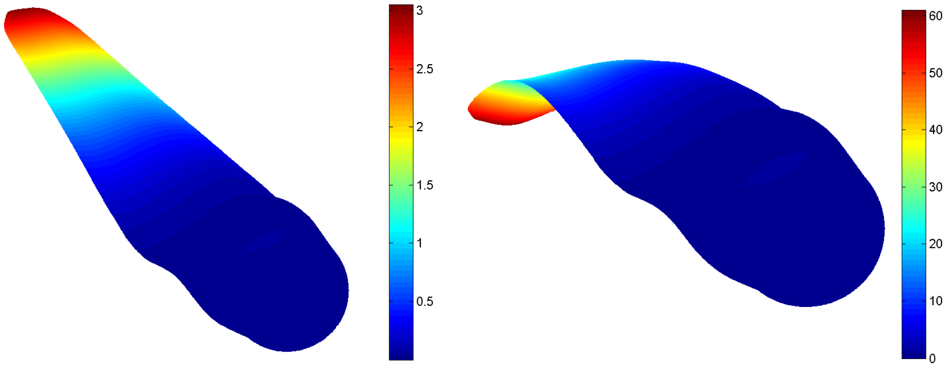

(a) (b)

Figure 8.26: Contour plot of displacement and deformed configuration (scaling factor = 20) of the wind turbine blade.

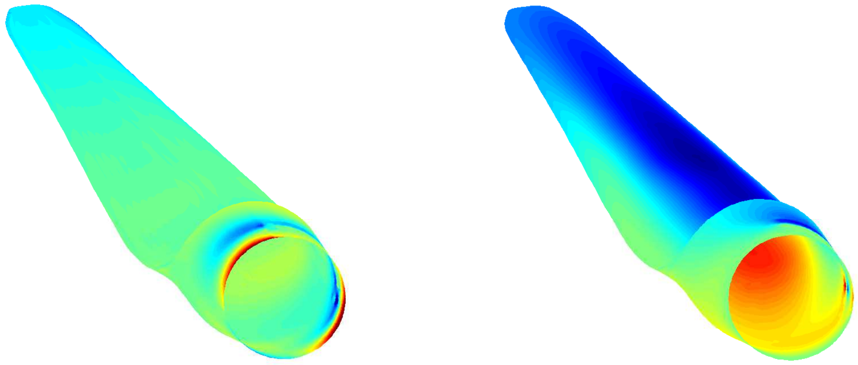

(a) Normal Force N11 (b) Normal Force N22

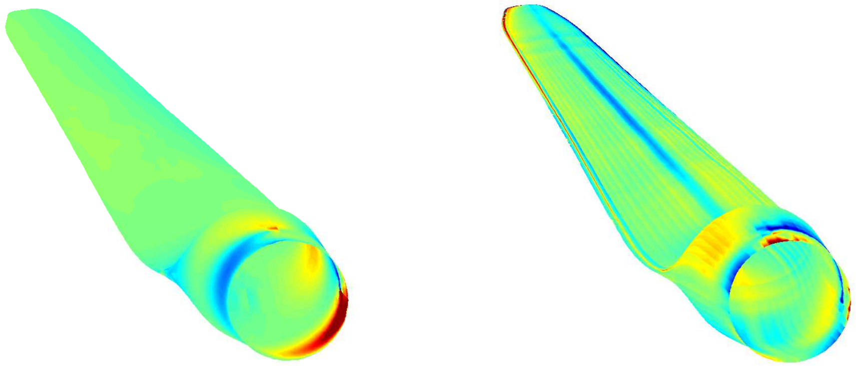

(c) Normal Force N12 (d) Bending Moment M11

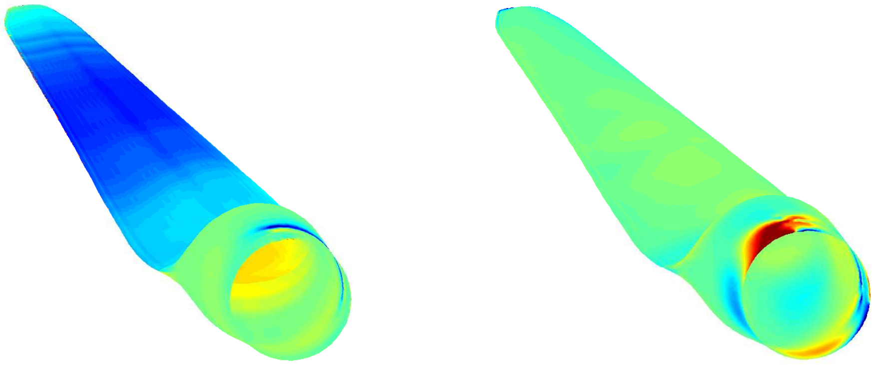

(e) Bending Moment M22 (f) Bending Moment M12

Figure 8.27: Contour plot of displacement, force and moment resultants of the wind turbine blade.

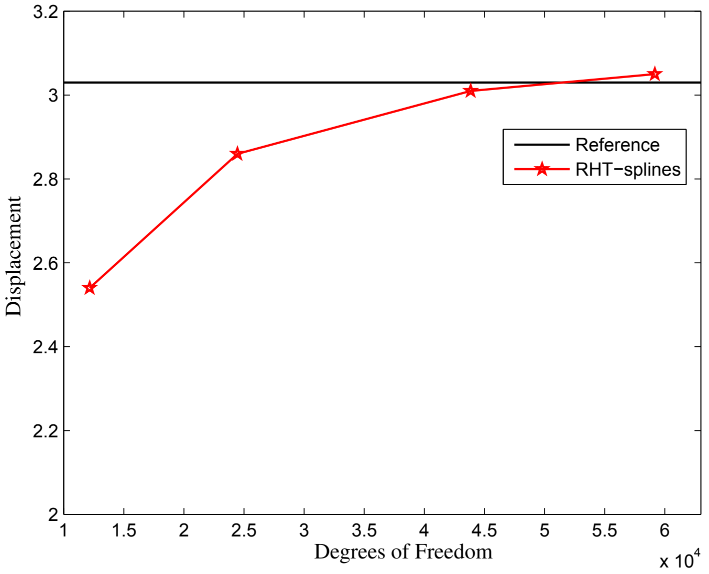

Figure 8.28: Convergence in displacement of the wind turbine blade.

8.5 Concluding remarks

An isogeometric approach based on RHT-splines has been formulated for the Kirchhoff-Love thin shell structures. Due to the C^1-continuity of the RHT-splines, I only discretize the mid-surface of the shell and automatically fulfill the Kirchhoff-Love constraint. Therefore, only 3 DOFs per node are needed. The RHT-splines possess C^1 continuity, so the Kirchhoff-Love theory for thin shell model can be used in pristine form. Moreover, RHT-splines allow a simple implementation for local refinement. By embedding the well-known finite element in the isogeometric framework, the advantage of exact geometry representation on the first coarsest mesh is inherited. The exact geometry representation is preserved throughout the refinement process without the need for additional communication with the CAD programs. The method is also efficient and can be easily applicable to complex surface modeling of multi-patch shell geometries.

Chapter 9

Conclusions

9.1 Summary of achievements

The present work improves accurate solutions for both displacement and energy norms and a superconvergent rate in the energy error norm. In this context, the main focus was placed on two specific concepts: an alpha finite element method and isogeometric analysis method.

An alternative alpha finite element method using triangular elements is proposed that significantly improves the accuracy of the standard triangular finite elements and provides a superconvergent solution in the energy norm. In the alpha finite element method, the piecewise constant strain field of linear triangular elements is enhanced by additional strain terms with an adjustable parameter α which results in an effectively softer stiffness formulation compared to the linear triangular element. To avoid the transverse shear locking of Reissner-Mindlin plates analysis the alpha finite element method is coupled with a discrete shear gap technique for triangular elements to significantly improve the accuracy of the standard triangular finite elements. The basic idea behind this element formulation is to approximate displacements and rotations as in the standard finite element method, but to construct the bending, geometrical and shear strains using node-based smoothing domains. The alternative alpha finite element method is equipped with an adjustable factor α ($\alpha \in [0,1]$) for plate problems. When $\alpha = 0$, the present element becomes the standard finite element and hence produces a lower bound in the strain energy. For $\alpha = 1$, the element becomes the node-based smoothed with discrete shear gap model and leads to an upper bound in the strain energy. The results obtained from static, free vibration and buckling analyses are shown that the alpha finite element method achieves high reliability compared to other existing elements in the literature.An alternative alpha finite element method using triangular elements is proposed that significantly improves the accuracy of the standard triangular finite elements and provides a superconvergent solution in the energy norm. In the alpha finite element method, the piecewise constant strain field of linear triangular elements is enhanced by additional strain terms with an adjustable parameter α which results in an effectively softer stiffness formulation compared to the linear triangular element. To avoid the transverse shear locking of Reissner-Mindlin plates analysis the alpha finite element method is coupled with a discrete shear gap technique for triangular elements to significantly improve the accuracy of the standard triangular finite elements. The basic idea behind this element formulation is to approximate displacements and rotations as in the standard finite element method, but to construct the bending, geometrical and shear strains using node-based smoothing domains. The alternative alpha finite element method is equipped with an adjustable factor α ($\alpha \in [0,1]$) for plate problems. When $\alpha = 0$, the present element becomes the standard finite element and hence produces a lower bound in the strain energy. For $\alpha = 1$, the element becomes the node-based smoothed with discrete shear gap model and leads to an upper bound in the strain energy. The results obtained from static, free vibration and buckling analyses are shown that the alpha finite element method achieves high reliability compared to other existing elements in the literature.

An isogeometric approach based on rational splines over hierarchical T-meshes has been formulated for two-dimensional, the Kirchhoff-Love thin shell structures and three-dimensional problems. The idea is based on rational splines and exploits the flexibility of T-meshes for local refinement. The RHT-splines basis functions fulfill all important properties in the context of numerical analysis such as non-negativity, partition of unity, linear independent and local support. Moreover, the RHT-splines formulation facilitates adaptive refinement that is cumbersome for NURBS or even T-spline based finite element formulations. The main drawback of the RHT-splines is that it can achieve only C^1 continuity which is nonetheless usually sufficient for most problems in solid and structural mechanics. By embedding the well-known finite element in the isogeometric framework, the advantage of exact geometry representation on the first coarsest mesh is inherited. The exact geometry representation is preserved throughout the refinement process without the need for additional communication with the CAD software. Numerical examples investigation proven that the convergence rate of the RHT-splines is higher than the higher order finite element FEM-Q16 and the NURBS while the total error is lower. The results are very encouraging as they not only serve to verify the theory but also demonstrate the robustness of the error estimators and the high order approximations provided by the adaptive spline space. The proposed method using superconvergent patch recovery technique is also capable to obtain results with higher accuracy and convergence rate than NURBS results. A good agreement was achieved between the numerical and analytical results for both static and free vibration problems. Another achieved of RHT-splines is C^1-continuity, the Kirchhoff-Love theory for thin shell model can be used in pristine form which is discretized the midsurface of the shell and automatically fulfill the Kirchhoff-Love constraint. Therefore, only 3 DOFs per node are needed. The results obtained from the proposal method for benchmark shell problems are higher accuracy than the NURBS based approach when the same order approximation used.

9.2 Outlook

Although the present method has shown to be effective for structural analysis, further investigations need to be considered for general engineering applications with complicate geometries. Therefore an extension of the present work with some of the possible future research topic as follow

- In the alpha finite element method, it is promising to extend the present method for the shells, 3D problems by combining the alpha FEM with DSG method to get rid of shear locking and to improve the accuracy of solutions. It also maybe useful to combine the alpha finite element method with h-adaptivity procedure for computing and simulating complex industrial structures (BM06, BCM$^+$07, RB06a, RBZ07).

- In the isogeometric analysis method, the exact geometry is taken into account for the numerical analysis. However, the construction of initial geometry function consume time, and the geometry function is not always unique. How to design the geometry automatically according to the analysis results, it should be investigated in next time.

- An extend the RHT-splines formula based thin-shell element without rotational degrees of freedom to fracture mechanics, large deformation and non-linear analyses (RB07b, RB04a, RAB07b, RA06a, BRZ08).

- Development of the RHT-splines method for a posteriori error estimators and adaptive refinement strategies with h-p refinement (dVBRS11, SR11).

- It also maybe extend to contact problems (Lau02, Wri06, LTWZ11, LWZ12).

- From an industrial perspective, the present method should be applied to engineering problems like marine or offshore structures (BHA$^+$11, BHK$^+$11, SHBB12).

References

[ABC$^+$08] I. Akkerman, Y. Bazilevs, V.M. Calo, T.J.R. Hughes, and S. Hulshoff. The role of continuity in residual-based variational multiscale modeling of turbulence. *Computational Mechanics*, 41:371–378, 2008. 83

[ADB98] Ayad, G. Dhatt, and J.L Batoz. A new hybrid-mixed variational approach for Reissner–Mindlin plate. *International Journal for Numerical Methods in Engineering*, 42:1149–1179, 1998. 47

[ADK87] F. Abbassian, D.J. Dawswell, and N.C. Knowles. Free vibration benchmarks. *Atkins Engineering Sciences*, 1987. 125, 126

[AHB00] M. Azhari, S. Hoshdar, and M.A. Bradford. On the use of bubble functions in the local buckling analysis of plate structures by the spline finite strip method. *International Journal for Numerical Methods in Engineering*, 48:583–593, 2000. 74

[All84] D.J. Allman. A compatible triangular element including vertex rotations for plane elasticity analysis. *Computers and Structures*, 19:1–8, 1984. 2

[ANW67] J. H. Ahlberg, E.N. Nilson, and J.L. Walsh. The theory of splines and their applications. *Academic Press, New York*, 1967. 3

[Bat96] K.J. Bathe. *Finite element procedures*. Englewood Cliffs, NJ: Prentice-Hall, Massachusetts (MIT), 1996. 39

[BB83] T. Belytschko and L.P. Bindeman. Assumed strain stabilization of the 4-node quadrilateral with 1-point quadrature for nonlinear problems. *Computer Methods in Applied Mechanics and Engineering*, 88:311–340, 1983. 17

[BB86] T. Belytschko and W.E. Bachrach. Efficient implementation of quadrilaterals with high coarse-mesh accuracy. *Computer Methods in Applied Mechanics and Engineering*, 54:279–301, 1986. 17

[BBHH11] D.J. Benson, Y. Bazilevs, M.-C. Hsu, and T.J.R. Hughes. A large deformation, rotation-free, isogeometric shell. *Computer Methods in Applied Mechanics and Engineering*, 200(13-16):1367–1378, 2011. 130

[BBR00] K.U. Bletzinger, M. Bischoff, and E. Ramm. A unified approach for shear-locking free triangular and rectangular shell finite elements. *International Journal for Numerical Methods in Engineering*, 75:321–334, 2000. 47, 51, 52

[BBWR04] M. Bischoff, K.-U. Bletzinger, W.A. Wall, and E. Ramm. *Models and Finite Elements for Thin-Walled Structures*. John Wiley and Sons, New York, 2004. 130

[BCC$^+$10] Y. Bazilevs, V.M. Calo, J.A. Cottrell, J.A. Evans T.J.R Hughes, S. Lipton, and M.A. Scottand T.W. Sederberg. Isogeometric analysis using T-splines. *Computer Methods in Applied Mechanics and Engineering*, 199:229–263, 2010. 4, 83, 108

[BCHZ08] Y. Bazilevs, V.M. Calo, T.J.R Hughes, and Y. Zhang. Isogeometric fluid-structure interaction: theory, algorithms, and computations. *Computational Mechanics*, 43:3–37, 2008. 83

[BCM$^+$07] S. Bordas, J.G. Conley, B. Moran, J. Gray, and E. Nichols. A simulation based on design paradigm for complex cast components. *Engineering Fracture Mechanics*, 23:25–37, 2007. 159

[BCS09] A. Buffa, D. Cho, and G. Sangalli. Linear independence of the T-spline blending functions associated with some particular T-meshes. *Computer Methods in Applied Mechanics and Engineering*, 199(23-24):437–1445, 2009. 4, 85, 108

[BD83] K.J. Bathe and E. Dvorkin. Our discrete Kirchhoff and isoparametric shell elements for non-linear analysis - An assessment. *Computers and Structures*, 16:89–98, 1983. 130

[BD85] K.J. Bathe and E.N. Dvorkin. A four-node plate bending element based on Mindlin-Reissener plate theory and a mixed interpolation. *International Journal for Numerical Methods in Engineering*, 21:367–383, 1985. 52, 53

[Bea91] Robert C. Beach. An introduction to curves and surfaces of computer-aided design. *Van Nostrand Reinhold*, 1991. 2

[BF85] P.G. Bergan and C.A. Felippa. A triangular membrane element with rotational degrees of freedom. *Computer Methods in Applied Mechanics and Engineering*, 50:25–69, 1985. 14

[BHA$^+$11] Y. Bazilevs, M.-C. Hsu, I. Akkerman, S. Wright, K. Takizawa, B. Henicke, T. Spielman, and T.E. Tezduyar. 3D simulation of wind turbine rotors at full scale. Part I: Geometry modeling and aerodynamics. *International Journal for Numerical Methods in Engineering*, 65(1-3):207–235, 2011. 159

[BHK$^+$11] Y. Bazilevs, M.-C. Hsu, J. Kiendl, R. Wüchner, and K.-U. Bletzinger. 3D simulation of wind turbine rotors at full scale. Part II: Fluid structure interaction modeling with composite blades. *International Journal for Numerical Methods in Engineering*, 65(1-3):236–253, 2011. 159

[BM06] S. Bordas and B. Moran. Enriched finite elements and level sets for damage tolerance assessment of complex structures. *Engineering Fracture Mechanics*, 73:1176–1201, 2006. 159

[Boo62] C. De Boor. Bicubic spline interpolation. *Journal of Mathematical Physics*, 41:212–218, 1962. 3

[BRB99] M. Bischoff, E. Ramm, and D. Braess. A class equivalent enhanced assumed strain and hybrid stress finite elements. *Computational Mechanics*, 21:444–449, 1999. 2

[BRNX$^+$10] S. Bordas, T. Rabczuk, H. Nguyen-Xuan, P. Nguyen Vinh, S. Natarajan, T. Bog, Q. Do Minh, and H. Nguyen Vinh. Strain smoothing in FEM and xFEM. *Computers and Structures*, 88:1419–1443, 2010. 24

[BRZ08] S. Bordas, T. Rabczuk, and G. Zi. Three-dimensional crack initiation, propagation, branching and junction in non-linear materials by an extended meshfree method without asymptotic enrichment. *Engineering Fracture Mechanics*, 75(5):943–960, 2008. 13, 159

[BSL$^+$85] T. Belytschko, H. Stolarski, W.K. Liu, N. Carpenter, and J.S.J. Ong. Stress projection for membrane and shear locking in shell finite elements. *Computer Methods in Applied Mechanics and Engineering*, 51:221–258, 1985. 117, 138, 143, 146, 150

[BTW84] C.A. Brebbia, J.C. Telles, and L.C. Wrobel. *Boundary Element Techniques*. Springer, Berlin, 1984. 33, 38

[CHB09] J. Austin Cottrell, T.J.R. Hughes, and Y. Bazilevs. *Isogeometric analysis : Toward integration of CAD and FEA*. John Wiley & Sons, Ltd, New York, 2009. 93

[CHR07] J.A. Cottrell, T.J.R Hughes, and A. Reali. Studies of refinement and continuity in geometry and mesh refinement. *Computer Methods in Applied Mechanics and Engineering*, 196:4160–4183, 2007. 3, 84, 108

[CLYC06] S. Cen, Y.Q. Long, Z.H. Yao, and S.P. Chiew. Application of the quadrilateral area co-ordinate method: A new element for Mindlin–Reissner plate. *International Journal for Numerical Methods in Engineering*, 66:1–45, 2006. 56

[COS00] F. Cirak, M. Ortiz, and P. Schröder. Subdivision surfaces: A new paradigm for thin shell analysis. *International Journal for Numerical Methods in Engineering*, 47:2039–2072, 2000. 130

[CRBH06] J.A. Cottrell, A. Reali, Y. Bazilevs, and T.J.R. Hughes. Isogeometric analysis of structural vibrations. *Computer Methods in Applied Mechanics and Engineering*, 195:5257–5297, 2006. 83

[CW06] J.S. Chen and D. Wang. A constrained reproducing kernel particle formulation for shear deformable shell in cartesian coordinates. *International Journal for Numerical Methods in Engineering*, 68:151–172, 2006. 130

[CWYY01] J.S. Chen, C.T. Wu, S. Yoon, and Y. You. A stabilized conforming nodal integration for Galerkin mesh-free methods. *International Journal for Numerical Methods in Engineering*, 50:435–466, 2001. 13

[CYM$^+$08] R.P.R. Cardoso, J.W. Yoon, M. Mahardika, S. Choudhry, R.J. Alves de Sousa, and R.A. Fontes Valente. Enhanced assumed strain (EAS) and assumed natural strain (ANS) methods for one-point quadrature solid-shell elements. *International Journal for Numerical Methods in Engineering*, 75:156–187, 2008. 47

[DBH10] M.C. Hsu D.J. Benson, Y. Bazilevs and T.J.R. Hughes. Isogeometric shell analysis: The Reissner-Mindlin shell. *Computer Methods in Applied Mechanics and Engineering*, 199:276–289, 2010. 84, 130

[DCF06] Jiansong Deng, Falai Chen, and Yuyu Feng. Dimensions of spline spaces over T-meshes. *Journal of Computational and Applied Mathematics*, 194:267–283, 2006. 87, 88, 110

[DCL$^+$08] Jiansong Deng, Falai Chen, Xin Li, Changqi Hu, Weihua Tong, Zhouwang Yang, and Yuyu Feng. Polynomial splines over hierarchical T-meshes. *Graphical Models*, 70:76–86, 2008. 4, 79, 85, 89, 91, 92

[Den] 108, 109

[DJS10] M. Dorfël, B. Juttler, and B. Simeon. Adaptive isogeometric analysis by local h-refinement with T-splines. *Computer Methods in Applied Mechanics and Engineering*, 199:264–275, 2010. 4, 108

[DL07] K.Y. Dai and G.R. Liu. Free and forced vibration analysis using the smoothed finite element method (SFEM). *Journal Sound and Vibration*, 301:803–820, 2007. 13

[DLN07] K.Y. Dai, G.R. Liu, and T.T. Nguyen. An n-sided polygonal smoothed finite element method (nSFEM) for solid mechanics. *Finite elements in analysis and design*, 43:847–860, 2007. 13

[DS10] T. Dokken and V. Skytt. Locally refined splines. *IV European Congress on Computational Mechanics (ECCM), Paris, France*, 2010. 108

[dSJVA02] J.M.A. César de Sá, R.M. Natal Jorge, R.A. Fontes Valente, and P.M.A. Areias. Development of shear locking-free shell elements using an enhanced assumed strain formulation. *International Journal for Numerical Methods in Engineering*, 53:1721–1750, 2002. 47

[dVBRS11] L. Beirao da Veiga, A. Buffa, J. Rivas, and G. Sangalli. Some estimates for h-p-k-refinement in isogeometric analysis. *Numerische Mathematik*, 118:271–305, 2011. 159

[EB10] R. Echter and M. Bischoff. Numerical efficiency, locking and unlocking of NURBS finite elements. *Computer Methods in Applied Mechanics and Engineering*, 199:374–382, 2010. 83

[FB98] D. Forsey and R. Bartels. Hierarchical B-spline refinement. *Comput. Graphics*, 22:205–212, 1998. 84

[Fel94] C.A. Felippa. A survey of parametrized variational principles and applications to computational mechanics. *Computer Methods in Applied Mechanics and Engineering*, 113:109–139, 1994. 14

[FO04] M. Fredriksson and N.S. Ottosen. Fast and accurate 4-node quadrilateral. *International Journal for Numerical Methods in Engineering*, 61:1809–1834, 2004. 17

[GJS12] Carlotta Giannelli, Bert Jüttler, and Hendrik Speleers. THB-splines: The truncated basis for hierarchical splines. *Computer Aided Geometric Design*, 29:485–498, 2012. 108

[GL01] Y.T. Gu and G.R. Liu. A meshless local Petrov-Galerkin (MPLG) method for free and vibration analyses for solids. *Computational Mechanics*, 27:188–198, 2001. 31, 38

[HÖ3] K. Höllig. Finite element methods with B-splines. *Society for Industrial and Applies Mathematics*, Philadelphia, 2003. 83

[HCB05] T. J.R. Hughes, J.A. Cottrell, and Y. Bazilevs. Isogeometric analysis: CAD, finite elements, NURBS, exact geometry and mesh refinement. *Computer Methods in Applied Mechanics and Engineering*, 194:4135–4195, 2005. 3, 83, 85, 108

[HGT12] Behrooz Hassani, Ahmad Ganjali, and Mehdi Tavakkoli. An isogeometrical approach to error estimation and stress recovery. *European Journal of Mechanics A/Solids*, 31:101–109, 2012. 109

[HRS08] T.J.R. Hughes, A. Reali, and G. Sangalli. Duality and unified analysis of discrete approximations in structural dynamics and wave propagation: Comparison of p-method finite elements with k-method NURBS. *Computer Methods in Applied Mechanics and Engineering*, 197:4104–4124, 2008. 83, 84

[Hug87] T.J.R. Hughes. *The Finite Element Method: Linear Static and Dynamic Finite Element Analysis*. Prentice-Hall, 1987. 13

[Kat93] Irwan Katili. A new discrete Kirchhoff-Mindlin element based on Mindlin-Reissner plate theory and assumed shear strain fields-part II: an extended DKQ element for thick-plate bending analysis. *International Journal for Numerical Methods in Engineering*, 36:1885–1908, 1993. 52

[KB96] Petr Krysl and Ted Belytschko. Analysis of thin shells by the element free Galerkin method. *International Journal of Solids and Structures*, 33(20-22):3057–3080, 1996. 130

[KBH$^+$10] J. Kiendl, Y. Bazilevs, M.-C. Hsu, R. Wüchner, and K.-U. Bletzinger. The bending strip method for isogeometric analysis of Kirchhoff-Love shell structures comprised of multiple patches. *Computer Methods in Applied Mechanics and Engineering*, 199:2403–2416, 2010. 130

[KBLW09] J. Kiendl, K.-U. Bletzinger, J. Linhard, and R. Wüchner. Isogeometric shell analysis with Kirchhoff-Love elements. *Computer Methods in Applied Mechanics and Engineering*, 198:3902–3914, 2009. 84, 130

[KJZ12] Stefan K. Kleiss, Bert Jüttler, and Walter Zulehner. Enhancing isogeometric analysis by a finite element based local refinement strategy. *Computer Methods in Applied Mechanics and Engineering*, 213-216:168–182, 2012. 108

[KKAb96] W. Karunasena, S. Kitipornchai, and F.G.A. Al-bermani. Free vibration of cantilevered arbitrary triangular mindlin plates. *Mechanical Sciences*, 38:431–442, 1996. 52

[KXWL93] S. Kitipornchai, Y. Xiang, C.M. Wang, and K.M. Liew. Buckling of thick skew plates. *International Journal for Numerical Methods in Engineering*, 36:1299–1310, 1993. 72, 73

[Lau02] T.A. Laursen. *Computational Contact and Impact Mechanics*. Springer, Berlin, 2002. 159

[LC04] K.M. Liew and X.L. Chen. Buckling of rectangular Mindlin plates subjected to partial in-plane edge loads using the radial point interpolation method. *International Journal of Solids and Structures*, 41:1677–1695, 2004. 52, 72

[LDC06] Xin Li, Jiansong Deng, and Falai Chen. Dimensions of spline spaces over 3D hierarchical T-meshes. *Journal of Information and Computational Science*, 3:487–501, 2006. 110

[LDC07] Xin Li, Jiansong Deng, and Falai Chen. Surface modeling with polynomial splines over hierarchical T-meshes. *Visual Computer*, (23):1027–1033, 2007. 85, 108

[LDC10] Xin Li, Jiansong Deng, and Falai Chen. Polynomial splines over general T-meshes. *Visual Computer*, (26):277–286, 2010. 85, 108

[Lee04] S.J. Lee. Free vibration analysis of plates by using a four-node finite element formulated with assumed natural transverse shear strain. *Journal Sound and Vibration*, 278:657–684, 2004. 52, 63

[Lei69] A.W. Leissa. Vibration of plates. *NASA*, SP-160:Washington DC, 1969. 63

[LH01] S.J. Lee and S.E. Han. Free-vibration analysis of plates and shells with a nine-node assumed natural degenerated shell element. *Journal Sound and Vibration*, 241:605–633, 2001. 52, 63

[Liu08] G.R. Liu. A generalized gradient smoothing technique and the smoothed bilinear form for Galerkin formulation of a wide class of computational methods. *International Journal Computation Methods*, 2:199–236, 2008. 1, 13

[LNTL08] G.R. Liu, T. Nguyen-Thoi, and K.Y. Lam. A novel alpha finite element method (αFEM) for exact solution to mechanics problems using triangular and tetrahedral elements. *Computer Methods in Applied Mechanics and Engineering*, 197:3883–3897, 2008. 14, 18

[LNTL09] G.R. Liu, T. Nguyen-Thoi, and K.Y. Lam. An edge-based smoothed finite element method (ES-FEM) for static, free and forced vibration analyses of solids. *Journal Sound and Vibration*, 320:1100–1130, 2009. 20, 31

[LNTNXL09] G.R. Liu, T. Nguyen-Thoi, H. Nguyen-Xuan, and K.Y. Lam. A node-based smoothed finite element method (NS-FEM) for upper bound solutions to solid mechanics problems. *Computational Structural*, 87:14–26, 2009. 14, 20

[LNXNTX09] G.R. Liu, H. Nguyen-Xuan, T. Nguyen-Thoi, and X. Xu. A novel Galerkin-like weakform and a superconvergent alpha finite element method (SαFEM) for mechanics problems using triangular meshes. *Journal of Computational Physics*, 228:4055–4087, 2009. 2, 14, 15, 16

[Lov98] C. Lovadina. Analysis of a mixed finite element method for the Reissner–Mindlin plate problems. *Computer Methods in Applied Mechanics and Engineering*, 163:71 – 85, 1998. 47

[LTWZ11] L. De Lorenzis, I. Temizer, P. Wriggers, and G. Zavarise. A large deformation frictional contact formulation using nurbs-based isogeometric analysis. *International Journal for Numerical Methods in Engineering*, 87:1278–1300, 2011. 159

[LWNT04] K.M. Liew, J. Wang, T.Y. Ng, and M.J. Tan. Free vibration and buckling analyses of shear-deformable plates based on FSDT meshfree method. *Journal Sound and Vibration*, 276:997–1017, 2004. 10, 73, 74

[LWZ12] L. De Lorenzis, P. Wriggers, and G. Zavarise. A mortar formulation for 3d large deformation contact using NURBS-based isogeometric analysis and the augmented Lagrangian method. *Computational Mechanics*, 49:1–20, 2012. 159

[LXZNT08] G.R. Liu, X. Xu, G.Y. Zhang, and T. Nguyen-Thoi. A superconvergent point interpolation method (SC-PIM) with piecewise linear strain field using triangular mesh. *International Journal for Numerical Methods in Engineering*, 77:1439–1467, 2008. 16

[MH85] R.H. MacNeal and R.L. Harder. A proposed standard set of problems to test finite element accuracy. *Finite Elements in Analysis and Design*, 1:3–20, 1985. 138

[MLH92] O.G. McGee, A.W. Leissa, and C.S. Huang. Vibrations of cantilevered skewed trapezodial and triangular plates with corner stress singularities. *Mechanical Sciences*, 34:63–84, 1992. 61, 66, 67

[Mor63] L.S.D. Morley. Skew plates and structures. *Pergamon Press*, 1963. 56

[MRA11] D. Millan, A. Rosolen, and M. Arroyo. Thin shell analysis from scattered points with maximum-entropy approximants. *International Journal for Numerical Methods in Engineering*, 85(6):723–751, 2011. 130

[Nag99] T. Nagashima. Node-by-node meshless approach and its applications to structural analyses. *International Journal for Numerical Methods in Engineering*, 46:341–385, 1999. 31, 42, 52, 119

[NR08] L. Noëls and R. Radovitzky. A new discontinuous Galerkin method for Kirchhoff-Love shells. *Computer Methods in Applied Mechanics and Engineering*, 197:2901–2929, 2008. 130

[NTKNX$^+$11] N. Nguyen-Thanh, J. Kiendl, H. Nguyen-Xuan, R. Wüchner, K.U. Bletzinger, Y. Bazilevs, and T. Rabczuk. Rotation free isogeometric thin shell analysis using PHT-splines. *Computer Methods in Applied Mechanics and Engineering*, 200(47-48):3410–3424, 2011. 4

[NTNXBR11] N. Nguyen-Thanh, H. Nguyen-Xuan, S. Bordas, and T. Rabczuk. Isogeometric analysis using polynomial splines over hierarchical T-meshes for two-dimensional elastic solids. *Computer Methods in Applied Mechanics and Engineering*, 200(21-22):1892–1908, 2011. 4

[NTRHXB08] N. Nguyen-Thanh, T. Rabczuk, H.Nguyen-Xuan, and S. Bordas. A smoothed finite element method for shell analysis. *Computer Methods in Applied Mechanics and Engineering*, 198(2):165–177, 2008. 117

[NTRHXB10] N. Nguyen-Thanh, T. Rabczuk, H.Nguyen-Xuan, and S. Bordas. An alternative alpha finite element method free and forced vibration analysis of solids using triangular meshes. *Journal of Computational and Applied Mathematics*, 233(9):2112–2135, 2010. 53, 119, 130

[NTRHXB11] N. Nguyen-Thanh, T. Rabczuk, H.Nguyen-Xuan, and S. Bordas. An alternative alpha finite element method with stabilized discrete shear gap technique for analysis of Mindlin-Reissner plates. *Finite Elements in Analysis and Design*, 47(5):519–535, 2011. 125, 130

[NTRNXB08] N. Nguyen-Thanh, T. Rabczuk, H. Nguyen-Xuan, and S. Bordas. A smoothed finite element method for shell analysis. *Computer Methods in Applied Mechanics and Engineering*, 198:165–177, 2008. 13, 130

[NTV92] B. Nayroles, G. Touzot, and P. Villon. Generalizing the finite element method: diffuse approximation and diffuse elements. *Computational Mechanics*, 10:307–318, 1992. 42

[NXLCHNT10] H. Nguyen-Xuan, G.R. Liu, C.Thai-Hoang, and T. Nguyen-Thoi. An edge-based smoothed finite element method with stabilized discrete shear gap technique for analysis of Reissner-Mindlin plates. *Computer Methods in Applied Mechanics and Engineering*, 199(9-12):471–489, 2010. 52, 54

[NXNT08] H. Nguyen-Xuan and T. Nguyen-Thoi. A stabilized smoothed finite element method for free vibration analysis of mindlin-reissner plates. *Communications in Numerical Methods in Engineering*, inpress:doi: 10.1002/cnm.1137, 2008. 13

[NXRBD08a] H. Nguyen-Xuan, T. Rabczuk, S. Bordas, and J.F. Debongnie. A smoothed finite element method for plate analysis. *Computer Methods in Applied Mechanics and Engineering*, 197:1184–1203, 2008. 13

[NXRBD08b] H. Nguyen-Xuan, T. Rabczuk, S. Bordas, and J.F. Debongnie. A smoothed finite element method for plate analysis. *Computer Methods in Applied Mechanics and Engineering*, 197:1184–1203, 2008. 130

[OZ92a] O.C.Zienkiewicz and J.Z. Zhu. The superconvergent patch recovery and a posteriori error estimators. part 1: The recovery technique. *International Journal for Numerical Methods in Engineering*, 33:1331–1364, 1992. 108

[OZ92b] O.C.Zienkiewicz and J.Z. Zhu. The superconvergent patch recovery and a posteriori error estimators part 2: Error estimates and adaptivity. *International Journal for Numerical Methods in Engineering*, 33:1365–1382, 1992. 109

[PT97] L. Piegl and W. Tiller. *The NURBS Book*. 2nd edition, Springer-Verlag, Berlin, 1997. 77, 78, 109

[PT00] R. Piltner and R.L. Taylor. Triangular finite elements with rotational degrees of freedom and enhanced strain modes. *Computers and Structures*, 75:361–368, 2000. 2, 17

[PW06] T.H.H. Pian and C.C. Wu. Hybrid and incompatible finite element methods. *CRC Press*, Boca Raton, 2006. 48

[RA06a] T. Rabczuk and P. Areias. A meshfree thin shell for arbitrary evolving cracks based on an external enrichment. *Computer Modeling in Engineering and Sciences*, 16(2):115–130, 2006. 13, 159

[RA06b] T. Rabczuk and P.M.A. Areias. A meshfree thin shell for arbitrary evolving cracks based on an external enrichment. *Computer Methods in Applied Mechanics and Engineering*, 16(2):115–130, 2006. 130

[RAB07a] T. Rabczuk, , P.M.A. Areias, and T. Belytschko. A simplified meshfree method for shear bands with cohesive surfaces. *International Journal for Numerical Methods in Engineering*, 69(5):993–1021, 2007. 13

[RAB07b] T. Rabczuk, P.M.A. Areias, and T. Belytschko. A meshfree thin shell method for non-linear dynamic fracture. *International Journal for Numerical Methods in Engineering*, 72(5):524–548, 2007. 13, 159

[RAB07c] T. Rabczuk, P.M.A. Areias, and T. Belytschko. A meshfree thin shell method for non-linear dynamic fracture. *International Journal for Numerical Methods in Engineering*, 72:524–548, 2007. 130

[RB04a] T. Rabczuk and T. Belytschko. Cracking particles: A simplified meshfree method for arbitrary evolving cracks. *International Journal for Numerical Methods in Engineering*, 61(13):2316–2343, 2004. 159

[RB04b] T. Rabczuk and T. Belytschko. Cracking particles: A simplified meshfree methods for arbitrary evovling cracks. *International Journal for Numerical Methods in Engineering*, (61):2316–2343, 2004. 86

[RB05] T. Rabczuk and T. Belytschko. Adaptivity for structured meshfree particle methods in 2D and 3D. *International Journal for Numerical Methods in Engineering*, 63(11):1559–1582, 2005. 13

[RB06a] T. Rabczuk and T. Belytschko. Application of meshfree particle methods to static fracture of reinforced concrete structures. *International Journal of Fracture*, 137(1-4):19–49, 2006. 13, 159

[RB06b] T. Rabczuk and T. Belytschko. Application of particle methods to static fracture of reinforced concrete structures. *International Journal of Fracture*, (137):19–49, 2006. 86

[RB07a] T. Rabczuk and T. Belytschko. A three dimensional large deformation meshfree method for arbitrary evolving cracks. *Computer Methods in Applied Mechanics and Engineering*, (196):2777–2799, 2007. 86

[RB07b] T. Rabczuk and T. Belytschko. A three dimensional large deformation meshfree method for arbitrary evolving cracks. *Computer Methods in Applied Mechanics and Engineering*, 196(29-30):2777–2799, 2007. 159

[RBZ07] T. Rabczuk, S. Bordas, and G. Zi. A three dimensional meshfree method for static and dynamic multiple crack nucleation/propagation with crack path continuity. *Computational Mechanics*, 40(3):473–495, 2007. 13, 159

[Red93] J.N. Reddy. *An Introduction to the Finite Element Method*. 2nd Edition, McGraw Hill, New York, 1993. 18

[RGSB10] T. Rabczuk, R. Gracie, J.H. Song, and T. Belytschko. Immersed particle method for fluid-structure interaction. *International Journal for Numerical Methods in Engineering*, 81(1):48–71, 2010. 130

[RS08] T. Rabczuk and E. Samaniego. Discontinuous modelling of shear bands with adaptive meshfree methods. *Computer Methods in Applied Mechanics and Engineering*, (197):641–658, 2008. 86

[RZBNX08] T. Rabczuk, G. Zi, S. Bordas, and H. Nguyen-Xuan. A geometrically nonlinear three-dimensional cohesive crack method for reinforced concrete structures. *Engineering Fracture Mechanics*, (75):4740–4758, 2008. 86

[SCF$^+$04] T.W. Sederberg, D.L. Cardon, G.T. Finnigan, N.S. North, J. Zheng, and T. Lyche. T-splines and local refinement. *ACM Trans. Graphics*, 23:276–283, 2004. 4, 85, 108

[Sch46] I.J. Schoenberg. Contributions to the problem of approximation of equidistant data by analytic functions. *Quarterly of Applied Mathematics*, 4:112–141, 1946. 3

[SCM08] R.H. Stogner, G.F. Carey, and B.T. Murray. Approximation of Cahn–Hilliard diffuse interface models using parallel adaptive mesh refinement and coarsening with C^1 elements. *International Journal for Numerical Methods in Engineering*, (76):636–661, 2008. 92

[SDR04] B. Szabo, A. Duester, and E. Rank. The p-version of the finite element method. *Fundamentals, Encyclopedia in Computational Mechanics, Wiley, New York*, 1:Chapter 5, 2004. 83

[SDS$^+$12] Dominik Schillinger, Luca Dede, Michael A. Scott, John A. Evans, Michael J. Borden, Ernst Rank, and Thomas J. R. Hughes. An isogeometric design-through-analysis methodology based on adaptive hierarchical refinement of NURBS, immersed boundary methods, and T-spline CAD surfaces. *Computer Methods in Applied Mechanics and Engineering*, 2012. 108

[Sed] 87, 109

[SFMH08] R. Sevilla, S. Fernandez-Mendez, and A. Huerta. Nurbs-enhanced finite element method (NEFEM). *International Journal for Numerical Methods in Engineering*, 76:56–83, 2008. 83

[SHBB12] P. Stein, M.-C. Hsu, Y. Bazilevs, and K. Beucke. Operator and template-based modeling of solid geometry for isogeometric analysis with application to vertical axis wind turbine simulation. *Computer Methods in Applied Mechanics and Engineering*, 213-216:71–83, 2012. 159

[SJ99] J.M.A. César De Sá and R.M. Natal Jorge. New enhanced strain elements for incompatible problems. *International Journal for Numerical Methods in Engineering*, 44:229–248, 1999. 2, 47

[SR90] J.C. Simo and M.S. Rifai. A class of mixed assumed strain methods and the method of incompatible modes. *International Journal for Numerical Methods in Engineering*, 29:1595–1638, 1990. 2, 17, 47

[SR08] A. Shaw and D. Roy. NURBS-based parametric mesh-free methods. *Computer Methods in Applied Mechanics and Engineering*, 197:1541–1567, 2008. 83

[SR11] Dominik Schillinger and Ernst Rank. An unfitted hp-adaptive finite element method based on hierarchical b-splines for interface problems of complex geometry. *Computer Methods in Applied Mechanics and Engineering*, 200:3358–3380, 2011. 159

[SZBA03] T.W. Sederberg, J. Zheng, A. Bakenov, and A. Nasri A. T-splines and T-NURCCs. *ACM Trans. Graphics*, 22:477–484, 2003. 4, 85

[TA93] R.L. Taylor and F. Auricchio. Linked interpolation for Reissner–Mindlin plate element: Part II-A simple triangle. *International Journal for Numerical Methods in Engineering*, 36:3043 – 3056, 1993. 47, 53, 54

[TCB05] T.J.R.Hughes, J.A. Cottrell, and Y. Bazilevs. Isogeometric analysis: CAD, finite elements, NURBS, exact geometry and mesh refinement. *Computer Methods in Applied Mechanics and Engineering*, 194:4135–4195, 2005. 84

[TG70] S.P. Timoshenko and J.N. Goodier. *Theory of Elasticity (3rd edn)*. McGraw, New York, 1970. 19, 20, 68, 72, 73, 75, 94, 97, 114

[TH85] A. Tessler and T.J.R. Hughes. A three-node Mindlin plate element with improved transverse shear. *Computer Methods in Applied Mechanics and Engineering*, 50:71–101, 1985. 52, 53

[TNXNT$^+$12] Chien H. Thai, H. Nguyen-Xuan, N. Nguyen-Thanh, T-H. Le, T. Nguyen-Thoi, and T. Rabczuk. Static, free vibration and buckling analysis of laminated composite Reissner-Mindlin plates using NURBS-based isogeometric approach. *International Journal for Numerical Methods in Engineering*, 91:571–603, 2012. 125

[TS90] L.G. Tham and H.Y. Szeto. Buckling analysis of arbitrary shaped plates by spline finite strip method. *Computers and Structures*, 36:729–735, 1990. 72, 73, 75

[TWK59] S. Timoshenko and S. Woinowsky-Krieger. *Theory of Plates and Shells (2nd edn)*. McGraw-Hill, New York, 1959. 130

[UO10] P.-A. Ubach and E. Onate. New rotation-free finite element shell triangle accurately using geometrical data. *Computer Methods in Applied Mechanics and Engineering*, 199(5-8):383–391, 2010. 130

[UY09] Tae-Kyoung Uhm and Sung-Kie Youn. T-spline finite element method for the analysis of shell structures. *International Journal for Numerical Methods in Engineering*, 80:507–536, 2009. 131

[VGJS12] A.-V. Vuong, C. Giannelli, B. Jüttler, and B. Simeon. A hierarchical approach to adaptive local refinement in isogeometric analysis. *Computer Methods in Applied Mechanics and Engineering*, 200:3554–3567, 2012. 108

[WC04] D. Wang and J.S. Chen. Locking-free stabilized conforming nodal integration for meshfree Mindlin-Reissner plate formulation. *Computer Methods in Applied Mechanics and Engineering*, 193:1065–1083, 2004. 130

[WC08] D. Wang and J.S. Chen. A hermite reproducing kernel approximation for thin plate analysis with sub-domain stabilized conforming integration. *International Journal for Numerical Methods in Engineering*, 74:368–390, 2008. 130

[WFC08] W.A. Wall, M.A. Frenzel, and C. Cyron. Isogeometric structural shape optimization. *Computer Methods in Applied Mechanics and Engineering*, 197:1976–1988, 2008. 83

[WHL$^+$08] H. Wang, Y. He, X. Li, X. Gu, and H. Qin. Polycube splines. *Computer-Aided Design*, 40:721–733, 2008. 108

[Wri06] P. Wriggers. *Computational Contact Mechanics*. 2th Edition, Springer, Berlin, 2006. 159

[WYJ+11] Jun Wang, Zhouwang Yang, Liangbing Jin, Jiansong Deng, and Falai Chen. Parallel and adaptive surface reconstruction based on implicit PHT-splines. *Computer Aided Geometric Design*, 28:463–474, 2011. 110

[ZL88] O.C. Zienkiewicz and D. Lefebvre. A robust triangular plate bending element of the Reissner–Mindlin type. *International Journal for Numerical Methods in Engineering*, 26:1169–1184, 1988. 47

[ZS95] C. Zhao and G.P. Steven. Analytical solutions of mass transport problems for error estimation of finite/infinite element methods. *Communications in Numerical Methods in Engineering*, 11:13–23, 1995. 37

[ZS96] C. Zhao and G.P. Steven. Asymptotic solutions for predicted natural frequencies of two-dimensional elastic solid vibration problems in finite element analysis. *International Journal for Numerical Methods in Engineering*, 39:2821–2835, 1996. 37

[ZT00] O.C. Zienkiewicz and R.L. Taylor. *The Finite Element Method*. 5th Edition, Butterworth Heinemann, Oxford, 2000. 1, 13, 16, 39

[ZTZ05] O.C. Zienkiewicz, R.L. Taylor, and J.Z. Zhu. *The Finite Element Method, sixth edition*. Elsevier Butterworth-Heinemann, Oxford, 2005. 113

[ZXZ+93] O.C. Zienkiewicz, Z. Xu, L.X. Zeng, A. Samuelsson, and N.E. Wiberg. Linked interpolation for Reissner-Mindlin plate elements: part I-a simple quadrilateral. *International Journal for Numerical Methods in Engineering*, 36:3043–3056, 1993. 52

Academic Curriculum Vitae

Nhon Nguyen-Thanh
Institute of Structural Mechanics
Bauhaus-University Weimar
Marienstrasse 15, 99423 Weimar, Germany
Email: nhon.nguyen.thanh@uni-weimar.de

Education

- Ph.D: Institute of Structural Mechanics, Bauhaus-University Weimar, Germany, 2013.
- M.Sc: European Master in Engineering Science of Mechanics of Construction (EMMC), Liege of University, Belgium, 2007.
- B.S: Department of Civil Engineering, University of Architecture, HoChiMinh City, Vietnam, 2003.

Research Interests

- Isogeometric Analysis
- Computational Mechanics
- Composite Materials
- Fracture Mechanics
- Numerical Methods

Scientific Activities

- Reviewer for international journals:
  - Computer Methods in Applied Mechanics and Engineering
  - British Journal of Applied Science & Technology
  - Journal of Solids and Structures
  - Journal of Applied Mathematics and Computing
  - Advances in Computational Mathematics
  - International Journal of Engineering, Science and Technology
  - Journal of Computational and Applied Mathematics
  - Mechanics of Advanced Materials and Structures
  - International Journal of Computational Methods
  - Journal of Mechanical Engineering Research
  - Journal of Civil Engineering (KSCE)

Professional Activities and Awards

- December 2011 to November 2012: Visiting academic at the University of the Witwatersrand, South Africa.
- October 2011: Best student award at Bauhaus University Weimar, Germany.
- February to April 2011: Visiting academic at the Cardiff university, UK.

Skills and Expertise

Matlab, Fortran, C++, Latex, Ansys, Abaqus, Numerical Analysis, Material Science, Finite Element Analysis.

Publications Refereed Journal Articles

International Journals

1. **N. Nguyen-Thanh**, H.Nguyen-Xuan, N.M. Nguyen, X. Zhuang, P. Areias, L. De Lorenzis and T. Rabczuk. An extended isogeometric shell analysis with Kirchhoff-Love elements, submitted, 2013.

2. H. Nguyen-Xuan, Loc V. Tran, **N. Nguyen-Thanh**, P. V. Nguyen and Stephane P.A. Bordas. Extended isogeometric elements for limit analysis of cracked structures, under review, 2013.

3. Lei Chen, **Nhon Nguyen-Thanh**, Yuan Tong Gu, Hung Nguyen-Xuan, Timon Rabczuk, Stephane Bordas and Georges Limbert. Explicit finite deformation analysis of isogeometric membranes, under review, 2013.

4. **N. Nguyen-Thanh**, J. Muthu, X. Zhuang, T. Rabczuk. An adaptive three-dimensional RHT-splines formulation in linear elasto-statics and elasto-dynamics, *Computational Mechanics*, in press, 2013.

5. Chien H. Thai, H. Nguyen-Xuan, S.P.A. Bordas, **N. Nguyen-Thanh** and T. Rabczuk. Isogeometric analysis of laminated composite plates using the higher-order shear deformation theory, *Mechanics of Advanced Materials and Structures*, in press, 2013.

6. C. Thai-Hoang, H. Nguyen-Xuan , **N. Nguyen-Thanh**, T.H. Le, T.Nguyen-Thoi, T. Rabczuk. Static, free vibration and buckling analyses of laminated composite Reissner-Mindlin plates using NURBS-based isogeometric approach, *International Journal for Numerical Methods in Engineering*, 91(6):571-603, 2012.

7. H. Nguyen-Xuan, T. Rabczuk, T. Nguyen-Thoi , T. N. Tran, **N. Nguyen-Thanh**. Computation of limit and shakedown loads using a node-based smoothed finite element method, *International Journal for Numerical Methods in Engineering*, 90(3):287-310, 2012.

8. **N. Nguyen-Thanh**, J. Kiendl, H. Nguyen-Xuan, R. Wüchner, K.U. Bletzinger, Y. Bazilevs, T. Rabczuk. Rotation free isogeometric thin shell analysis using PHT-splines, *Computer Methods in Applied Mechanics and Engineering*, 200(47-48):3410-3424 ,2011.

9. C. Thai-Hoang, **N. Nguyen-Thanh**, H. Nguyen-Xuan, T. Rabczuk. An alternative alpha finite element method with discrete shear gap technique for analysis of

laminated composite plates, *Applied Mathematics and Computation*, 217(17):7324-7348, 2011.

10. **N. Nguyen-Thanh**, H. Nguyen-Xuan, S. Bordas, T. Rabczuk. Isogeometric analysis using polynomial splines over hierarchical T-meshes, *Computer Methods in Applied Mechanics and Engineering*, 200(21-22):1892-1908, 2011.
11. **N. Nguyen-Thanh**, Timon Rabczuk, H. Nguyen-Xuan, Stephane Bordas. An alternative alpha finite element method with stabilized discrete shear gap technique for analysis of Mindlin-Reissner plates, *Finite Elements in Analysis and Design*,47(5):519-535, 2011.
12. C. Thai-Hoang, **N. Nguyen-Thanh**, H. Nguyen-Xuan, Timon Rabczuk, Stephane Bordas. A cell based smoothed finite element method for free vibration and buckling analysis of shells, *KSCE Journal of Civil Engineering*,15(2):347-361, 2011.
13. **N. Nguyen-Thanh**, C.Thai-Hoang, H. Nguyen-Xuan, Timon Rabczuk. A smoothed finite element method for the static and free vibration analysis of shells. Journal of Civil Engineering and Architecture, 4(34):13-25, 2010.
14. H. Nguyen-Xuan, T. Rabczuk, **N. Nguyen-Thanh**, T. Nguyen-Thoi, Stephane Bordas. A node-based smoothed finite element method (NS-FEM) for analysis of Reissner-Mindlin plates. *Computational Mechanics*, 46:679-701, 2010.
15. **N. Nguyen-Thanh**, Timon Rabczuk, H. Nguyen-Xuan, Stephane Bordas. An alternative alpha finite element method (AαFEM) free and forced vibration analysis of solids using triangular meshes, *Journal of Computational and Applied Mathematics*, 233:2112-2135, 2010.
16. **N. Nguyen-Thanh**, Timon Rabczuk, H. Nguyen-Xuan, Stephane Bordas. A smoothed finite element method for shell analysis, *Computer Methods in Applied Mechanics and Engineering*, 198:165-177, 2008.

Conference papers

1. **N. Nguyen-Thanh**, J. Muthu, T. Rabczuk. A three dimensional static and free vibration analysis using RHT-spline formulation. *Conference on Computational and Applied Mechanics*, Johannesburg, South Africa, September-2012.
2. **N. Nguyen-Thanh**, H. Nguyen-Xuan, S. Bordas, T. Rabczuk. Isogeometric finite element analysis using polynomial splines over hierarchical T-meshes,

9*th World Congress on Computational Mechanics (WCCM)*, Sydney, Australia, July-2010.

3. **N. Nguyen-Thanh**, H. Nguyen-Xuan, S. Bordas, T. Rabczuk. Isogeometric finite element analysis using polynomial splines over hierarchical T-meshes, *IV European Conference on Computational Mechanics (ECCM)*, Paris, France, May-2010.

4. **N. Nguyen-Thanh**, T. Rabczuk. A smoothed finite element method for the static and free vibration analysis of shells, *18th International Conference on the Application of Computer Science and Mathematics in Architecture and Civil Engineering*, Weimar, Germany, July-2009.